An Adaptive Amplifier for Cuff Imbalance Correction and Interference Reduction in Nerve Signal Recording

By

IASONAS F. TRIANTIS

A thesis submitted for the degree of Doctor of Philosophy

June 2005

Department of Electronic and Electrical Engineering

UNIVERSITY COLLEGE LONDON

ProQuest LLC
789 East Eisenhower Parkway
P.O. Box 1346
Ann Arbor, MI 48106-1346

The author's personal motives for pursuing this field of research lie in his belief that engineering can have a directly humanitarian role in improving current medical treatment practices, which until now have been mainly based on chemical rather than electrical interventions. The fact that electrical signals are the main form of transmission of information within the human body offers a great chance for investigating new routes for rehabilitation of conditions previously considered untreatable. The author believes that it is an honour to use his studies in the field of electronic engineering for contributing to the advance of medical electronics.

To my family

Abstract

Damage to the central nervous system because of spinal cord injury (SCI) or stroke results in loss of motor function in various parts of the body, mainly these located below the area of injury. Some of the most common consequences include loss of mobility and continence, degrading the quality of life of anyone affected. Currently, conventional medicine does not offer any method for curing the damage and fully restoring function, and therapy is focused on rehabilitation. Neuroprostheses may assist in partial restoration of function and mobility using functional electrical stimulation (FES), which involves the process of passing pulses of electrical current into the muscle tissue of interest or into nerve branches, which cause the activation of the muscle.

Fully implantable FES systems may use naturally occurring nerve signals (electroneurogram or ENG) as feedback or control inputs. However, the usefulness of ENG signals recorded from nerve cuffs depends on the amount of muscle signal (electromyogram or EMG) interference present. The EMG amplitude can be as large as three orders of magnitude greater than the μV ENG and their spectra overlap. The cuff electrode, used for measuring ENG, is appropriate for chronic implantation and reduces interference when made tripolar. Tripolar cuff amplifier configurations include the "quasi tripole" (QT) and the "true tripole" (TT). However, as a result of parameters including cuff asymmetries and impedance irregularity due to tissue growth, cuff performance suffers from imbalance, which causes widely reported EMG contamination at the output of these amplifier configurations.

Therefore, in order to avoid the use of high order filters for removing the EMG, a system has been developed to balance the cuff and remove EMG interference. This thesis describes the design, implementation and evaluation, both in-vitro and in-vivo, of an adaptive amplifier configuration, named the "adaptive tripole" (AT). The AT performs both tasks of imbalance correction and interference reduction simultaneously and the extracted ENG can be used in neuroprosthetic devices for the improvement of FES systems. The system has been built both in discrete-component and in integrated forms, the first one used to evaluate the principle and to form the specifications for the latter. Prior to the full description of the system, some limited research is presented on the causes of imbalance, to clarify the causes of the problem and to better define the specifications of the AT. The relationship between imbalance and cuff proximity to interfering fields is also examined.

The results from experiments on the discrete AT indicated that it provides up to 60 times greater output signal-to-interference ratio (SIR) than the TT for high imbalance values (>20%). Also, even when disadvantaged by the presence of two imbalances due to proximity effects it performs better than both the TT and the QT in 60% of the cases. In-vitro experiments on the IC version demonstrated the output SIR of the AT to be up to 200 to 300 times greater than the QT and TT equivalent SIRs respectively, for 40% imbalance. The average AT output SIR achieved by the IC version was 2:1 and the highest was approximately 4:1. The system will be used in the Conditional Neuromodulation (CNM) implant developed in the departments of Electronic and Electrical Engineering and Medical Physics and Bioengineering in UCL, and will contain the AT as well as a stimulator and an RF power and signal transmission transcutaneous link.

Acknowledgements

I would like to express my greatest thanks to Andreas Demosthenous, my supervisor, for the guidance, the support, the knowledge, the collaboration and the friendship throughout my PhD. I am grateful for all of these and for his very important contribution to the work done in this project.

I would also like to express my thanks and appreciation to Prof. Nick Donaldson, my second supervisor, for the very important practical medical physics knowledge he gave me and for introducing me to the experimental processes that gave me some of my most significant results.

I would like to thank Prof. J.J. Struijk and the people in Aalborg University for the hospitality and the useful experimental experience they offered me.

I would like to express my gratitude to my family for their immense help, support and contribution and for being there for me all these years. I am proud to be a member of this "crazy" family...

I would like to express additional thanks to my parents for their guidance and for being much more than parents to me. I would like to thank Katerina, my sister, for being my very best friend and Alex Dimitrakoudis, my best friend, for being like a brother to me. Also I want to thank, in alphabetical order, Alex "Karp", Stamatis "brother in arms", Takis and Vagelis "Svig" my best friends. I also want to thank Vaso, Maria and Eleni for their friendly encouragement, which I appreciate. To all of you above, I want to say a huge thank you for being there for me and supporting my effort through the tough times.

I would like to thank my colleagues and good friends Giannis Liabotis, Anne Vanhoest, Massimo Audrito, Martin Schuettler, Veronique Sauret, Mladen Panovic, Jide Adeniran, Mouhammed Rahal, Sarmad Al-Taei, Xiao Liu and Yiqiang Zhao for their good company during relaxing coffee brakes accompanied with our strictly technical and scientific conversations...

I would like to thank Panos Liatsis for being a good friend and for his interest and support during my effort.

Many thanks to Mike Brent, Tom Crummey, Scott Landers and Lee Heagney for their very prompt and helpful technical support.

To Viky, "ta"...

Finally, to Prof. John Taylor, I would like to say thank you for showing me how to swim by dropping me in the middle of the ocean. You have helped me understand how strong I can be.

Επιτελους τελος!!! Σας ευχαριστω ολους...

Table of contents

Chapter 1

Chapter 2

Chapter 3

Chapter 4

Chapter 5

Chapter 6

Chapter 7

Glossary of terms

Action current	Ionic current due to the action potential
Action potential	Nerve "firing" pulse-like potential
AT	Adaptive tripole amplifier (main subject of this thesis)
CAP	Compound action potential (nerves in a bundle activated together)
CNM	Conditional neuromodulation-implant for avoiding nerve cutting
CNS	Central nervous system (brain and spinal cord)
Cuff	Insulating tube with ring electrodes, placed around nerve
Cuff imbalance	Cuff electrode systematic error (also in text as *imbalance*)
EMG	Electromyogram, muscle electrical signal
ENG	Electroneurogram, neural electrical signal
EPSP	Excitatory postsynaptic potential
Extracellular	External to the nerve membrane
Fascicle	Small nerve group (roughly joint destination) inside nerve bundle
FES	Functional electrical stimulation
Intracellular	Inside the nerve cell
In-vitro	Experiments in the laboratory, emulating in-vivo conditions
In-vivo	Animal experiments
IPSP	Inhibitory postsynaptic potential
M-wave	Compound muscle signal (generated by stimulation)
Myelin	Insulating cover of myelinated nerve fibres
Nerve bundle	Large group of fibres or fascicles exiting spine
Node of Ranvier	Myelin insulation "gap"
PNS	Peripheral nervous system (voluntary and involuntary)
QT	Quasi-tripole – common neural amplifier configuration
SCI	Spinal cord injury
SFAP	Single nerve fibre action potential
SIR	Signal-to-interference ratio. Here: ENG/EMG amplitude ratio
Stimulus artefact	Interference due to stimulus pulses
TT	True-tripole – common neural amplifier configuration
UPAP	Unidirectional propagating action potential

Chapter 1

INTRODUCTION

Damage to the central nervous system because of spinal cord injury (SCI) or stroke results in loss of motor function in various parts of the body, mainly these located below the area of injury. As a result tens of thousands of people involved in accidents every year (about 11,000 in Europe every year [1]) see their life becoming a daily routine of continuous effort for meeting their basic needs.

According to the USA National Institute of Neurological Disorders and Stroke (NINDS) SCI is more common to people in their early twenties, because of lifestyle, and to elderly people due to falls and spinal disease [2]. In the first case patients usually require treatment for decades and this is both devastating and costly. Some of the most common consequences of spinal cord injury (figure 1.1) include loss of mobility and continence, degrading the quality of life of anyone affected and resulting in loss of independence, as continuous support by other people becomes a necessity. Currently, conventional medicine does not offer any method for curing the damage and fully restoring function, and therapy is focused on rehabilitation, which involves training and exercise to assist patients to get used to their new condition and to re-establish some daily routine, although full independence is usually not achievable. On top of the

functional problems, treatment sometimes involves solutions that are unpleasant and can even introduce social difficulties [3].

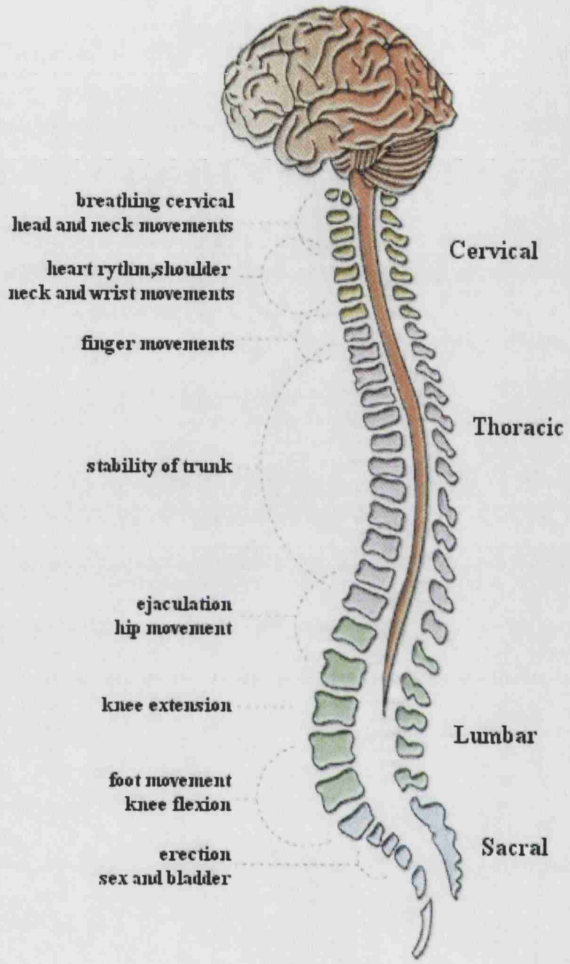

Figure 1.1 Bodily functions affected by spinal cord injury (figure from [4]).

1.1 Neuroprostheses

1.1.1 Neuroprostheses and Functional Electrical Stimulation

Neuroprostheses may assist in partial restoration of function and mobility using functional electrical stimulation (FES), which involves the process of passing pulses of electrical current into the muscle tissue of interest or into nerve branches, which cause the activation of the muscle. It is possible to use FES for rehabilitation in the cases mentioned above, as following SCI most functions of the peripheral nerves are usually not affected. Implantable stimulators have been introduced in 1959 with the

development of the heart pacemaker and the first FES systems were reported in the early sixties. Since then such systems have developed to fully implantable devices, using RF links for the power supply and for the transmission of control signals. Various electrodes, such as nerve cuffs (figure 1.2(a) - described in chapter 2), book electrodes, helical electrodes (figure 1.2(b)) and epimysial electrodes apply stimulus pulses either to nerves or directly on muscle motor points [5-7].

(a) (b)

Figure 1.2 (a) Cuff electrode used for stimulation (picture from [6]) (b) Huntington helical electrode (picture from [7]).

Enhanced stimulators allow the application of *selective stimulation*, aiming to achieve selectivity of small groups of muscles or even individual ones, by stimulating selected nerves of a bundle (group of nerve fibres). This allows the implantation of both the device and the electrodes relatively close together, with the electrodes placed close to the spinal cord, making the system more robust, requiring less cabling and allowing the control of several organs from a specific location. Another requirement for FES systems is the capability of applying *anodal blocking*, a method that allows the recruitment of smaller diameter fibres first using specially shaped stimulus waveforms, which prevent the conduction in thicker nerve fibres, thus avoiding the "inverse recruitment" of nerve fibres.

Anodal blocking in combination with asymmetrical cuffs can also be used for generating unidirectional propagating action potentials (UPAPs). These are particularly useful because in conventional stimulation the neural activation is bidirectional as shown in figure 1.3. Thus, it excites both motor and sensory nerves that may exist in a nerve bundle resulting not only in activating a specific muscle but also causing pain and unwanted reflexes by activating sensory nerves that carry signals towards the spinal cord.

Therefore using UPAPs and anodal blocking, restoration of function may be achieved without the need for rhisotomy (nerve root cutting) of sensory pathways that may be

intact after an injury, allowing pain avoidance and prevention of sensation during stimulation [5].

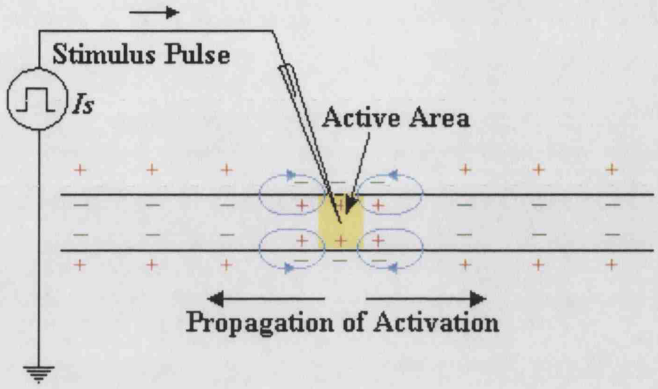

Figure 1.3 Stimulation applied to a nerve fibre using a needle electrode (picture from [8])

1.1.2 Neural recording for FES control

Stimulators can be used in open-loop FES systems, requiring external control of the stimulus, where the stimulation parameters are usually fixed and the usage of the device by the patient has to be planned based on a daily routine. Such systems have been applied [9] and work satisfactorily, but they can result in muscle fatigue, they cannot compensate for external disturbances and they often require rhisotomy to be applied. For this reason closed-loop systems are the main focus of FES research reducing the need for external control and helping in avoiding rhisotomy [10-12]. In conventional closed-loop stimulators, information is collected from sources around the body, using artificial sensors attached to it to monitor parameters like joint angles or joint torque (figure 1.4(a)) and feed information to a controller that applies appropriate control to the stimulator [13]. However, artificial sensors pose various disadvantages, including low quality of information, attachment difficulties, drift and increased power consumption [3]. Moreover a system involving artificial sensors cannot easily be fully implanted.

For this reason the use of natural sensors has been the subject of recent research attempting to use naturally occurring nerve signals for control inputs or feedback to stimulators (figure 1.4(b)), making use of information from various parts of the body, greatly improving the operation of FES neuroprostheses for application in cases involving phrenic pacing, bladder emptying, foot-drop, standing and hand grasp [3, 10-

12, 14-18]. As mentioned previously, SCI leaves most of the peripheral nerves under the area of injury intact, although the patient cannot use them for voluntarily commanding organs nor for sensing. Recordings can be obtained from sensory nerves containing afferent nerve fibres from mechanoreceptors located in the skin and proprioceptors located in muscles [19-21].

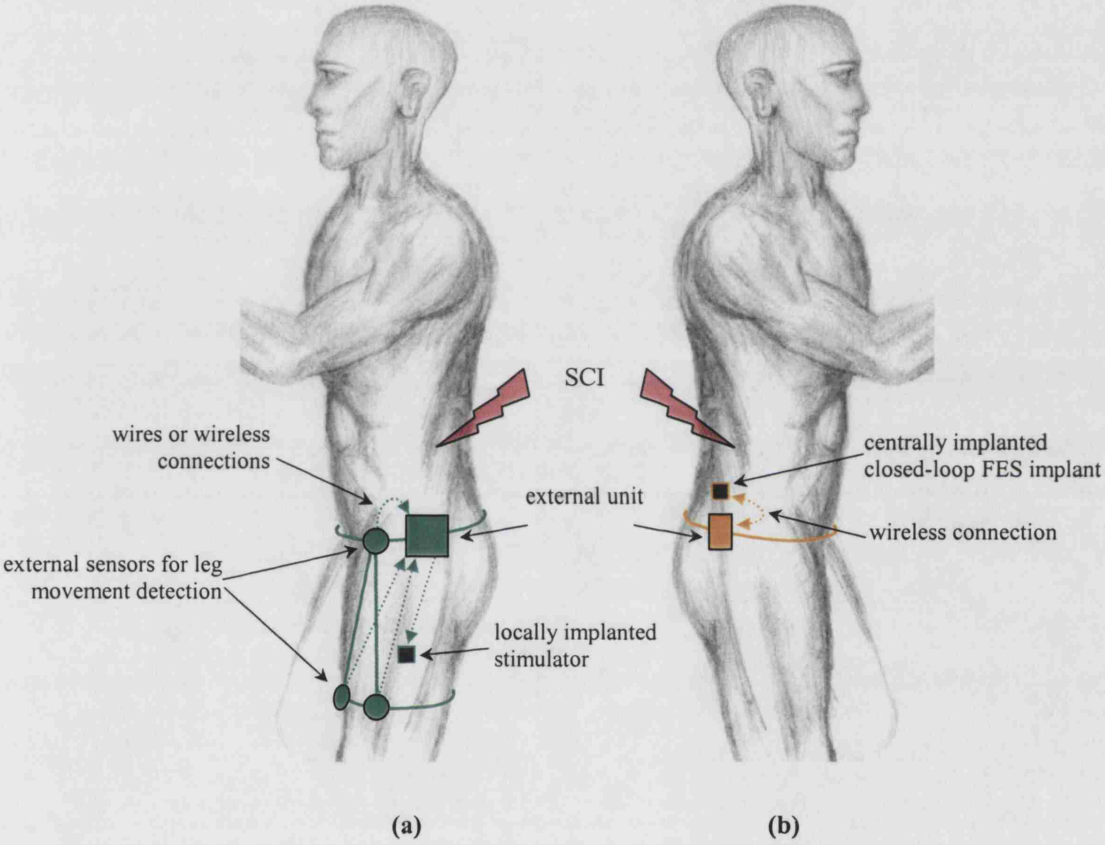

Figure 1.4 Examples of closed loop FES systems, with stimulation control making use of (a) artificial external sensors (*imaginary example by author*) and (b) neural monitoring. In the first case some nerve branches have to be cut and the overall system is more bulky. In the second case a compact system can be used without severing any nerves and some of the stimulation can take place automatically, without external intervention.

In order to obtain natural sensory information and use it for feedback several tasks need to be accomplished. Studies have to be conducted on the nerve that will be used for the recordings, using histological and anatomical analyses and the diameter of the nerve fibre or bundle in interest has to be measured. These data will allow for the specification and design of the appropriate neural interface. The material and shape of electrodes to

be used will depend on the application and their effect on the bioelectric signals involved has to be established.

After the electrodes are developed and tested, a data acquisition system has to be designed. This will have to take into account all the neural interface factors that affect its input signal and it has to be designed so that the signal amplitude is adequately amplified over the maximum possible spectrum, in order to retain most of the signal features intact. Noise and interference have to be taken into account, and if implantable, the system will also have to be efficient in terms of power. At the same time it should obtain an adequate dynamic range with linear behaviour using the supply rails available in the implant.

The next step is to process the extracted neural signal and then some post-processing will be applied to achieve feature definition. Making the front-end analogue will allow signal preamplification and suppression of interference without the need of a high resolution ADC stage and a digital pre-processing stage that would increase area, power consumption and complexity. Converting the extracted neural signal into digital after amplifying it, will allow for better feature extraction and then a post-processing stage can select the appropriate threshold of neural activity for triggering a stimulator.

1.1.3 The need for an improved neural amplifier for implantable FES systems

Cuff electrodes are the most suitable electrodes to use for long-term recordings. They are suitable for chronic implantation [22] and reduce interference when made tripolar [23]. However, the usefulness of the recorded neural signal, the electroneurogram (ENG), depends on the interference from other bio-potentials, the dominant one being the muscle signal or electromyogram (EMG). The EMG amplitude is in the order of a few mV, sometimes three orders of magnitude larger than the μV ENG detected by cuff electrodes, and the spectra of the two signals overlap.

The standard, fixed-gain amplifier configurations used with tripolar cuffs (described in chapter 2) achieve EMG cancellation by employing the properties of cuff electrodes when these operate similarly to their ideal model. In theory, provided ideal cuff parameters are achieved, the EMG can be cancelled and only the ENG is present at the

output of the tripolar ENG amplifiers. However, the cuff is always affected by factors like manufacturing tolerances and biological changes in the neural interface after implantation, contributing to the presence of systematic errors in the cuff characteristics that degrade the performance of neural amplifiers. As a result it has been extensively reported that EMG interference contaminates measurements significantly reducing signal quality or even eradicating the ENG signal of interest [10-12, 16, 18, 21, 22, 24-35].

Although the frequency spectra of the ENG and the EMG overlap, the peaks of their power spectral densities differ by about an order of magnitude. Based on that, methods involving very high-order digital filters have been proposed for separating ENG from the slower EMG [18, 30]. However, since the spectra of the ENG and EMG signals overlap considerably [16, 24], the use of post-filtering results in reduction of the usable ENG bandwidth. Other ways for extracting high fidelity ENG could involve digital signal post-processing using microprocessors and specialized algorithms (e.g., blind signal separation [36]). Clearly, all of the above methods increase the overall complexity of the recording system dramatically and they are essentially non-implantable solutions.

In this project, an adaptive tripolar amplifier configuration has been proposed and developed to automatically compensate for cuff errors and remove EMG interference while recording naturally-occurring ENG [35, 37, 38]. The system uses a frequency independent method, thus reducing the interference and at the same time retaining neural information throughout the bandwidth of interest. The amplifier has evolved from previous theoretical proposals [34] and has been analysed in system-level, and then developed and tested in-vitro and in-vivo using discrete components. Finally an integrated and fully implantable realisation has been designed, developed and tested.

1.2 Motive for this project and project aims

The project described in this thesis is one of the main parts of the Conditional Neuromodulation (CNM) implant, which provided the motive for researching an improved neural amplifier. The implant is under development in the departments of

Electronic and Electrical Engineering and Medical Physics in University College London, for treating neurogenic incontinence. A block diagram of the implant is illustrated in figure 1.5, along with connections to cuff electrodes fitted on nerve bundles close to the spinal cord, depicted for visualising the proposed connectivity.

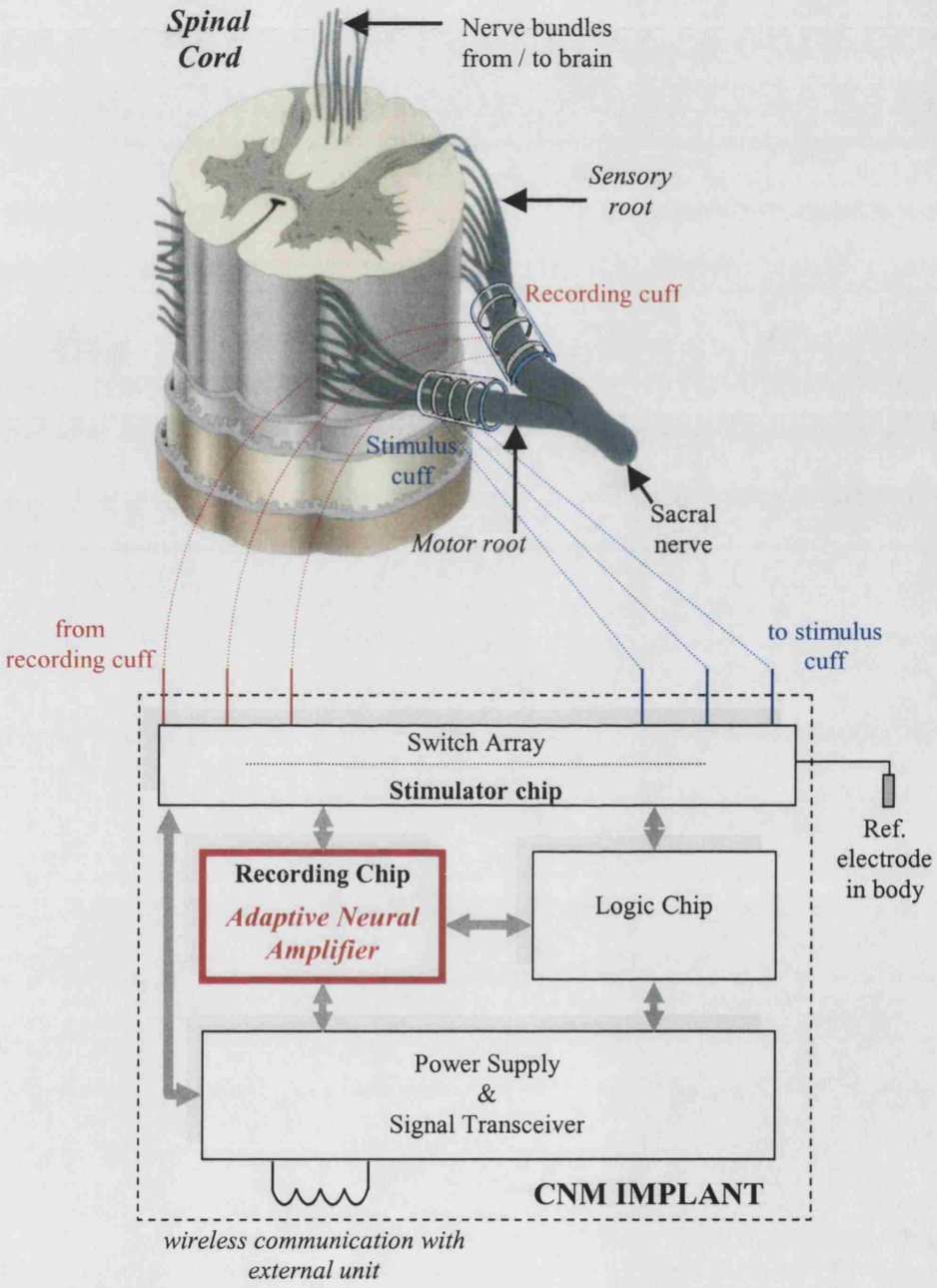

Figure 1.5 The main blocks of the CNM implant and representation of cuff connections to sensory and motor roots of the sacral nerve (spine picture from [39]).

The main aim of this overall project is the use of ENG recording as feedback to a stimulator employing selective stimulation to achieve neuromodulation, which could allow the avoidance of dorsal root rhisotomy. The implant connects to four cuffs, all four of which can be used for stimulation (approximately half cuff length of cuffs used for recording) and two can be also used for recording.

The other main parts of the implant are being developed in the context of other PhD projects within the two departments involved. They include an integrated stimulator, that allows the application of selective stimulation, anodal blocking and generation of UPAPs together developed by Martin Bugbee [5] and the transcutaneous (through the skin) RF transceiver is developed by Lixia Zhou.

The aims of the project described here, include the creation of an IC neural amplifier configuration whose power consumption will be within the acceptable levels for the CNM implanted device (10mW). The device will allow the detection of naturally-occurring ENG signals to be used for controlling the stimulator of the implant. Acquisition will be stopped during stimulation, as the recording cuffs will switch to stimulation mode. The *main aim* of the amplifier will be to reduce muscle interference and, at the same time, compensate for cuff error. Objectives include investigation of cuff error sources and comparison of the amplifier with the previous fixed-gain configuration that it has been based on.

1.3 Novelty and contributions of this thesis

Although the central aim of this thesis was the development of an implantable neural amplifier, to the knowledge of the author, there is original content in all the main research chapters (chapters 3-6). Chapter 2 serves in collecting relevant information from literature to compose the theoretical background.

The cuff error (termed cuff imbalance) investigation in chapter 3 presents totally original work both in presenting the cuff in bioelectric field simulations and in evaluating the simulations and expanding the research experimentally. The methods used and the parameters investigated have not been previously presented in literature.

Although bioelectric fields are not by any means the main context of the project, the cuff interface had to be investigated, mainly to understand the sources of cuff parameter variation as well as the range of their variation. Equally important for the specifications of the adaptive system proposed was to estimate whether the parameters would vary slowly with time after implantation (days) or whether a faster response was necessary (seconds). The in-vivo experiments conducted supported some of the previous findings and highlighted the severity of some sources of error was not very significant in real muscles.

Although the system developed has been previously described by Rahal in [34] as a concept in terms of ideal Simulink® blocks, mostly as a possible future development, it was never described using system-level mathematics. The realisation of a theoretical system cannot be attempted without defining its basic operational specifications. Some specifications were already defined by the implant requirements and chapter 3 contributed to them as well. Chapter 4 was very important in describing the system operation in ways that allowed for error parameters to be included. In this way, the design parameters and guidelines for the system development were formed. The system-level calculations presented in the chapter have not been developed elsewhere.

Although chapter 4 appears before chapter 5, as is the logical order, some of the error sources described in it were first observed in the discrete-component system. Thus the development of this version of the amplifier configuration turned out to be very useful. Again the experiments conducted and the results obtained are novel and they were very significant in establishing that the system could be realised. The in-vitro experiments conducted demonstrated clearly the extent of the improvement that could be achieved by the newly developed configuration. The in-vivo experiments also demonstrated the system's superiority in the majority of the tests. Novelty can also be found in the in-vitro experimental setup ("obstacle experiment") and in the comparative experiments between the newly introduced amplifier and previous configurations.

Finally chapter 6 describes a novel fully implantable ASIC that has been designed with minimum complexity based on the architecture of the discrete-component system. Although the individual stages do not present great originality in terms of electronic design, the chip worked better than the specifications and constitutes a novel

architecture, overall design and application. Its performance offers the possibility of completing the CNM implant as soon as all the systems are complete and neural information can be extracted over the whole spectrum of interest for the first time even in the presence of muscle interference.

1.4 Thesis organisation

The rest of this thesis is organised as follows:

Chapter two offers some background to neurophysiology and ENG measurement. Then neural interfacing is discussed, focusing on cuff electrodes and presenting the advantages of tripolar cuffs when used in conjunction with two conventional amplifier configurations. Based on ideal cuff behaviour, the main characteristics of amplifiers are described in terms of their ability to reduce interference while amplifying the neural signal.

Due to lack of a theoretical background on the main causes of the failure of conventional neural amplifiers to eliminate EMG, chapter three investigates the reasons behind the realistic cuff's non-ideal behaviour. Bioelectric field simulations and saline-bath experiments have been carried out to assess the behaviour of the cuff followed up by in-vivo tests in rabbits with stimulation-induced signals. This investigation into the electrode interface was necessary for understanding the limitations of the existing electrode-amplifier systems and for forming the specifications for the amplifier configuration described in this thesis.

Chapter four offers a mathematical system-level analysis of the proposed amplifier configuration, based on the cuff-error theory developed in the previous chapter. The analysis takes into consideration basic sources of error affecting the design, evaluating the capabilities and the limitations of the system in order to establish whether it is feasible as an analogue implementation. Thus the specifications for an analogue realisation are formed.

Chapter five describes a discrete component version of the proposed ENG amplifier, used to carry out further testing and evaluation before integrating the system. Transformer-coupled and saline-bath tests constitute the in-vitro experiments performed to assess the system's capabilities in terms of output ENG-to-EMG ratio as a function cuff error severity. The performance of the developed system is compared with its predecessors under various conditions. In-vivo tests have allowed another comparison of all three tripolar amplifier configurations under severe interference conditions.

Chapter six describes the design and testing of the integrated version of the system. The architecture of a first integrated approach is followed by the description of a second much improved version. The circuit design of the main stages of the chip are described and then measured results are presented and discussed. Additional optional components developed are also presented. The amplifier described in this chapter is fully implantable and it is an outcome of the work done in the previous three chapters.

Finally chapter seven is the general conclusion of the thesis, repeating the main points concluded from each chapter and combining them to an overview of the project. It is followed by proposals for future work, concerning further development or improvement of parts of the work presented or issues that have occurred during this investigation. Some ideas on possible combinations of this work with other applications are also discussed.

1.5 List of publications

The research conducted during this work led to the following publications.

Book chapters:

I. F., Triantis, A., Demosthenous, N., Donaldson, and M. S., Rahal "ENG recording amplifier configurations for tripolar cuff electrodes" in "Brain and Neuron", *edited by Metin Akay, Wiley/IEEE Press*, vol. IV, chapter 14 - *in press*

Journal publications:

1) Triantis I. F., and Demosthenous, A. "The Effect of Interference Source Proximity on Cuff Imbalance" *IEEE Transactions on Biomedical Engineering, accepted May 2005 – awaiting publication.*

2) Demosthenous, A., and Triantis I. F. "An Adaptive ENG Amplifier for Tripolar Cuff Electrodes" *IEEE Journal of. Solid-State Circuits*, vol. 40, pp. 412 – 421, 2005.

3) Triantis I. F., Demosthenous, A., and Donaldson, N. "On Cuff Imbalance and Tripolar ENG Amplifier Configurations" *IEEE Transactions on Biomedical Engineering*, vol. 52, pp. 314 – 320, 2005.

4) Demosthenous, A., Taylor, J., Triantis, I.F., Rieger, R., and Donaldson, N. "Design of an adaptive interference reduction system for nerve-cuff electrode recording" *IEEE Transactions on Circuits and Systems I: Regular Papers*, vol. 51, pp. 629 – 639, 2004.

Conference publications:

1) Triantis I. F., and Demosthenous, A. "An Improved, Very Long Time-Constant CMOS Integrator for use in Implantable Neuroprosthetic Devices", *IEEE ECCTD*, Cork, Ireland, 2005 – *to be presented*

2) Triantis I. F., and Demosthenous, A. "A BiCMOS ENG Amplifier with High SIR Output", *IEEE ISCAS*, Kobe, Japan, 2005 – *to be presented*

3) Triantis I. F., and Demosthenous, A. "An Adaptive ENG Amplifier for FES Applications", *IFESS/FESnet*, Bournemouth, UK, 2004

4) Triantis I. F., and Demosthenous, A. "A High-Performance Adaptive Eng Amplifier", IEEE BioCAS, Singapore, 2004.

5) Triantis I. F., Demosthenous A., and Donaldson N. "Comparison of Three ENG Tripolar Cuff Recording Configurations" *EMBS 2003*, Capri, Italy, 2003.

6) Triantis I. F., Demosthenous A., Donaldson N., and Struijk J. J. "Experimental Assesment of Imbalance Conditions in a Tripolar Cuff for ENG Recordings" *EMBS 2003*, Capri, Italy, 2003.

7) Triantis I. F., Demosthenous, A., and Donaldson, N. "An ENG Amplifier for EMG Cancellation and Cuff Imbalance Removal" *EPSRC PREP '03*, Exeter, England, 2003.

8) Triantis I., Rieger, R., Taylor, J., Demosthenous, A., and Donaldson N. "A CMOS Adaptive Interference Reduction System for Nerve Cuff Recordings" *Proc. 28th European Solid-State Circuits Conf. (ESSCIRC'02)*, pp. 113-116, Florence, Italy, 2002.

9) Triantis I. F., Donaldson, N., and Demosthenous, A. "Saline-bath testing of a system for removing artifact from ENG signals" *FESnet '02*, Glasgow, UK, 2002.
10) *(http://fesnet.eng.gla.ac.uk/conference/prog.html)*

11) Triantis I. F., Rieger R., Taylor J., and Donaldson N. "Adaptive Interference Reduction in Nerve Cuff Electrode Recordings" *ICECS*, Malta, 2001.

12) Donaldson N., Zhou, L., Taylor, J., Triantis, I. and Craggs, M. "Towards an Advanced Implant for Controlling Neurogenic Incontinence" *Proc IMechE Meeting Incontinence - The Engineering Challenge*, 21st November, 2001.

Chapter 2

PRINCIPLES OF NERVE CUFF RECORDING

The propagation of potentials along nerves is based on both electrical and chemical operations, involving potentials travelling along them, their amplitude conserved by the cell membrane exchanging ions with the surrounding conductive fluids and tissue through ion "pumps". The fact that the medium surrounding the nerves is used when they conduct allows measurements to take place, using electrodes outside the actual nerve fibres, a method which is non-intrusive and can therefore be used chronically. The amplitude of the signals recorded by such electrodes is a few microvolts, however it is slightly increased when the extracellular space (space surrounding the nerve) is restricted as happens when cuff electrodes are used. Implanted cuff electrodes are appropriate for chronic electroneurogram (ENG) recording [22] because they are non-invasive to the nerve and assist in reducing interference from sources outside the cuff, such as the electromyogram (EMG) generated from muscles nearby [10-12, 16, 18, 21, 22, 24-27]. Ideally, the ability of the cuff to linearize the internal potential field generated by external sources [27] allows for interference to be eliminated with the use of tripolar cuffs (i.e., cuffs with three equally spaced ring electrodes), in combination with appropriate amplifier configurations such as the *quasi-tripole* (QT) [21, 22, 24] and the *true-tripole* (TT) [28, 29].

This chapter offers a background to nerve conduction and neural signal measurement, focusing on cuff electrodes and presenting the advantages of tripolar cuffs when used in conjunction with the QT and the TT amplifiers.

2.1 Nerve fibre conduction and nerve anatomy

2.1.1 The nervous system and parts of the neuron

The nervous system consists of the central nervous system (CNS) and the peripheral nervous system (PNS). The CNS includes the brain and the spinal cord, while the PNS carries information between the CNS and the various parts of the body [5] (figure 2.1).

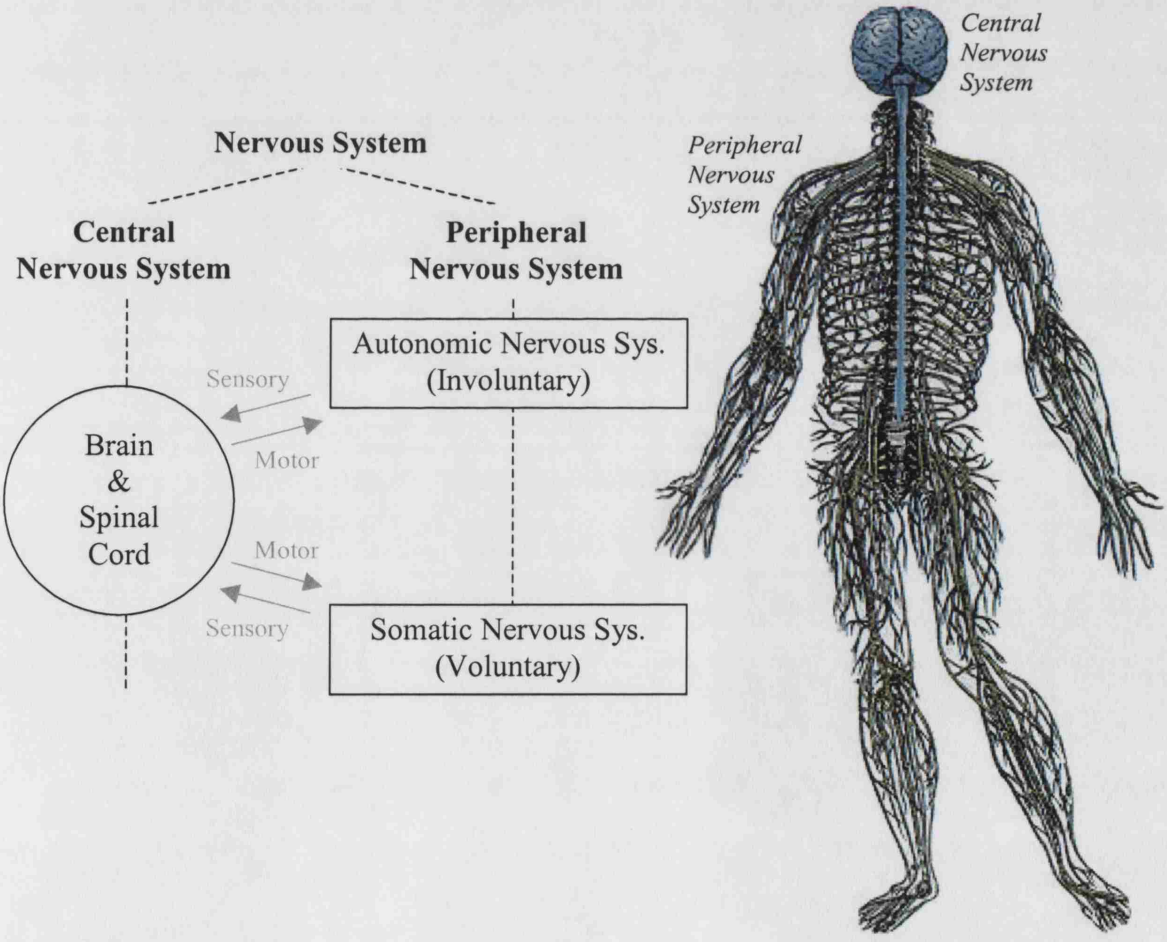

Figure 2.1 The Nervous System. Diagram and anatomical view [40]

There are two types of cell in the nervous system, the glia, which perform "support" functions and the neurons (figure 2.2), which carry out the communication of information in and between the CNS and the PNS. The neurons are thinner and longer than the usual cells and they transmit information using chemical and electrical signals. They appear in a variety of shapes and sizes (from fractions of a millimetre up to over a meter). The three main parts of a neuron are the dendrites, the soma and the axon (figure 2.2). The dendrites receive chemical input from other neurons, the soma is the main cell body and the axon conveys electrical signals. There are three main types of neuron: the interneuron (common in brain, connecting with other neurons), the sensory neuron (no dendrites, receives input from sensors around body) and the motor neuron, which supplies signals to muscles and organs [40].

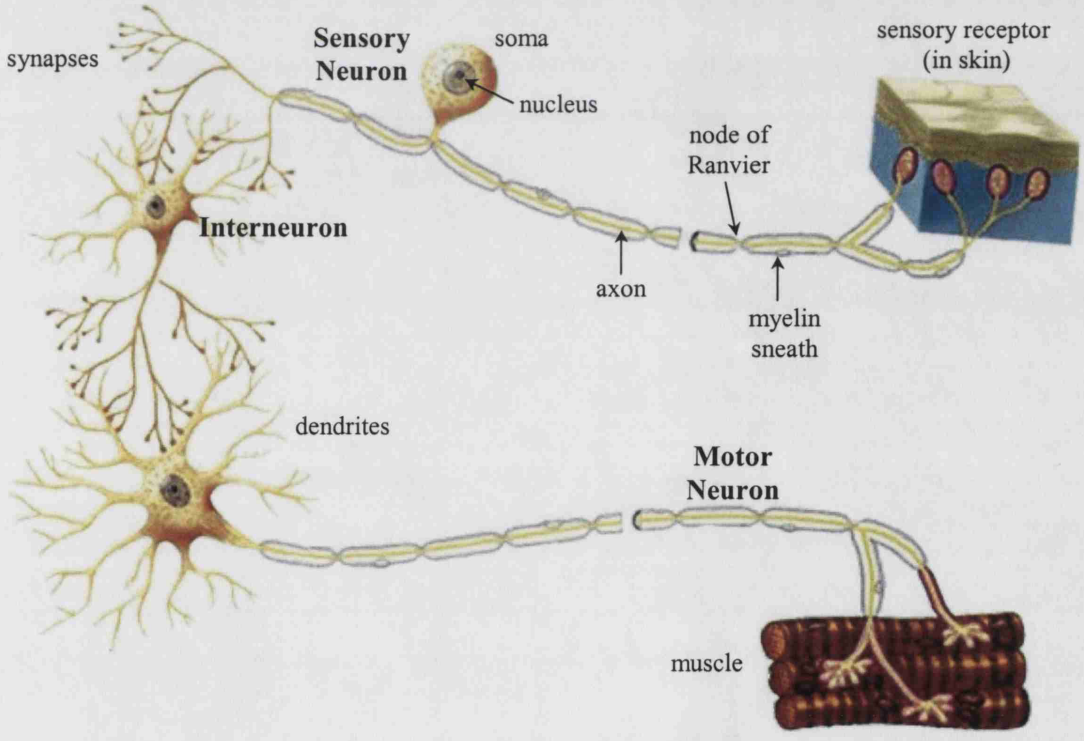

Figure 2.2 Neuron types [41]

The nucleus of the neuron contains chromosomes and is located within the soma along with mitochondria which supply the cell with energy from glucose and oxygen. In most vertebrates' nerves [42, 43], the axon, which transmits electrical signals (action

potentials), is covered by layers of insulating myelin, which improves the conduction and is interrupted by gaps, named "nodes of Ranvier". The end of the axon sometimes makes contact with other neurons using synapses, which convert the action potentials to chemical signals for the dendrites of the next cell [40].

2.1.2 Neurophysiology and the action potential

The voltage difference between the extracellular fluid and the inside of the neuron is the membrane potential, which is called the "resting potential" when the neuron is in a state of readiness to "fire". The resting potential, with typical values around –70mV across the membrane (with the internal being more negative), is established by the sodium-potassium pump maintained by a concentration gradient and an electrical gradient. The membrane potential of a neuron whose dendrites are connected to other neurons is affected by the inputs resulting from the signals of the connecting synapses. There are two main types of synapses, the inhibitory and the excitatory. The inhibitory synapses result in inhibitory postsynaptic potentials (IPSPs), which cause hyperpolarisation of the neuron, decreasing its membrane potential by allowing into the neuron negative ions (e.g. Cl^-) making it less likely to fire. The excitatory synapses result in excitatory postsynaptic potentials (EPSPs) which cause depolarisation of the neuron, increasing its membrane potential by allowing into the neuron positive ions (e.g. Na^+), thus making it more likely to fire (generate an action potential) [44].

The summation of inputs to the dendrites of the neuron may result to the generation of the *action potential* (depicted later in figure 2.8), a pulse occurring when the membrane potential reaches the firing threshold (typically –60mV). Sodium (Na^+) and potassium (K^+) ions are allowed to enter or to exit the cell by their respective ion channels (gates). Sodium channels are voltage activated and therefore, as the membrane potential becomes less negative, the channels open to allow sodium ions into the neuron. Once the firing potential is reached, the neuron fires an action potential, which results from a great and rapid inflow of Na^+ ions and is then followed by an outflow of K^+ ions resulting in rebalancing the membrane potential. The inflow of Na^+ depolarises the adjoining part of the membrane causing it to follow the same procedure and therefore the action potential propagates as a wave along the axon, when the axon is not myelinated.

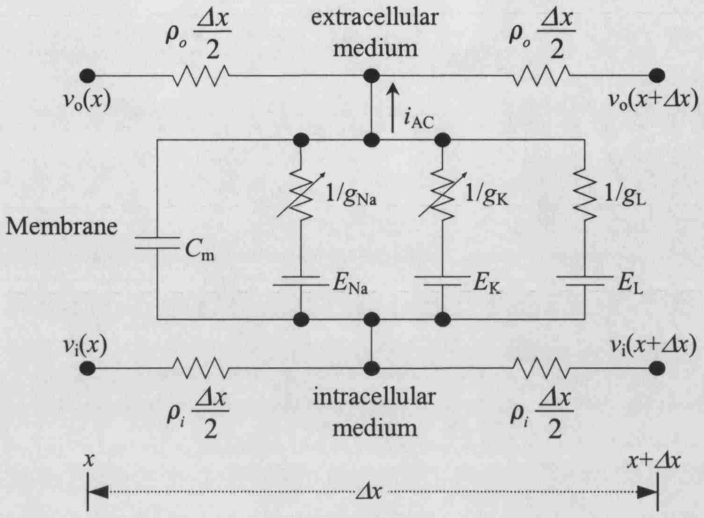

Figure 2.3 Equivalent circuit diagram of a part of an unmyelinated nerve fibre with length Δx [43].

The electrical operation of a small segment of an unmyelinated nerve fibre is illustrated in figure 2.3. The segment has length Δx and the extracellular and intracellular media are considered purely resistive [43], with resistivities ρ_e *and* ρ_i respectively, defining the resistance of the external and the internal paths of the transmembrane current i_{AC}. The external and internal potentials are v_e and v_i respectively and are shown in the figure as functions of distance x along the fibre segment. The membrane representation includes capacitance C_m (in μF per unit area), which depends on the area of the membrane under consideration, and the conductances g_{Na}, and g_K (in mS per unit area) corresponding to the Na^+ and the K^+ channels as defined by the Hodgkin-Huxley equations ([45] in [42]). The conductance g_L, which is usually neglected, corresponds to leakage currents from ions other than Na^+ or K^+ (e.g. Cl^-) [43].

Figure 2.4(a) illustrates the charge distribution along the membrane of an unmyelinated fibre. As the action potential propagates along the nerve, the membrane of the segment of the fibre that is active (labeled "active region" in the figure) is depolarised (polarity reversed), the membrane before the active region has repolarised while the one after is still in the resting state. The polarity differences of the adjacent regions cause closed path (solenoidal) ionic current flow, as shown in figure 2.4(a). The currents flowing towards the region after the active membrane region cause the membrane there to

depolarise and to become active as well. However, the currents flowing towards the region before the active one cannot re-excite the membrane, as this is in the refractory state, during which no stimulus can excite the membrane. As a result the action potential propagates along the fibre in a self-excitatory manner (i.e. membrane excitation occurs and propagates on its own, without the need for extra stimulus being applied), without being attenuated [43].

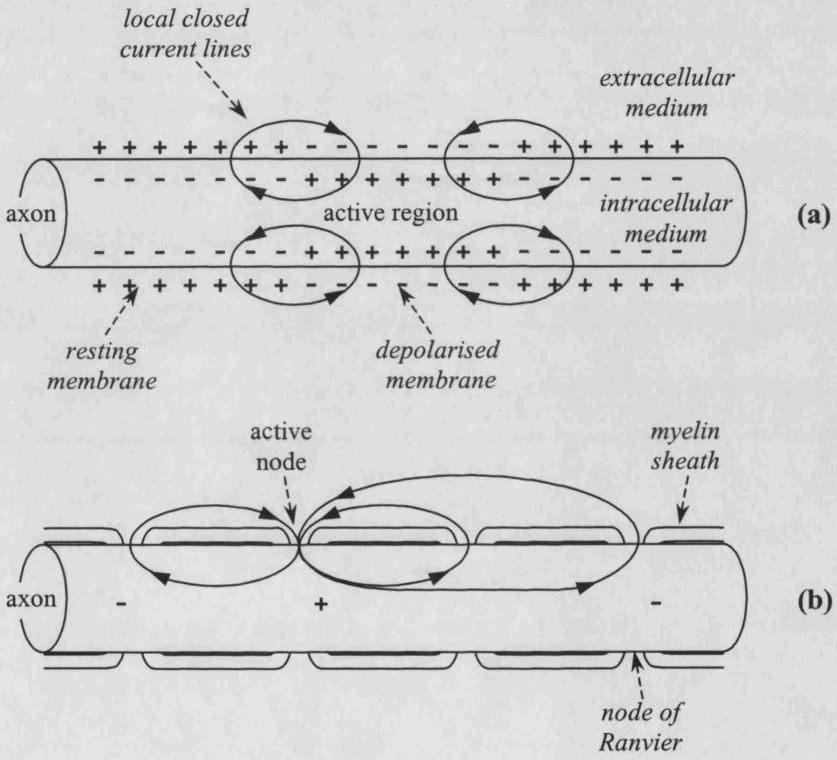

Figure 2.4 Neuron conduction: (a) Unmyelinated fibre (b) Myelinated fibre [43]

When the axon is myelinated the action potential is conducted in two ways. Ion exchange is used in the nodes of Ranvier and cable properties [46] describe conduction in the myelinated sections. Conduction in an activated nerve fibre is achieved again via solenoidal currents, as in the unmyelinated fibres, however the current loops flow between the nodes (figure 2.4(b)), where almost all ion channels are concentrated. This method provides faster and less energy consuming pulse propagation. However, the pulse amplitude decreases under the myelin sneath and if not amplified, it is difficult to reach the end of the axon. The nodes of Ranvier serve in reinstating ion exchange with

the extracellular fluid, thus amplifying the action potential by restoring the pulse's amplitude to its initial value. This type of conduction, which occurs by the alternation between ion exchange and cable conduction is called *saltatory conduction* and is much faster than the conduction that takes place in the unmyelinated neurons, where conduction is based on ion exchange only. The amplitude of the action potential (approx. 30mV) and the length of the myelin sections (approximately 1 to 2mm) ensure that the amplitude of the signal does not fall below the firing threshold, as this would stop the ion exchange from being reinstated at the node of Ranvier [34, 44, 47].

2.2 Cuff and bioelectric signals

Although the action potentials mentioned in section 2.1.2 are of mV order, recording such potentials is not straightforward. *Intrafascicular* electrodes (figure 2.5), needle electrodes penetrating the nerve, have been used for recording during open surgery and have the advantage of providing both the option of recording from selected nerves inside nerve bundles, as well as providing relatively high output ENG amplitudes (mV). However this type of electrode is both intrusive and damaging to the nerve and inappropriate for long term implantation [3, 34].

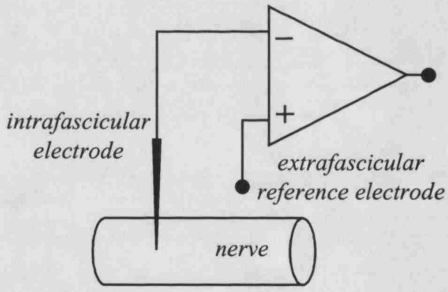

Figure 2.5 Measurement between an intrafascicular electrode and a reference electrode.

2.2.1 Cuff description

ENG recording techniques for peripheral nerves using cuff electrodes were introduced by Hoffer [48] and Stein [21]. The increase in signal amplitude due to the cuff in recording the ENG extraneurally was shown in [49] to be the result of the local restriction of the extracellular space which, in effect, increases the resistance of the extracellular return path of the fibre's action currents. Cuff electrodes are suitable for

chronic implantation [3, 22, 34] because they are non-intrusive to the nerve and do not cause substantial damage to it if they have the appropriate size and they are implanted by specialised neurosurgeons.

Typical cuffs consist of insulating tubes, consisting of biocompatible flexible insulating materials such as silicone rubber, polytetrafluoroethylene or polyaimide [50], with ring electrodes made of platinum-iridium or stainless steel attached to the inside wall, covering most of the circumference but leaving a gap for a longitudinal opening so that the nerve may be inserted into the cuff (figure 2.6(a)). Originally, closure of the slit along the cuff was achieved by tying threads around it [22]. Later methods included injecting a liquid polymer into the cuff to fill the space between the nerve and the cuff to make the fitting tighter [51]. Naples et al. introduced the "spiral cuff" (figure 2.6(b)) in [52] which curls up to fit the nerve tightly but is still able to expand if the nerve swells, perhaps due to inflammation. This design has been used for stimulation and recording and is made to curl by gluing an unstretched sheet onto a pre- stretched sheet of rubber. A cuff made by dip-coating a mandrel and pre-formed platinum electrodes was presented in [53], where the cuff closure mechanism was implemented using interdigitating cubes (figure 2.6(c)). Typically, the slit along the tube is glued or covered by a silicone flap attached to the cuff [54] (figure 2.6(a)). It is important for the cuff to insulate the whole circumference of the nerve (or nerve bundle), as this ensures that the flow of ions in the extrafasciculllar fluid remains within the cuff when action potentials propagate the nerve. In this way extracellular ion currents create potential differences inside the cuff as the action potential moves across its length, which can be measured by the ring electrodes placed inside it.

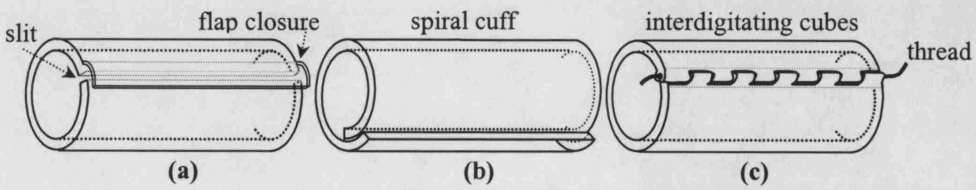

Figure 2.6 Three different types of cuff closure: (a) slit along the tube covered by silicone flap [54] (b) "spiral cuff" [52] (c) closure mechanism using interdigitating cubes and thread through them [53].

The placement of the cuff around the nerve causes some changes in the nerve after a period of implantation, as connective tissue covers and fills up the cuff. The nerve may also change shape to adapt to the internal space [55].

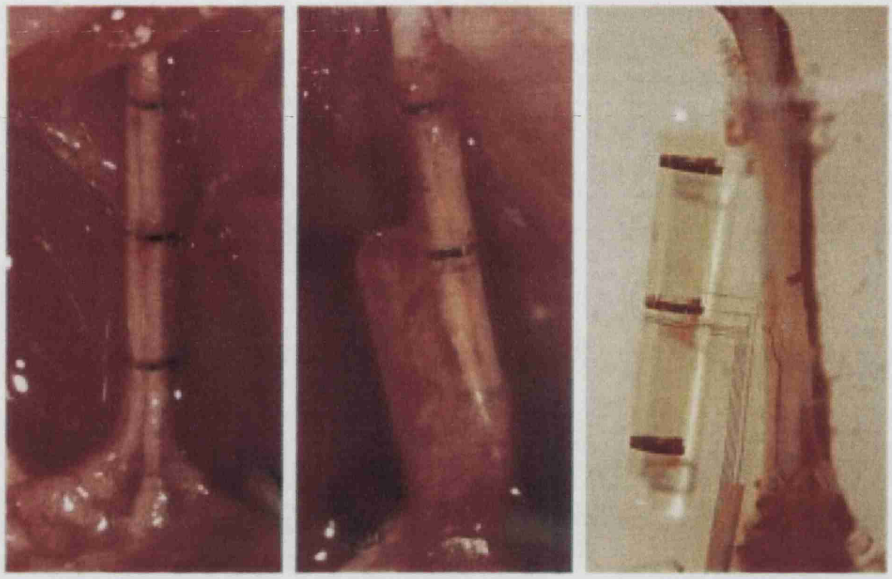

(a) (b) (c)

Figure 2.7 Accurately-fabricated polyamide cuff (length 12mm, diameter 1.7mm - image from [50]). (a) Cuff after implantation around the sciatic nerve of a rat. (b) Tissue development around the implantation area after two months. (c) The cuff is removed from the nerve, which is placed into saline and its surface is left relatively clean.

Figure 2.7(a) illustrates a tripolar spiral cuff (image from [50]) after implantation around the sciatic nerve of a rat. Part (b) of the figure illustrates the implanted cuff after two months, where tissue has developed and part (c) gives a clear illustration of the cuff after being removed from the nerve, which is immersed in saline. The interface between the nerve and the cuff was reported to be filled with extrafasciculllar fluid and its surface was relatively clean after the cuff removal. The cuff in this particular study was a polyamide cuff fabricated on a wafer, similar to PCB fabrication processes, and then rolled and heated to retain the cylindrical shape. The electrode placing and spacing precision using this modern fabrication method is sub-micrometer.

To avoid compression neuropathy (nerve damage due to compression), the cuff diameter has to be at least 20% larger than that of the nerve bundle [56] and its length must be at least ten times larger than its inner diameter [20]. The cuff length must be

equal or larger than the distance between the nodes of Ranvier and at least ten times larger than its inner diameter [20]. Increasing the length significantly reduces interference as the impedance inside the cuff increases, however there are limitations depending on the location of implantation. The optimum cuff length was shown experimentally in [21] and [56] to be between 20 and 30mm with the neural signal amplitude decreasing when the length is smaller than 15mm. The amplitude of the signal was also shown in [57] to decrease with the square of the cuff diameter for diameters up to 4mm indicating that the effectiveness of cuff electrodes improves for tighter fitting cuffs as shown experimentally in [48, 56, 58] where single fibre action potentials ranging from 3μV to 20μV were recorded using cuffs with inner diameters of 2.6mm and 0.3mm, respectively.

There are three main application areas for recording cuffs [22]. They can be used in chronic studies of physiology and pathology of the neuromuscular system by measuring naturally occurring signals in animals as in [59-61]. Furthermore, they can be used for studying the regeneration of axotomised nerve fibres and the status of the nerves after damage [62, 63]. Finally, sensory signals recorded using cuff electrodes can be used for feedback in neuroprostheses as shown by animal studies in [18, 19, 24, 64, 65] and in humans, where recorded signals have been used for control of foot-drop stimulation in hemiplegics [14, 30] and in hand-grasp applications in tetraplegics [12, 66, 67].

2.2.2 Cuff effect on bioelectric signals

2.2.2.1 Nerve signal detection

The neural signal recorded using a cuff depends on various parameters including cuff slit closure, number of electrodes inside the cuff, and interference present. The cuff can be placed around a single nerve, or if close to the spinal cord it can be placed around a nerve bundle, which later separates into single nerve fibres close to its related organs. The ENG signal recorded from a cuff placed around a nerve bundle represents the summation of the action potentials of the active nerve fibres. If one fibre is active the ENG represents a single-fibre action potential (SFAP) and if all nerves are activated (as is the case when stimulation is applied to a bundle) the resulting signal is a compound action potential (CAP), which usually has greater amplitude than the naturally occurring

ENG [3, 18, 21]. The principle of cuff electrode ENG measurements in the literature [21, 25, 49, 57, 68] were developed and described in terms of SFAP measurements.

The analysis of SFAP measurements using cuffs was generalised to cover all types of nerve fibres by Stein et. al [49] and Marks and Loeb [21, 25, 57] who applied to myelinated fibres earlier analysis from Stein and Pearson [20, 21, 68] on SFAP detection in restricted extracellular space from unmyelinated fibres. Work in [41] showed that the shape and amplitude of the recorded signal is affected by cuff dimensions. Experiments in [69] indicated that the amplitude of the recorded SFAP reaches a maximum and saturates after the cuff is made longer than the wavelength of the transmembrane action potential. The latter is approximately linearly related with fibre diameter and for a 10μm diameter it is between 20mm and 30mm.

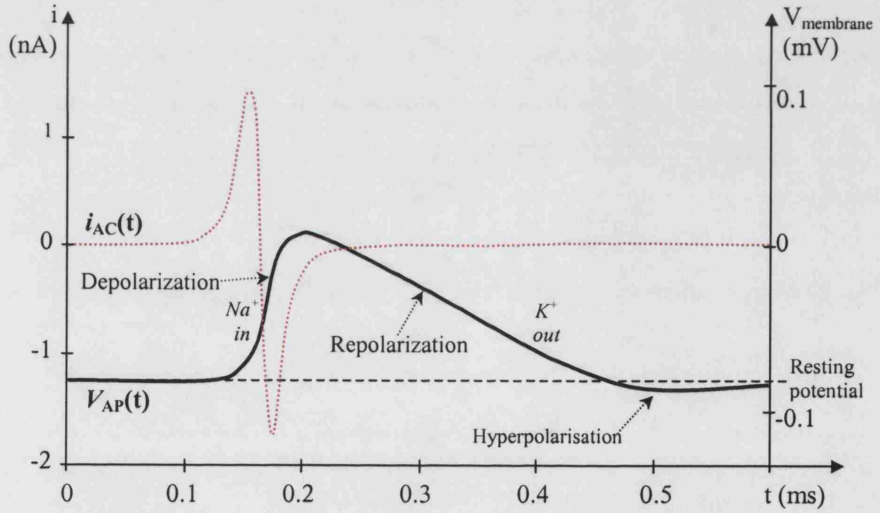

Figure 2.8 The action potential $V_{AP}(t)$ [57] and the action current $i_{AC}(t)$ superimposed (image reproduced from [69]).

By modelling the nodes of Ranvier of a myelinated fibre as point current sources [27] the cuff recorded signal is the sum of the contributions of all sources (nodes) located inside it [70]. These current sources are activated in sequence as the action potential (solid line in figure 2.8) propagates in the fibre and as its maximum amplitude reaches each node the corresponding current source produces an action current i_{AC} (figure 2.8).

As a result the same signal appears at the different contacts inside the cuff at different times [25, 57].

As the action potential is spread over numerous nodes of Ranvier [69], the SFAP recorded in the middle of the cuff, where the signal peaks, can be calculated as the superposition of the contributions of these current sources (figure 2.9(a)) multiplied by a weighting function which relates to each node's position in the cuff [54]:

$$SFAP(t) = \sum_{n=1}^{N} i_{AC}(x_n - ut)\, w(x_n) \qquad (2.1)$$

where $i_{AC}(x_n - ut)$ is the action current at node n located at position x_n inside the cuff and u is the conduction velocity. According to [69] the weight function $w(x_n)$ (in Ohms) can be represented by the voltage caused only by node n in position x_n inside the cuff measured by an electrode in the cuff, divided by the current of the node reaching the electrode.

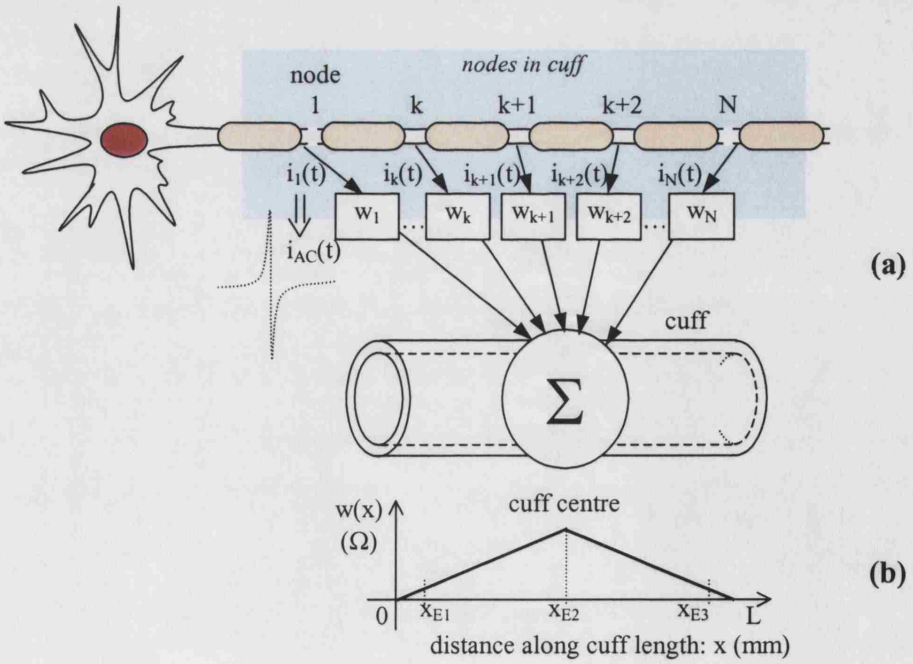

Figure 2.9 (a) Schematic representation of the summation of contributions of current sources representing nodes of Ranvier [49] (b) The cuff weighting function affects the SFAP amplitude along the cuff length [69].

The plot of the weight function versus the position x of the node along the cuff is shown in figure 2.9(b). Based on the above and on the work by Stein and Pearson [69], and taking into consideration the cable theory which states that the transmembrane action current is proportional to the second-order difference of the transmembrane action potential V_{AP}, the measured SFAP can be expressed by [34]:

$$SFAP(t) = \alpha_R \left[-\frac{1}{2} V_{AP}(t) + V_{AP}(t - \frac{L}{2u}) - \frac{1}{2} V_{AP}(t - \frac{L}{u}) \right] \qquad (2.2)$$

and $\alpha_R = \frac{R_e}{R_e + R_i} \approx \frac{R_e}{R_i}$, which is a proportionality factor with R_e, R_i being the extracellular and the intra-axonal resistances per unit cuff length respectively ($R_e << R_i$).

Equation (2.2) shows that the measured SFAP is the result of scaling and superposition of three transmembrane action potentials. For a specific fibre diameter, the overlap of these action potentials is determined by the cuff length [25, 57]. For a tripolar cuff with electrodes E_1, E_2 (middle) and E_3 placed in respective positions x_{E1}, x_{E2} and x_{E3} inside it, the SFAP measured will comprise from the three action potentials measured at these positions, given by the action current multiplied by the corresponding weighting function [14].

The measured SFAP in eq. (2.1) occurs by the convolution of the action current with the electrode weight function, and therefore it occurs by the weighted and delayed action currents of each node summed together (ignoring a negligible frequency dependency of the weight functions) [69]. The relationship of the internodal distance to fibre diameter is assumed to be linear, similar to the diameter's relationship with the conduction velocity, making the delay between adjacent nodes independent of fibre size. Effectively the dominant parameter determining the overlap of the three transmembrane potentials [69] in eq. (2.2) and the shape of the recorded SFAP, is the number N of nodes of Ranvier inside the cuff. If the internodal distance is proportional to the fibre diameter d_{fibre} by β (β = 100 in [69]), N is related to d_{fibre} and cuff length L by: $N = \beta L / d_{fibre}$. Another parameter linearly related to d_{fibre} is the area of each node of Ranvier leading to the assumption [57] that i_{AC}, and therefore the measured SFAP amplitude are

linearly related to d_{fibre} as well, provided the action current has constant duration. As a result, SFAP amplitude is related to N and it will reach a maximum value and then saturate for certain cuff lengths. The assumptions for the linear relationships mentioned are true for fibres with diameters ranging from 5μm to 20μm. As a result [71]:

$$L = L_{ref} \frac{d_{fibre}}{d_{ref}} \tag{2.3}$$

This allows the calculation of the desired cuff length L to be used with a fibre of diameter d_{fibre} provided a calculated length L_{ref} is known to be optimum for a fibre with diameter d_{ref}. As mentioned before the optimum cuff length is equal to the action potential wavelength. Therefore, the optimum number of nodes inside a cuff can be expressed by: $N = uT_{\text{VAP}}$, where $u \approx 55800$ nodes/s [71] and $T_{\text{VAP}} \approx 0.4$ms is the duration of the action potential. Therefore, $N \approx 22$ (for nerve fibre diameters between 5μm and 20μm) giving $L = 22$mm, the optimum cuff length for a 10μm diameter fibre.

The dimensions of the cuff affect the spectrum of the recorded ENG and therefore the cuff acts as a spatial filter [72]. The characteristics of this linear filter depend on the number and the position of the electrodes inside the cuff and are affected by the cuff length but not so much on its diameter. The spatial filter has a broad band-pass characteristic with a peak in the spectrum for each conduction velocity and, therefore, fibre diameter [34]. As pointed out by Upshaw [73], this means that the signal to noise ratio should be improved by using narrow band-pass filters, centred on the spectral peak corresponding to the propagation velocity for the fibres from which one wishes to record. The spectrum $G(\text{f})$ of the tripolar cuff recorded nerve signal depends on the spectrum $V_{\text{AP}}(\text{f})$ of the transmembrane action potential and the transfer function $H(\text{f})$ of the cuff:

$$G(\text{f}) = H(\text{f})V_{AP}(\text{f}) \tag{2.4}$$

Excluding scaling factor α_{R}, $H(\text{f})$ is given by [74]:

$$H(f) = 2e^{\left(-\frac{2j\pi f x_{E2}}{u}\right)} - e^{\left(-\frac{2j\pi f x_{E1}}{u}\right)} - e^{\left(-\frac{2j\pi f x_{E3}}{u}\right)} \quad (2.5)$$

where x_{E1}, x_{E2} and x_{E3} represent the position of the three electrodes inside the cuff, with E_1 and E_3 being the end electrodes and E_2 the middle one.

2.2.2.2 EMG and cuff linearising property

Interference signals, as for example EMG from muscles in the vicinity of the recording cuff, cause ionic currents to flow through the tissue inside the cuff. The muscle can be represented by a dipole [70]. Its field lines and the respective isopotential lines are distorted by the cuff (figure 2.11(a)), due to the silicone having much lower conductivity than the tissue and the surrounding fluid. As a result, due to the limited conductive cross-sectional area formed by the cuff's diameter minus the nerve diameter, most of the ionic currents flow outside it. This is similar to the perturbation of the dipole field of an electric fish in sea water (figure 2.10) due to lower conductivity obstacles [74], an analogous volume-conductor model as biological tissue is often simulated with saline [27, 34] which has similar conductivity to sea water (for both $\sigma \approx 1\Omega^{-1}m^{-1}$).

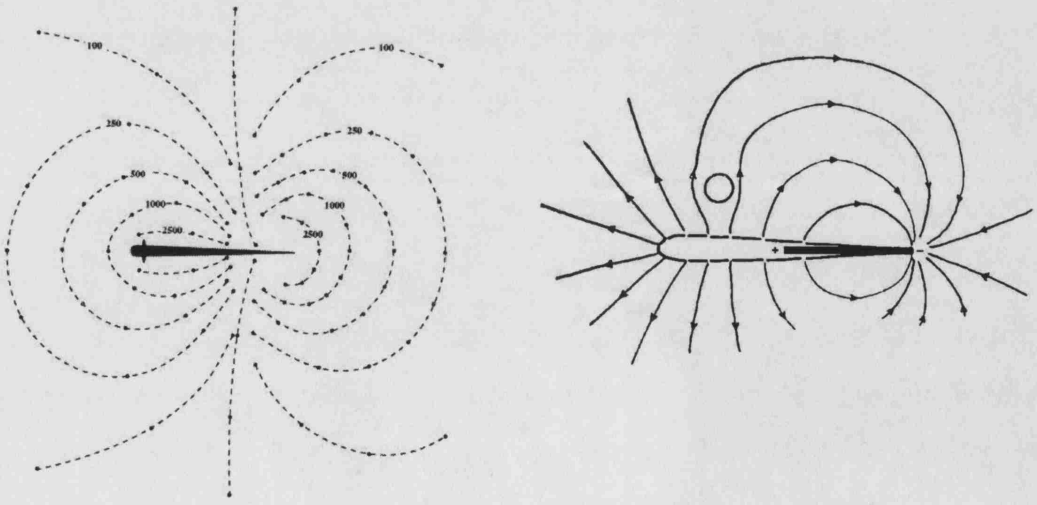

(a) **(b)**

Figure 2.10 (a) Fish generates an electric field around its body (isopotential lines shown) (b) nearby objects in the sea water perturb the electric field and affect the paths of the generated currents (images from [27]).

As the cuff is placed between the isopotential lines, a voltage drop appears between its ends. As a result ionic current flows through the tissue inside it causing potential difference between the internal ring electrodes [75]. As the medium inside the cuff is only resistive, there are no significant phase variations to the interfering potentials across the electrodes and the potential varies linearly with distance across the length of the cuff (figure 2.11(b)). This is of great significance for the amplifier configurations used to reduce the interference and extract the ENG, and it results to the *linearising property* of the cuff [74, 75]. This makes it appear like a potential divider, and the constant phase means that the equivalent model has no capacitors (though the tissue-electrode interface models do have capacitance).

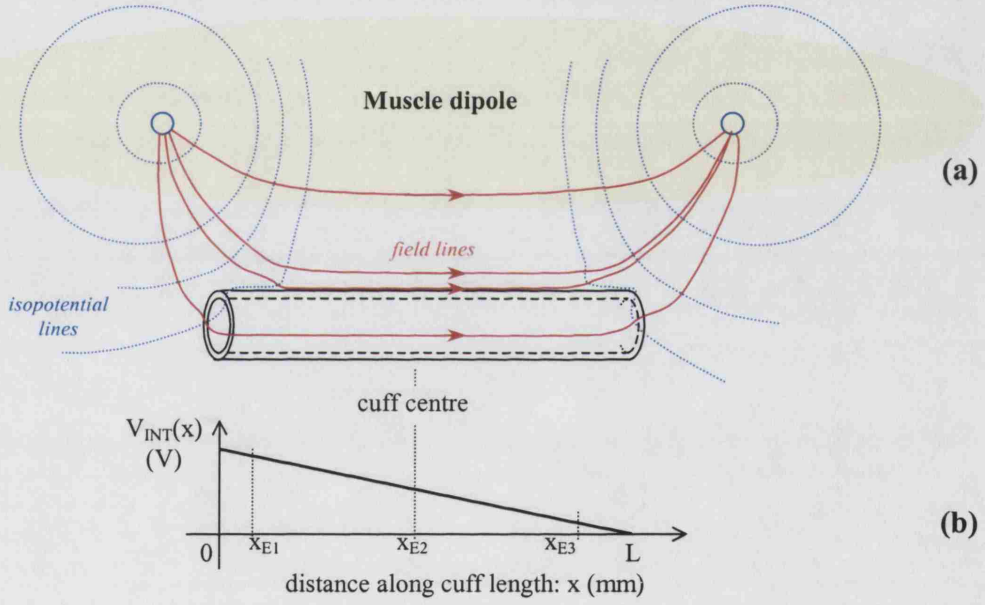

Figure 2.11 (a) The perturbation of the muscle dipole field by the cuff, similar to the effects described in [22] (b) The cuff linearises the EMG field [24]

Longer cuffs result in greater interference reduction, as the resistance of the tissue inside the cuff becomes higher and therefore less current flows through the cuff due to external fields. According to Rahal in [27] if the linear variation of the interference potential $V_{INT}(x)$ (x is the distance along the cuff) inside the cuff is assumed to be independent of the location of the external field, it can be represented by:

$$V_{INT}(x) = \gamma x + V_{INT}(0) \tag{2.6}$$

The gradient γ is defined by the potentials at the cuff ends and the cuff length:

$$\gamma = \frac{V_{INT}(L) - V_{INT}(0)}{L} \tag{2.7}$$

where $V_{INT}(0)$ and $V_{INT}(L)$ are the interference potentials at the length 0 (one end of cuff) and at length L (other end of cuff) respectively.

2.2.3 Signal characteristics

2.2.3.1 Naturally-occurring signal and SIR definition

In general naturally-occurring ENG signals, seen at the tripolar electrodes, lie in the frequency range of 500Hz to 10kHz, usually with maximum power between 1kHz and 3kHz. The amplitude of the ENG signal appearing between the electrodes of a cuff is a few μV. An example of mechanically-evoked ENG, generated by tapping a rabbit's toe, is shown in figure 2.12 [22, 27, 34], where peak-to-peak ENG amplitude is shown to vary from approximately 2μV to 7μV. Frequencies at the low end are often difficult to record due to interference from the surrounding muscles. Myoelectric (EMG) potential amplitudes are around 1 millivolt pk-pk, with a frequency range of 1Hz to 3kHz [21].

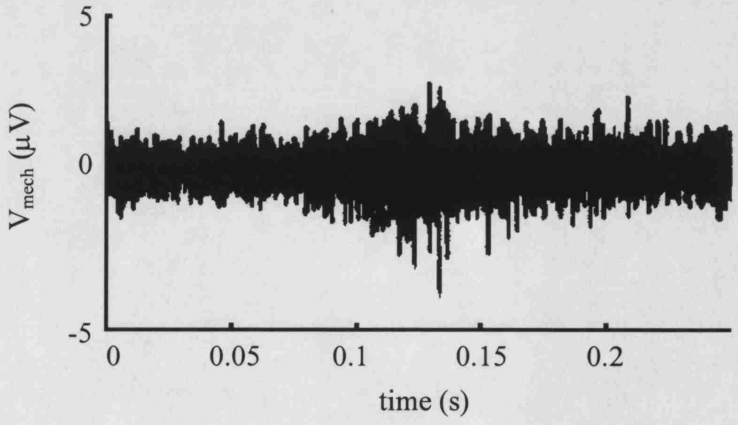

Figure 2.12 Example of mechanically evoked ENG (graph from [33]).

Therefore, the spectra of the two signals overlap and although the ENG signal power concentrates mainly around 800Hz and 2kHz, while the EMG peaks between 100Hz and 250Hz, EMG greatly degrades ENG measurements, because it can be up to three orders of magnitude larger [22]. A measure of EMG contamination of ENG measurements is the ENG-to-EMG ratio, as used in [3, 24]. In this project this ratio is expressed as the signal-to-interference ratio (SIR), used for expressing the signal quality both at the input and at the output of amplifier configurations used with cuff electrodes. The output SIR of systems described later in the thesis is often denoted as SIR_{out}.

2.2.3.2 Stimulation-induced signals

In the case of stimulation-induced signals, the ENG recorded has greater amplitude (few tenths of a mV), as all the neurons in the nerve bundle being stimulated, fire simultaneously producing a *compound action potential* (CAP). The reaction of the muscles activated by the stimulated nerves is the *M-wave*, which may be two or three times larger than the naturally occurring EMG and peaks at higher frequencies. An additional source of interference is the *stimulus artefact*, which is the signal picked-up by the recording cuff when stimulation is applied close or onto the nerve branch that the cuff is attached to. It is a spike-like signal caused directly by the current pulses produced by the stimulating electrodes and it may reach several mV [34]. Typical stimulation-induced signals are shown in figure 2.13.

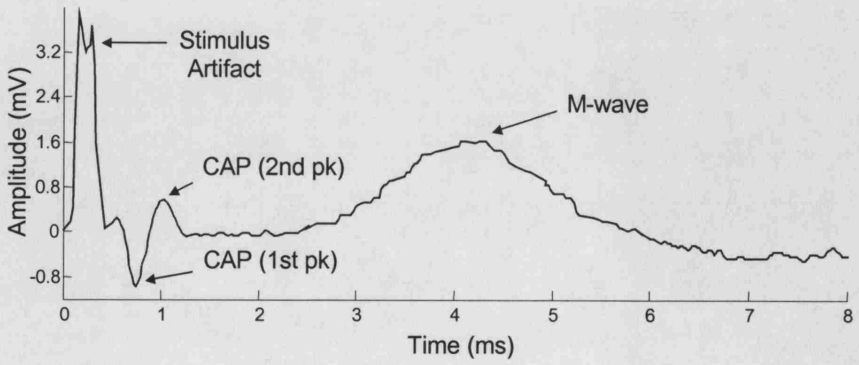

Figure 2.13 Typical stimulus artefact, CAP and M-wave signals, recorded from a tripolar cuff [34].

2.3 Cuff electrode configurations and tissue interface

2.3.1 Characteristics of different cuff electrode configurations

Comparisons between monopolar, bipolar and tripolar cuffs conducted in [76] have shown that the latter offer better SIR and can be connected to amplifier configurations that achieve greater interference reduction. Tripolar cuff properties and amplifier configurations are described in more detail in section 2.4.

In monopolar cuffs (figure 2.14(a)), the recording is carried out between a ring electrode inside the cuff and a reference electrode outside: the inner electrode has to be close to the centre of the cuff to maximize the amplitude of the measured ENG. In bipolar cuffs (figure 2.14(b)), where the measurement is taken differentially between the two electrodes, the amplitude of the measured signal is proportional to the separation between the electrodes, however, as the electrodes approach the edges of the cuff the amplitude drops, as the low resistivity area of the fluid outside the cuff comes into effect. In tripolar cuffs (figure 2.14(c)) measurements are taken between the middle and the two end electrodes. In order to maximize the amplitude of the signal, the end electrodes have to be placed close to the ends of the cuff. However, the main factor affecting ENG measurements in tripolar cuffs is the spacing between the electrodes and not their actual position or the length of the cuff. The monopolar and tripolar cuffs have similar frequency responses and their lengths affect their properties as spatial filters.

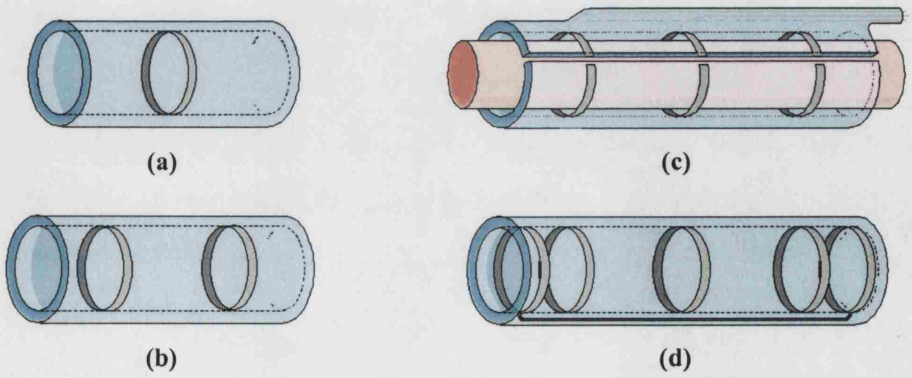

Figure 2.14 (a) Monopolar cuff electrode. External reference electrode not shown. (b) Bipolar cuff. (c) Tripolar cuff around nerve (or nerve bundle, depending on the application). Wiring and slit along cuff are also shown (flap not shown for clarity). (d) Screened tripolar cuff. The additional end electrodes are shorted together.

Overall, the tripolar cuff gives higher signal amplitudes than the monopolar and bipolar counterparts and measurements are less sensitive to the cuff length, as the most significant parameter is the electrode pitch. Moreover, it allows the use of specific amplifier configurations to eliminate EMG interference. A *screened tripolar cuff* (figure 2.14(d)), has two extra electrodes, close to the ends, outside the end electrodes of the tripole, and shorted together. This arrangement further decreases the amplitude of EMG interference, but for best effect the additional electrodes should not be placed right at the ends of the cuff, and so this tends to increase the overall length. However, according to [58], a screened tripole has the same effect on interference as increasing the length of the cuff because it effectively decreases the potential gradient caused by the interfering field inside it.

2.3.2 Electrode-tissue interface

Ring electrodes in cuffs are usually made of platinum due to its long-term stability after implantation both in terms of robustness and in terms of electrical properties [76]. Recordings of neural activity are also stable, as signals characteristics remain similar over time [76]. Stein et al [77] have reported that after implantation, platinum electrode tissue interface impedance increases, first abruptly and then slowly, mainly due to the nerve changing diameter and to growth of tissue between the nerve and the internal wall of the cuff. The work described the electrode-tissue interface in terms of electrical components within the bandwidth of interest (10Hz to 10kHz) using the circuit diagram shown in figure 2.15.

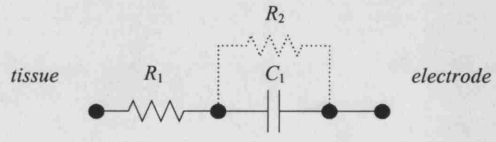

Figure 2.15 Equivalent circuit of the tissue-electrode interface (R_2 can be omitted) [76].

Capacitance C_1 is a result of the layer formed by the interface between the electrode and the adjacent tissue or fluid. The resistance R_2 can be omitted because platinum

electrodes are polarizable and as a result its value approaches infinity. If the electrodes were non-polarizable, as would be the case with silver-chloride electrodes, R_2 would allow direct currents to flow from and to the subsequent amplifier connected to the electrodes and the tissue. Capacitance between the electrodes or between the leads and the ground were found to be unimportant within the bandwidth of interest. The resistor R_1 represents the spreading resistance of the tissue near the electrode [24, 29, 33, 77, 78]. The overall impedance due to R_1 and C_1 was shown in [24, 29, 33, 77, 78] to vary with frequency from 10Hz up to approximately 100Hz and then its value settled and stabilized around 2kΩ throughout the rest of the bandwidth of interest (up to 10kHz). For this reason, it is often represented by a resistor of 1 to 2kΩ (depending on the size of the electrodes) in literature concerning cuff electrode recordings [24, 29, 33, 77, 78].

2.4 Ideal tripole cuff model and amplifier configurations

2.4.1 Tripole cuff interface: ideal simplified impedance model

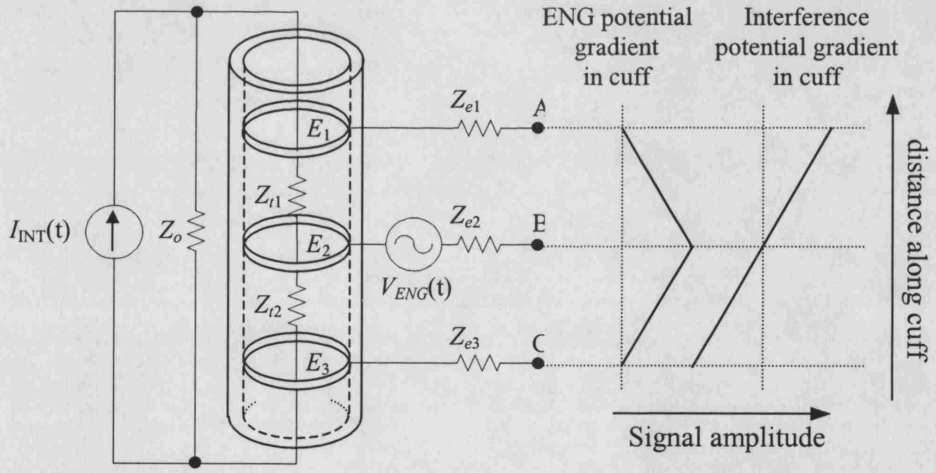

Figure 2.16 Basic cuff interface impedances[1] and linearised ENG and interference fields (not to scale). ENG currents not shown [24, 29, 79]. Taking electrode impedances into consideration, electrodes E_1, E_2 and E_3 correspond to connection points A, B and C respectively.

[1] Typical values: Z_o=200Ω, Z_t=2.5kΩ, Z_e=1kΩ, I_{EMG}=1μA

Based on the preceding theory, various studies [24, 29, 79] have proposed close approximations of circuit models for the cuff, similar to that in figure 2.16, illustrating the equivalent signal sources, the interface impedances of the cuff and the internal potential gradients of the ENG and interference sources due to its linearising property. This schematic diagram allows an analysis of the voltages appearing between the electrodes in terms of the currents of the nerve and muscle sources and the tissue and electrode impedances. The tissue impedance outside the cuff is Z_o and inside it is separated into Z_{t1} and Z_{t2} between the middle and each of the end electrodes resulting in $Z_{t1}+ Z_{t2} = Z_t$. In the ideal model, the cuff will be perfectly symmetrical and the tissue inside it will be evenly spread, similar to the cuff being immersed into saline, resulting to $Z_{t1}= Z_{t2} = 0.5\times Z_t$. The electrode impedances are Z_{e1}, Z_{e2} and Z_{e3} and it is assumed here that $Z_{e1} = Z_{e2} = Z_{e3} = Z_e$. The current source I_{INT} produces the interference signal from its field outside and inside the cuff. The interfering voltages across points AB and BC appear as anti-phase while the respective ENG signals appear in-phase.

2.4.2 Conventional tripolar amplifier configurations

2.4.2.1 General ENG amplifier requirements

The designer of ENG amplifiers to be used with cuff electrodes should consider several requirements that are shared with other biopotential amplifiers. The differential gain must be high, usually to raise the signal level from μV to the appropriate range for A-D conversion, but lower gains may be necessary if the same system is to be used for stimulation-induced signals. The front-end noise of the amplifiers must be very low and care must be taken to choose the optimal technology [18]. Amplification can be implemented in two stages, the first one providing low-noise preamplification to remove the necessity for low-noise design for the subsequent stage. Although transformer-coupled ENG recordings have been reported in the literature (e.g. in [24]) for scaling up the signal before introducing amplifier noise from subsequent stages, the use of transformers in implants is completely impractical [21, 22, 24]. Low power *integrated circuit* design is desirable for a recording system that is to be integrated into an implant [28, 29]. As implanted devices cannot be grounded the amplifiers have to be connected to a reference electrode somewhere inside the body, usually in the vicinity of the cuff.

2.4.2.2 The quasi-tripole and the true-tripole amplifier configurations

The amplifier configurations used with tripolar cuffs are the so-called *quasi-tripole* (QT) [26, 27] (figure 2.17(a)) and *true-tripole* (TT) [34] (figure 2.17(b)). In both arrangements, EMG cancellation is achieved by harnessing the ability of the cuff to *linearise* the fields of the external sources [21]. In theory, provided the cuff is symmetrical, the EMG is cancelled and only the ENG is present at the output of the amplifier configuration.

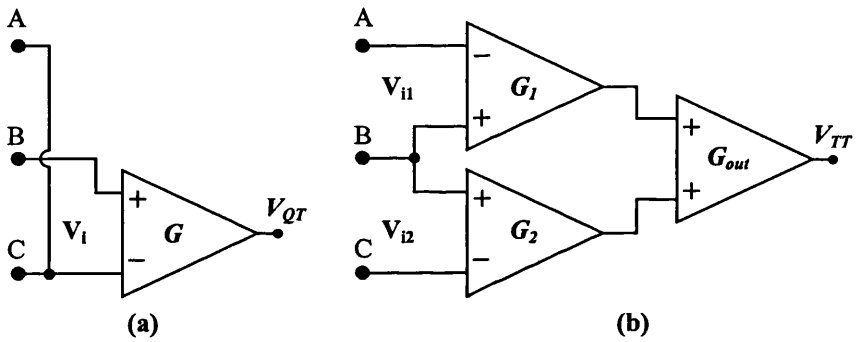

Figure 2.17 (a) The quasi tripole (QT) and its cuff connectivity (based on figure 2.16) **(b)** The true tripole (TT)

The performance of the QT and the TT can be compared in terms of interference reduction. Using the parameters of Figure 2.16, the residual EMG at the output of the QT and the TT can be expressed in terms of tissue and electrode impedances, ignoring any cuff end-effects [80].

The QT achieves interference reduction due to the connection of the outer electrodes, a connectivity that was initially assumed by Stein et al. [29] to offer EMG screening due to short-circuiting. However, due to the electrode-tissue interface impedances the cuff ends are not short-circuited and the interconnected end electrodes were shown by Thomsen [34] to act as a terminal which gives their average voltage provided their impedances are equal and the cuff is perfectly sealed. Ideally, the linearising property of the cuff results to the EMG voltage of the middle electrode being the average of the voltages at the end electrodes. As a result, by connecting a differential amplifier

between the short-circuited end electrodes and the middle electrode of a tripolar cuff results to interference elimination. If the gain of the QT amplifier is unity (i.e. G=1), the QT EMG output is [29]:

$$V_{EMG\_QT} = I_{INT} \frac{Z_o(Z_{t2} - Z_{t1})}{2Z_o + 2Z_t + \frac{Z_t Z_o}{Z_e}} \tag{2.8}$$

For an ideal cuff $V_{EMG\_QT} = 0$, because $Z_{t1} = Z_{t2}$ and therefore the QT offers interference elimination.

The TT reduces EMG interference using *only* the linearising property of the cuff [29]. Based on this, the EMG potential amplitudes of the unconnected end electrodes will be symmetrically valued around the amplitude at the middle electrode. Hence, using the middle electrode as reference, they will have equal amplitude and opposite polarity. Similarly, with the ENG linearised potential peaking at the centre of the cuff, the two ends of the cuff will provide ENG signals of equal amplitude and polarity. The ideal true-tripole uses the middle electrode as the common input between two differential amplifiers whose other inputs are connected to the end electrodes and therefore doubles the ENG amplitude while completely eliminating the interference. Generally, assuming unity gain for G_{out}, the TT output interference is [29]:

$$V_{EMG\_TT} = I_{INT} \frac{Z_o(G_1 Z_{t1} - G_2 Z_{t2})}{Z_o + Z_t} \tag{2.9}$$

Again assuming an ideal cuff, the internal tissue impedances of the two halves of the cuff are equal, and setting the gains so that $G_1 = G_2 = G$, then $V_{EMG\_TT} = 0$. Combined with the doubling of the ENG, the TT is theoretically preferable for ENG recording.

A brief theoretical comparison between the quasi-tripole and the true-tripole in terms of interference reduction was presented in [28]. The calculations involved the impedances formed inside a tripolar cuff and showed that the quasi tripole has higher SIR, but the TT offers relatively higher ENG amplitude and the input stage gains may be adjusted to increase of its S/I ratio. The use of a screened tripolar cuff, a tripolar cuff with two extra

external electrodes shorted together was shown to further decrease the amplitude of EMG interference especially when the electrodes were placed slightly towards the inside of the cuff, to avoid end effects. Using a screened tripole has the same effect as increasing the length of the cuff as it effectively decreases the gradient of the interfering field inside the cuff.

2.5 Conclusion

This chapter offered theoretical background information on neural physiology and conduction. Recording interfaces were described, with focus on cuff electrodes, because they are non-invasive to the nerve and appropriate for chronic implantation. When cuff size and closure are appropriate these electrodes offer significant advantages in ENG recording when used with specialised amplifiers. Cuffs linearize the fields of both the nerve signal and the muscle interference. The latter can be about three orders of magnitude greater than the microvolt neural signal of interest. Tripolar cuffs allow for the use of amplifier configurations that ideally eliminate the interference and amplify the neural signal. In particular the quasi-tripole and the true-tripole amplifiers have been described, with the latter generally offering a higher ENG output in ideal conditions.

Chapter 3

CUFF DEPARTURE FROM IDEAL MODEL

Ideally, interference in ENG measurements due to EMG from nearby muscles can be completely eliminated with the use of tripolar cuffs, in combination with appropriate amplifier configurations such as the QT and the TT (see chapter 2, section 2.4.2.2). As reported in the previous chapter, in both systems interference rejection is based on the ability of the cuff to linearize the internal potential field generated by external sources [27]. However, it has been widely reported [10-12, 16, 18, 21, 22, 24-32] that EMG contaminates ENG measurements, even when tripolar cuff amplifiers are used. This means that the cuff departs from the ideal model, which is the basis of the design of the QT and the TT. This effect, which causes the presence of interference at the output of tripolar cuff amplifiers, is termed in this thesis as *cuff imbalance*. This chapter offers a theoretical background on the main causes of cuff imbalance. These have been investigated to an extend that will assist in forming the specifications for the amplifier configuration described in this thesis.

3.1 Cuff Imbalance

3.1.1 Definition and measurement

According to equations (2.8) and (2.9) (chapter 2) the ability of the quasi-tripole and the true-tripole to eliminate at their output interference signals from sources outside the cuff, such as EMG, depends on the impedances Z_{t1} and Z_{t2} being equal. In this case the voltages across the two halves of the cuff would have equal amplitudes. As a result, the voltages U_{AB} and U_{BC} between the electrode connection points A, B and C of the cuff in figure 2.12 would be related by:

$$|U_{BC}| = |U_{AB}| = 50\%|U_{AC}| \tag{3.1}$$

However, the assumption that $Z_{t1} = Z_{t2}$ is not true in real implanted cuffs, for reasons described later (in section 3.1.3). Therefore, EMG presence at the outputs of the TT and the QT is not possible to avoid because $Z_{t1} \neq Z_{t2}$, and:

$$Z_{t1} = 0.5(1 + X_{imb})Z_t \tag{3.2}$$

$$Z_{t2} = 0.5(1 - X_{imb})Z_t \tag{3.3}$$

These lead to the introduction of the following definition of cuff imbalance X_{imb} (as a percentage):

$$X_{imb} = \left[\frac{Z_{t1} - Z_{t2}}{Z_t}\right] \times 100\% \tag{3.4}$$

where $|X_{imb}| < 100\%$. In terms of U_{AB} and U_{BC}, this can be expressed by:

$$X_{imb} = \left[\frac{|U_{AB}| - |U_{BC}|}{|U_{AB}| + |U_{BC}|}\right] \times 100\% \tag{3.5}$$

3.1.2 Effect of imbalance on the quasi-tripole and the true-tripole

Using the parameters above and assuming equations (2.8) and (2.9) can be expressed in terms of cuff imbalance, as follows:

$$V_{EMG\_QT} = I_{INT} \frac{X_{imb}}{1/Z_o + 1/Z_t + 1/2Z_e} \tag{3.6}$$

$$V_{EMG\_TT} = I_{INT} \frac{2GX_{imb}}{1/Z_o + 1/Z_t} \tag{3.7}$$

Clearly, in both cases, interference elimination would occur if X_{imb} was zero. Setting the TT gains to unity, it is apparent from (3.6) and (3.7) that $V_{EMG\_TT} \geq 2V_{EMG\_QT}$. Thus, the doubling of the ENG output in the TT case is less than the increase in interference for a given cuff imbalance value. This shows that in the presence of imbalance the TT will have a smaller SIR output than the QT.

In general, when cuff imbalance is present, the QT does not provide any means of correcting this imbalance externally. However, the TT can be modified to use externally controlled adjustable–gain amplifiers for G_1 and G_2 for imbalance correction, and this is analysed and demonstrated in chapters 4 – 6 of this thesis.

Some additional factors affecting the performance of each configuration individually include the dependence of the QT interference reduction on electrode – tissue interface impedance Z_e and the requirement for matching between the preamplifier gains G_1 and G_2 in the TT.

3.1.3 Causes of cuff imbalance

The two known causes of cuff imbalance are: i) cuff asymmetry (imperfect electrode placement) due to manufacturing tolerances [16, 27, 34], and ii) inhomogeneous tissue growth inside it after implantation [18, 34]. In other words, the assumption that $Z_{t1} = Z_{t2}$ (chapter 2) is based on the ideal case where the cuff is symmetrical and the tissue distribution inside it is uniform. In realistic implanted cuffs these two conditions cannot

be satisfied and although the first one can be minimised with novel cuff fabrication techniques [50], the second one is not possible to control.

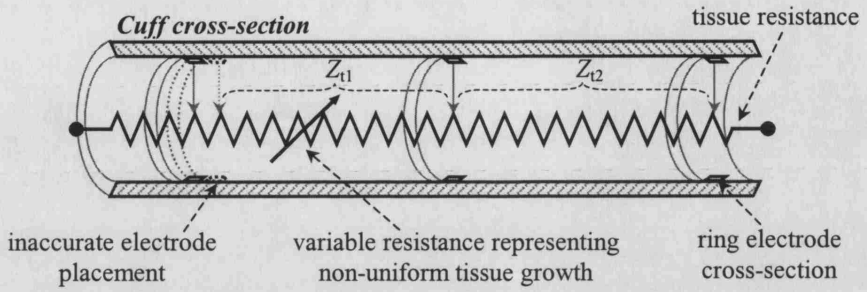

Figure 3.1 Cuff cross-sectional view, with the tissue between the nerve and cuff walls as a resistor and the cuff as a potential divider. Cuff asymmetry and inhomogeneous tissue growth affect the relative values of Z_{t1} and Z_{t2} and cause imbalance.

Another factor that has been reported to cause the deviation of the cuff behaviour from its ideal model is the cuff "end-effects" [81]. Calculations for a cuff immersed in saline, simulating uniform tissue distribution inside the cuff, indicated that the volume of fluid inside the cuff approximates an ideal distributed resistance, however there are some end effects close to the cuff edges, which reduce the linearity of the interference field inside it. The study in [81] found that longer cuffs result in great interference reduction, as the resistance of the volume inside the cuff becomes higher and less ion currents due to external fields are allowed to flow inside the cuff. As the end electrodes become more separated, interference is reduced but when they are in the proximity of the cuff ends interference is increased again. The solution in this case is to place the end electrodes a few millimetres away from the cuff edges (towards the inside of the cuff). The final choice about the cuff's length may be limited by the considerations related to surgical procedures and by the choice of location of the cuff inside the patient's body.

3.2 Proximity imbalance simulations

The end effects were shown in [81] to affect the linearising property of the cuff close to its ends, but they have not been previously connected to cuff imbalance. Furthermore, the connection of this effect to the proximity of the interference source to the cuff has not been studied. Such a connection could in some cases result to the cuff imbalance

depending on the relative distance and orientation of the interference source and the cuff. This would add the interference proximity component to asymmetry and tissue-related cuff imbalance, a component named here "proximity imbalance".

In order to illustrate how the cuff interacts with an external field and how cuff imbalance is affected by variations in distance and orientation, bioelectric field simulations were performed in Ansoft® Maxwell® software package. This software was chosen because it allows volume conductor [8, 82-84] simulations, with fields in conductive materials like saline used to simulate biological tissue. Some volume conductor expressions are presented in Appendix A. A monopole source was used for the interference field in [81], however the muscle source is usually represented by a dipole [85] and that was preferred here.

3.2.1 Procedure

The software allowed for two-dimensional simulations only, hence the cuff model used consisted of the upper and lower walls of the cuff cross-section (shaded areas in figure 3.1) placed in a saline plane close to an electric dipole representing the interference field. The distance between the cuff walls (corresponding to the cuff diameter) was 2mm and the cuff length was 20mm. The cuff model, which did not include electrodes, was rotated in different angles relative to the source and field simulations were performed for each angle (figures 3.2 - 3.4). The model material was polyamide. The range of cuff orientation φ_{or} varied from 0° to 135°. The signal amplitude of the dipole was chosen empirically so that the voltage across the cuff was approximately 1mV. The dipole was placed at 4cm away from the cuff centre. Distance variation was not examined at this stage.

3.2.2 Results

The effect of cuff rotation to the isopotential lines of the dipole is illustrated in the four different cases shown in figure 3.2, which correspond to φ_{or} = 0°, 45°, 60° and 90°. In the first case, for φ_{or} = 0°, the cuff is shown to turn the concentric and circular isopotential lines outside it to mostly linear and parallel ones inside it, indicating linear variation of potential. The next two values of φ_{or} demonstrate a similar effect, however,

it is evident that the potential close to the edges varies in a different fashion. For φ_{or} = 90° the cuff is again shown to perturb the potential distribution, however the lines inside the cuff do not suggest linear potential variation. Moreover the distance between the internal field lines in the first three cases varies along the length of the cuff, suggesting a slight variation of the potential slope inside it, especially close to the edges

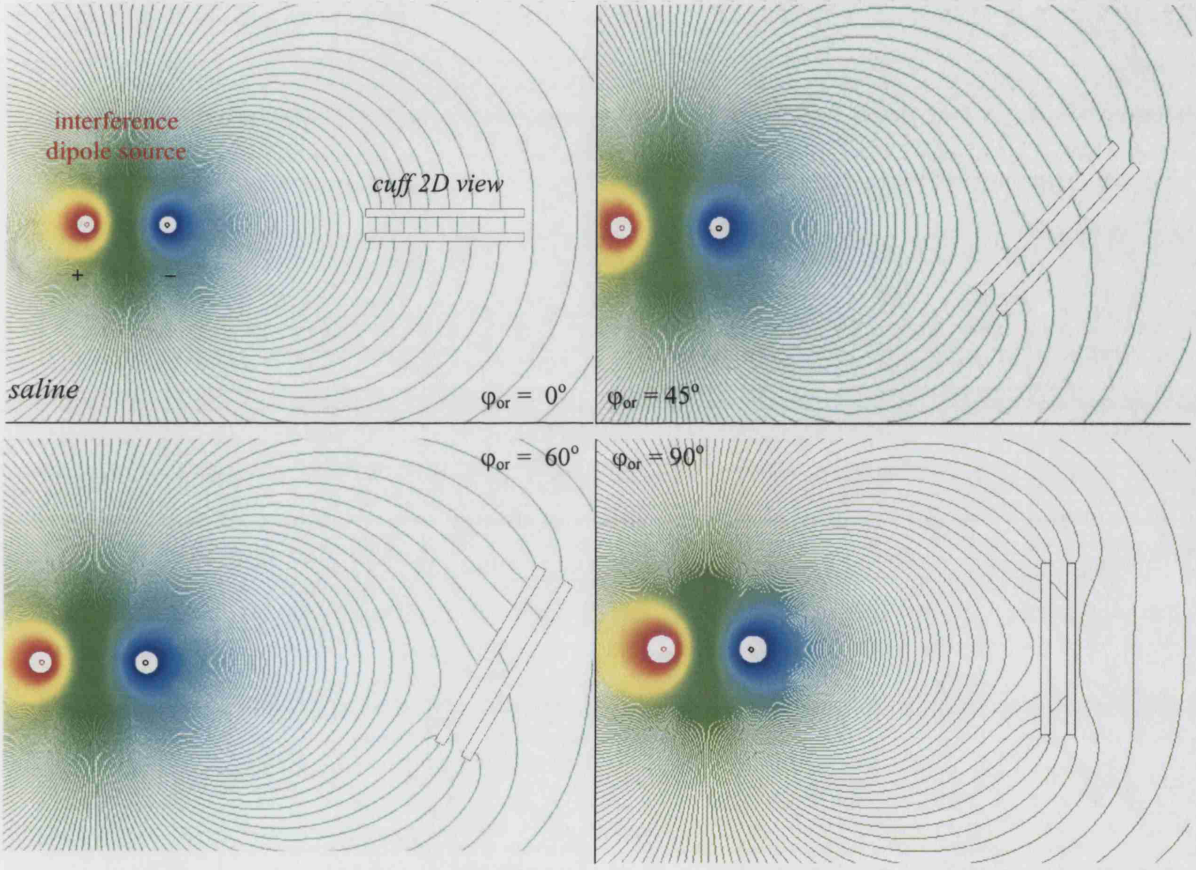

Figure 3.2 Two-dimensional view of cuff cross-section corresponds to shaded cuff cross-sections in figure 3.1 (electrodes excluded). For the simulations, the cuff was placed in a saline plane and an electric dipole represented the muscle. The cuff was rotated and electric field simulations were performed for various angles. Here, the effect of cuff rotation to the isopotential lines of the dipole is shown for four values of φ_{or}.

The electric field lines and, in effect, the ionic current paths are illustrated in figure 3.3 for φ_{or} = 30°. The arrows follow almost a straight-line course inside the cuff, with the slope of the current path approximately parallel to the cuff walls. The current path becomes curved close to the edges, due to the end-effects, also illustrated by the shape of the isopotential lines in the previous figure.

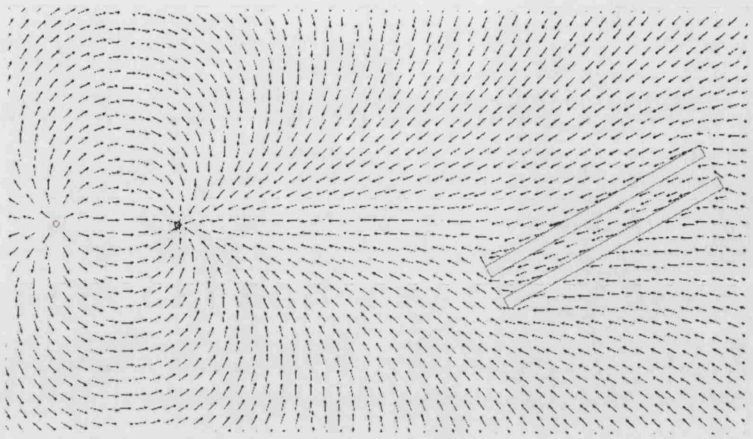

Figure 3.3 Electric field lines for $\varphi_{or} = 30°$

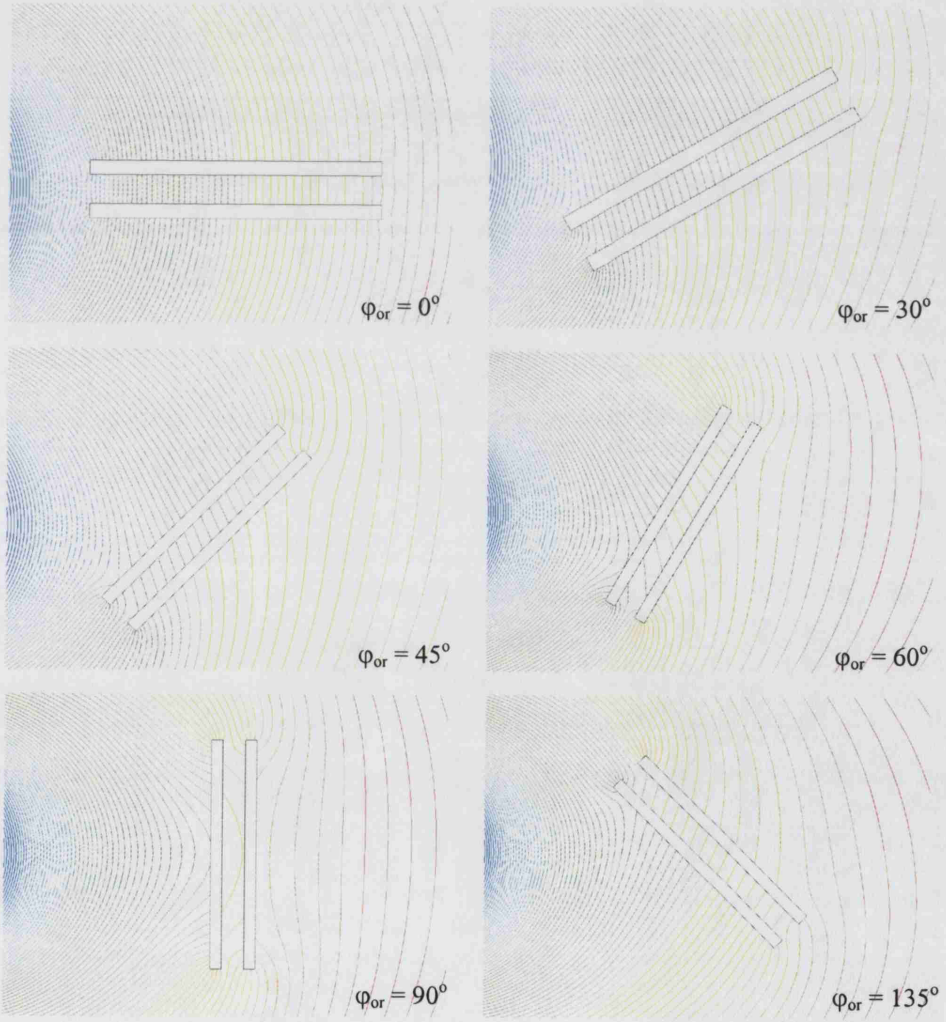

Figure 3.4 Higher resolution plots of isopotential lines inside cuff.

Figure 3.4 offers a more detailed view of the isopotential line distribution inside the cuff for φ_{or} = 0°, 30°, 45°, 60°, 90° and 135°. The variation in the density of the lines inside the cuff suggests that the two halves of the cuff, or the two areas that would occupy the space between the end electrodes and the middle one, may not possess the same potential across them, resulting in cuff imbalance.

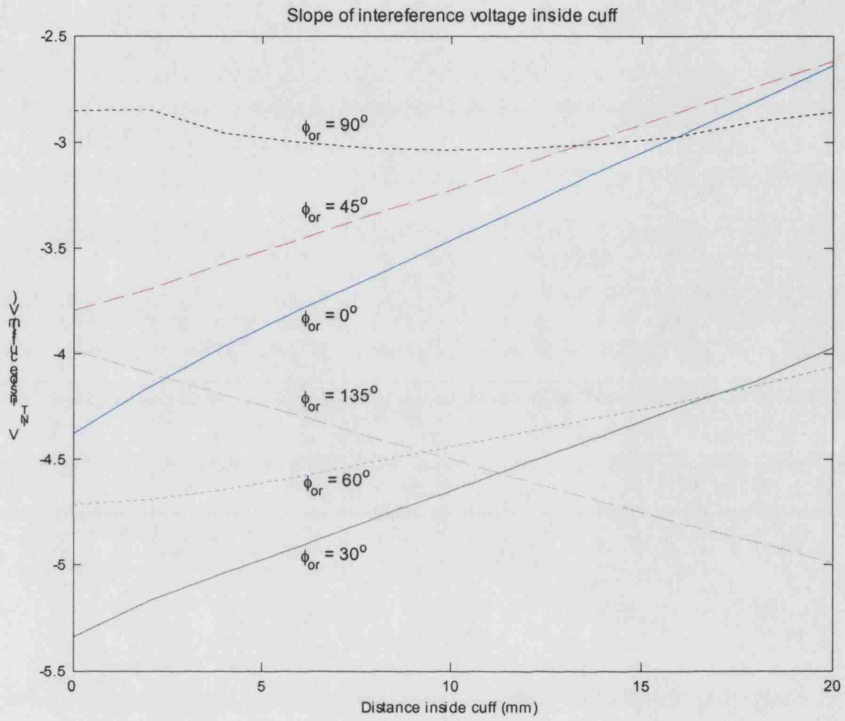

Figure 3.5 Interference potential gradients inside the cuff along its length

In the case of φ_{or} = 90°, it is again evident using this higher resolution illustration that the potential inside the cuff does not vary in similar fashion to the other orientations. Based on these plots, the interference potential gradients inside the cuff, for the values of φ_{or} mentioned before, were calculated and are illustrated in figure 3.5. The figure indicates that, apart from the case where φ_{or} = 90°, the potential gradient inside the cuff is mostly linear, as theory suggests (see chapter 2), especially if the regions very close to the edges are excluded. The gradients for different values of φ_{or} appear with different offsets, as the potential values at the cuff edges change as they perturb different isopotential lines when the cuff rotates. The negative polarity of the displayed voltages has to do with the fact that the most negative pole of the dipole was closer to the cuff during the simulations.

The amplitude variation of the signal across the cuff as a function of φ_{or} is illustrated in figure 3.6(a). The potential across the cuff decreases as φ_{or} varies from 0° to 90° and then increases again (with opposite polarity, absolute values are displayed). The amplitude is in the vicinity of 1mV for 30°, 45° and 135°, while the 0° and 90° cases are the extremes where the potential between the cuff edges takes values of 1.73mV and 7μV respectively. Interference potential variation is also displayed for electrode positions inside the cuff, with the amplitude dropping as the electrodes are shifted from 1mm to 2mm away from the cuff edges. The pattern of the interference potential with cuff orientation is similar in all three cases, with the amplitude decreasing for φ_{or} variation from the horizontal to the vertical positions and then starts increasing again.

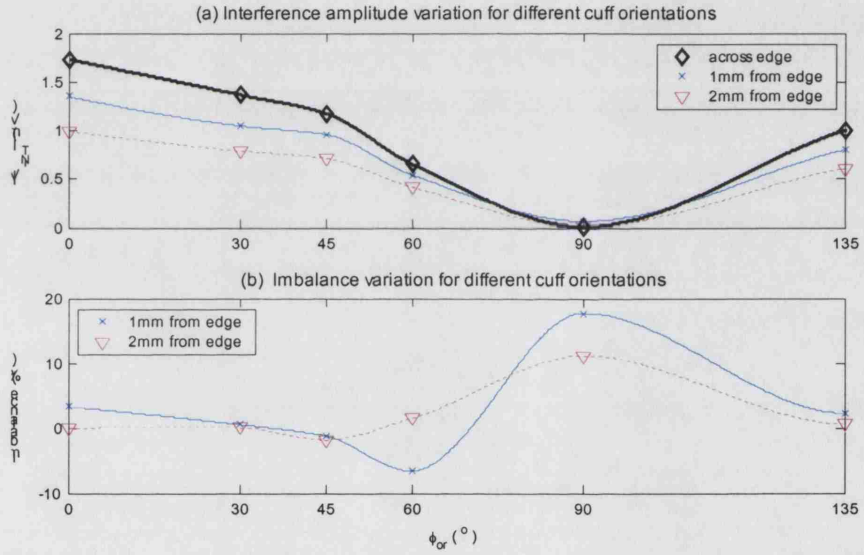

Figure 3.6 (a) Absolute voltage variation due to cuff orientation variation. Voltages across the cuff ends and across end electrodes placed at 1mm and 2mm inside the cuff ends are displayed. (b) Imbalance variation for different cuff orientations for end electrodes placed 1mm and 2mm inside the cuff edges.

Similarly, the cuff imbalance variation with φ_{or} using equation (3.5) for end electrodes placed either at 1mm or at 2mm inside the cuff edges, and a third electrode in the middle of the cuff in each case, is presented in figure 3.6(b). In the first case the imbalance values peak for φ_{or} of 60° and 90°, where the lowest amplitudes across the cuff were previously observed. As the electrodes move further inside the cuff, imbalance becomes less dependent on orientation for small φ_{or} values and then peaks

again at the vertical cuff position. The graphs in figure 3.6 indicate clearly that both interference amplitude and imbalance vary with changes in cuff orientation.

3.3 Experimental assessment of cuff imbalance in-vitro

3.3.1 Tissue growth imbalance

3.3.1.1 Procedure

In order to provide realistic conditions to test a tripolar cuff amplifier configuration in the laboratory a saline bath can be used [70, 86]. To examine the effect of imbalance caused by tissue growth, the saline impedance distribution inside the cuff was unbalanced using an almost spherical piece of silicone glue (diameter ≈ 1mm) on a thread, introduced inside a tripolar cuff immersed in saline (1% NaCl). The tripolar cuff used was handmade and had inner diameter of 2mm and length of 20 mm and each of the platinum foil ring electrodes had width of 1 mm and was placed 2mm from the cuff edges.

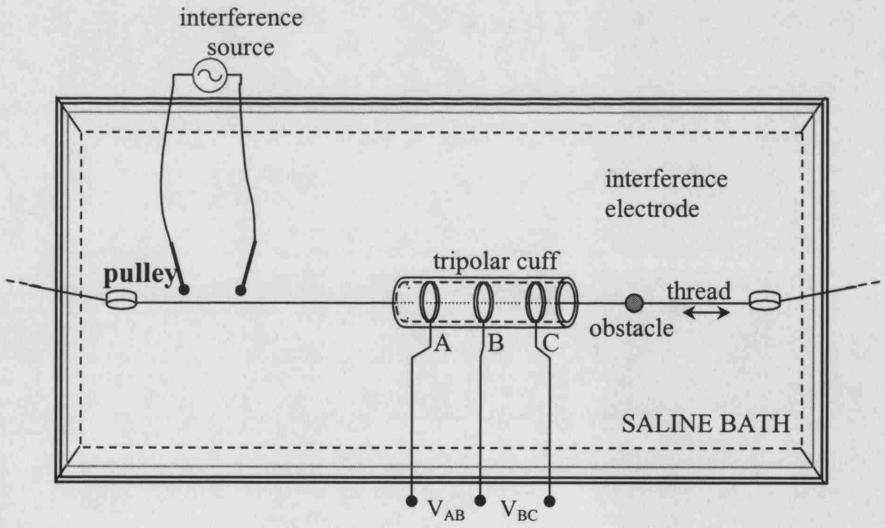

Figure 3.7 Saline bath setup for "tissue growth" imbalance measurements (cuff and bath not to scale). A silicone glue obstacle is introduced inside the cuff to change the impedance conditions inside it and produce imbalance. A transformer-coupled function generator and two electrodes inside the saline generated the interference signal.

In the configuration illustrated in Figure 3.7, the interference field was generated by a function generator connected through a transformer to two platinum electrodes inside the bath placed in line with the cuff at a distance of 2cm approximately. Cuff asymmetry was present, indeed it is difficult to avoid, and the silicone glue obstacle was moved through several positions inside the cuff [87] to cause imbalance variation. Using two differential amplifiers, each connected between an end electrode and the middle one (similar to the TT preamplifiers), imbalance measurements based on equation (3.5) were taken for various positions of the obstacle inside the cuff, to demonstrate that impedance changes inside the cuff result to imbalance.

3.3.1.2 Results

The graph in figure 3.8 illustrates the variation of cuff imbalance as the obstacle moves from one end of the cuff to the other. Asymmetry imbalance of 5.4% is present, evident from the initial obstacle positions, while it is still outside the cuff. As the obstacle enters the cuff, imbalance rapidly appears, with negative values peaking at –13.56% when the obstacle reaches the first outer electrode. The negative sign indicates that $|U_{AB}| < |U_{BC}|$, which is expected as the same ionic current goes through the cuff, but the impedance between A and B is reduced as the obstacle limits the saline volume between these two points.

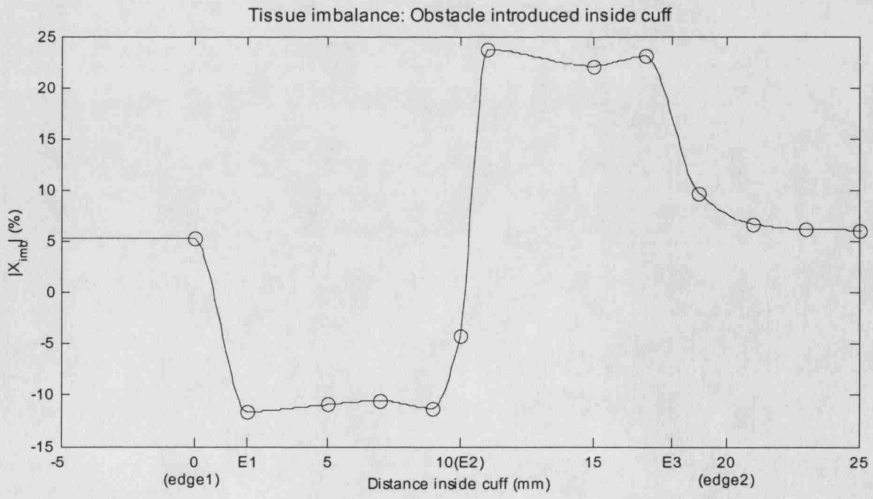

Figure 3.8 Cuff imbalance variation with obstacle position along the cuff.

Imbalance magnitude remains roughly constant slightly dropping by approximately 0.6% and then peaking again at –13.2% just before the middle electrode. Approaching the middle, imbalance starts becoming more positive and shortly after the middle electrode it peaks at around 21.5%. A similar pattern is observed, with the values peaking close to the electrode positions, with positive values indicating that $|U_{AB}|$ is now greater. Finally as the obstacle exits the cuff imbalance values drop again, to values close to 6.2%, with asymmetry imbalance becoming dominant again.

The slight difference between the cuff imbalance values for the cases where the obstacle is outside the cuff is possibly due to small pieces of glue residing on the thread that remained in the cuff after the obstacle had come out from the other end during the final measurements. Another possibility is that the obstacle disturbed slightly at least one of the electrodes causing a small change to the symmetry. The obstacle did come in contact with the electrodes during the procedure.

3.3.2 Proximity imbalance

3.3.2.1 Procedure

Extending the procedure followed in the simulations for understanding proximity imbalance, saline bath experiments were carried out with the interference dipole being generated by a 10mm cuff with two electrodes placed close to the cuff edges and some silicone glue in the middle of the cuff providing insulation between the electrodes. The recording cuff had similar dimensions to the one used in the previous saline-bath experiment (section 3.3.1.1). In this case, on top of variations in the orientation φ_{or} of the recording tripolar cuff, two cases of the orientation θ of the dipole source as well as two distances between the source and the recording cuff were also examined (figure 3.9).

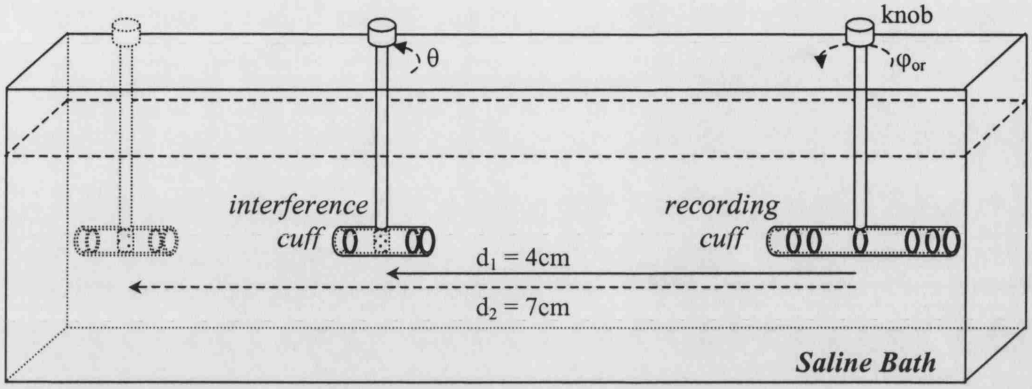

Figure 3.9 Saline bath proximity imbalance setup. The recording cuff was rotated through fixed values of φ_{or} using a rod glued to it. Measurements were taken with end electrodes placed at 2mm or 4mm from the edges or the screened tripole [29, 31]. The interference dipole was a cuff, which could be either on the recording cuff's axis or vertical to it. It was placed at positions d_1 or d_2.

The cuffs were glued on perspex rods (figure 3.10) and knobs were fitted at their ends to allow for the rotation over various angles. Measurements were taken for a φ_{or} range from 0° to 180° with angle shifts of 20° plus angles of 45° and 90°, θ values of 0° (as in the simulations) and 90° and for distances d_1 and d_2 corresponding to 4cm and 7cm respectively between the dipole and the recording cuff centres. Two more end electrodes placed 4mm from the edges inside the cuff were added to the cuff and measurements for various values of φ_{or} with $\theta = 0°$ and distance d_1, as in the simulations, were repeated. Then the outer electrodes were short-circuited and a set of measurements was repeated using a screened tripole [29, 31].

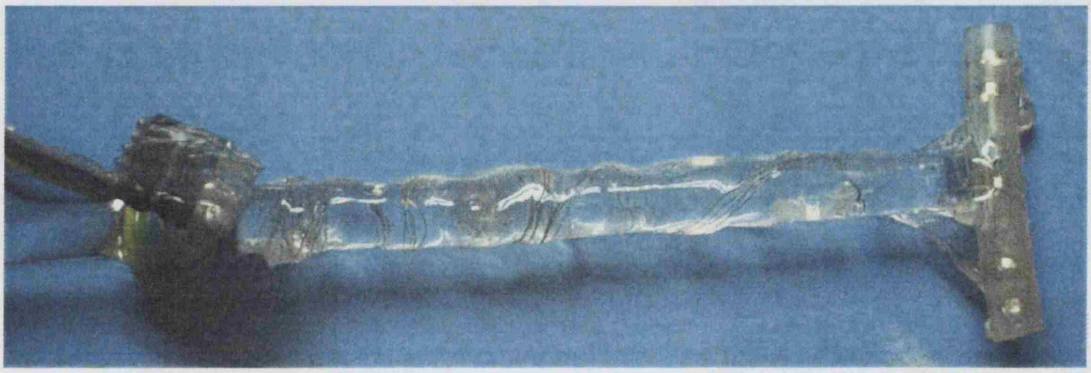

Figure 3.10 Five-electrode cuff, glued on a perspex rod. Platinum wires are connected to copper wires and glued to reduce strain. The cuff could be used as tripolar or screened tripole.

3.3.2.2 Results

With the dipole at $\theta = 0°$, the measurements produced similar results as the ones displayed in figure 3.6. Thus, the amplitude of the signal across the end electrodes (figure 3.11(a)) was on a maximum value for $\varphi_{or} = 0°$ and then it decreased to a minimum value of for $\varphi_{or} = 90°$ before increasing again for each value up to 180°. The amplitudes for these three angles for distance d_1 were 0.78mV, 0.025mV and 1.1mV respectively (solid line in the figure). The slight difference between the values corresponding to 0° and 180° could be due to unequal spacing between each end electrode and its nearby cuff edge, as well as cuff positioning precision error. The graph is more curved than the corresponding graph form the simulation results, as it has more data points due to more φ_{or} values being used. When the distance increases to 7cm (dotted line in figure 3.11(a)), the amplitude of the interference decreases to values of 0.094mV, 0.009mV and 0.107mV, again for respective φ_{or} values of 0°, 90° and 180°. The shape of the graph is similar to that for d_1 with the end values being approximately ten times smaller and the minimum being approximately three times smaller, indicating a smaller amplitude change with φ_{or} variation.

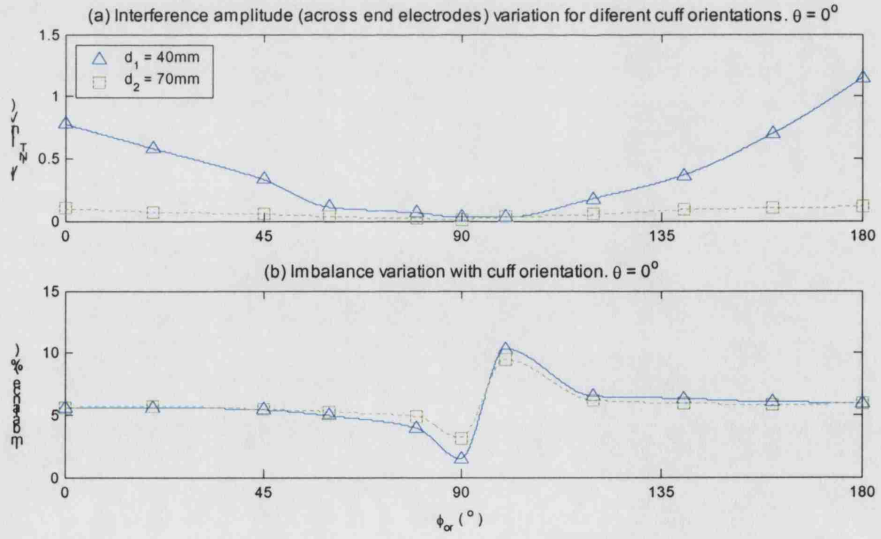

Figure 3.11 $\theta = 0°$: (a) Interference voltage across the end electrodes for d_1 and d_2. (b) Imbalance variation for different cuff orientations for d_1 and d_2.

Again, similar to the simulation, cuff imbalance (figure 3.11(b)) remains relatively constant until φ_{or} approaches 45° and then it starts becoming more negative, as the

relative size of the voltages between the two halves of the cuff changes. A minimum appears at 90° and then a sudden increase leads to a maximum at approximately 100° followed by another decrease, which settles to a relatively constant imbalance value from 135° to the end. The mean "imbalance offset" value along the small and large angles is 5.9% for both d_1 and d_2, corresponding to the asymmetry imbalance for this cuff. The main effect with greater distance is reduction of imbalance variation at φ_{or} = 90°, with the minimum values being 1.49% for d_1, a drop of 4% from the mean value, compared to a drop of approximately 3% to a value of 3.17% for d_2. The maximum peak at 100° is 10.3% for d_1 and 9.4% for d_2.

Changing the orientation of the dipole to θ = 90° had roughly the effect of shifting the characteristics of the graphs of figure 3.11 by 90° on the φ_{or}-axis (figure 3.12). The minimum amplitude of the interference signal across the end electrodes now appears at φ_{or} = 0° and 180° and a φ_{or} range from approximately 45° to 135° provided little amplitude variation (figure 3.12(a)). For d_1, the minimum values of interference amplitude were 0.04mV and 0.1mV (extremes of φ_{or} range) and the maximum was 0.35mV and as the source amplitude was kept constant this indicates that this particular interference source orientation results to a smaller amplitude range. For φ_{or} = 90°, the amplitude was 0.3mV and the recording cuff was parallel to the dipole. Again amplitude reduction was the result of increasing the distance. The minimum values (φ_{or} = 0°, 180°) were 0.019mV and 0.015mV and the maximum at φ_{or} = 90° was 0.099mV. The form of the two graphs in figure 3.12(a) indicates that for d_1 the amplitude saturates at 45° and 135°, dropping slightly for the φ_{or} values in-between.

Regarding cuff imbalance variation, figure 3.12(b) indicates that from φ_{or} = 0° to φ_{or} = 20° values decreased sharply, from a maximum of 14.05% (for d_1), to 6.45% respectively and then dropped further to 6.2% at φ_{or} = 45°. This value remained relatively constant (within 1%) until approximately 135°, where it increased slightly to a local maximum of 9% and then dropped sharply to –2.06% at 180°. Again cuff imbalance values peaked for φ_{or} values that corresponded to minima in the amplitude graph. Reducing the distance to d_2 dropped the imbalance variation in the segments of the graph surrounding the peak values, with the constant value segments remaining at

similar levels corresponding to cuff asymmetry imbalance for the particular cuff used in this experiment.

Imbalance reduction at the peaking values for greater distances between the cuff and the source could be due to reduced curvature of the isopotential lines and the field lines as distance from the dipole centre increases, causing less curvature inside the cuff close to the edges.

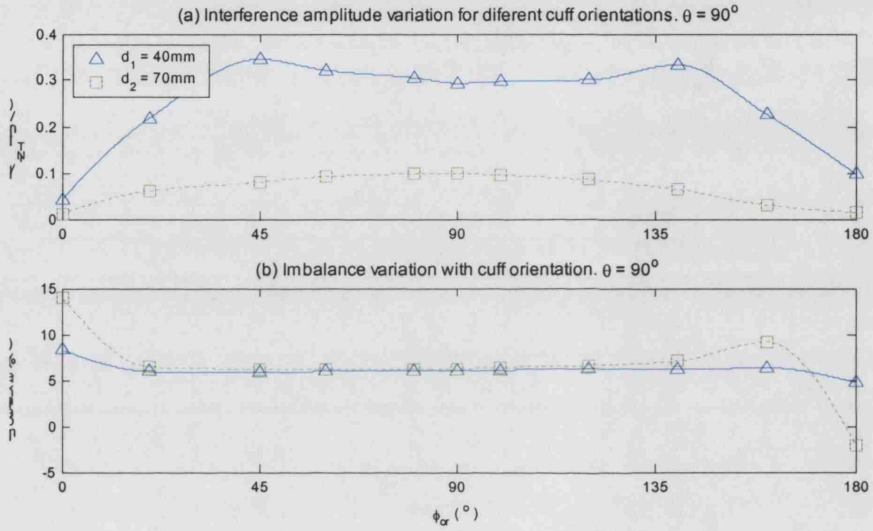

Figure 3.12 Similar to figure 3.11, but for $\theta = 90°$.

The graphs in figure 3.13 show the effect of moving the end electrodes further inside the cuff (dotted line) compared to the effect of using a screened tripole (solid line), for $\theta = 0°$ and distance of 4cm between the cuff and the dipole.

In terms of interference amplitude (figure 3.13(a)), both setups reduce interference by an approximately 0.3mV in the extremes (φ_{or} values close to 0° and 180°) relative to the tripole used previously, but only a small reduction is observed between 60° and 120°. For the smaller tripole (end electrodes further inside) the first maximum is 0.52mV, the minimum is now 0.022mV and the last maximum is 0.67mV. The screened tripole offers a slight reduction with values of 0.44mV, 0.015mV and 0.56mV respectively.

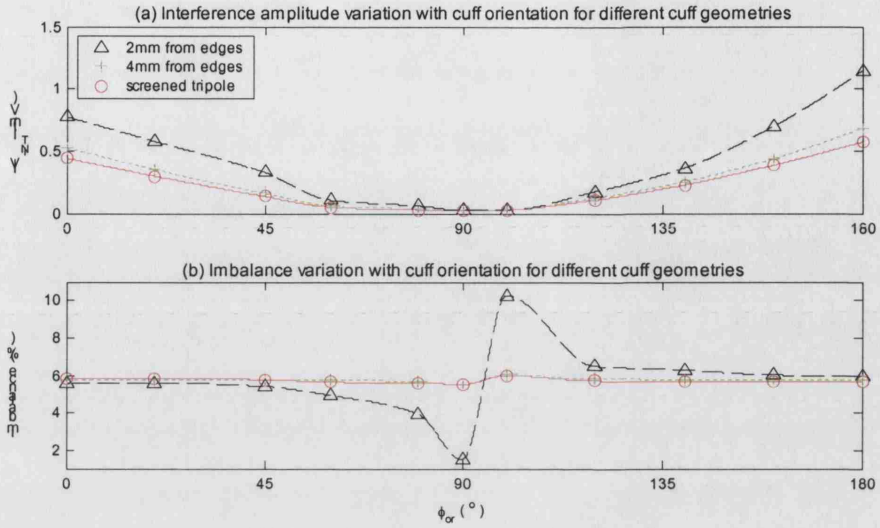

Figure 3.13 $\theta = 0°$, d_1. (a) Interference amplitude. (b) Cuff imbalance. Solid and dotted lines represent respective variation with φ_{or} when a screened tripole is used or the end electrodes of the original tripole are moved 2mm further inside it. The dashed line is the original tripole case illustrated in the graph of figure 3.11.

Both configurations minimised imbalance values relative to the original end electrode position (dashed line in graph), especially at the peaks. The first case provided 5.72% imbalance from $\varphi_{or} = 0°$ up to 45°, dropping to a minimum of 5.48% at 90° and then rising to a maximum of 5.97% at 100°. The respective values for the screened tripole were 5.78%, 5.49% and 6.02%. With a mean imbalance difference of 0.03% the two configurations provide virtually the same imbalance reduction of approximately 4% relative to the original configuration. This leads to the conclusion that the end electrode position is the dominant factor in both cases.

3.4 Discussion of simulation and in-vitro results

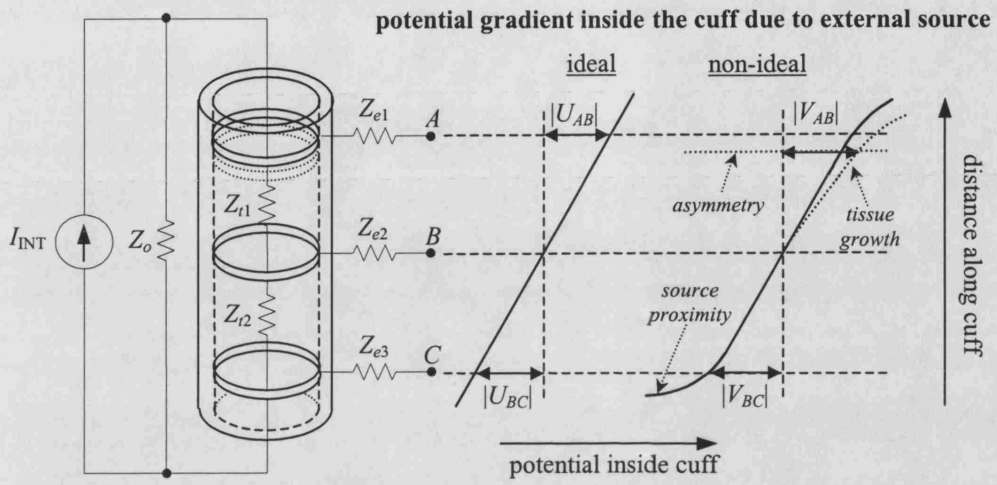

Figure 3.14 Model of the tripolar cuff with ideal and non-ideal interference potential gradients. U_{AB} and U_{BC} in the ideal model become V_{AB} and V_{BC}.

The model previously presented in figure 2.12 (chapter 2) can be now altered to take into account all the effects causing imbalance. Figure 3.14 illustrates the effects of asymmetry (example of end electrode misplacement), tissue growth in one side (changing the potential gradient) and end effects (curvature close to cuff ends). Imbalance can now be defined by:

$$X_{imb} = \left[\frac{|V_{AB}| - |V_{BC}|}{|V_{AB}| + |V_{BC}|} \right] \times 100\% \qquad (3.6)$$

The dependence of cuff imbalance on tissue growth and cuff symmetry is relatively straightforward from the definition of imbalance and from the factors defining Z_{t1} and Z_{t2}, which are the resistivity of the tissue or fluid between the respective electrodes multiplied by their distance. It is now evident from both the simulations and the saline bath experiments that imbalance also depends on the proximity of the external source to the cuff. Variation was observed with both distance and orientation, with the latter causing a more severe effect especially when the source dipole and the cuff are vertical to each other. Proximity variation had also a strong effect on signal amplitude. The

greatest imbalance variations were observed for the angles that caused the interference amplitude to be at a minimum.

Using a screened tripole had some effect in the interference amplitude, as reported in literature [29, 31], however the effect was similar when the end electrodes were just placed well inside the cuff. In the case of imbalance variation, the difference between using a screened tripole and the smaller tripole had a very small effect. In both types of measurements cuff orientation dependency remained, although in the case of imbalance it was greatly reduced. Within 0.5% cuff imbalance remained relatively constant. The use of a screened tripole with the dimensions used here does not make a significant difference and requires two additional electrodes and extra wiring.

Regarding proximity imbalance, the degree of non-linearity close to the edges depends on the curvature of the field lines entering and exiting the cuff (figure 3.3). The ionic current follows the path of the field lines. Since the curvatures on entrance and exit depend on the position of the interference source to the cuff when the end electrodes are placed close to the cuff edges, the proximity of the interference source to the cuff will influence cuff imbalance (i.e., $|V_{AB}| \neq |V_{BC}|$) even without asymmetry or tissue growth. As a result, different interference signals could appear with different cuff imbalance values, which is not the case when asymmetry and tissue growth are the only causes of cuff imbalance.

3.5 ENG and cuff imbalance

It has now been established that cuff imbalance affects the interference signals across the cuff, such as EMG. However, it is also important to examine whether ENG is affected.

From the three causes of imbalance mentioned before, proximity imbalance caused by cuff end-effects related to cuff orientation and position does not have a direct connection to ENG. However tissue growth and cuff asymmetry could have some effect. It was stated in chapter 2 that the recorded ENG signal depends on both intracellular and extracellular impedance. However, as equation (2.2) indicates, the

recorded signal is almost independent of impedance variations inside the cuff because the extracellular and the intracellular impedances R_e and R_i affect only the scaling factor α_R. Also according to [34, 49, 69], $R_e << R_i$ and this is also shown by the data in [88], where average longitudinal resistivities of rabbit nerve (white matter) and muscle for 1kHz signals are 957Ω/cm and 125Ω/cm respectively. Therefore slight variations to the value of R_e do not greatly affect this scaling factor. Moreover, the current summation in equation (2.1) is the result of closed current loops between nodes activated by the action potential. Therefore, the node that has the highest potential at a given instant in time will cause current loops flowing from it to its neighbouring nodes, as shown in figure 2.4 (chapter 2). As a result, the tissue impedance is separated in segments between active nodes. Consequently, the difference in impedance between the two halves of the cuff is not dominant in the current summation process.

ENG is somewhat related to cuff symmetry as the placement of the electrodes defines the three terms in equation (2.2) however, as mentioned in chapter 2, the dominant parameter determining the overlap of the three transmembrane potentials in eq. (2.2) and the shape of the recorded SFAP, is the number of nodes of Ranvier inside the cuff [69]. As a result of the theory in chapter 2, the ENG is often represented as a voltage source in series with the middle electrode [24, 29, 79]. Moreover, the QT ENG output is the result of averaging the two ENG terms across the two halves of the cuff and the TT adds these terms together. Hence, the ENG term can be considered unaffected by imbalance.

3.6 In vivo assessment of proximity effect on EMG

The fact that different interference sources may create signals across the cuff that appear with different proximity imbalance could mean that several muscles would create distinct interference artefacts at the output of tripolar cuff configurations. In this case, even if a method to eliminate cuff imbalance was developed, it would be very difficult to minimise all EMG interference in ENG recordings. In-vitro experiments have been very useful in investigating the basic causes of cuff imbalance. However, *in-vivo* experiments can provide real data about whether different groups of muscles appear

with different imbalance. Moreover, in-vivo experiments can assist in investigating experimentally whether ENG amplitude depends on cuff asymmetry imbalance.

In order to investigate these issues and, in addition, to demonstrate the relationship of cuff imbalance with asymmetry, experiments were carried out on rabbits, with stimulation-induced signals [32]. The experiments were carried out with a modified TT in order to evaluate its use in reducing imbalance. They took place in Aalborg Denmark, in collaboration with the Centre for Sensory-Motor Interaction (SMI) of Aalborg University.

3.6.1 Implementation of the Recording System

A recording system based on the TT was built with discrete components, with the option of varying the gain around the previously fixed value. A variable gain stage was connected between the preamplifiers and the output stage as shown in figure 3.15.

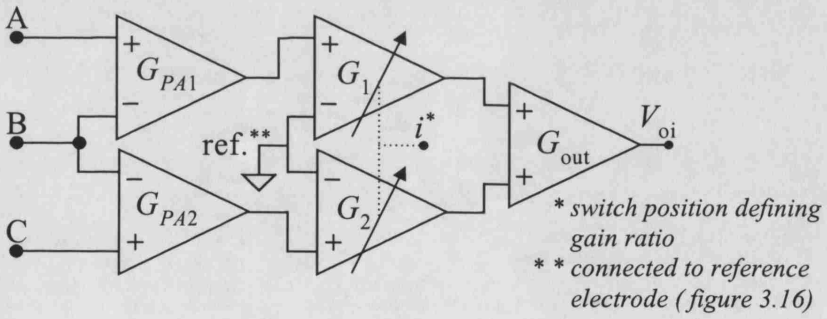

Figure 3.15 Configuration of the recording amplifier setup. Modified TT, with variable gain stage connected after the preamplifiers to manually reduce imbalance.

The preamplifiers were two AMP01 differential amplifiers with a gains $G_{PA1} = G_{PA\,2} =$ 400, the variable gain amplifiers were AD633 multipliers with a mean gain of 1 setup to allow maximum gain variation of ± 0.85 around this value. The output stage was realised using an OPA277 summing amplifier with a gain of 10.

The gains G_1 and G_2 of the variable gain amplifiers (see figure 3.15) were selected via a rotary switch with 11 positions (i) giving the values of gain-ratio G_2/G_1 listed in Table

3.1. In order to define the imbalance value corresponding to gain ratio values, equation (3.6) can be redefined by the outputs of the variable gain amplifiers G_1 and G_2 (figure 3.15), assuming they are in the initial condition where $G_1 = G_2$:

$$X_{imb} = \left[\frac{G_{PA1}G_1|V_{AB}| - G_{PA2}G_2|V_{BC}|}{G_{PA1}G_1|V_{AB}| + G_{PA2}G_2|V_{BC}|} \right] \times 100\% \qquad (3.7)$$

The preamplifier gains are equal and $G_{PA1} = G_{PA2} = G_{PA}$, and setting the ratio $G_2/G_1 = \gamma$, equation (3.7) becomes:

$$X_{imb} = \left[\frac{|V_{AB}| - \gamma|V_{BC}|}{|V_{AB}| + \gamma|V_{BC}|} \right] \times 100\% \qquad (3.8)$$

If the gain ratio is adjusted so that cuff imbalance is eliminated, the value of γ corresponding that specific imbalance value can be found by setting $X_{imb} = 0$ in equation (3.8). This results to:

$$\gamma = \frac{|V_{AB}|}{|V_{BC}|} \qquad (3.8)$$

Replacing this in equation (3.6), gives the imbalance value in terms of its corresponding value of γ:

$$X_{imb} = \left[\frac{\gamma - 1}{\gamma + 1} \right] \times 100\% \qquad (3.8)$$

Each of the eleven predefined values of γ corresponded to the cuff imbalance values also listed in Table 3.1. For each switch position *i* the system produced a corresponding output V_{oi}. The recording system had a bandwidth of 1.5 Hz to 25 kHz, the lower-end provided by input AC coupling.

Parameter	Value										
Switch pos. (i)	1	2	3	4	5	6	7	8	9	10	11
γ	1/11	1/5	1/3	1/2	5/7	1	7/5	2	3	5	11
X_{imb} (%)	-83.3	-66.7	-50	-33.3	-16.7	0	16.7	33.3	50	66.7	83.3

Table 3.1 Rotary switch positions (*i*) and corresponding values of γ and X_{imb}.

3.6.2 Experimental procedure

Acute experiments were performed on eight New Zealand white rabbits with weights of 3 to 3.5 kg. Each rabbit was anesthetized with a mixture of 50mg/ml ketamin, 20mg/ml xylazin and 10mg/ml plegicil, administered intramuscularly, first dose 5 ml and subsequent hourly doses of 2 ml. A split type cuff with flap cover (similar to figure 2.6(a), chapter 2) with inner diameter of 2 mm and length of 22 mm was used with four platinum foil ring electrodes, each with a width of 1 mm (figure 3.16). The two middle electrodes (denoted E_{M1} and E_{M2}) were placed on either side of the cuff centre, 2 mm apart (electrode edge separation). The end electrodes were placed at 2 mm from the cuff edges to allow observations of the effects of proximity imbalance. A switch was connected between the cuff and the recording system to allow the cuff middle electrode to be E_{M1}, E_{M2} or E_{M1M2}, the latter denoting that the two electrodes were shunted together to represent a more balanced middle electrode. The purpose of switching between these three electrode positions was to allow some manual control over cuff asymmetry, thus controlling part of the cuff imbalance. The reference electrode for the recordings was a subcutaneous needle at the back of the animal. Another tripolar cuff, with an inner diameter of 2 mm and length of 12 mm, was used to apply square biphasic stimulation pulses of amplitude between 1 mA and 1.5 mA, with pulse width of 200 μs and frequency of 5 Hz. The stimulating cuff was placed around the sciatic nerve and the recording cuff around the tibial nerve approximately 2 cm apart from each other (figure 3.16).

Measurements were taken on one leg of each rabbit, for each middle electrode position (E_{M1}, E_{M2} and E_{M1M2}), with all nerve branches present and after cutting ramus muscularis. This resulted in forty-eight sets of measurements, six of which were

considered invalid when analyzed due to the absence of nerve signal. The measurements were captured using a TEAC RD-145T DAT recorder with a sampling frequency of 20 kHz. The interference signals that occurred were the *stimulus artefact* and the *M-wave*. The nerve signal recorded was the compound action potential (CAP) [3] which is much larger than the naturally occurring ENG.

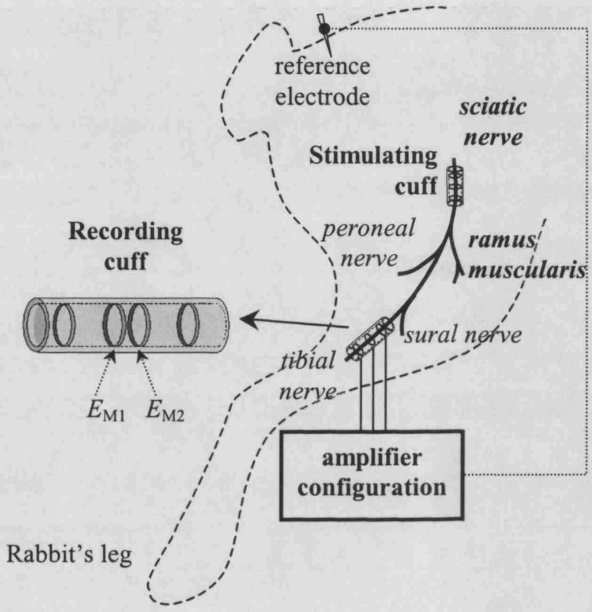

Figure 3.16 Experimental set-up; nearby nerve branches, position of cuffs and recording cuff illustration (not to scale).

3.6.3 Results And Discussion

3.6.3.1 Proximity imbalance

Examples of the effect of different gain-ratios to the residual stimulus artefact and *M-wave* signals at the output of the modified TT (E_{M1M2} middle electrode position) are shown in figures 3.17 and 3.18.

In figure 3.17 all nerves are intact and figure 3.18 displays some output traces after the ramus muscularis was cut. The first peak is the system output due to the stimulus artefact, the second and the third comprise the CAP, and the next two constitute the M-wave. These correspond to the peaks indicated in figure 2.13 (chapter 2), where an input to the system was displayed. The second peak of the CAP, which is not overlain by the stimulus artefact, is generally undistorted in form and in time by the change through the

gain-ratios (the slight level-shifting is caused by the overlapping stimulus artefact). In both graphs the gain ratio values that would give close to zero amplitude stimulus artefact are different to the ones that would eliminate the M-wave. This is expected due to the proximity imbalance discussed earlier in the chapter. The same effect was observed in the remaining forty recordings.

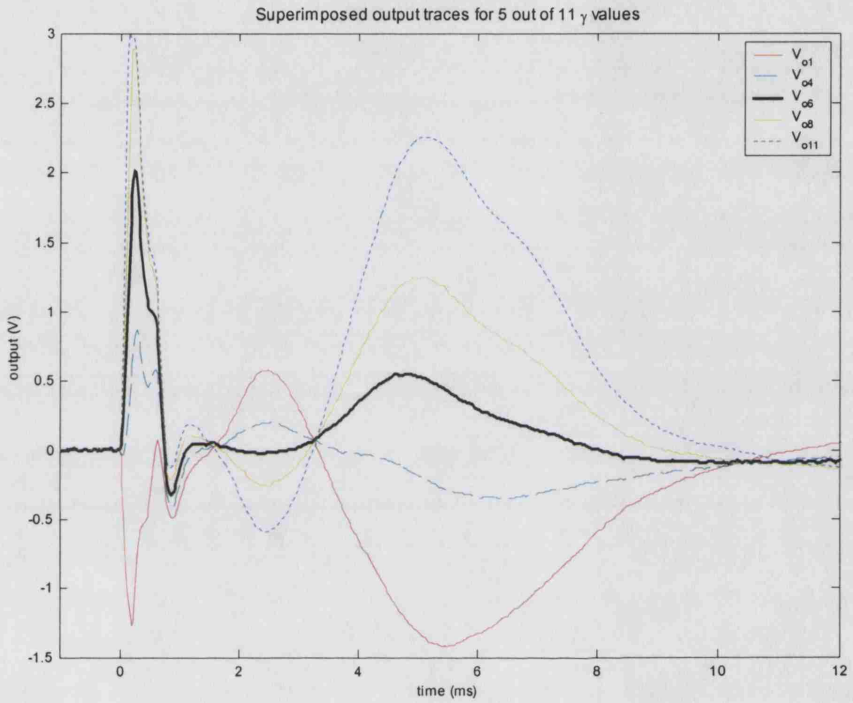

Figure 3.17 An example of superimposed system outputs for five values of γ, *before cutting the ramus muscularis*. The bold line corresponds to switch position 6 and γ = 1. Not all eleven outputs are shown for clarity.

In figure 3.17, the *M-wave* changes polarity for γ between 4 and 6 while stimulus artefact crosses zero between γ = 1 and γ = 4. Similarly, in figure 3.18 the M-wave is close to zero for unity gain-ratio but this gives a non-zero stimulus artefact. The stimulus artefact peak changes polarity somewhere between γ values of 1 and 1/2, its corresponding cuff imbalance being between 0 % and –33.3 %, closer to the latter (see Table 3.1).

An important observation in figures 3.17 and 3.18, as well as in all similar data obtained throughout the experiment, was that the muscle activity was generally represented by a single M-wave with specific imbalance values, before and after the ramus muscularis was cut. Therefore, the fact that different groups of muscles were active in each case did not result to different M-waves with different imbalances. It resulted to one M-wave with one corresponding imbalance value. Therefore, although this value is affected by proximity, the muscle activity appears as a single signal, which is the superposition of all individual muscle signals active in the vicinity of the cuff.

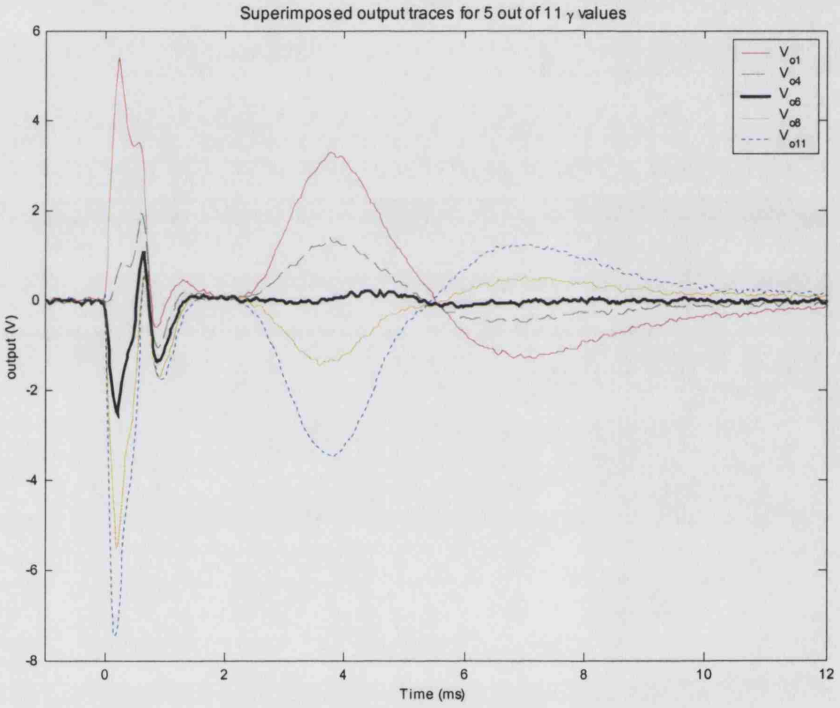

Figure 3.18 An example of superimposed system outputs for five values of γ, *after cutting the ramus muscularis*. The bold line corresponds to γ = 1 and near-zero cuff imbalance value for the *M*-wave in this case.

By interpolating between the peak amplitudes of the stimulus artefact and the *M*-wave of figure 3.18 for the eleven gain-ratios, as shown in figure 3.19, the γ values that would eliminate the imbalance and minimise the interference corresponded to the zero crossings (dashed arrows). These in turn corresponded to the imbalance value of each interference signal, according to the values of table 3.1, and an imbalance x-axis is also displayed in the figure. In this case, the cuff imbalance due to the stimulus artefact was

–26.2 %, and due to the *M*-wave was +4.52 %. The two sources had different proximity towards the recording cuff and as a result they appeared with different imbalance values.

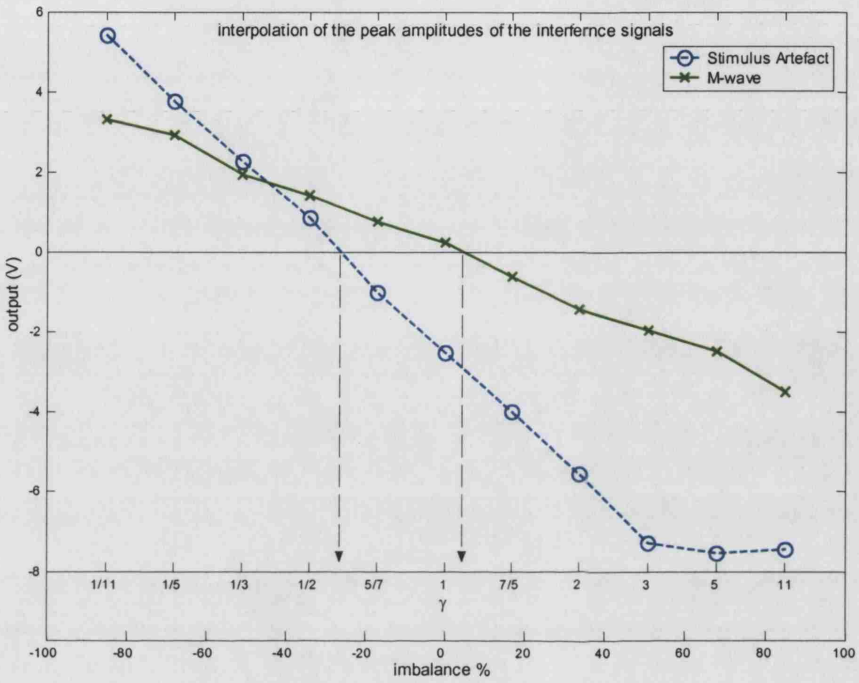

Figure 3.19 Peak values of stimulus artefact and *M*-wave (1st peak) for the outputs in figure 3.18. As γ and the corresponding cuff imbalance vary, each interference signal crosses zero when the gain-ratio corresponds to its cuff imbalance.

3.6.3.2 Asymmetry imbalance

Figure 3.20 shows how the stimulus artefact cuff imbalance and *M*-wave cuff imbalance (all forty-two recordings), changed with middle electrode position. The fourteen sets of lines joining the data points for E_{M1}, E_{M1M2} and E_{M2}, correspond to measurements from individual rabbits. The middle electrode varied by 1 mm either side of the cuff centre, which was approximately 10% of the distance between it and each of the end electrodes. This resulted in a mean cuff imbalance change of about 10% for both interference signals.

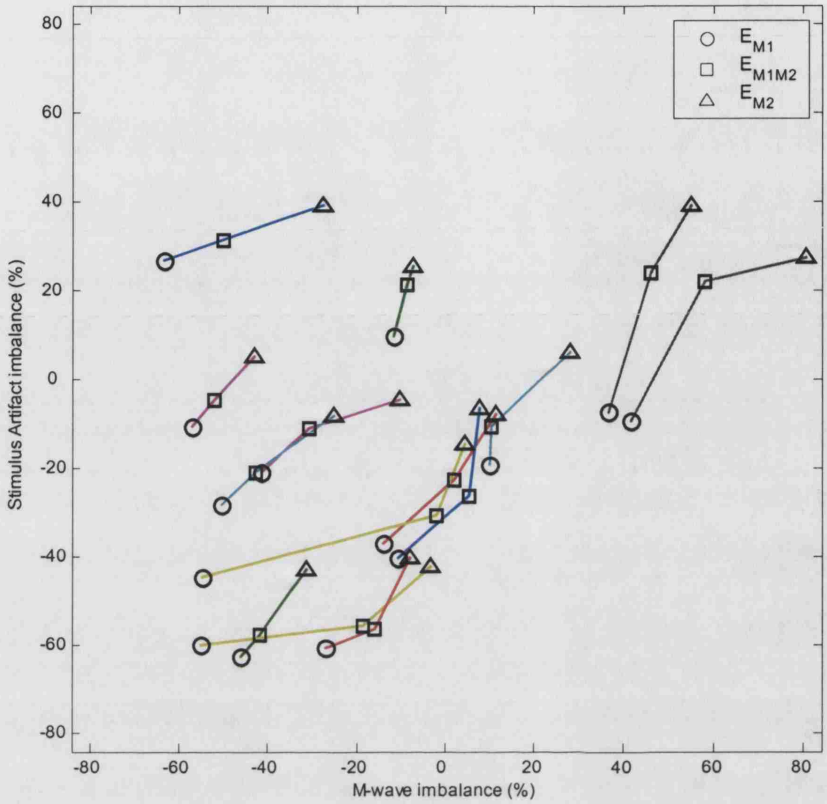

Figure 3.20 Variation of stimulus artefact and *M*-wave cuff imbalances with middle electrode position. The fourteen sets of lines joining data points for E_{M1}, E_{M1M2} and E_{M2} correspond to all valid measurements before and after any nerve cutting.

A gradient of 45° for the lines representing the electrode transitions would indicate that the symmetry change affected the cuff imbalance of both signals similarly. In order to assess whether that was the case, the mean gradients for the fourteen E_{M1} to E_{M1M2} and E_{M1M2} to E_{M2} electrode transitions were calculated (figure 3.21).

The transitions from E_{M1} to E_{M1M2} resulted in a mean gradient of 45.1° (standard deviation 23.7°), and the transitions from E_{M1M2} to E_{M2} resulted in a mean gradient of 48.1° (standard deviation 20.5°). These results confirm that changing the geometrical symmetry of the cuff had the expected effect of proportionally altering cuff imbalance. The high standard deviation is attributed to the fact the setup was somewhat distorted during some sessions (e.g., small air bubbles and clotted blood in the cuff). Furthermore, the cuff imbalance values obtained were somewhat high because the recordings were done immediately after implantation [76].

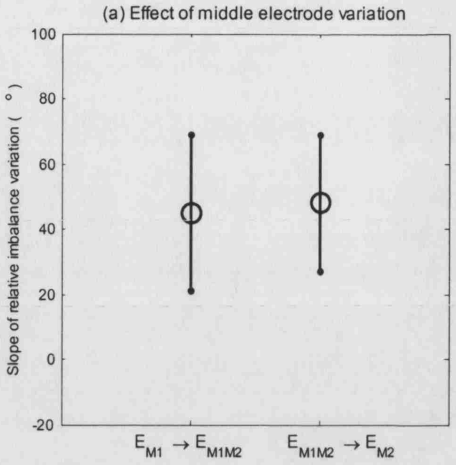

Figure 3.21 Mean gradients of relative imbalance variation of stimulus artefact versus *M*-wave imbalance for middle electrode connection change from E_{M1} to E_{M1M2} and from E_{M1M2} to E_{M2} to. The error bars represent the standard deviation.

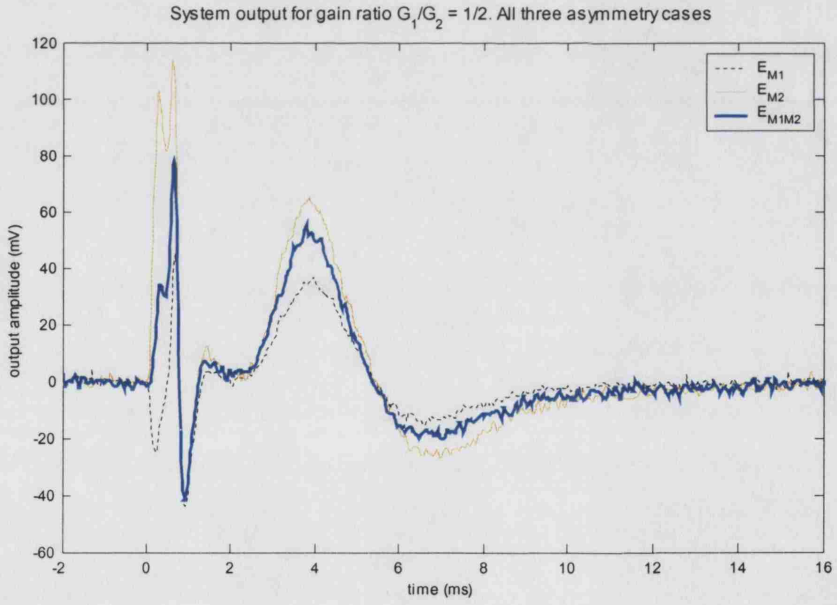

Figure 3.22 The output of the "test TT" amplifier configuration for gain ratio ½, after cutting the ramus muscularis. The three cases of cuff asymmetry are shown to affect only the interference signals.

Figure 3.22 illustrates three superimposed outputs corresponding to the three middle electrode connections for $\gamma = ½$ after cutting ramus muscularis. The recordings were made from the same rabbit. The variation in stimulus artefact and M-wave amplitudes is visible, however the 2nd peak of the CAP, which is not overlain by the stimulus artefact,

shows that the CAP amplitude is unaffected by the change in cuff symmetry. Therefore it is evident that cuff imbalance is a cuff-related error that affects almost only the interference signals, making their elimination more difficult during ENG measurements.

3.7 Conclusion

This chapter investigated the reasons causing EMG contamination of the output of tripolar cuff amplifier configurations, ideally employed to eliminate such interference during ENG measurements. The cause was established to be cuff imbalance and three main causes and types of cuff imbalance were presented. Some of these have been mentioned as possible reasons before, but to the author's knowledge they have not been previously investigated. Tissue growth, cuff asymmetry and relative cuff and interference source orientation and distance were shown to be the main causes. The last two factors were described with the term "proximity imbalance". The connection of tissue growth and asymmetry to imbalance was straightforward, however proximity was somewhat more complex to understand. For this reason, electric field simulations in saline were performed. The resulting plots indicated that the cuff does indeed cause the internal potential gradient to be linear but curving occurs close to the edges, which depends on cuff orientation. The procedure was repeated and expanded using saline bath experiments, which established that both imbalance *and* interference amplitude vary with relative changes in the distance and orientation of the cuff and the dipole interference source. It is evident that proximity imbalance can be minimized by moving the end electrodes sufficiently inside the cuff. This could also be achieved by increasing the cuff length while keeping the electrode spacing constant, as this affects the recorded ENG amplitude (chapter 2). The choice of cuff length depends on the space available for a particular application.

Based on the experiments conducted in this chapter, asymmetry and tissue growth can result in a combined cuff imbalance value of about 10%-15%, but proximity imbalance may cause higher imbalances. The values observed in the in-vivo session are also related with conditions observed during that experiment, such as poor cuff closure, and possible air bubbles inside the cuff, affecting imbalance and electrode-nerve interfacing dramatically.

Regarding imbalance variation with time, the first one is expected to have a fixed value as symmetry is mainly defined during cuff fabrication. Tissue growth is expected to vary slowly with time (weeks), with more rapid changes (hours / days) occurring directly after implantation [76]. The proximity component of cuff imbalance will depend on the rate of activation of different interference sources.

It is very important to note here that the in-vivo experiments indicated that all active muscle groups behaved as a single interference source. Moreover, the in-vitro experiments indicated that high imbalance values combined with low interference amplitude and therefore, the residual output interference from tripolar amplifier configurations may not be very highly affected by proximity imbalance.

This chapter described measurement types and procedures that to the author's knowledge have not been described elsewhere. However, although the imbalance and the signal behaviour observed are sometimes related to bioelectric fields, this thesis is not concerned with field mathematics. The purpose of this chapter was to establish the reasons behind ENG output degradation in tripolar cuff amplifiers in order to form the foundation for an advanced amplifier design that can improve neural measurements by tackling the problem of cuff imbalance. Again to the author's knowledge, cuff imbalance has not previously been well documented and established, either with simulations or experimentally. An effort to balance the cuff using a potentiometer between the end electrodes was presented in [27] and Rahal in [34] mentioned the lack of balance in the cuff as a reason of non-ideal cuff behaviour. However, even in those cases cuff imbalance was neither studied nor established as the definite cause of EMG throughput to the output of the recording schemes. Therefore this chapter was fundamental for the direction of the work presented in the remaining chapters.

Chapter 4

ADAPTIVE TRIPOLE SYSTEM-LEVEL ANALYSIS

As mentioned in the previous chapters, neural activity monitoring for providing feedback in FES systems requires amplifier schemes that provide immunity to EMG contamination [21, 26, 58, 78, 89]. The "quasi-tripole" and the "true-tripole" amplifier configurations have been used for reducing muscle interference taking advantage of the properties of the cuff (see chapter 2). However, EMG contamination has been commonly reported as one of the most serious problems in ENG recordings even when tripolar cuff amplifier configurations are used [10-12, 16, 18, 21, 22, 24-32]. This problem was attributed to cuff imbalance, as discussed in chapter 3. Various solutions have been proposed, including analogue filtering [24], high-order digital filtering and statistical analysis [30, 90] or digital post-processing using specialised algorithms like, for example, blind signal separation [36]. However these solutions aim at minimising EMG without dealing with imbalance and suffer from limitations making them undesirable; they reduce the bandwidth of the recorded signal, they increase system complexity and they are often non-implantable [30].

Here, a simple analogue automatic gain control configuration is presented which is essentially a modification of the TT, offering adaptive cuff imbalance correction using a frequency independent method, thus reducing the interference and at the same time

retaining neural information throughout the bandwidth of interest. The concept was first reported in [34], where it was simulated in Simulink, in terms of ideal mathematical blocks, presenting only the output of the system to demonstrate that it could eliminate interference.

The system-level analysis is taken a step further here, taking into consideration the basic sources of error affecting the design, to evaluate the capabilities and the limitations of the system and to establish whether it is feasible as an analogue implementation. This will lead to the definition of the specifications for an analogue realisation (see chapter 5). Using appropriate analogue IC design methods the system can be integrated (see chapter 6) and be made implantable.

4.1 System-level description

The first stage of the system (figure 4.1) consists of fixed-gain preamplifiers, optimised for low noise and impedance-matched to the cuff electrodes, followed by a variable gain stage, controlled by the differential feedback signals $V_{fb}(t)$ and $-V_{fb}(t)$. The control stage performs a comparison of the EMG amplitudes from the two halves of the cuff (mentioned later as the two channels), by first rectifying the signals and then comparing the difference of their absolute values, using a comparator.

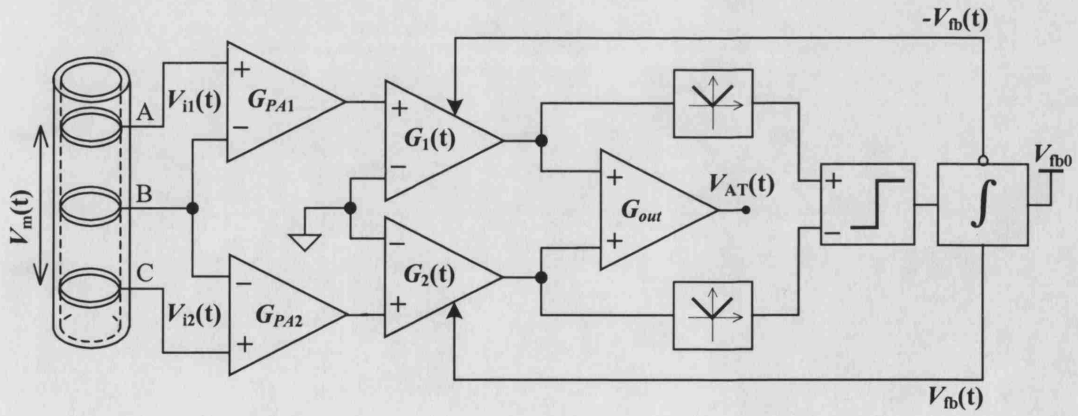

Figure 4.1 The AT block diagram. Gains of $G_1(t)$ and $G_2(t)$ are controlled by feedback signals $V_{fb}(t)$ and $-V_{fb}(t)$

The description of the control part of the AT that follows makes assumptions approximating ideal conditions, which will be revisited in the next section where sources of error are discussed. Assume that the ENG does not affect the feedback stage, as it is much smaller than the dominant EMG. Also assume that the rectifiers produce DC values equivalent to the amplitudes of their inputs.

Say that the EMG component in channel 1 is greater than that of channel 2 and the initial condition of the variable gain stage is such that $G_1 = G_2$. The output of the comparator is applied to a long time constant integrator, which produces the differential feedback signals $V_{fb}(t)$ and - $V_{fb}(t)$. In this case, the comparator output will be fixed to its positive output level, causing $V_{fb}(t)$ to be a rising ramp, thus increasing gain $G_2(t)$ and reducing $G_1(t)$. As a result the two inputs of the comparator will reach the same value and its output will oscillate because the comparator is a bistable. Therefore, ideally, the operation of the comparator can be described as a square wave generator with fixed output amplitude, whose frequency is either zero or very high, depending on the input amplitude difference. When the EMG components in both channels are brought to the same amplitude, the high frequency oscillations at the output of the comparator will cause the long time constant integrator to keep its current state. As a result, $V_{fb}(t)$ will ideally be a DC level, corresponding to the feedback required to equalize the EMG signals.

In this way, the variable-gain amplifiers, which can be implemented by multipliers, counterbalance the cuff imbalance by equalising the amplitudes of the EMG signal at the outputs of the two channels that are applied to summing amplifier G_{out}, similar to the TT. As a result the equalised and anti-phase interfering signals from the two channels are eliminated and in-phase ENG signals are summed, amplified and then extracted at the system output $V_{AT}(t)$.

The inputs $V_{i1}(t)$ and $V_{i2}(t)$ can be expressed as follows:

$$V_{i1,2}(t) = V_{m1,2}(t) + V_{n1,2}(t) \quad (4.1)$$

where $$V_{m1}(t) = 0.5(1 + X_{imb})V_m(t) \quad (4.2)$$

and $$V_{m2}(t) = - 0.5(1 - X_{imb})V_m(t) \quad (4.3)$$

Some of the characteristics of ENG and EMG discussed in chapter 2 include respective spectral peaks at approximately 1-3kHz and 100-250Hz, and respective bandwidths of 500Hz to 10kHz and 1Hz to 3kHz. Therefore the bandwidth of interest for the system is 500Hz to 10kHz. The imbalance was defined in the previous chapter to be:

$$X_{imb} = \frac{|V_{m1}(t)| - |V_{m2}(t)|}{|V_m(t)|} \times 100\% \tag{4.4}$$

$V_m(t)$ is the EMG across the cuff, split into $V_{m1}(t)$ and $V_{m2}(t)$ across channels 1 and 2 respectively. Say $V_{emg} = |V_m(t)| = |V_{m1}(t)| + |V_{m2}(t)|$ and $|X_{imb}| < 100\%$. Also, $V_{n1}(t) = V_{n2}(t) = V_n(t)$ represents the ENG measured by each channel. Assuming $G_{PA1} = G_{PA2} = G_{PA}$ (figure 1), the output of the AT is given by:

$$V_{AT}(t) = G_{PA}G_{out}\,(G_1(t)V_{i1}(t) + G_2(t)V_{i2}(t)) \tag{4.5}$$

The multiplier gains are given by:

$$G_1(t) = g(V_{fb0} - V_{fb}(t)) = G_{fb0} - G_{fb}(t) \tag{4.6}$$

and

$$G_2(t) = g(V_{fb0} + V_{fb}(t)) = G_{fb0} + G_{fb}(t) \tag{4.7}$$

where g is the voltage-to-gain conversion factor of the multipliers (here, $g = 1V^{-1}$). The resulting multiplier gains consist of a fixed gain G_{fb0} corresponding to a balanced cuff and a $G_{fb}(t)$, the time-varying part of the gain. To ensure that multiplier outputs don't change phase: $V_{fb0} > 0$, and $|V_{fb}(t)| < V_{fb0}$ therefore $G_1(t), G_2(t) > 0$.

From eq. (4.1) - (4.7), the output $V_{AT}(t)$ of the system in terms of signal, interference and imbalance will be:

$$V_{AT}(t) = G_{PA}G_{fb0}G_{out}[(X_{imb} - \frac{G_{fb}(t)}{G_{fb0}})V_m(t) + 2V_n(t)] \tag{4.8}$$

If $X_{imb} \neq 0$, EMG elimination in $V_{AT}(t)$ occurs when the integrator output $V_{fb}(t)$ settles to a value V_{fbX}, which is ideally DC and corresponds to the current imbalance value. As a result $G_{fb}(t)$ settles to G_{fbX} and $G_{1,2}(t)$ settle to $G_{1,2}$ so that:

$$G_1|V_{m1}(t)| - G_2|V_{m2}(t)| = 0 \tag{4.9}$$

The gain ratio is the inverse of the amplitude ratio of the two input EMG signals. From equations (4.4), (4.6) - (4.8) and after replacing $G_{fb}(t)$ with its settled value, G_{fbX} is expressed by the following:

$$G_{fbX} = G_{fb0}X_{imb} \tag{4.10}$$

Therefore, when the output settles the coefficient of the EMG term $V_m(t)$ in eq. (4.8) will be zero.

4.1.1 AT convergence time

Assuming at present that the comparator is an open-loop amplifier with a high gain, say G_{co}, its output $V_{co}(t)$ can be represented relative to the rectifier outputs $V_{r1,2}(t)$ by:

$$V_{co}(t) = G_{co}(V_{r1}(t) - V_{r2}(t)) \tag{4.11}$$

leading to

$$V_{co}(t) = G_{PA}G_{co}(G_{fb0}X_{imb}V_{emg} - G_{fb}(t)(V_{emg} + 2|V_n(t)|) \tag{4.12}$$

$2|V_n(t)| << V_{emg}$ and therefore this can be approximated by:

$$V_{co}(t) = G_{PA}G_{co}V_{emg}(G_{fb0}X_{imb} - G_{fb}(t)) \tag{4.13}$$

If an abrupt imbalance variation occurs, say from previous value X_{imbP} to current X_{imb}, G_{fbX} will be provided by the output of the integrator, $V_{fb}(t)$, after it settles:

$$V_{fb}(t) = \frac{G_i}{\tau_{int}} \int V_{co}(t)dt \tag{4.14}$$

Therefore $$\frac{dV_{\text{fb}}(t)}{dt} = \frac{G_{\text{i}}}{\tau_{\text{int}}} G_{PA} G_{co} V_{emg} (G_{\text{fb0}} X_{\text{imb}} - g V_{\text{fb}}(t)) \tag{4.15}$$

where G_{i} is the integrator gain and τ_{int} is its time constant. This results to:

$$V_{\text{fb}}(t) = \frac{G_{\text{fb0}} X_{\text{imb}}}{g} \left(1 - e^{-\left(\frac{G_{PA} G_{co} G_{\text{i}} g V_{\text{emg}}}{\tau_{\text{int}}} \right) t} \right) \tag{4.16}$$

Therefore $$G_{\text{fb}}(t) = G_{\text{fb0}} X_{\text{imb}} \left(1 - e^{-\left(\frac{G_{PA} G_{\text{co}} G_{\text{i}} g V_{\text{emg}}}{\tau_{\text{int}}} \right) t} \right) \tag{4.17}$$

This leads to the system time constant being: $\tau_{sys} = \frac{\tau_{\text{int}}}{G_{PA} G_{\text{co}} G_{\text{i}} g V_{\text{emg}}}$. However, the comparator is not really an amplifier and therefore its gain has to be replaced by output over input. In this case the input includes the feedback gain G_{fbXP} due to the previous settled integrator output, which corresponded to X_{imbP}. This leads to:

$$\tau_{sys} = \tau_{\text{int}} \frac{G_{\text{fb0}}}{G_{\text{i}} g V_{\text{co}}(t)} \left(X_{\text{imb}} - \frac{G_{\text{fbXP}}}{G_{\text{fb0}}} \right) \tag{4.18}$$

For simplification say G_{i} g V_{co}[t] = G_{i} gV_{comp} f[t], where V_{comp} is the comparator's output amplitude, which is fixed. As mentioned before, when the feedback stabilizes the comparator output may be approximated by a high frequency square wave, denoted here by f[t], which has unity-amplitude. Assume at this stage of the analysis that the frequency of f(t) is sufficiently high so that its integral leads to a purely DC integrator output. Therefore the gain term G_{i} gV_{comp} can be named G_{int}. As a result:

$$\tau_{sys} = \tau_{\text{int}} \frac{G_{\text{fb0}}}{G_{\text{int}}} \left(X_{\text{imb}} - X_{\text{imbP}} \right) \tag{4.19}$$

As the output of the integrator, and therefore the multiplier gain variation is exponential, the system convergence time will be approximately $5\tau_{\text{sys}}$.

$$t_s \approx 5\tau_{sys} \tag{4.20}$$

Using a comparator makes the system settling time independent of the EMG amplitude and it depends only on imbalance. However, the comparator is very sensitive to offsets and it is a high bandwidth component in circuit that works in low frequencies. Therefore, if not chosen or designed carefully it can become power consuming and create power supply distortion.

4.1.2 Sinusoidal signal representation

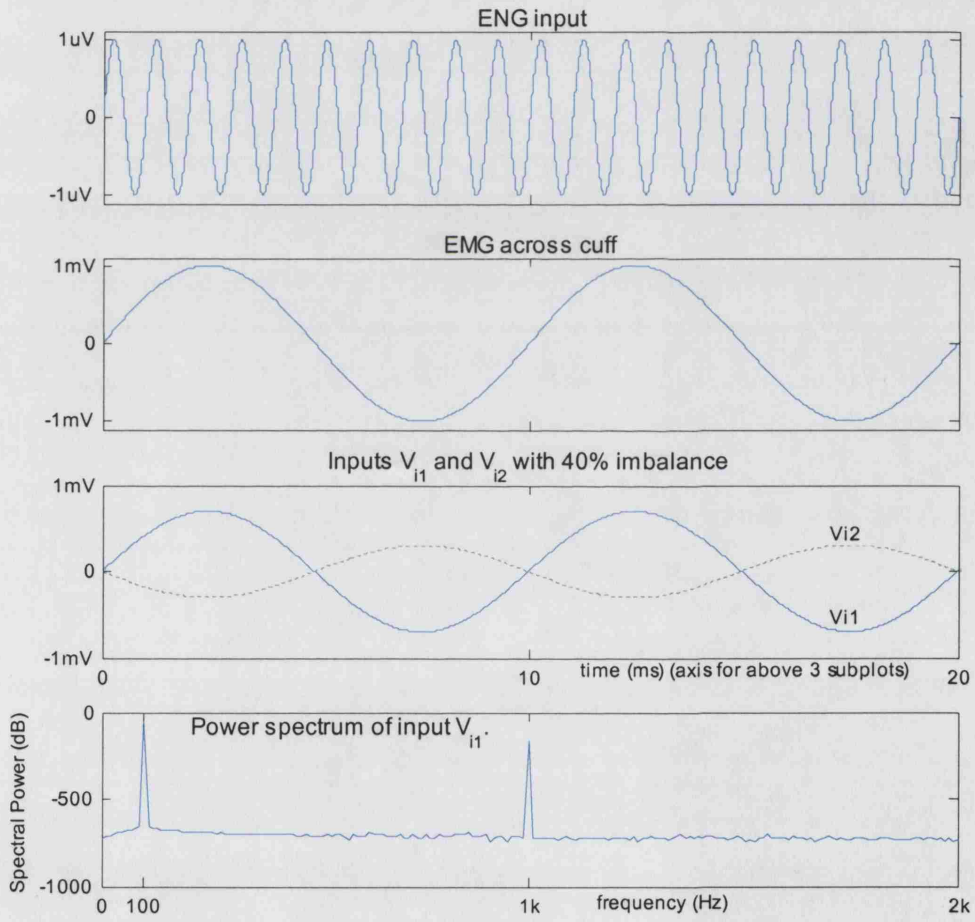

Figure 4.2 The ENG and EMG signals and the resulting AT inputs, applying 40% imbalance. The relative size of the signals is evident, as the ENG component is not visible on the system input traces. Input spectrum shows the peaks of both signals

In order to visualize the corrective action of the AT and to demonstrate the effect of the error factors, the EMG and ENG signals can be represented as sinusoids:

$$V_m(t) = V_{emg} \sin(\omega_1 t) \tag{4.21}$$

and

$$V_n(t) = V_{eng} \sin(\omega_2 t) \tag{4.22}$$

where V_{emg} and V_{eng} are the EMG (across the cuff) and ENG amplitudes respectively, while ω_1 and ω_2 are their respective frequencies. Using V_{emg} = 1mV, $\omega_1 = 2\pi\times100$Hz, V_{eng} = 1μV, $\omega_2 = 2\pi\times1$kHz and X_{imb} = 40% the graphs in figure 4.2 are produced. Thus the AT output becomes:

$$V_{AT}(t) = G_{PA}G_{fb0}G_{out}[(X_{imb} - \frac{G_{fb}(t)}{G_{fb0}})V_{emg}\sin(\omega_1 t) + 2V_{eng}\sin(\omega_1 t)] \tag{4.23}$$

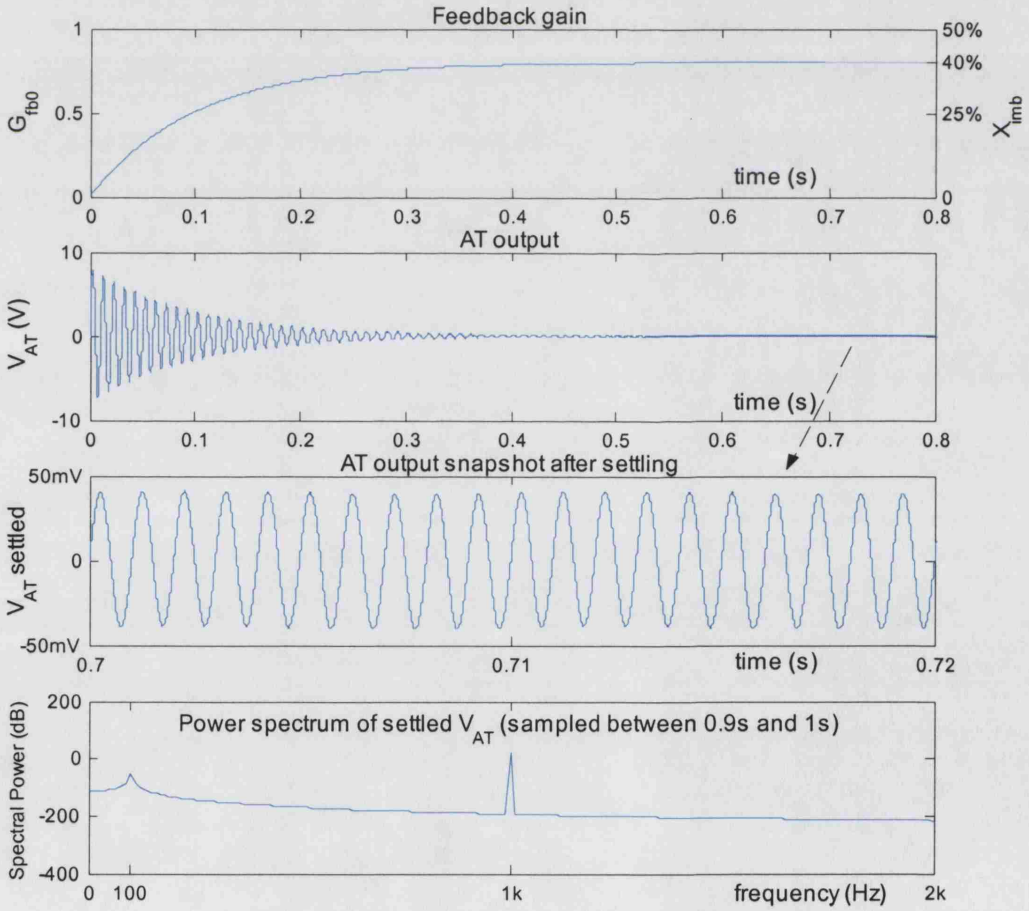

Figure 4.3 The feedback and the system output. The calculated settling time is a close approximation to that indicated by the plot. A snapshot of the settled output clearly shows the extracted ENG, which is amplified by $2G_{PA}G_{fb0}G_{out}$ = 40,000.

Using the values used for figure 4.2 and $G_{PA} = 1000$, $G_{fb0} = 2$, $G_{out} = 10$, $G_{INT} = 8$, $\tau_{int} = 1s$ and $X_{imbP} = 0$ in equations (4.19) – (4.20), (4.23) the resulting system settling time is $t_s \approx 0.5s$ and the feedback and the system output are shown in figure 4.3, along with a snapshot of the extracted ENG after the system has settled.

4.2 Sources of error

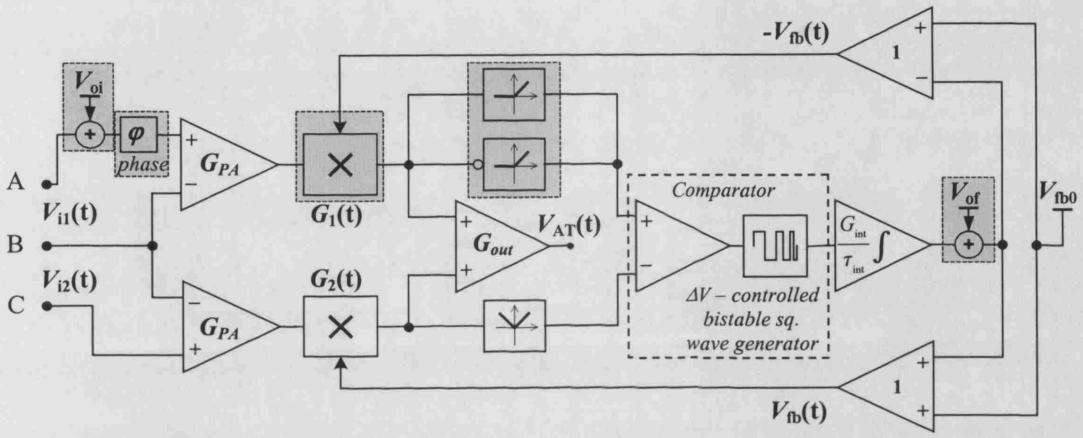

Figure 4.4 The AT block diagram, including functional representation of some blocks and main sources of error. The latter are indicated by the shaded areas and they include phase errors (φ), DC offsets at the input (V_{oi}) and in the feedback loop (V_{of}) and harmonic distortion. A Simulink model corresponding to the figure, as well as the Mathematica scripts, can be found in Appendices B1- B3.

This section examines the operation of the system under the influence of the most important error sources, to examine the system limitations, as well as to define some of the design specifications and to identify the key components of the AT before any circuit – level realisation is developed. The error sources to be examined include phase errors (φ), input DC offsets (V_{oi}), feedback loop DC offsets (V_{of}) and harmonic distortion introduced in the multipliers due to ripple on the settled feedback. figure 4.4 shows the block diagram of the system modified to indicate the error sources and the functional representation of some blocks based on the analysis in this chapter. Describing a rectifier in terms of two half-wave rectifiers (one with inverting and one with non-inverting input) and the comparator as a bistable frequency generator, controlled by its input voltage difference, assists in establishing the effects of these errors on the control stage and at the output of the system. In the following sections of

this chapter, the equations used previously to describe the system will be modified accordingly for each case and appropriate subscripts will be added to the variable notations used until now.

4.2.1 Phase errors

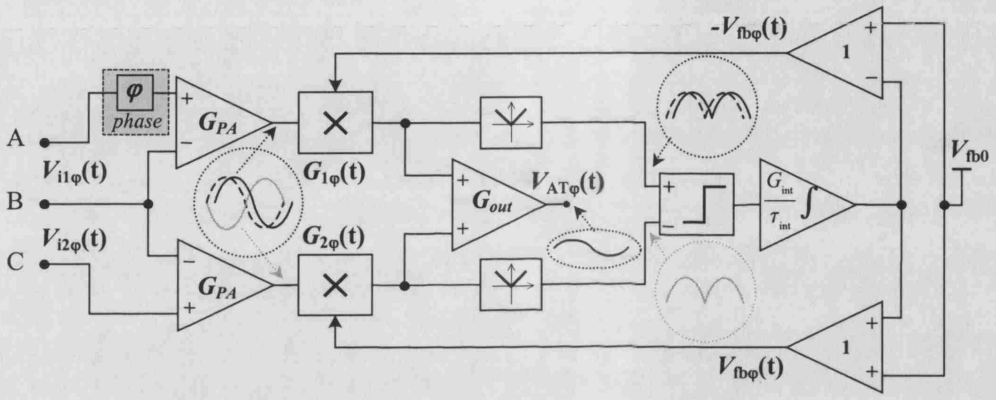

Figure 4.5 The AT block diagram, affected by input phase error (φ), indicated by the grey block. Channel 1 waveforms are shown with (solid line) and without (dashed line) the error. System variables' subscripts are followed by subscript "φ".

In order to avoid electrolysis by DC currents flowing through the tissue, the system has to be preceded by a DC isolation stage. Thus, high-pass filters need to be connected in series with the electrodes before the inputs of the system for safety reasons. Therefore, even if the components of the two channels of the AT are well-matched to avoid different delays between identical signal paths, mismatches between the input filters can cause phase shifts between the two channels, making EMG elimination difficult. Phase shifts introduced by filters with low cut-off frequencies will affect the slow EMG signals but they will cause only small distortion to the higher frequency ENG and it will still be possible to observe whether there is neural activity in the nerve bundles of interest.

In the case of EMG even small phase shifts may result in a considerable artefact left at the output, making ENG detection difficult or impossible. Therefore it is crucial to define the maximum acceptable EMG phase-shift φ between the two channels that would provide an acceptable output and then define the specifications for the input high pass filters of the system. Based on (4.2), (4.3) and (4.21), with channel 1 input $V_{m1\varphi}(t)$

having phase shift φ relative to channel 2 input $V_{m2\varphi}(t)$, the two EMG inputs to the system are defined as follows:

$$V_{m1\varphi}(t) = 0.5(1 + X_{imb})V_{emg}\sin(\omega_1 t + \varphi) \quad (4.24)$$

and

$$V_{m2\varphi}(t) = -0.5(1 - X_{imb})V_{emg}\sin(\omega_1 t) \quad (4.25)$$

Now, based on (4.23) - (4.25) the output of the system is now $V_{AT\varphi}(t)$:

$$V_{AT\phi}(t) = G_{PA}G_{fb0}G_{out}[0.5V_{emg}((1-\frac{G_{fb\phi}(t)}{G_{fb0}})(1+X_{imb})\sin(\omega_1 t+\phi)-(1+\frac{G_{fb\phi}(t)}{G_{fb0}})(1-X_{imb})\sin(\omega_1 t))+2V_{eng}\sin(\omega_2 t)]$$

$$\therefore V_{AT\phi}(t) = V_{AT}(t) + G_{PA}G_{fb0}G_{out}\left(0.5V_{emg}(1-\frac{G_{fb\phi}(t)}{G_{fb0}})(1+X_{imb})(\sin(\omega_1 t+\phi)-\sin(\omega_1 t))\right) \quad (4.26)$$

Assuming at this stage that the feedback is not affected (effect of phase shift error on the feedback will be examined in section 4.2) and assuming the integrator has already settled to a DC output producing $G_{fbX\phi} = G_{fb0}X_{imb}$:

$$V_{AT\phi}(t) = G_{PA}G_{fb0}G_{out}[0.5V_{emg}(X_{imb}^{\ 2}-1)(\sin(\omega_1 t)-\sin(\omega_1 t+\phi))+2V_{eng}\sin(\omega_2 t)] \quad (4.27)$$

The EMG sinusoidal terms can be replaced, as shown below:

$$\sin(\omega_1 t)-\sin(\omega_1 t+\phi) = (1-\cos(\phi))\sin(\omega_1 t)-\sin(\phi)\cos(\omega_1 t) \quad (4.28)$$

Say $(1-\cos(\varphi)) = a_\varphi$ and $(-\sin(\varphi)) = b_\varphi$, then:

$$a_\varphi\sin(\omega_1 t) + b_\varphi\cos(\omega_1 t) = c_\varphi\sin(\omega_1 t+\Phi) \quad (4.29)$$

where

$$c_\phi = \sqrt{a_\phi^{\ 2}+b_\phi^{\ 2}} = \sqrt{2-2\cos(\phi)} \quad (4.30)$$

and

$$\tan(\Phi) = \frac{b_\phi}{a_\phi} \quad \therefore \Phi = \tan^{-1}\left(-\frac{\sin(\phi)}{(1-\cos(\phi))}\right) \quad (4.31)$$

Φ is the phase shift of the overall output artefact (delay of $\frac{2\pi\Phi}{360\omega_1}$ relative to the input EMG), and doesn't affect the output signal-to-interference ratio (SIR_{out}). The value of Φ

is unimportant at this stage and it can be calculated after the appropriate value of φ is calculated. Using (4.29) – (4.31) in (4.27) gives:

$$V_{AT\phi}(t) = G_{PA}G_{fb0}G_{out}[0.5V_{emg}(X_{imb}{}^2 - 1)\sqrt{2-2\cos(\phi)}\sin(\omega_1 t + \Phi) + 2V_{eng}\sin(\omega_2 t)] \quad (4.32)$$

If φ = 0, $\sqrt{2-2\cos(\phi)} = 0$. Therefore, if there is no phase shift, the system will eliminate EMG. However, if φ ≠ 0 the amplitude of the EMG output term depends on φ. In general we want:

$$\mathrm{SIR}_{out} = \frac{2V_{eng}}{0.5V_{emg}(X_{imb}{}^2 - 1)\sqrt{2-2\cos(\phi)}} \leq \mathrm{SIR}_{outMIN} \quad (4.33)$$

where SIR_{outMIN} is the minimum allowed signal to interference ratio at the output.

$$\begin{aligned} &0.5\mathrm{SIR}_{out}V_{emg}(X_{imb}{}^2 - 1)\sqrt{2-2\cos(\phi)} = 2V_{eng} \\ &\therefore \mathrm{SIR}_{out}(X_{imb}{}^2 - 1)\sqrt{2-2\cos(\phi)} = 4\mathrm{SIR}_{in} \end{aligned} \quad (4.34)$$

This results to:

$$\phi = \pm\cos^{-1}\left(1 - 8\left(\frac{\mathrm{SIR}_{in}/\mathrm{SIR}_{out}}{(X_{imb}{}^2 - 1)}\right)^2\right) \quad (4.35)$$

Assume the worst case where $\mathrm{SIR}_{out} = \mathrm{SIR}_{outMIN}$ and say $\mathrm{SIR}_{outMIN} = 1$, a value that allows ENG detection and provides an improvement of three orders of magnitude relative to an input SIR ($\mathrm{SIR}_{in} = \frac{V_{eng}}{V_{emg}}$) of, say, 1:1000. In this case:

$$\phi = \pm\cos^{-1}\left(1 - 8\left(\frac{\mathrm{SIR}_{in}}{(X_{imb}{}^2 - 1)}\right)^2\right) \quad (4.36)$$

Assuming a "worst case scenario", say SIR_{in} = 1:1000 and X_{imb} = 40%. In that case φ = 0.27°, is the maximum acceptable phase-shift between the two channels. Figure 4.6 shows how SIR_{out} varies with φ.

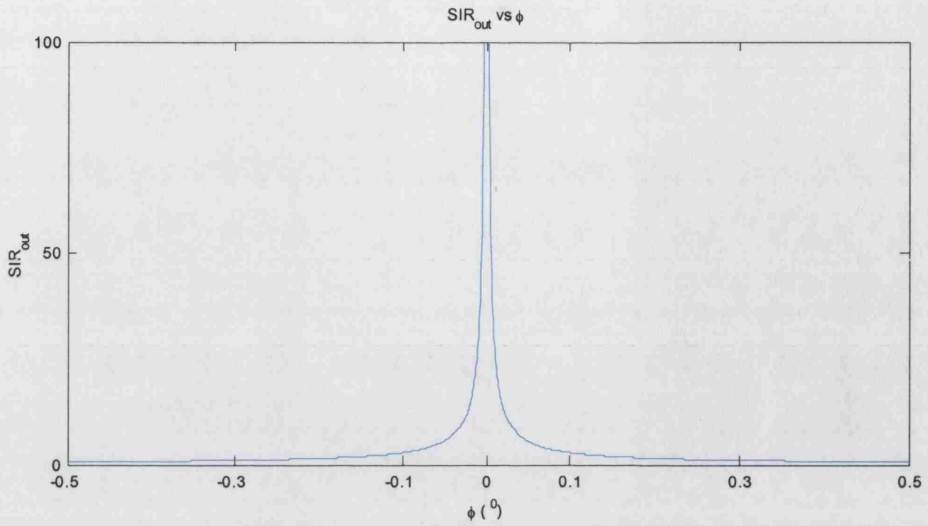

Figure 4.6 .AT output SIR variation with channel phase difference

Although the system has three inputs, the middle input is common to both channels and therefore a filter connected there will affect the phase shift of both channels by the same amount. Therefore, the phase-shift φ can be converted into the phase difference of two high-pass filters HP_1 and HP_2 connected to the two end-electrodes, with respective phases θ_1, θ_2 and cut-off frequencies f_{c1}, f_{c2} as follows:

$$\theta_1 - \theta_2 = \varphi \tag{4.37}$$

where

$$\theta_1 = \tan^{-1}\left(\frac{f_{c1}}{f_1}\right) \tag{4.38}$$

and

$$\theta_2 = \tan^{-1}\left(\frac{f_{c2}}{f_1}\right) \tag{4.39}$$

The filters cause phase shift φ between the two EMG input components, which have fundamental frequency $f_1 = \frac{\omega_1}{2\pi}$. From (4.37) - (4.39) and applying the formula:

$$\tan(\theta_1 - \theta_2) = \frac{\tan(\theta_1) - \tan(\theta_2)}{1 + \tan(\theta_1)\tan(\theta_2)} \tag{4.40}$$

The result is:

$$\frac{f_1(f_{c1} - f_{c2})}{f_1^2 + f_{c1}f_{c2}} = \tan(\phi) \tag{4.41}$$

If there is a matching error ε between the components of HP_1 and HP_2 it will result to $f_{c2} = f_{c1}(1 \pm \varepsilon)$. Therefore:

$$\frac{f_1 f_{c1} \epsilon}{f_1^2 + f_{c1}^2 \pm \epsilon f_{c1}^2} = \pm \tan(-\phi) \tag{4.42}$$

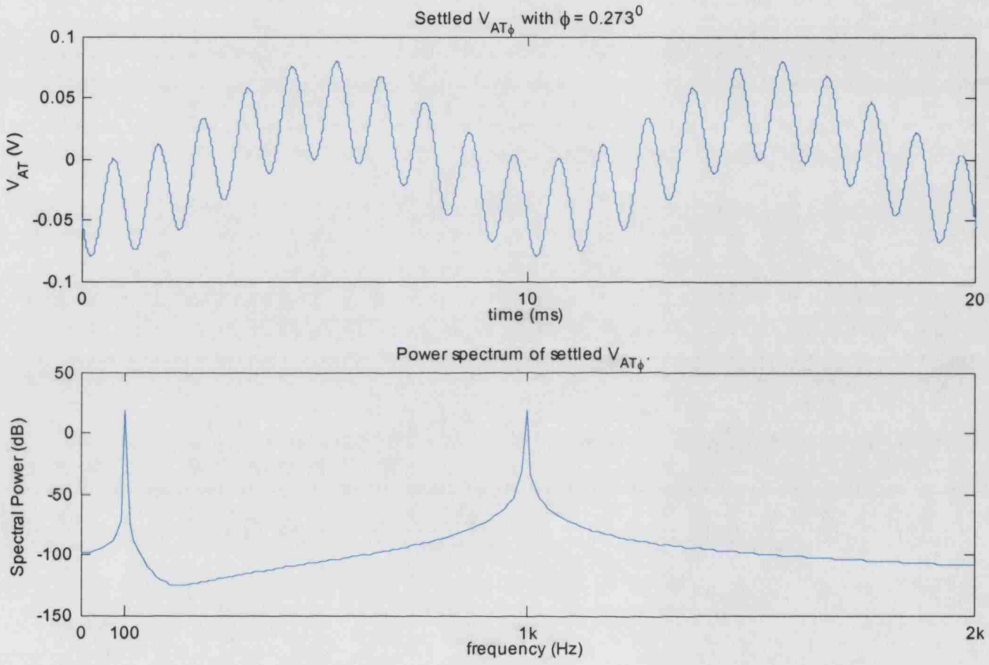

Figure 4.7 The settled AT output degraded by an input phase error φ = 0.273° resulting to $SIR_{out} = 1$.

For a matching error ε = 1% and φ = 0.27° the maximum allowed cut-off frequency of the high pass filters is f_{c1} = 74Hz. Any higher cut-off frequency, with this particular matching between the filters' components will introduce higher φ. Finally, for φ = 0.27°, Φ = -89.9° and the output EMG will have a delay of 2.5ms. Figure 4.7 illustrates the effect of phase error to the settled AT output.

4.2.2 Input DC offsets

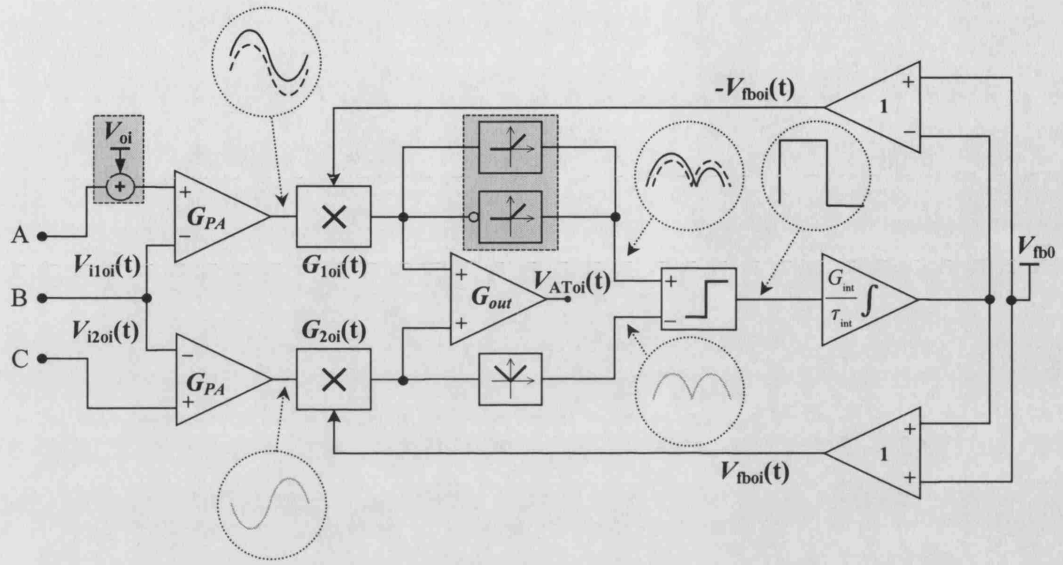

Figure 4.8 The AT block diagram, with channel 1 input DC offset V_{oi}. Channel 1 waveforms are displayed both without (dashed lines) and with (solid line) offset. The grey boxes indicate the error source, as well as the rectifier affected. Subscript "oi" is added to the system variables.

Although the system has to be preceded by high pass filters, as mentioned earlier, DC offsets may appear at the inputs if, for example, the filters employ very high resistors connected to ground and the input stage is bipolar. In this case the base current will flow through the filter resistor causing a DC offset. Also, an offset introduced by the preamplifiers will have a similar effect on the operation of the system. The only case where such offsets will not degrade the system is when their polarities opposite for each channel, and their values are affected by the same imbalance as the EMG. Even in this case though they may cause some stages to saturate before being cancelled at the output stage.

It is likely that the two channels' offsets will not have the EMG characteristics in terms of relationship between polarity and amplitude. The simplest case to assume is that of a DC offset V_{oi} applied only to channel 1. In this section the notation of the system variables will be followed by a subscript "oi".

$$V_{m1oi}(t) = (0.5 + X_{imb})V_{emg}\sin(\omega_1 t) + V_{oi} \qquad (4.43)$$

and $$V_{m2oi}(t) = -(0.5 - X_{imb})V_{emg}\sin(\omega_1 t) \quad (4.44)$$

Ignoring possible phase errors the effect of input offset on the output can be examined:

$$V_{ATOi}(t) = G_{PA}G_{fb0}G_{out}[(1-\frac{G_{fb}(t)}{G_{fb0}})V_{oi} + (X_{imb} - \frac{G_{fb}(t)}{G_{fb0}})V_{emg}\sin(\omega_1 t) + 2V_{eng}\sin(\omega_2 t)]$$
$$\therefore V_{ATOi}(t) = V_{AT}(t) + G_{PA}G_{out}(G_{fb0} - G_{fb}(t))V_{oi} \quad (4.45)$$

The above shows that if the feedback is unaffected by the input DC offset, the latter results simply to a DC offset at the output. That said, if the feedback is unaffected by the offset and it settles to G_{fbXoi}, where $G_{fbXoi} = X_{imb}G_{fb0}$, the output will be:

$$V_{ATOi\_idealFB}(t) = G_{PA}G_{fb0}G_{out}[(1 - X_{imb})V_{oi} + 2V_{eng}\sin(\omega_2 t)] \quad (4.46)$$

Therefore even a small input offset will saturate the system, as it will get multiplied by $G_{PA}G_{out}G_{fb0}$. The dependence of the output offset on imbalance is due to the feedback gain (assumed here to be settled) being directly related to the latter. For example, if G_{PA} = 1000, G_{out} = 10 and G_{fb0} = 2 and assuming X_{imb} = 40%, the output DC offset is 12,000 V_{oi}. Therefore if the system operates with ±5V supplies, to avoid saturation the offset should be $V_{oi} < 5/12000$ V, therefore: Voi < 417 μV.

The assumption that the control stage is unaffected by the offset assisted in illustrating the effect of the input offset to the system's output. However, the output will not reach its settled state when such offsets occur. To examine the reasons for that, two cases can be examined:

Case 1: X_{imb} = 0. If EMG components of both channels were equal the outputs of the rectifiers should result to zero differential input for the comparator. However, V_{oi} will cause the rectifier of channel 1 to malfunction. This can be explained by describing its output as the summation of two half-wave rectifiers, as illustrated in figure 4.8. The non-inverting half-wave rectifier will replicate the positive cycle, which will have amplitude of V_{emg} + V_{oi} and its output during the negative cycle will be zero. Similarly, the inverting stage will stay to zero during the originally positive cycle and will replicate the negative component, which will have amplitude of V_{emg} - V_{oi}. Therefore, as

a result and assuming at this point that the feedback loop is open, the output of the comparator will be a square wave with the EMG frequency and variable pulse width, its first part having a duration of $\frac{2\pi}{\omega_1}\left(\frac{1}{2}+\frac{2\sin^{-1}\left(V_{oi}/V_{emg}\right)}{\omega_1}\right)$ and the second part $\frac{2\pi}{\omega_1}\left(\frac{1}{2}-\frac{2\sin^{-1}\left(V_{oi}/V_{emg}\right)}{\omega_1}\right)$.

Closing the loop, the integrator's output should normally (feedback unaffected by V_{oi}) stay stable to zero providing equal gains to both channels and the EMG AC components would cancel at the output leaving only a DC offset as mentioned previously. However this is not the case, and based on the comparator output discussed above the AC components will not cancel because even if the integrator was quick enough to settle well within half EMG period (which is not the case as the integrator has to be slow to avoid harmonic distortion, as discussed later) the resulting EMG components of the two channels would be distorted unevenly and therefore they would not be antiphase versions of the same waveform anymore. The result would be severe harmonic distortion at the output.

Case 2: $X_{imb} \neq 0$. If the EMG component of channel 1 was greater, the integrator output $V_{fb}(t)$ should increase, applying a decreasing gain G_{fb0} - $G_{fb}(t)$ to this channel, and an increasing gain to channel 2 until EMG in both amplitudes would become equal. However as described previously, because of the offset, the rectifier output of channel1, will have one large and one small component and even if the latter is still greater than the EMG component of channel 2, its zero crossing will not occur at the same time. Therefore as some part of the output of channel 1 rectifier becomes lower than the corresponding signal of channel 2, the comparator output will be have negative pulses occurring instead of being constantly high, resulting in some part of the feedback actually increasing the amplitude of channel 1 EMG component instead of reducing it. Therefore the feedback will not converge to G_{fbX} and the output will be distorted, obstructing ENG detection. Overall, input offsets can result in saturation and severe feedback malfunction.

4.2.3 Feedback loop DC offsets

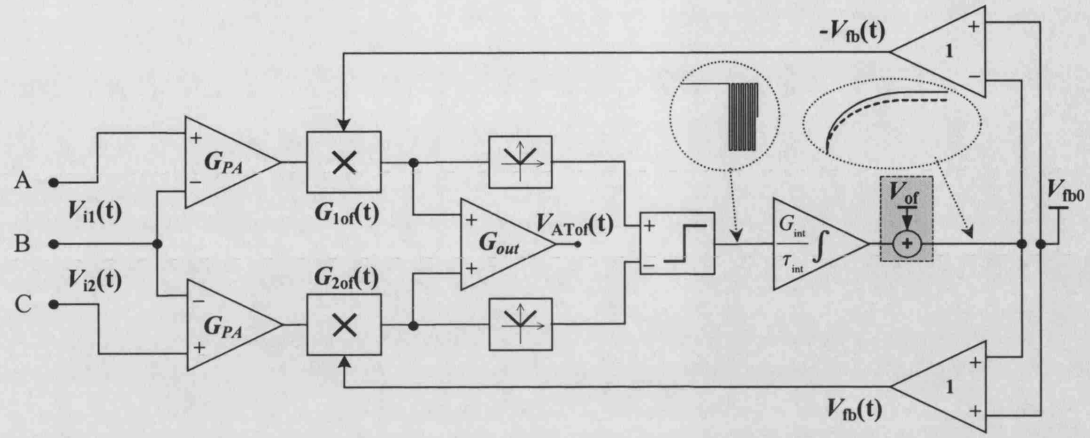

Figure 4.9 The AT block diagram, with DC offset V_{of} at the integrator output (indicated by the grey box). Integrator output waveform is displayed both without (dashed line) and with (solid line) DC offset. Subscript "of" is added to the system variables.

This section investigates the effects of DC offsets in the feedback loop. Assume a DC offset V_{of} at the output of the integrator. The effect on the feedback signals will be:

$$G_{1of}(t) = G_{fb0} - G_{fb}(t) + gV_{of} \tag{4.47}$$

and

$$G_{2of}(t) = G_{fb0} + G_{fb}(t) + gV_{of} \tag{4.48}$$

This will result to:

$$V_{ATof}(t) = G_{PA}G_{out}(G_{fb0} + gV_{of})[(X_{imb} - \frac{G_{fbof}(t)}{G_{fb0} + gV_{of}})V_{emg}\sin(\omega_1 t) + 2V_{eng}\sin(\omega_1 t)] \tag{4.49}$$

The above shows that the system will operate normally with the variable part of the gain now settling to:

$$G_{fbXof} = (G_{fb0} + gV_{of})X_{imb} \tag{4.50}$$

This does not seem to cause problem to the operation of the AT, however, depending on the amplitude and polarity of the offset, two errors may occur:

1) The feedback level-shift voltage V_{fb0} has to be chosen during the system design so that the multiplier outputs will never change phase, thus, $|V_{fbXof}| < V_{fb0}$, as mentioned earlier in this chapter. Therefore if the feedback offset is negative and depending on its amplitude, this may seize to be the case for one of the channels, at least for large imbalance values, where the value of V_{fbXof} approaches that of V_{fb0}. In that case the EMG and ENG components of the two channels will not be anti-phase and in-phase respectively and the operation of the system will be jeopardised.

2) The feedback output stage (i.e. the integrator output stage) is also designed so that the feedback will not saturate. Therefore, if V_{of} is large enough, it may saturate one of the feedback channels, providing unbalanced gain adjustment.

Overall, large feedback loop offsets may cause the system to malfunction for large imbalance values, where one of the channels' gain reaches its maximum value and the other reaches its minimum. This can be partly compensated for by allowing some margin of error between 0 and C_{fb0} - G_{fbX}, as well as between V_{cc} and C_{fb0} + G_{fbX}.

4.2.4 Harmonic distortion

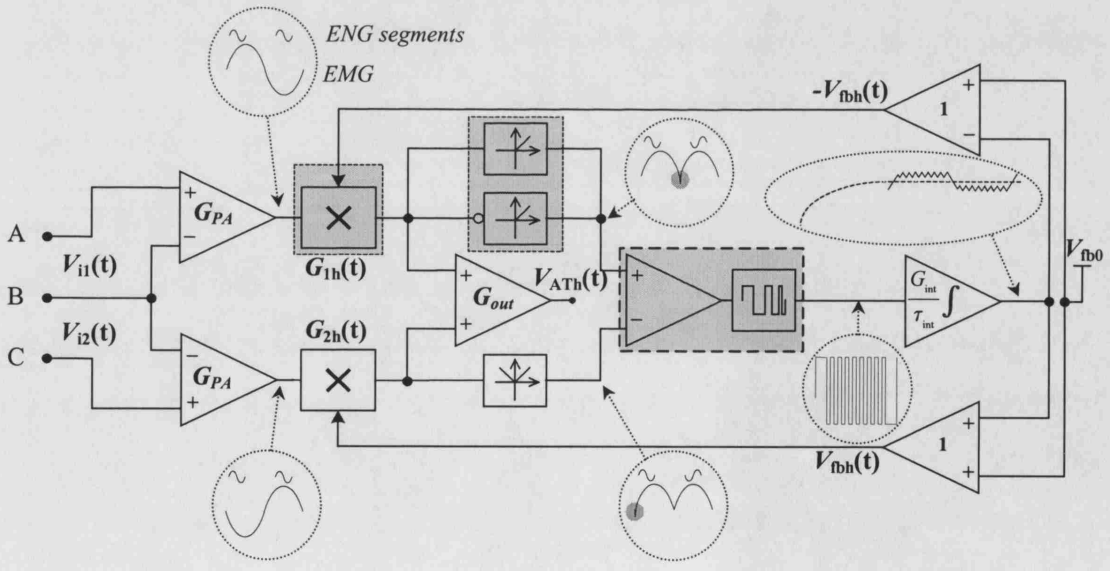

Figure 4.10 The AT block diagram, illustrating the ripple on top of the settled feedback, causing output harmonic distortion due to its multiplication with the signals of interest. The blocks causing such ripple are indicated by the grey areas. Subscript "h" is added to the notation of the system variables.

Spectral harmonic distortion will occur at the AT output due to the settled feedback not being a pure DC value. Some of the ripple on top of the DC value V_{fbX} will contain frequency components that are multiples of the bioelectric signals' fundamental frequencies (or spectral peaks). The multiplication of the feedback with the input signals will create some new harmonics at the output, which may not cancel after the system converges. In order to find out the harmonic content of the feedback ripple and use it in the output expression $V_{ATh}(t)$, the analysis will commence from the rectifier inputs with a settled system (at this stage assuming zero φ, V_{oi} and V_{of}), where the current integrator output has the initial DC condition V_{fbX}.

If spectral peaks are related to EMG, they may cause some interference - related artefact at the output, degrading ENG measurements. The effect of the ENG on the control stage can be considered negligible due to its amplitude being so much smaller than the EMG amplitude, which defines the feedback behaviour. However the case of ENG affecting the feedback is also examined in this section.

4.2.4.1 Harmonic distortion due to comparator oscillations

After the feedback has settled, ideally the comparator will produce a high frequency square wave, its frequency ω_{comp} depending on the characteristics of the actual device used. This can be represented using Fourier series, as follows:

$$V_{coh}(t) = \frac{4V_{comp}}{\pi}\left(\sin(\omega_{comp}t) + \frac{1}{3}\sin(3\omega_{comp}t) + \frac{1}{5}\sin(5\omega_{comp}t) + \ldots\right) \qquad (4.51)$$

Therefore the settled value of the integrator will be:

$$V_{fbh}(t) = V_{fbX} + \frac{G_{INT}}{\tau_{int}}\int V_{coh}(t)dt \qquad (4.52)$$

This results to a triangular wave around the DC value V_{fbX} that should ideally be the only output of the settled integrator, corresponding to G_{fbX}. This can be described by:

$$G_{\text{fbh}}(t) = G_{\text{fbX}} - \frac{4gV_{\text{comp}}G_{\text{INT}}}{\pi\tau_{\text{int}}\omega_{\text{comp}}}\left(\cos(\omega_{\text{comp}}t) + \frac{1}{9}\cos(3\omega_{\text{comp}}t) + \frac{1}{25}\cos(5\omega_{\text{comp}}t) + \ldots\right) \quad (4.53)$$

Call the comparator-introduced series ripple term of the gain $G_{rippleC}(t)$:

$$G_{\text{rippleC}}(t) = -\frac{4gV_{\text{comp}}G_{\text{INT}}}{\pi\tau_{\text{int}}\omega_{\text{comp}}}\left(\cos(\omega_{\text{comp}}t) + \frac{1}{9}\cos(3\omega_{\text{comp}}t) + \frac{1}{25}\cos(5\omega_{\text{comp}}t) + \ldots\right) \quad (4.54)$$

$$\therefore G_{\text{fbh}}(t) = G_{\text{fbX}} + G_{\text{rippleC}}(t) \quad (4.55)$$

$$V_{\text{ATh}}(t) = G_{PA}G_{\text{out}}(V_{\text{emg}}(G_{\text{fb0}}X_{\text{imb}} - G_{\text{fbX}} - G_{\text{rippleC}}(t))\sin(\omega_1 t) + 2G_{\text{fb0}}V_{\text{eng}}\sin(\omega_2 t)) \quad (4.56)$$

That leads to two important conclusions:

- The ENG term is not harmonically distorted
- Replacing the settled DC gain: $G_{\text{fbX}} = X_{\text{imb}}G_{\text{fb0}}$, the EMG fundamental term will be zero, but EMG-related harmonic content will be residual in the output, its frequency and amplitude depending on the comparator and integrator characteristics:

$$V_{\text{ATh}}(t) = G_{PA}G_{\text{out}}(-V_{\text{emg}}G_{\text{rippleC}}(t)\sin(\omega_1 t) + 2G_{\text{fb0}}V_{\text{eng}}\sin(\omega_2 t)) \quad (4.57)$$

$$\begin{aligned} V_{\text{ATh}}(t) = G_{PA}G_{\text{out}}\Bigg[& \frac{2gV_{\text{comp}}V_{\text{emg}}}{\pi\tau_{\text{int}}\omega_{\text{comp}}}\Big\{\sin\left((\omega_1 - \omega_{\text{comp}})t\right) + \sin\left((\omega_1 + \omega_{\text{comp}})t\right) + \\ & \frac{1}{9}\left(\sin\left((\omega_1 - 3\omega_{\text{comp}})t\right) + \sin\left((\omega_1 + 3\omega_{\text{comp}})t\right)\right) + \\ & \frac{1}{25}\left(\sin\left((\omega_1 - 5\omega_{\text{comp}})t\right) + \sin\left((\omega_1 + 5\omega_{\text{comp}})t\right)\right)\ldots\Big\} + \\ & 2G_{\text{fb0}}V_{\text{eng}}\sin(\omega_2 t)\Bigg] \end{aligned} \quad (4.58)$$

Therefore a high comparator frequency will serve both for reducing the amplitude of the ripple and for making sure it is outside the bandwidth of interest.

Figure 4.11 illustrates the ripple on the settled feedback and its effect on the system output. The comparator frequency used for this plot was $\omega_{\text{comp}} = 2\pi\times 10\text{kHz}$, which is

very low relative to standard devices for example to National Instruments LM311, whose response time is 200ns corresponding to a theoretical maximum square wave frequency of approximately 1.25MHz (200ns rising edge + 200ns falling edge + 2×200ns pulse width). A low frequency, at the higher end of the bandwidth on interest (10kHz) is used here as the worst-case scenario.

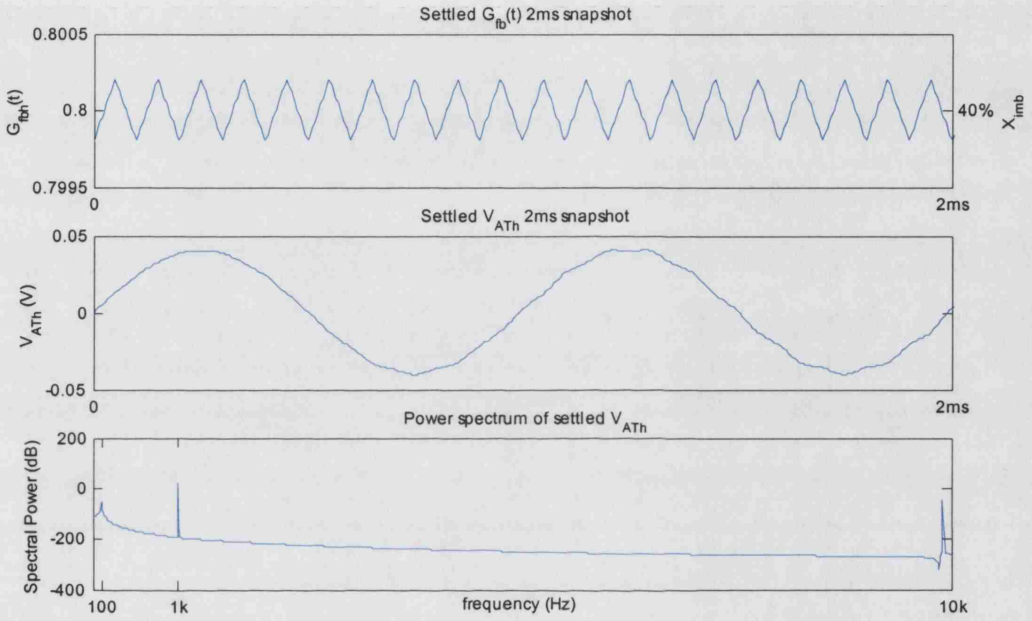

Figure 4.11 Effect of comparator oscillations to the settled feedback and the AT output. A relatively low comparator frequency is used here, $\omega_{comp} = 2\pi \times 10\text{kHz}$.

If the time constant of the integrator is not long enough the AT output will be quick in converging but distorted. Therefore, to reduce this distortion, a long-time constant has to be used for the integrator. The distortion can also be reduced by making the comparator faster.

4.2.4.2 Harmonic distortion due to residual ENG at the comparator input

ENG feedthrough to the control stage can little effect if the ENG is a naturally occurring SFAP (single fibre action potential) with amplitude of a few μV. The ENG components of the two channels, as indicated by the waveforms in figure 4.10, will be antiphase after rectification, as the EMG waveform is rectified. The ENG being just a small ripple on top of the interference does not affect the polarity of the rectifiers' inputs. Moreover, even in the case of $V_{emg} = 0$ the ENG components out of the rectifiers will be antiphase.

As a result, the residual ENG at the input of the comparator will not be significant, however as the imbalance is not considered in this analysis to affect the ENG, its antiphase components at the outputs of the two rectifiers will be scaled by the multiplier gains. Therefore, based on the imbalance present some ENG-related ripple will go through to the comparator inputs. Based on the values used previously, the amplitude of this ripple at the input of the comparator will be $-2G_{PA}G_{fbX}V_{eng}$ = 1.6mV. Its effect will be similar as the comparator ripple described before, with the ripple's frequency becoming ω_2. Figure 4.12 is similar to figure 4.11 with $\omega_{comp} = \omega_2$.

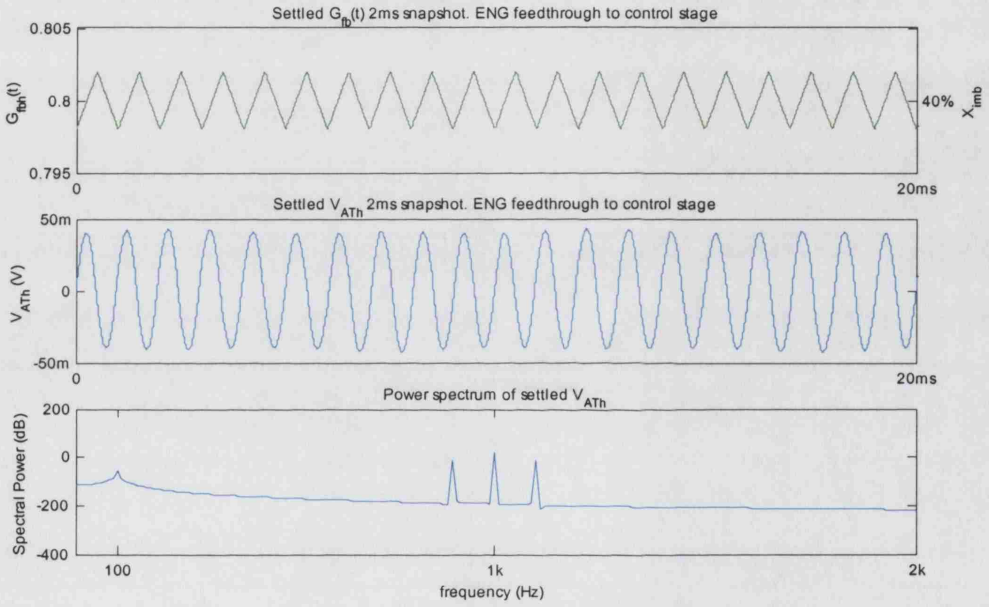

Figure 4.12 Effect of comparator oscillations to the settled feedback and the AT output. The comparator here oscillated at the ENG frequency due to ENG going through to the control stage.

Again the ripple can be reduced using a long time constant integrator.

4.2.4.3 Harmonic distortion due to rectifier polarity transition error

As shown in figure 4.10, small rectifier polarity transition errors can occur at rectifier outputs in the form of spikes at the rectifier output when the positive polarity cycle turns off and the negative turns on. Such spikes will cause corresponding pulses to appear at the comparator output, when the EMG amplitudes of both channels have been equalised, and this results to what can be approximated by a square wave at the integrator output, with fundamental frequency ω_1 (EMG frequency). This square wave,

superimposed to the target feedback value of G_{fbX}, can be expressed as an additional feedback gain ripple component:

$$G_{rippleR}(t) = \frac{4gV_{ampR}}{\pi}\left(\sin(\omega_1 t) + \frac{1}{3}\sin(3\omega_1 t) + \frac{1}{5}\sin(5\omega_1 t) + ...\right) \tag{4.59}$$

The amplitude V_{ampR} of the square wave term depends on the duration t_{spike} of the rectifier polarity transition error. The integrator's output $V_{fb}(t)$ described in (4.39) is an exponential function of time and it will tend to rise or fall during the rectifier-introduced pulses by an amount that depends on t_{spike}:

$$V_{ampR} = V_{fbX}\left(1 - e^{-\frac{t_{spike}}{\tau_{sys}}}\right) \tag{4.60}$$

The overall time-varying part of the distorted feedback gain $G_{fbh}(t)$ now becomes:

$$G_{fbh}(t) = G_{fbX} + G_{rippleC}(t) + G_{rippleR}(t) \tag{4.61}$$

This leads to the following output expression:

$$V_{ATh}(t) = G_{PA}G_{out}(V_{emg}(G_{fb0}X_{imb} - G_{fbX} - G_{rippleC}(t) - G_{rippleR}(t))\sin(\omega_1 t) + 2G_{fb0}V_{eng}\sin(\omega_2 t)) \tag{4.62}$$

Using (4.10) and (4.59) to (4.61), the output representation up to 10th EMG harmonic becomes:

$$\begin{aligned} V_{ATh}(t) = G_{PA}G_{out}\Bigg\{-V_{emg}\Bigg[G_{rippleC}(t)\sin(\omega_1 t) + \frac{4gV_{fbX}}{\pi}\left(1 - e^{-\frac{t_{spike}}{\tau_{sys}}}\right)\Big(\frac{1}{2} - \frac{1}{3}\cos(2\omega_1 t) - \\ \frac{4}{3\times5}\cos(4\omega_1 t) - \frac{6}{5\times7}\cos(6\omega_1 t) - \frac{8}{7\times9}\cos(6\omega_1 t) - \\ \frac{10}{9\times11}\cos(10\omega_1 t) - ...\Big)\Bigg] + 2G_{fb0}V_{eng}\sin(\omega_2 t)\Bigg\} \end{aligned} \tag{4.63}$$

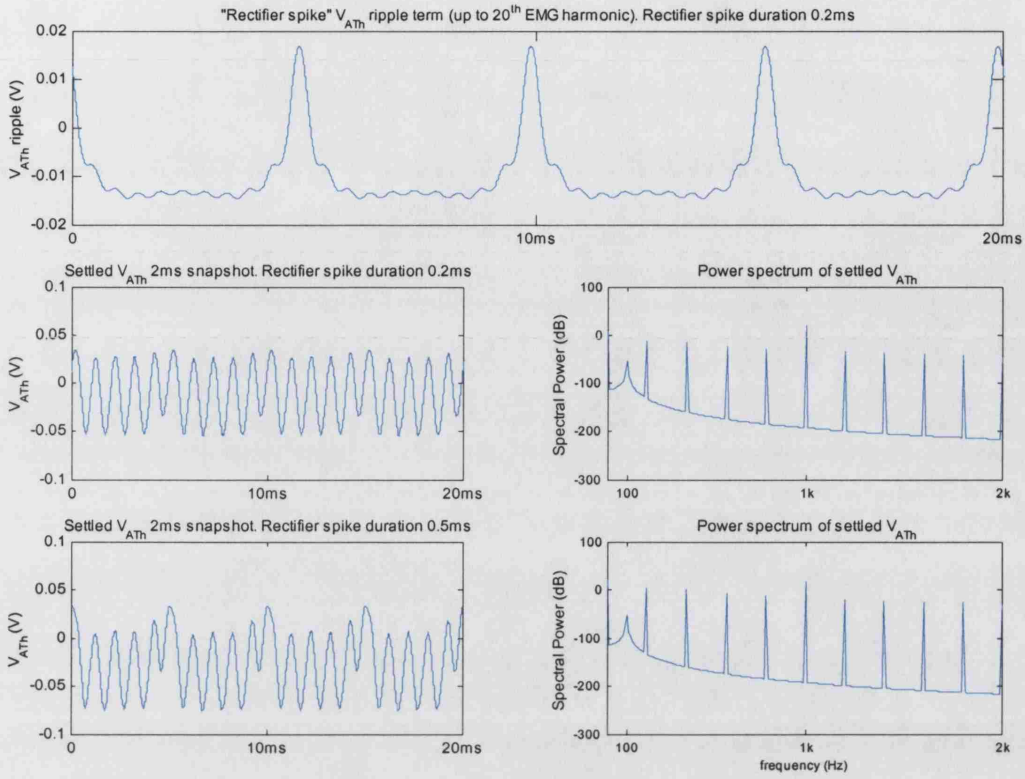

Figure 4.13 Effect of rectifier spikes to the AT output. The top plot illustrates the ripple term of the output (up to 20th EMG harmonic), while the bottom is the settled $V_{ATh}(t)$ taking into consideration both comparator and rectifier introduced harmonic distortion parameters.

As indicated by figure 4.13, where the ripple term of the above equation is plotted using the values used previously, the distortion of the system's output will get worse with longer lasting rectifier transition spikes. This is evident by the settled output plots illustrated in the same figure, where two cases of distortion are considered, resulting to different pulse widths at the comparator output due to the rectifier malfunction. An important design factor reducing such distortion is again the integrator time constant, which provides harmonic distortion reduction, as it gets greater.

4.2.4.4 Harmonic distortion due to the phase error

The input phase error φ examined in section 4.2.1 distorted the system output with a residual EMG component, however the analysis assumed ideal feedback operation. The effect of phase to the feedback will be very similar to the rectifier error discussed in the previous section. However there will be a pulse produced at the comparator output four times in the EMG period, with alternating polarity, producing a square wave at the

integrator output that will have fundamental frequency of $2\omega_1$. The pulse duration will be $t_\phi = \frac{2\pi\phi}{360\omega_1}$ and therefore the settled output $V_{\mathrm{ATh}\varphi}(t)$, affected by both harmonic distortions and the phase error will now be:

$$V_{\mathrm{ATh}\phi}(t) = V_{\mathrm{AT}\phi}(t) - G_{PA}G_{\mathrm{out}}V_{\mathrm{emg}}(G_{\mathrm{rippleC}}(t) + G_{\mathrm{rippleR}}(t) + G_{\mathrm{ripple}\phi}(t))\sin(\omega_1 t) \tag{4.64}$$

where $G_{\mathrm{ripple}\varphi}(t)$ is the feedback ripple due to the phase, given by:

$$G_{\mathrm{ripple}\phi}(t) = \frac{4gV_{\mathrm{amp}\phi}}{\pi}\left(\sin(2\omega_1 t) + \frac{1}{3}\sin(6\omega_1 t) + \frac{1}{5}\sin(10\omega_1 t) + \ldots\right) \tag{4.65}$$

The amplitude $V_{\mathrm{amp}\varphi}$ of the square wave term will be:

$$V_{\mathrm{amp}\phi} = V_{\mathrm{fbX}}\left(1 - e^{-\frac{2\pi\phi}{360\omega_1\tau_{\mathrm{sys}}}}\right) \tag{4.66}$$

The overall output, plotted using the same parameters before is illustrated in figure 4.14.

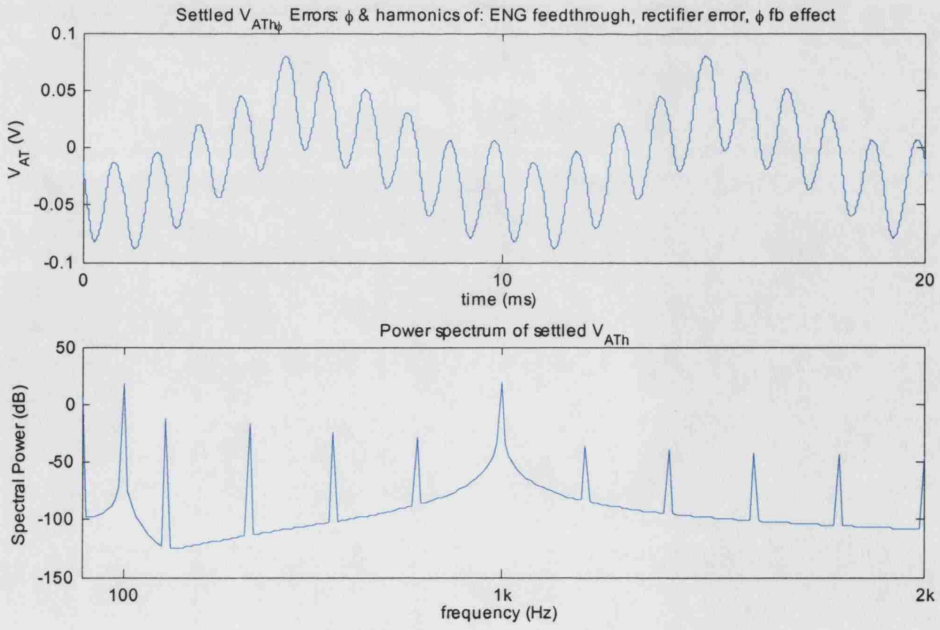

Figure 4.14 The AT output affected by three kinds of harmonic distortion and by the phase error φ.

4.2.5 Additional sources of error

Other sources of error dictating the design approach for the AT include multiplier nonlinearity, common mode input interference (e.g. mains interference), rectifier offsets and mismatches between components.

The linearity of the variable gain stage is vital, throughout all the input dynamic range, which has to be greater than the maximum expected EMG amplitude. If the limits of the linear range are adjusted to the maximum expected EMG signal without taking imbalance into consideration, the latter may cause one of the channels to exceed its linear range. In that case the harmonic content of each channel will be different. Hence, even if the feedback compensates for the imbalance, some spectral peaks of the interference will not be eliminated at the output.

Common mode interference by sources not affected by the cuff, as for example mains interference is very often the most dominant disturbance of measurements, in the lowest end of the bandwidth, during an experiment either in-vitro or in-vivo. This is mainly related with the fact that the system supplies as well as the measuring instruments inside a laboratory suffer from mains interference, whose spectral peaks, along with its 2^{nd} and 3^{rd} harmonics often overlap with the EMG peak making it difficult to assess how much the latter has been suppressed at the system's output. However, in the case of an implant, positioned inside the body and powered by a floating supply (e.g. batteries or RF) such interference is not expected to be vital and the lower end of the bandwidth of interest will be around 500Hz.

Rectifier offsets will affect the threshold of the comparator, essentially affecting the DC level of the settled integrator output, causing feedback offsets.

Finally, matching is a very important design objective, especially in the IC version of the system, as the main purpose of the AT is to correct cuff mismatches and this will be jeopardised by mismatches in the system itself. Mismatches in the preamplifier gains are not important, as they will be treated by the system as imbalance, but mismatches between the two channels in terms of offsets, harmonic content or phase shifts / delays can have a significant effect.

4.3 Conclusion

This chapter has investigated the system-level operation of the AT examining its ability to address its main objectives and presenting its main limitations. The system's ability to compensate for cuff imbalance has been demonstrated and ENG detection has been successfully simulated in the presence of high imbalance and very low input SIR. The main sources of error examined include phase error between the two channels, input and feedback DC offsets and harmonic distortion caused by several parameters.

The phase error can be harmful for any ENG amplifier configuration applied to tripolar cuffs (e.g. QT, TT) or cuffs with more electrodes (multi-electrode cuff recording as in [91]). High pass filters for AT-cuff interface will probably be on implant, not on chip, therefore their cut-off frequencies can be made adequately low, as they will not be integrated. However, if the preamplifiers of the AT have output DC offsets AC-coupling will have to be applied between them and the multipliers. To keep the filter component values as low as possible, the front-end high-pass filters have to be designed with the highest cut-off frequency acceptable. A cut-off frequency of around 75Hz is proposed in this chapter as a reasonable value for keeping the phase error within the maximum allowed range.

Input offsets could also affect the QT and the TT, causing their output to saturate, but they are more severe for the AT as they can prevent its output from converging. Even if the input is high-pass filtered, the preamplifiers may introduce offset, and therefore, as mentioned above, an extra filtering stage will have to be implemented after that stage.

There are four possible causes of harmonic distortion: comparator-introduced ripple in the feedback within the bandwidth of interest, ENG feedthrough to the feedback stage, rectifier polarity transition error and phase errors. Making the comparator quick (frequency well outside the bandwidth of interest) addresses the first and the third case. The preferable solution is to make the integrator time constant large so that the feedback ripple is reduced in all cases. In that respect that stage's cut-off frequency has to be smaller than the main EMG frequency component. A choice of 1s or greater will reduce the feedback distortion significantly, as it corresponds to a frequency component more

than 50 times lower than the lowest end of the bandwidth allowed by the previously selected input high-pass filter.

The aforementioned errors could be addressed using complicated sub-stages in various positions within the main system diagram. However, the main design objective is to keep the system complexity low to retain the benefits of the analogue solution relative to other possible solutions, like filters or DSP algorithms (e.g. blind signal separation) and to allow the system to be implantable.

Chapter 5

DISCRETE–COMPONENT SYSTEM

After assessing the capabilities and limitations of the AT in system level analyses in the previous chapter, the system was developed using discrete components to carry out further testing and evaluation before proceeding to an IC design. It is quite common in FES-related applications for systems to be made using discrete components, either for experimental "proof-of-principle" studies [14, 17, 19, 22, 24, 28, 89, 92] similar to the work described in this chapter or for implantable devices [11, 77, 93]. This configuration made it easier to experiment with values of specific components and to carry out in-vitro testing in order to define better the specifications for the integrated version. The importance of the configuration of subsystems would not be easily assessed in the IC, other than in simulations. Prior knowledge of design issues was gained through this initial development, which allowed rearrangement of setups and the comparison of the AT with the TT (and the QT in the last session of tests) using the same PCB. Some of the error sources analysed in the previous chapter became evident after testing various setup options in the discrete system. The design was based on the system-level analysis and the errors were minimised. As it was certain that the necessary matching between the two channels and individual components could not be achieved in discrete level as in the IC, inter-stage filters were used as additional error-reduction stages. Unity output SIR for input SIR of 1:1000 and 10% imbalance was the

optimistic target for this circuit. Transformer-coupled and saline-bath tests constituted the in-vitro experiments performed to assess the system's capabilities in terms of SIR_{out} as a function of imbalance and thus to compare the AT with the TT under various imbalance conditions. *In-vivo* tests were later performed in rabbits with stimulation-induced signals in the presence of proximity imbalance and all three tripolar amplifier configurations were compared in terms of their output SIRs.

5.1 Circuit description and Design

5.1.1 ENG signal path: Preamplifiers, multipliers and output stage

The basic circuit diagram of the discrete version of the AT is shown in figure 5.1 and it was built on a PCB and placed in metal encapsulation for reduction of interference pick-up. The three inputs V_{in1+}, V_{in-} and V_{in2+} were connected respectively to points A, B and C in figure 2.16 (chapter 2). They were AC coupled with a cut off frequency of 1.5Hz, to avoid severe phase shifts (typical tolerance of components used: ±5%, $\varphi \approx 0.075°$) and connected to the pre-amplifiers. The latter were realised by two AD AMP01 differential-amplifiers with gain of 1000, typical input noise voltage of 0.12μV pk-pk and 26kHz bandwidth. The AMP01s have been previously used in experimental and implantable neuroprosthetic devices in the literature [14, 17, 28, 77], mainly due to their low-noise performance.

The variable-gain stage consisted of two AD633 multipliers, which set the system supplies to ±8V (minimum required). They were chosen because they allowed both the multiplication and the level shifting of the feedback signals, as well as the application of extra fixed gain, should this be needed. Resistor pairs $R_{5\text{-}8}$ and $R_{49\text{-}50}$ in figure 5.1 set the fixed gain to 1. The overall gain of the adaptive stage is given by equations (4.6) and (4.7), with $g = 1V^{-1}$ and $V_{fb0} = 2V$ (set by R_{14}). The value of 2V for V_{fb0} along with limiting diodes at the integrator output ensured that $0 < (V_{fb0} \pm V_{fb}(t)) < 4V$, therefore for $V_{emg} = 1mV$ the multiplier outputs would reach a maximum of 4V. This was chosen taking into consideration that with ±8V supplies the AD633 has a maximum output range of ±5V. The typical linearity of the multipliers was 0.4% over the chosen input range.

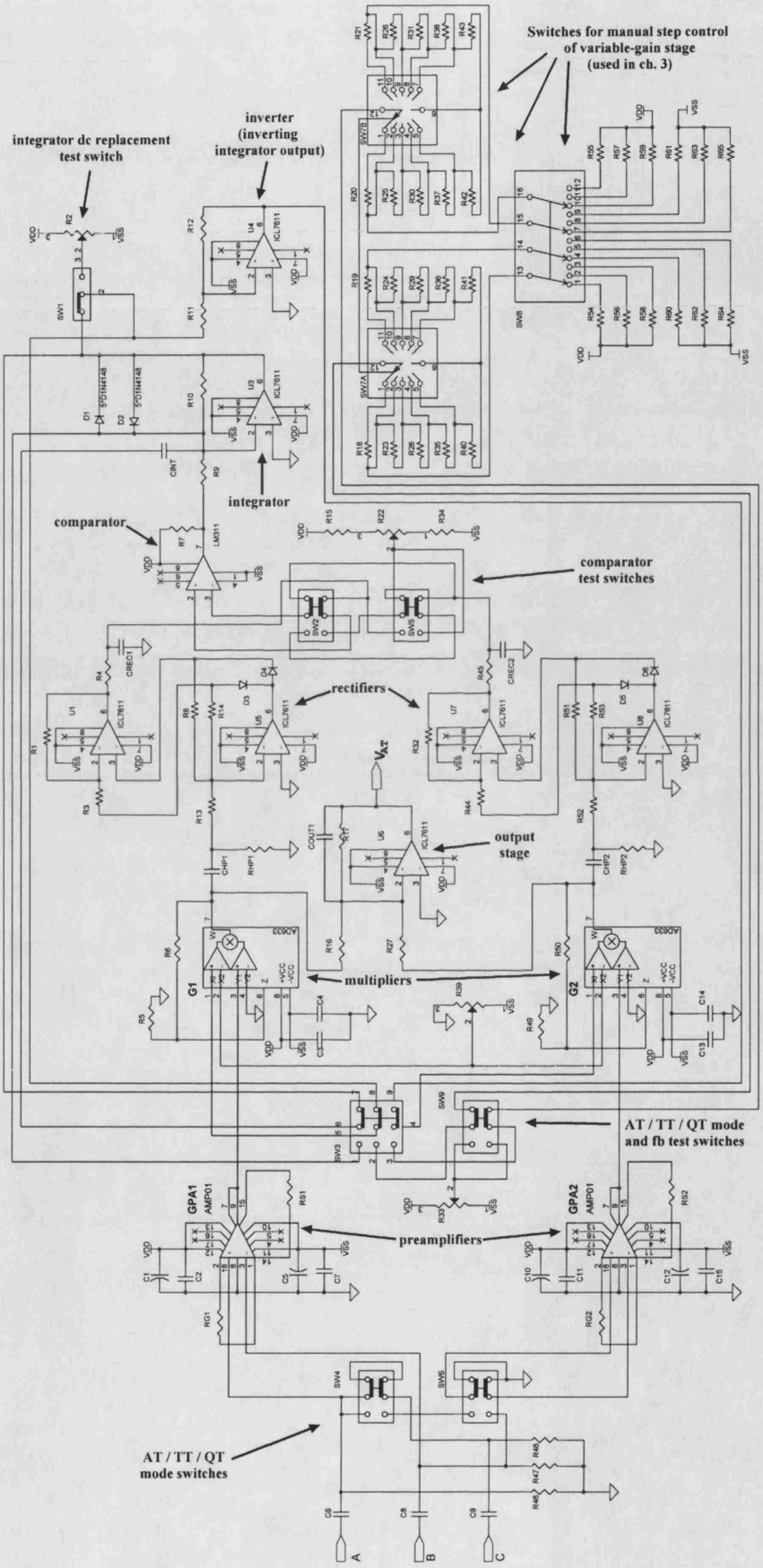

Figure 5.1 Circuit diagram of the discrete version of the AT.

The output stage was an OPA277 summing amplifier with a gain G_{out} = 10 resulting in an overall ENG signal path gain of 40000, providing 40mV for a 1μV ENG input, sufficient for an 8-bit ADC succeeding stage (150μV resolution). The output was band-pass filtered making the overall bandwidth of the system 1.5Hz to 10kHz to allow the assessment of the AT operation over the full spectrum of interest.

5.1.2 Control stage: Rectifiers, comparator and integrator

The rectification stage is very sensitive to offsets and for this reason the rectifier inputs were AC coupled to eliminate the offsets introduced from both the AMP01 and the AD633 stages. Attempting to trim the multiplier offsets was not effective, because DC components at their inputs made their output offsets dependent on the variable gains. Moreover offset trimming made the system sensitive to trimmer drift. Fixed-value components made the circuit more robust and its performance more consistent between experiments. The high pass filter used was the same as the input ones and it was connected after the junction to the output stage to avoid additional phase shifts affecting the elimination of the antiphase EMG signals.

Each rectifier consisted of two OPA277 low offset operational amplifiers and they were made using the connectivity of amplifier pairs $U_{1\text{-}5}$ and $U_{7\text{-}8}$ [94] in figure 5.1, which ensured amplifier stability by providing feedback loops for both positive and negative inputs, buffering the first and inverting the latter. This configuration overcame the rectifier polarity transition error described in chapter 4, which was initially observed with simpler rectifier configurations (e.g. the configuration in [95]). Care was taken to ensure unity gain for the inverters used and 500Hz low-pass filters turned the rectifiers into peak detectors, to further reduce the effects of spikes occurring at input zero-crossings, to reduce the effect of phase shifts introduced by the two AC coupling stages and to remove any ENG frequency components from the feedback path, thus reducing ENG harmonic distortion.

The comparator was a National Semiconductor LM311, whose output saturated at ±8V. Power supply decoupling was applied to every IC used to reduce supply rail distortion caused by the comparator output oscillations. The prospect of using a high-gain

differential amplifier instead of the comparator was also considered in the last sets of experiments described later in the chapter, as it would make the system time constant independent of imbalance (see short analysis in section 5.4). However its output depends on V_{emg} making it inappropriate for naturally occurring signals that do not have a standard amplitude level. An advantage of the differential amplifier was that it allowed much easier and stable offset trimming than the comparator.

The last stage of the control part of the system consisted of an active integrator with RC time constant of 10s and an inverter, both realised using the same operational amplifiers as above. The time constant was chosen to be large to eliminate feedback ripple and because discrete components allowed for such a high value. The integrator's output was limited to 1.8V, so that $V_{fb}(t) < V_{fb0}$ and the feedback signals never caused the multiplier outputs to change phase, as their overall gain never changed polarity (always positive). The multiplier gains ranged from 0.2 to 3.8, corresponding to ±90% imbalance.

5.1.3 TT mode and in-vivo setup switches

Switches SW4 and SW6 in figure 5.1 were used to allow selection between the three amplifier configurations. The TT mode could be turned to a "manual AT" (mainly used in section 3.6.1, chapter 3) where the gain ratio of G_1 and G_2 of the multipliers could be manually selected, using rotary switches SW_{7A}, SW_{7B} and SW_8. The 11 switch positions listed in table 3.1 altered the gain-control voltage (V_{sw}) through the values listed in table 5.1.

V_{sw}	-1.67	-1.33	-1	-0.67	-0.33	0	0.33	0.67	1	1.33	1.67
X_{imb} (%)	-83.3	-66.7	-50	-33.3	-16.7	0	16.7	33.3	50	66.7	83.3

Table 5.1 Relationship between the V_{sw} (manual gain) and imbalance X_{imb}.

5.2 In-vitro experiments and comparison of systems

5.2.1 Transformer-coupled testing

5.2.1.1 Experimental set-up

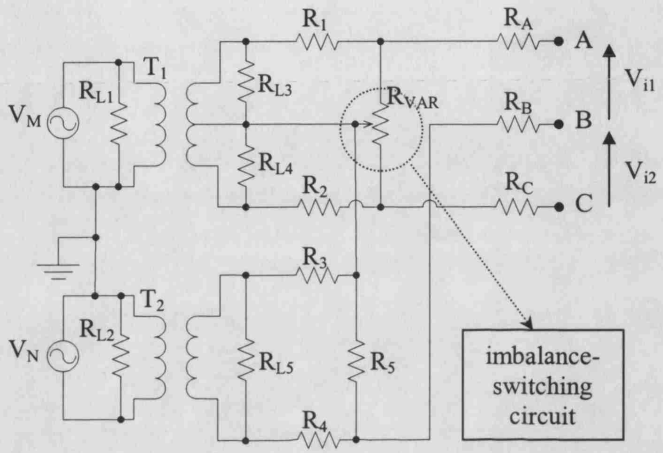

Figure 5.2 Transformer circuit providing the test inputs to the system.

The transformer circuit in figure 5.3 was made to provide floating inputs and sufficient attenuation to achieve mV EMG and μV ENG-type signals. R_{Lin1}, R_{Lin2} and R_{L1}, R_{L2} and R_{L3} were the input and output load resistances as defined by the data sheet of the transformers, arranged to ensure the minimum waveform distortion. The transformers T1 and T2 were 2:1 audio transformers with operating frequency range from 30Hz to 35kHz. T1 was used for producing two EMG signals from input V_M, while T2 produced the floating ENG signal from V_N, in series with R_B. R_1 to R_5 and R_{VAR} resulted to an overall attenuation of 1:40 and 1:200 for the EMG and the ENG signals respectively and $R_{A\text{-}C}$ were 1kΩ resistors representing typical electrode impedance values, while outputs A to C represented the three electrodes of the tripole cuff. The initial tests made use of R_{VAR}, whose variation provided a maximum of ±90% imbalance. They were performed using sinusoidal waveforms, while a more complex EMG waveform was applied after the initial evaluation of the system. In order to partially automate the procedure, R_{VAR} was eventually replaced by a resistor ladder and a set of relay switches (indicated in figure15 as the imbalance switching cct.) controlled by a pulse. Switching between 8 fixed resistor ratios allowed a repeating imbalance sequence between the

values of -98%, -20%, -10%, 0%, 10%, 20%, 40% and 98%. These imbalance values were derived using the ratios of the typical values of the resistors used.

5.2.1.2 Results

In order to compare the AT's output with that of the TT for various X_{imb} values and with a more realistic interference signal, random EMG was applied to the transformer circuit using 50Hz - 300Hz band-limited white noise with a maximum peak to peak value of approximately 6mV, corresponding to 3mV pk-pk for each channel when X_{imb} = 0%. The signal representing the ENG was a 1kHz sinusoid with amplitude 5μV pk-pk and therefore the input SIR was 1:1200. The imbalance varied automatically by the imbalance-switching circuit through the eight fixed values mentioned before. Each imbalance value was applied for 10s to allow the output of the system to settle and the preamplifier outputs as well as the system output were recorded over 80s using a data acquisition (DAQ) card connected to a PC, sampling at 25kHz.

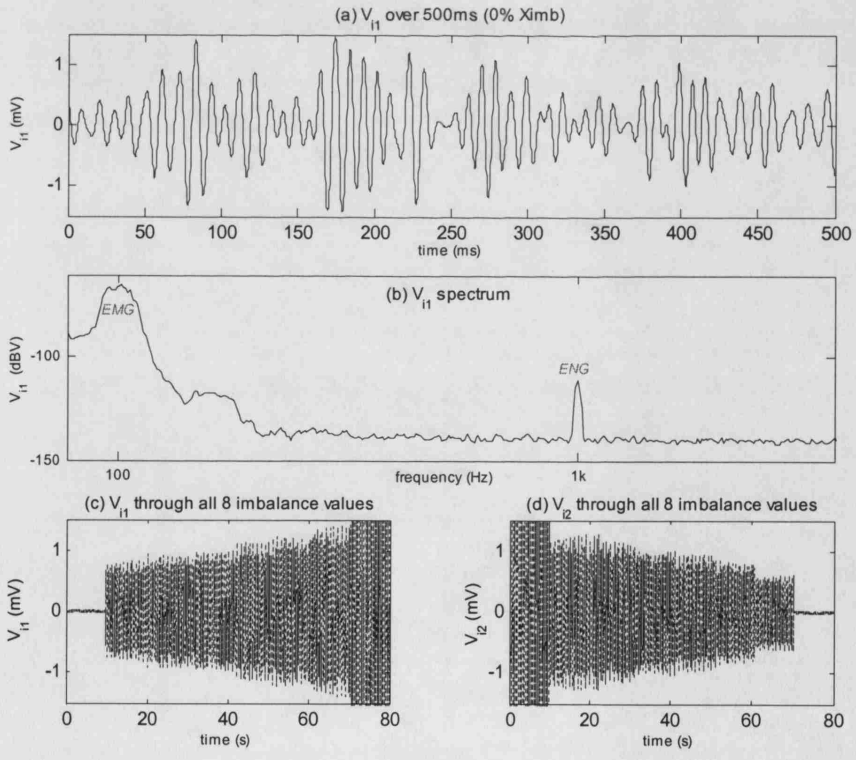

Figure 5.3 (a) Input of channel 1 over 500ms (X_{imb} = 0%) **(b)** Corresponding spectrum with EMG and ENG spectral peaks labelled **(c)** V_{i1} and **(d)** V_{i2} recorded over 80s, through all eight fixed imbalance values.

Recordings for the TT were performed with the feedback loop open and both multiplier gains fixed to 1. This corresponded to $0.5 \times V_{fb0}$, each multiplier gain halved relative to the AT mean multiplier gain, to reduce saturation at the TT output, allowing its observation over a greater imbalance range.

Figure 5.3(a) shows channel 1 input over 500ms for $X_{imb} = 0\%$, derived by the recorded output of the corresponding preamplifier over its gain due to its small amplitude. This graph gives an indication of the form of the random EMG applied at the input. The spectral peaks of the input "EMG" and "ENG" signals are shown in the spectrum in part (b) of the figure, as indicated by the corresponding labels. The plots in figure 5.3(c) and (d) indicate how the corresponding system inputs varied as the fixed imbalance values were applied.

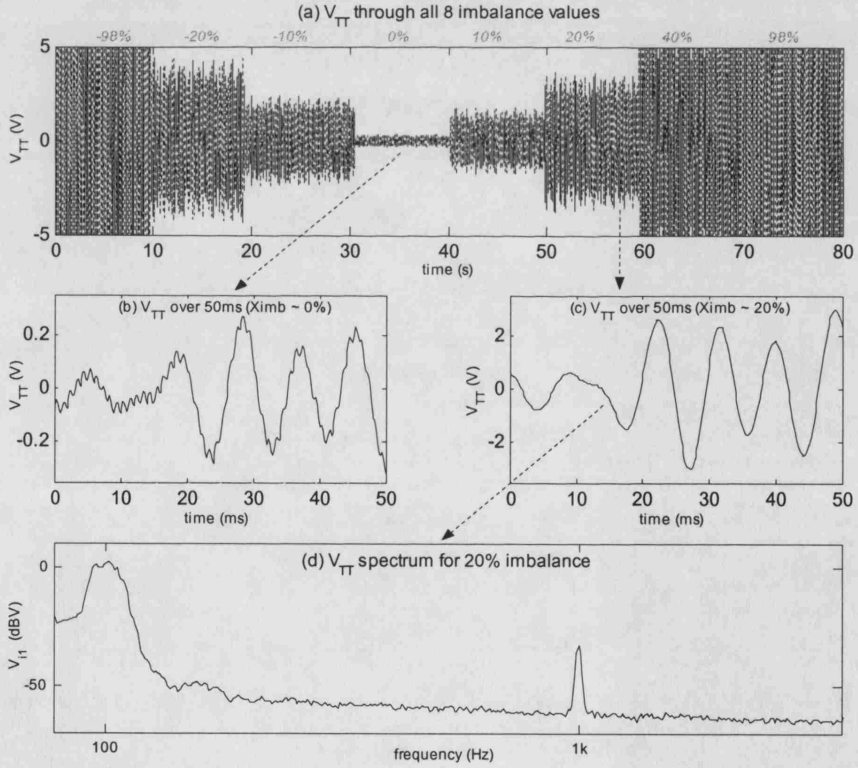

Figure 5.4 (a) V_{TT} through all eight imbalance values. **(b)** V_{TT} for $X_{imb} = 0\%$ **(c)** V_{TT} for $X_{imb} = 20\%$ **(d)** TT output spectrum for $X_{imb} = 20\%$

The TT output is shown in Figure 5.4(a) over 80s. The corresponding imbalance values for each output state are shown just above the plot (grey fonts). The graph indicates that the residual EMG was minimal only for 0% imbalance position. Magnified snapshots of

the open-loop output over 50ms are illustrated in figure 5.4(b) and (c) for 0% and 20% imbalance respectively. The plots indicate that the ENG at the output of the TT is not easily detectable neither for 0% imbalance, with $SIR_{out} \approx 1/3$, nor for 20% imbalance which resulted to $SIR_{out} \approx 1/42$. The latter is the ratio of the peaks in part (d) of the figure that depicts the spectrum of the TT output for $X_{imb} = 20\%$. The TT performed poorly even for 0% imbalance due to unmatched preamplifier gains for the two channels as well as inaccurate resistance ratios used to generate imbalance values and the measured imbalance value for the imbalance position denoted as 0% was approximately 1.5%.

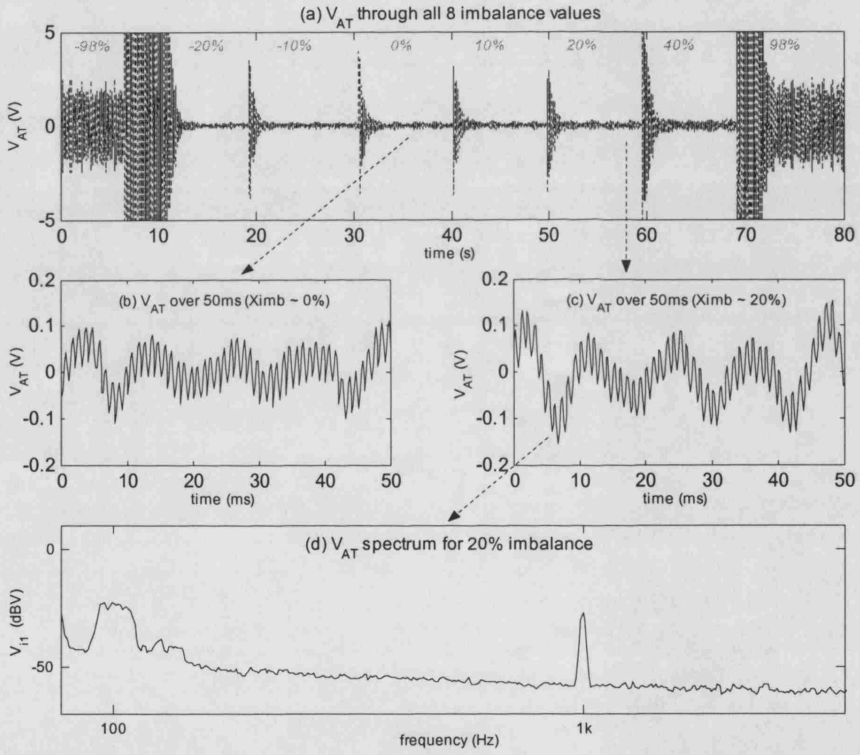

Figure 5.5 (a) V_{AT} through all eight imbalance values. **(b)** V_{AT} for $X_{imb} = 0\%$ **(c)** V_{AT} for $X_{imb} = 20\%$ **(d)** AT output spectrum for $X_{imb} = 20\%$

The recordings were repeated with the feedback loop closed and the output of the AT is shown over 80s for all imbalance values in figure 5.5(a). The residual output interference is greatly reduced for all but the extreme imbalance values as the feedback was limited to values corresponding to $X_{imb} = \pm 90\%$. 50ms snapshots of V_{AT} for 0% and 20% imbalance are shown in Figure 5.5 (b) and (c) respectively, similar to the snapshots of V_{TT} in Figure 5.4. The respective output SIRs were approximately 4/3 and

34/42, 4 and 34 times greater than the TT output SIRs for the respective imbalance values. Using the AT, ENG was detectable for both imbalance values. The preamplifier mismatches that degrade the TT performance are addressed in the AT by the feedback and its output has minimum residual interference for all imbalance values apart from the extreme ones. The spectrum of V_{AT} for X_{imb} = 20% (figure 5.5(d)) demonstrates that the harmonic distortion was kept to a minimum by taking into consideration the design issues discussed in the previous chapter

Using relay switches to change imbalance values abruptly allowed the assessment of the settling time, with the measured values in Table 5.2 being on average 1.1 times greater than the predicted values (defined by equation (4.20)). The calculated t_{sys} is 99% of the settling time of the feedback signal which settles exponentially and the RC values used for the integrator were accurate within 5%, thus the integrator time constant was slightly different than the value calculated.

X_{imb} transitions (%)	69.95	9.86	9.98	9.94	10.01	19.59	54.37
Theoretical t_{sys} (s)	8.74	1.23	1.25	1.24	1.25	2.45	6.79
Measured t_{sys} (s)	9.1	1.5	1.54	1.47	1.48	2.97	7.94

Table 5.2 Comparison of measured and theoretical settling times for each measured X_{imb} transition

Measurements of the output SIRs of both systems are shown in figure 5.6(a) versus the absolute measured imbalance values, along with the corresponding linear data fits (least squares fit by Matlab®). The fit line for the TT crosses zero for imbalance close to 40% because the corresponding TT SIR_{out} value was 0.012 (close to zero but positive). The standard regression errors corresponding to 95% confidence intervals were 0.12 and 0.14 for the TT and the AT data fits respectively. Both systems were affected by imbalance, but the AT possessed 55.1 times greater SIR for 40% imbalance (AT SIR_{out} = 0.66). This is illustrated in figure 5.6(b), where the ratio $\frac{\text{AT SIR}_{out}}{\text{TT SIR}_{out}}$ was plotted versus imbalance in similar fashion to figure 5.6(a), to offer a comparison of the EMG reducing performance of each system, irrespective of gain. This ratio is denoted as *comparison ratio* and here it shows the level of improvement achieved by employing feedback control relative to using fixed-gain amplifiers. The gradient of the comparison

fit was 54.1° and the regression error corresponding to 95% confidence interval was 3.8. The improvement for large imbalance values is great, the AT reaching about sixty times greater SIR_{out} than the TT. This makes a strong case in advantage of the use of the AT in implantable devices, justifying the slightly increased complexity.

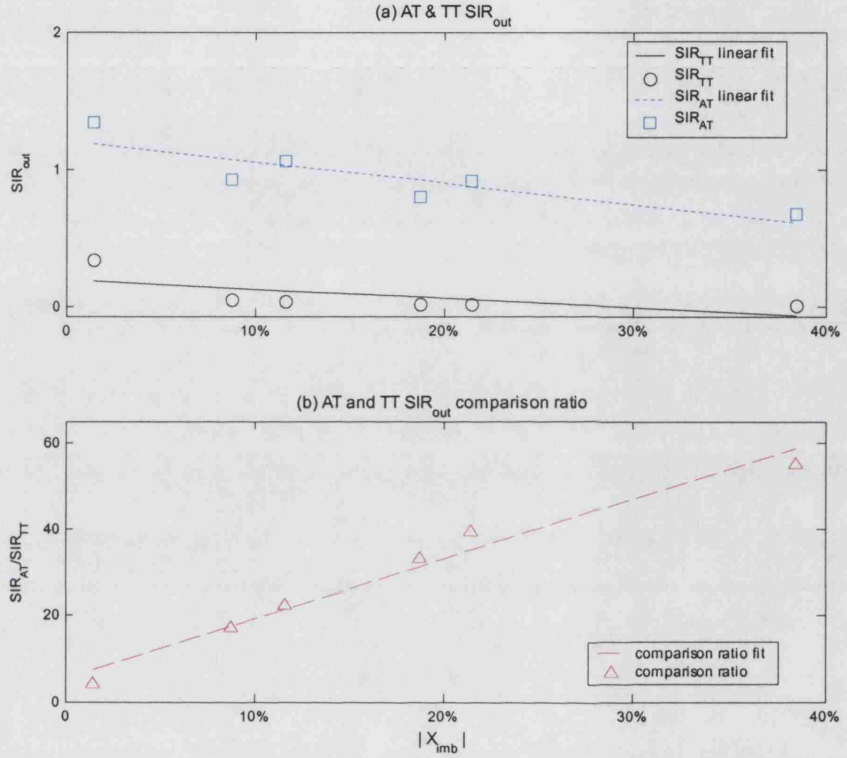

Figure 5.6 (a) TT and AT output SIR versus imbalance **(b)** Comparison ratio (AT SIR / TT SIR) versus X_{imb}.

To further illustrate the effectiveness of the AT in reducing interference, as well as to show that it is independent of signal frequency - as opposed to filters being used to separate EMG and ENG – the input illustrated by the spectrum at the top of figure 5.7 was applied to both systems, with 20% imbalance. The ENG remained as before with the EMG now being represented by a random signal occupying the full recording spectrum and pk-pk amplitude corresponding to approximately 2mV across the cuff. The output spectra of V_{TT} and V_{AT} are shown in the bottom of the figure. The ENG peak is not visible in the TT output, while the AT suppresses the interference providing a detectable ENG signal at its output.

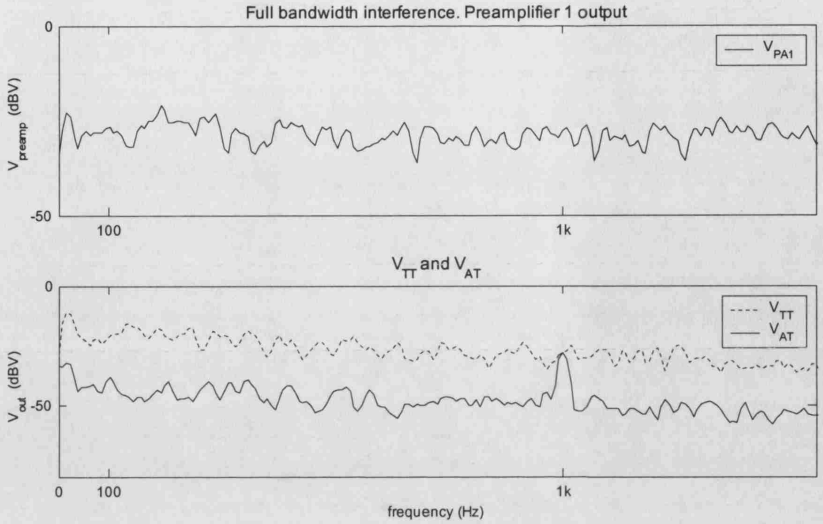

Figure 5.7 (a) Full bandwidth interference input spectrum. **(b)** TT and AT output spectra. AT's operation is independent of signal BW

5.2.2 Saline bath testing: "Tissue-growth" experiment

5.2.2.1 Experimental set-up

Using the setup described in section 3.3.1 (chapter 3) an obstacle on a thread was placed in various positions inside the cuff to simulate tissue-growth imbalance. The EMG signal was again applied using two electrodes in the saline bath and the ENG signal was injected by a transformer in series with the middle electrode. The signal characteristics were the same as the signals illustrated in the top and middle of figure 5.3. The setup is again depicted in figure 5.8 (side view of figure 3.7). The recording system allowed the feedback to be turned on and off, offering the option of comparing the AT with the TT.

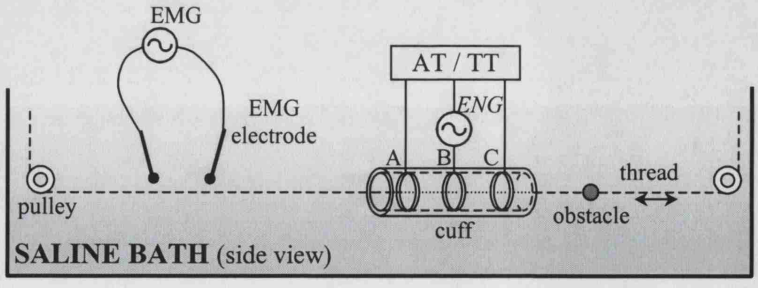

Figure 5.8 Saline bath setup for "tissue growth" imbalance AT and TT assessment.

5.2.2.2 Results

The output was recorded over 20s, the first 10s with the system operating as TT and the rest as the AT configuration. Figure 5.9(a) illustrates the integrator output $V_{fb}(t)$, diode-limited when the feedback loop was open. As soon as the system turned into the AT the feedback converged to compensate for the imbalance. In this case, with the obstacle positioned 3mm inside the cuff the imbalance was 23.4% measured using the preamplifier outputs in equation (3.6) (chapter 3). The graph shows that the feedback settled at a value corresponding to X_{imb} = 23.21%, indicating an error of 0.19% relative to measure input imbalance value. The corresponding system output is illustrated in figure 5.9(b), where the transition from the TT to the AT lasted approximately 3.4s. The outputs of the two recording configurations are shown over a 40ms period in the bottom subplots of the same figure and it is evident that the AT significantly improves ENG detection.

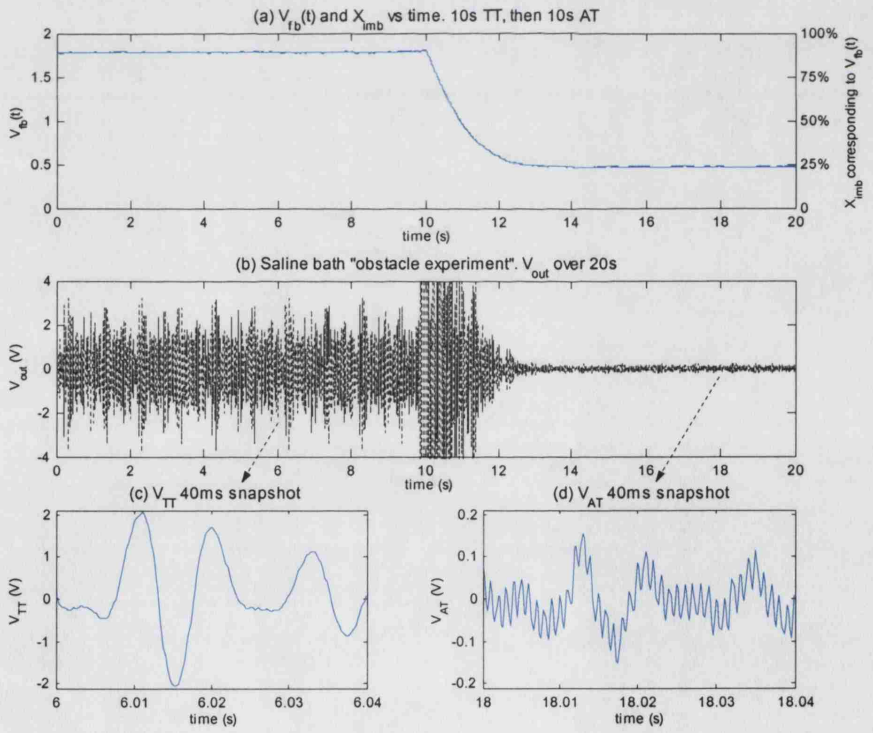

Figure 5.9 (a) System feedback **(b)** System output for 23.4% imbalance. Obstacle position: 15mm inside cuff. System operates for 10s as TT, then is switched to AT. **(c), (d)** 40ms snapshots of TT and AT respectively

The S/I ratio in Figure 5.9(c) is improved 19.16 times from 1/46 for the TT to 5/12 for the AT (figure 5.9(d)). When the AT output settled, the residual EMG interference was

visibly reduced relative to the initial TT condition. The feedback settled within 0.19% of the applied imbalance value, which indicates the accuracy of the discrete-component system.

5.2.3 Saline bath testing: Proximity experiment

5.2.3.1 Experimental set-up

A second saline-bath test was subsequently performed, using the apparatus described in section 3.3.2.1 (chapter 3). The AT was configured with a differential amplifier replacing the comparator to investigate it would improve performance. Initially, with the distance between the two cuffs fixed at 40mm the orientation of the recording cuff relative to the EMG-producing one was varied to observe the effects of proximity imbalance on the AT, the TT and the QT. The EMG and ENG were sinusoidal with respective frequencies of 130Hz and 1kHz and amplitudes of 0.21mV pk-pk and 6μV pk-pk respectively. Measurements of SIR_{out} were recorded and then the EMG source (denoted EMG_1 in figure 5.10) was turned to $\theta = 90°$ and the systems were tested in the presence of a second interference source (EMG_2 in figure 5.10). That was placed at 70mm from the recording cuff with $\theta = 0°$ and its frequency and amplitude were 730Hz and 0.62mV pk-pk respectively. The interference amplitudes were relatively low, but they were the same for all three systems. Thus the corresponding output spectra were recorded and the systems were compared in terms of output SIR for each of the two interferences.

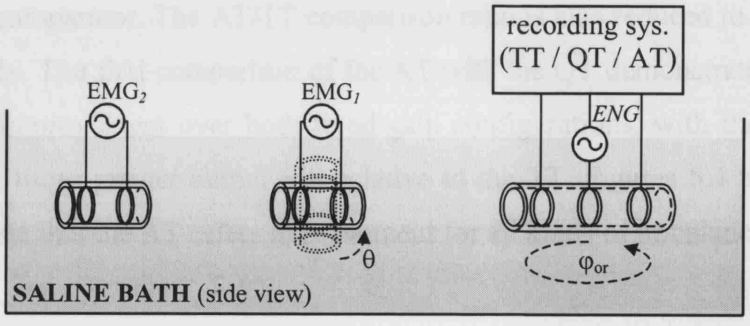

Figure 5.10 Saline bath setup for comparing the AT, TT and QT in the presence of proximity imbalance.

5.2.3.2 Results

Figure 5.11 illustrates AT/QT and AT/TT comparison ratios in similar fashion as figure 5.6(b) for the imbalance range caused by proximity (1.5% to 10.3% with φ_{or} values used in figure 3.11). The slopes of the linear fits (AT/QT: 45.3° and AT/TT: 48.7°) show that QT was slightly less sensitive to imbalance than the TT, and it offered an average of 1.2 times greater SIR_{out}. The output SIR of the AT was on average 6.95 and 5.9 times greater than the respective ratios of the TT and the QT and the respective regression errors corresponding to 95% confidence intervals were 0.59 and 0.44.

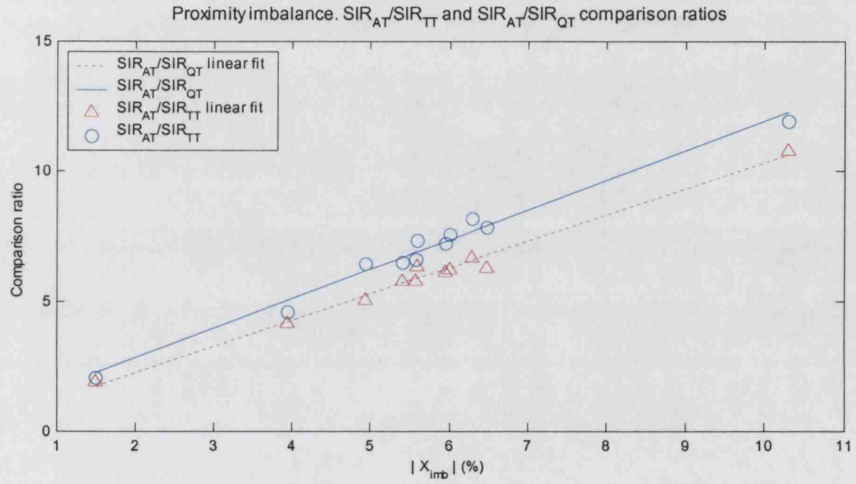

Figure 5.11 Proximity tests. AT/TT and AT/QT comparison ratios for imbalance values caused by variation in cuff orientation.

The gradient (48.7°) of the AT/TT comparison-ratio fit shows that the AT improvement with increasing imbalance is somewhat reduced when using the differential amplifier instead of the comparator. The AT/TT comparison ratio is also reduced to 11.92 relative to 19 previously. The first comparison of the AT with the QT demonstrates that the AT offers similar improvement over both fixed-gain configurations, with the QT offering on average 1.2 times greater output SIR relative to the TT. Figures 5.4 to 5.7, 5.9 and 5.11 demonstrate that the AT offers improvement for all kinds of imbalance.

The input spectrum recorded after two interference sources were applied is shown in figure 5.12(a) where the spectral peaks of the ENG and the two EMG signals are labelled. Saline bath shielding was inadequate and as a result mains interference was intense, with main peaks at 50Hz and at 150Hz corresponding to 1st and 3rd harmonics.

The mains interference present in the spectra in figure 5.12 was one of the main external interferences degrading the measurements in the laboratory, but is not expected to be present in an implanted device.

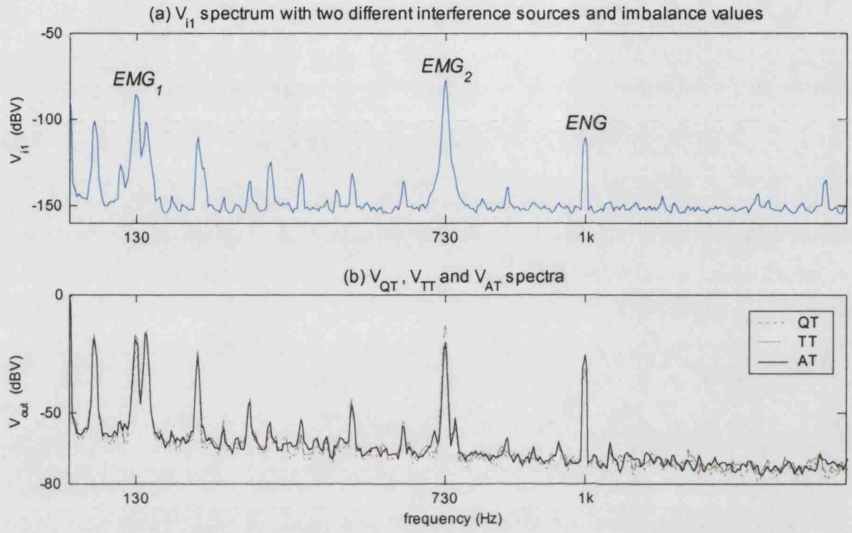

Figure 5.12 Input and QT, TT and AT output spectra in the presence of two sinusoidal EMG sources. Mains interference was intense due to reduced shielding.

The two EMG sources, their spectral peaks labelled EMG_1 and EMG_2 possessed 2.17% and 6.32% imbalance respectively. The SIRs for EMG_1 at the outputs of the QT, TT and AT were 0.43, 0.35 and 0.457 respectively. The corresponding ratios for EMG_2 were 0.28, 0.23 and 0.51. The AT SIR was greater for EMG_2 because its integral was greater than that of EMG_1 over the settling time required for imbalance range of 0% to 7% making the integrator to settle closer to its corresponding imbalance. When two different sources of interference with different imbalances are present, the AT's improvement over the TT and the QT is greatly reduced. In the case presented in figure 5.12 the AT/QT and AT/TT comparison ratios are 1.068 ($\approx$ 16/15) and 1.306 ($\approx$ 19.5/15) respectively for EMG_1. Similarly for EMG_2 the respective comparison ratios were approximately 27/15 and 33/15. The ratios are still greater than unity, corresponding to improvement, and the imbalance values for EMG_1 and EMG_2 were relatively small (2.17% and 6.32% respectively) providing less severe conditions for the QT and the TT than the higher imbalance values in previous experiments.

5.3 In-vivo experiments and comparison of systems

This section describes in-vivo experiments, performed shortly after the last saline-bath experiment, using stimulation-induced signals with the system having the circuit setup described in the last part of the previous section. These sessions took place in the context of an overall in-vivo experiment mainly performed for proximity imbalance investigation in chapter 3, section 3.6. However it offered a chance to compare the AT, TT and QT in terms of output SIR in the presence of two imbalance values corresponding to two different interferences due to M-wave and stimulus artefact. Stimulation was chosen as opposed to other methods (e.g toe tapping [19]) used to produce nerve activity in in-vivo experiments, because it caused both muscle and nerve activity and it allowed the signals to be triggered with the stimulus pulse applied facilitating measurements. Moreover the signals are clearly separated in the transient domain, making the data analysis more straightforward, while frequency spectra were not useful in this case as some of the ENG and stimulus artefact frequency components were not distinctly different. The presence of two different interferences with different characteristics and in two different positions relative to the cuff allowed the assessment of the systems in the presence of intense proximity imbalance.

5.3.1 Experimental Setup

The experimental procedure was fully described in chapter 3, section 3.6.2 and a diagram of the setup is shown in figure 5.13 (similar to figure 3.16). After preliminary measurements, the preamplifier gains were reduced from 1000 to 400 to avoid saturation of the system's front-end. Measurements were taken from the outputs of the AT, TT and QT on one leg of each rabbit, for each middle electrode position (E_{M1}, E_{M2} and E_{M1M2} – connectivity described in section 3.6.2), with all nerve branches present and after cutting ramus muscularis. As in chapter 3, this resulted in forty-eight sets of measurements (sessions), six of which were considered invalid when analyzed due to the absence of nerve signal. Again, the measurements were captured using a TEAC RD-145T DAT recorder with a sampling frequency of 20 kHz.

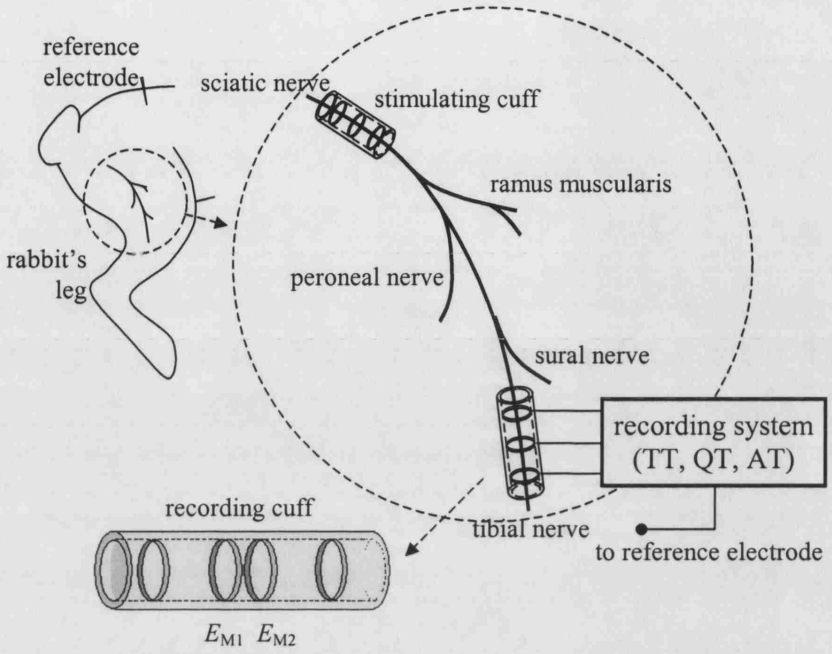

Figure 5.13 In-vivo experimental setup: Leg of rabbit and magnification of testing area with relevant nerve branches, position of cuffs and recording cuff illustration (not to scale).

5.3.2 Results

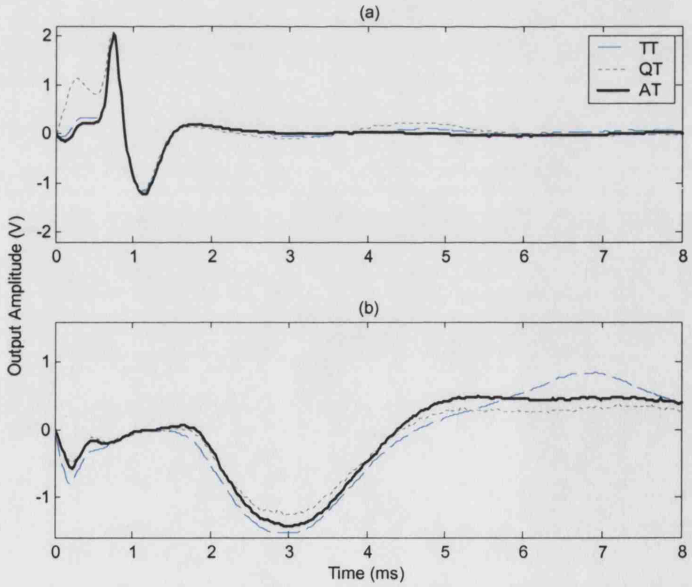

Figure 5.14 (a) An example of valid output signals, where the CAP and the interference peaks are present for all three systems. **(b)** An example of invalid outputs where no comparison can be performed, as the *S/I* cannot be calculated due to the absence of a CAP signal.

As shown from the results of the section of this experiment described in chapter 3, the two interference signals possessed different imbalances. The *S/I* ratio of interest was the CAP pk-pk over the *M*-wave pk-pk since the AT was not developed to address stimulation interference and if necessary the stimulus artefact can be blanked out. Figure 5.14(a) illustrates a sample of output signals from all three amplifier configurations scaled to have the same CAP amplitude (2^{nd} CAP peak) for better visual comparison. In some cases however, the measurements recorded were considered invalid (as mentioned in the end of section 5.3.1) for all three amplifiers, either because of absent or distorted *M*-wave signals or because of absent CAP signals, which is the case in the example illustrated in figure 5.14(b). In these cases the *S/I* ratios for the three amplifiers were not calculated.

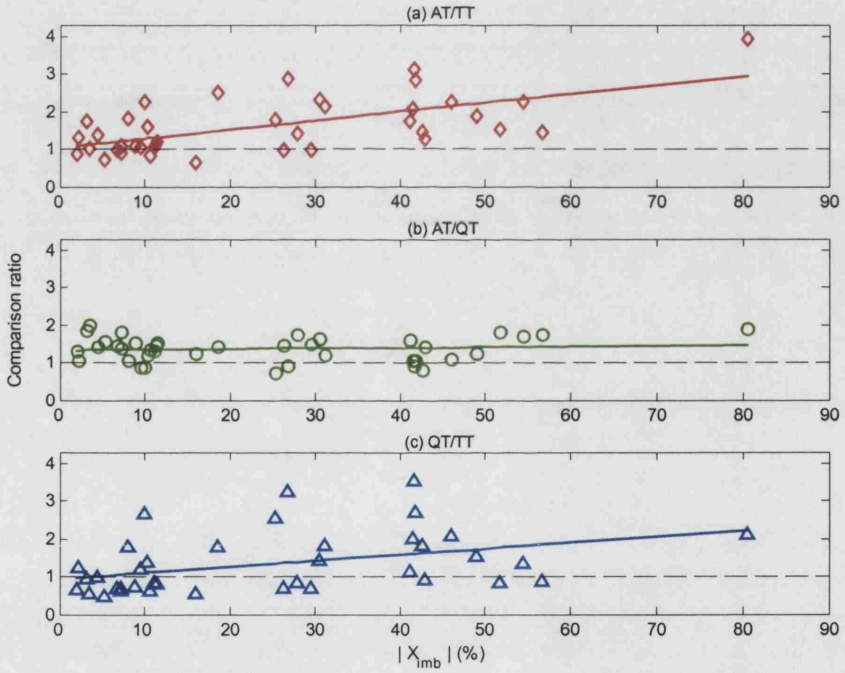

Figure 5.15 Comparison in terms of relative *S/I* ratios versus imbalance values measured throughout the tests performed. **(a)** AT/TT **(b)** AT/QT **(c)** QT/TT

The three amplifier configurations were compared in terms of their output SIR for all valid forty-two in-vivo sessions. At each session, the recording system was switched successively from TT to QT to AT mode, and the respective SIR values were calculated. In this section SIR is defined as the ratio of the CAP (pk-pk) over the residual *M*-wave (pk-pk) seen at the output of each system. For each session, the AT/TT, AT/QT and

QT/TT comparison ratios were calculated. These comparison ratios were plotted in figure 5.15 (subplots a, b and c respectively) versus cuff imbalance values measured in chapter 3. The AT results used were recorded after its output had reached a steady state.

The trends of the scatter plots formed by the comparison ratios in each session, are demonstrated by the linear fit (least squares fit performed in Matlab®), which allows an assessment of the relative sensitivity of each system to cuff imbalance. The plots are presented in the form suggested in [96], and the regression coefficients for the AT/TT, the AT/QT and the QT/TT are 0.047, 0.0032 and 0.0315, respectively, corresponding to respective gradients of 2.71°, 0.18° and 1.82°. These gradients indicate the relative sensitivity of each system to cuff imbalance. The TT is more sensitive to cuff imbalance than both the AT and the QT, and this is evident by the slope of the data trends. In both Figs 5.15(a) and 5.15(b) it is evident that for high cuff imbalance values (over 20 %) the AT is generally better than both the TT and the QT. The slope of the regression line corresponding to the AT/QT comparison indicates that the AT is slightly less sensitive to cuff imbalance (*M*-wave), however, it generally provides greater SIR for all cuff imbalance values as the line is above unity. In both the AT/TT and the AT/QT scatter plots, the last point illustrates how the AT performs even for extreme cuff imbalance values.

The respective standard errors of the regression corresponding to 95 % confidence intervals for the AT/TT, the AT/QT and the QT/TT, were 0.6, 0.34 and 0.75, respectively. In low cuff imbalance conditions the systems were expected to perform similarly.

Overall, the AT performed the best in 61.9 % of the trials, while the QT and TT performed the best in 23.8 % and 14.3 % of the trials, respectively. The fact that the AT is not always better as indicated by previous saline-bath experiments (sections 5.3.1 to 5.3.3) is attributed to the presence of different cuff imbalances for the two interference signals. This means that the AT settled to a cuff imbalance value between that of the *M*-wave and the stimulus artefact, mostly closer to the former since the *M*-wave lasted longer. Nevertheless, the AT is intended for cases where only naturally occurring signals are present, i.e., only one cuff imbalance is present due to the absence of

stimulation. Thus, the results strongly indicate that in such an environment, the AT will be superior to the other two systems, as indicated also by previous experiments where only one cuff imbalance was present. If the stimulus artefact is present in other applications, it may still be possible to cancel the EMG cuff imbalance accurately by blanking the recording system during stimulation. In these in-vivo experiments blanking was not employed because the effect of the stimulus artefact on the AT's ability to reduce the M-wave needed to be examined.

The results in figure 5.15 also show the QT is generally superior to the TT, as expected. This is partly due to the shorting of the end electrodes. However, Rahal [29] and Andreasen [31] showed that shorting electrodes can be used beneficially with the TT as well, and this would also be true for the AT. Even if the AT and the QT perform equally well for particular cuff imbalances, the AT has the advantage, being adaptive, of providing constant interference reduction with changing cuff imbalance conditions.

5.4 Control stage: comparator versus differential amplifier

Using a differential amplifier instead of a comparator after the rectifiers was considered because the differential amplifier would be slightly less sensitive to offsets and to the noise floor and it would not oscillate in the case where its two inputs were equal. However, its output is not a square wave and this means that the integrator will not ramp to the desired DC level although increasing its gain will cause it to saturate for small input differences resembling the comparator's output.

One of the main issues when using a differential "comparing" amplifier (gain G_{dif}) instead of a comparator is the dependence of the system's convergence time on input EMG amplitude, with τ_{sys} of equation (4.19) in chapter 4 becoming:

$$\tau_{sys} = \frac{\tau_{\text{int}}}{G_{PA} G_{dif} G_i g V_{emg}} \tag{5.1}$$

Thus if the EMG activity is due to a distant muscle and its amplitude is small, the system will take longer to converge.

The amplifier output will resemble a square wave only when imbalance is high making the difference between the EMG components of the two channels great, but will follow the form of the signal difference between V_{m1} and V_{m2} when this is small. Effectively, in sinusoidal EMG representation this would cause the integrator to produce a cosine feedback signal instead of a ramp or a DC with triangular distortion as it happens when the comparator is used. Generally, only the maximum expected amplitude of the bio-electric signals can be estimated, but there is uncertainty about the conditions between muscle and nerve activities. Therefore, it is not considered a safe design practice to make the system dependent on EMG amplitude. Moreover, although the comparator is certain to introduce more ripple at the feedback signals the harmonic distortion caused by its high frequency oscillations will be outside the bandwidth of interest. Regarding EMG-related harmonics, they will be similar in the case of the differential amplifier if this produces a square wave output and in the case of a small cosine feedback signal the multipliers will produce EMG 2^{nd} harmonics. Overall, based on the above arguments and considering the results of the first part of the saline bath experiment of section 5.2.3 (see figure 5.11), the use of a well-balanced comparator is preferable.

5.5 Conclusion

The development and testing of the discrete-component system described in this chapter was very useful in applying theory to practice and assessing the validity of the AT as a neural amplifier that will offer significant advantages if made implantable. Various functional practicalities were addressed and the validity of the analysis done in the previous chapter was demonstrated by the achieved results in terms of imbalance correction range and output SIR. The system was actually used in its first stages to point out some of the sources of error analysed in chapter 4.

The results were encouraging in terms of ENG detection, even for high imbalances as shown in figures 5.5(c) and 5.9(d). The AT was shown to be superior than the TT, on which it is based, but it also performed clearly better than the QT (figure 5.11). The target of AT output SIR equal to or greater than unity with 10% imbalance was achieved (figure 5.6(a)) even with a lower input SIR than initially planned. The advantage of the AT relative to a system employing filtering was demonstrated as the

system separated ENG from EMG even when the bandwidth of the latter covered the full spectrum. The AT is a solution independent of signal frequency and allows ENG detection even in the presence of interference signals with equal or higher frequency components than the nerve signal.

Although sources of error mentioned in chapter 4 were suppressed in this design, it is not possible to fully eliminate them, therefore the maximum SIR_{out} of the AT was limited by their presence. Additional errors in the discrete system included the generation of the two feedback signals by two different components instead of one with differential outputs. Effectively if the inverter gain was not unity or if it generated DC offsets to one branch only, the two feedback signals would be mismatched. In the final version of this system these errors were minimised with manual trimming, however in the implantable version they should be avoided by using differential output in the feedback generation stage. Moreover, considering the results in the later experiments and the discussion in section 5.4, a comparator is preferable for the AT's control stage.

Based on the observations and the assessment of the system in this chapter, a fully implantable version of the AT in BiCMOS technology was developed, as described in the next chapter.

Chapter 6

INTEGRATED REALISATION

The previous chapter demonstrated the improvement that the AT can offer in neural recordings, due to its ability to minimize cuff imbalance and to significantly reduce EMG interference. Numerous established implanted devices described in the literature [11, 77, 93] consist of discrete components, in surface-mount versions. Most IC solutions for neural recording that have been reported in the literature are designed for neural recording with QT front-end configuration [97-102]. An implantable version of AT could be realized simply by using surface-mount versions of the components comprising the circuit in chapter 5, possibly replacing some operational amplifiers with dual or quad packages to reduce the overall circuit area and the number of components and to improve matching. However, it was required that the CNM implant (described in chapter 1) would include a stimulator and other sub-systems (developed in the context of other projects in UCL). The inclusion of all these subsystems in discrete form on an implant would increase the area and usually the power consumption and in some cases it would reduce system flexibility. Therefore it was considered advantageous to integrate the AT for these reasons and to provide improved matching between the two channels of the system resulting in a higher output SIR. This chapter describes the design steps followed for the integration of the AT using 0.8 BiCMOS technology and

measured results from the fabricated system are presented. The design of the IC was carried out using the Cadence® Virtuoso package for analogue schematic and layout.

The remaining sections of the chapter are organized as follows. Section 6.1 describes the first approach to the architecture of the integrated AT, followed by a description of the improved second version. The circuit design of the main stages of the chip are described in section 6.2 and section 6.3 offers an overview of the system circuit diagram and the chip microphotograph. Measured results are presented and discussed in section 6.4. Section 6.5 presents an integrated integrator followed by chapter conclusions in section 6.6.

6.1 Integrated Adaptive Tripole Architecture

6.1.1 System Description and Overview

Two main integrated versions of the AT have been implemented during this project. Their topologies are illustrated in figure 6.1. In both versions the integrator was not in the objectives of the integrated realization, because it could be easily realized using external R and C components. External components would be available on the surface-mount PCB comprising the implant. The aim of the IC was to reduce the power consumption to approximately 10mW from approximately 150mW if surface-mount versions of the discrete components in chapter 5 were used.

It was also important to reduce the space the AT would occupy on the implant relative to the discrete-component version and the area objective for the IC was approximately $4mm^2$ (die) occupying approximately $22mm^2$ (16-pin SOIC package) of implant area (or even less if the layout is combined with other stages of the implant in one chip) at least 20 times less than a very tightly arranged discrete surface-mount AT. Another main objective was to keep complexity low so that even in low imbalance situations the system would be attractive relative to its fixed-gain predecessors that were simpler. With these specifications the analogue IC AT version would also be a better choice than some digital version, which would generally require higher complexity on top of greater power and area.

6.1.1.1 First IC version

The first version (figure 6.1(a)) will only be described briefly in this section, as it showed poor performance in terms of output signal to interference ratio and harmonic distortion, cuff imbalance correction range and yield. The reasons for this poor performance were analysed and addressed in the second one. In this version an effort for simplicity in circuit level led to a relatively complicated system-level architecture to reduce errors. The preamplification stage was implemented in the context of another project for fixed-gain cuff recording [91] and it made use of bipolar input transistors to reduce 1/f noise. The rest of the system operated in *current mode* and the variable gain stage was realized by operational transconductance amplifiers (OTAs). However, the use of simple OTAs comprising from a long-tail pair terminated in a single current mirror resulted to load mismatch between the two sides of the differential pair, causing DC offsets. In order to reduce these offsets, two OTAs were connected to each channel, one inverting and one noninverting, ideally resulting to two equal and opposite signals with the same DC offset.

The presence of offsets caused the corresponding outputs of the subsequent rectifiers to suffer from the effect described in section 4.2.2 (chapter 4). However, following a sinusoidal analysis, the two rectifiers in each channel produced half cycles of rectified signals with opposite offsets, due to their input half cycles having opposite polarity and equal offsets. Hence, adding the outputs of the rectifiers in each channel would ideally produce the modulus of each channel's signal without the offsets introduced by the OTAs. The rectifiers were realized by two half-wave stages, one rectifying positive and the other negative input signals and their gain was 0.5 to retain the signal amplitude at the same level as the OTA output. Using half-wave rectifiers with dual output stages allowed the offset-free current output of the OTAs to be recomposed. This was realised by reversing the polarity of the extra output of each second quadrant half-wave stage and adding it to the corresponding first quadrant ones.

Operating in current mode made signal additions and subtractions easy and did not require extra subcircuits, as currents were joined in nodes leading to the subsequent stages [103, 104]. The output stage was a transimpedance amplifier and the rest of the control stage comprised of a current comparator and a transconductance feedback stage.

The comparator produced a voltage output applied to an external RC integrator whose output voltage was in turn applied to the feedback transconductance stage producing the feedback currents.

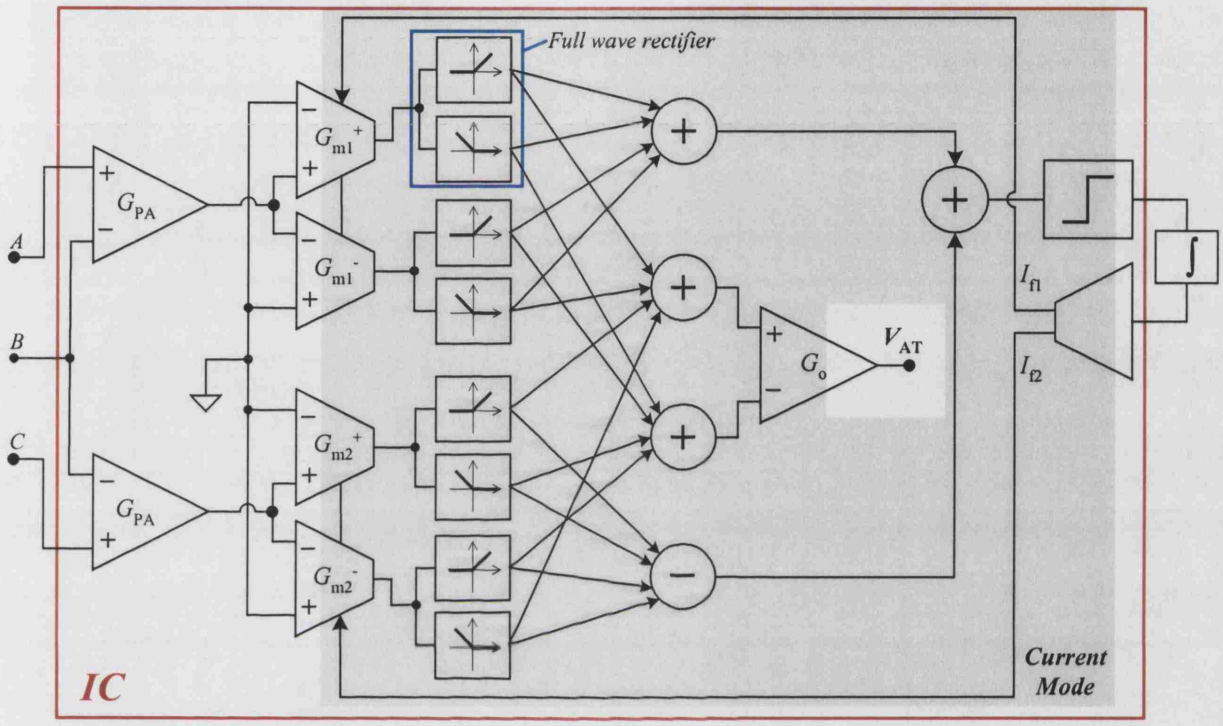

(a)

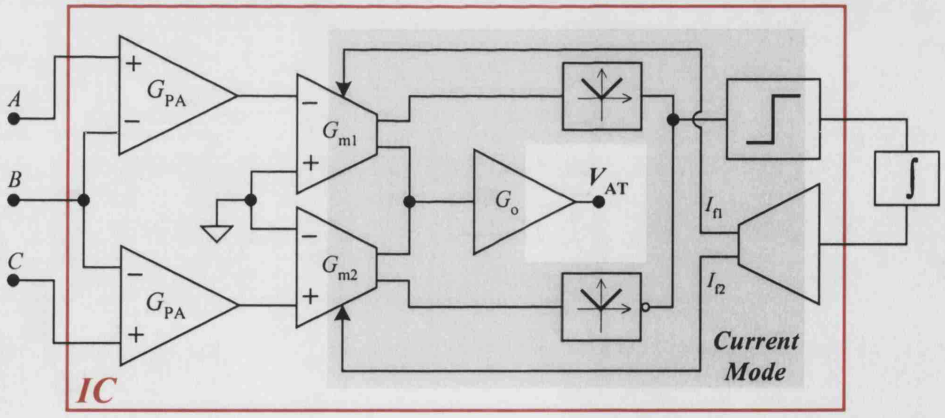

(b)

Figure 6.1 The adaptive-tripole (AT) architecture. Current mode used to simplify mathematical operations (addition and subtraction blocks represent current summation nodes): (a) Version 1 [86, 105]. Simple circuit design lead to complicated system-level architecture to reduce errors. (b) Version 2 [32, 106] More advanced circuit design simplified the architecture. Errors were minimised. Imbalance range and output SIR were greatly increased.

This first approach had very poor performance mainly because of the following points:

i) The simple current mirrors used in the variable-gain OTAs resulted to loading difference between the two branches of each differential pair causing DC offsets.
ii) DC bias currents in the current rectifiers caused additional offsets
iii) The reconstruction of each channel's signal through the rectifiers introduced sensitivity to minute delays between the resulting channels and caused severe harmonic distortion.
iv) The twin OTA architecture required a substantial number of very well matched devices to reduce OTA output offsets and mismatches in general.
v) Even if all 4 input OTAs were well matched, cuff imbalance translating to different gains for the two channels would result to different harmonic distortion between them due to non-optimum sizing of the input transistors resulting to limited linear range. This would cause distortion at the system output.

6.1.1.2 Second IC version

The second version was an improved integrated realization of the AT and it overcame the limitations of the first design by employing a much simpler architecture achieved by a slight increase in the circuit complexity of some sub-systems. These enhancements were necessary in order to make the system fully implantable for the specific biomedical application (i.e., bladder implant). The design process was also more thorough for the second version of the integrated AT, as Monte Carlo post-layout simulations were carried out.

In the second IC version of the system (figure 6.1(b)), the preamplifiers were based on the design described in [79, 91, 105] with the front-end noise analysis being the same, but slight adjustments were made in the design to lower the noise floor even further. The variable gain stage was realised by just two operational transconductance amplifiers (OTAs) with variable gains G_{m1} and G_{m2}, controlled by the differential feedback currents $I_{f1}(t)$ and $I_{f2}(t)$. Balanced OTAs were used in this version. The difference with the OTAs used previously was that each of the two branches of the differential pair terminated to a mirror and the corresponding currents were summed in a third branch, improving the balance of the pair and thus virtually removing the DC offsets. This also

allowed the duplication of the OTA output currents allowing direct connection to the output stage. Moreover, the use of advanced current mirrors increased the output impedance. The linear range of the variable gain stage was expanded by increasing the length of the input transistors. The overall power consumption of the OTAs did not rise relative to the first version, because even though the output branches were doubled only one differential pair was used for each variable gain transconductor. Using only one input OTA per channel also allowed for easier matching as the transistors to be matched were halved. In combination with the increased lengths of the input transistors the level of matching achieved was greatly improved.

The rectifiers were more balanced and there was no unwanted DC current flow thus avoiding any DC offsets in the control path. The system again took advantage of *current mode* operation, which eases signal manipulations, such as addition and subtraction. The comparator was again implemented using the circuit chosen initially [107], with the design parameters slightly altered to provide more balanced operation and to remove some slight offsets previously observed. The comparator voltage output was subsequently applied to an external RC acting as a large time-constant integrator, whose output was applied to a feedback OTA generating $I_{f1}(t)$ and $I_{f2}(t)$. The output stage was again a transimpedance amplifier amplifying the summed variable –gain OTA current outputs and providing the final ENG voltage output.

Overall, in comparison to the first version, the second IC provided corrective action for a much greater imbalance range (±40% compared to ±5% with the first IC) and at the same time the output SIR was greater than 1 (up to 4) compared to sub-unity SIR_{out} observed in the previous version. Moreover, the signal distortion was significantly reduced, as a result of a straightforward ENG signal path. The ENG signal was not disassembled and reconstructed through the rectifiers, but it was just amplified, through the same path that the interference (e.g. EMG) was eliminated, as in the original system-level block diagram (figure 4.1, chapter 4). Moreover experience in analogue layout techniques developed through the first version resulted in much better matching and compact layout in the last version, improving the overall system performance.

6.2 Circuit design

6.2.1 Low-Noise Preamplifiers

6.2.1.1 Preamplifier design

The preamplifiers being the front-end interface with the cuff electrodes were required to exhibit very low-noise performance and have reasonable voltage gain (about 40dB), so that low-noise is not a concern for the design of the subsequent system stages. Matching the gains of the two preamplifiers was not considered significant as any slight gain mismatch between the preamplifiers will be compensated by the control stage of the AT. Thus, a simple feed-forward architecture was employed as depicted in figure 6.2, thereby avoiding the complexity and noise of feedback networks. Noise optimization of the preamplifiers was explicitly described in [79] where it was shown that in order to achieve the required noise specification with minimum die area and power dissipation, the input differential pair transistors Q_1 and Q_2 in figure 6.2 should be bipolar. Because of this requirement, the complete adaptive ENG amplifier was implemented in BiCMOS technology, although the control stage utilizes MOS transistors only.

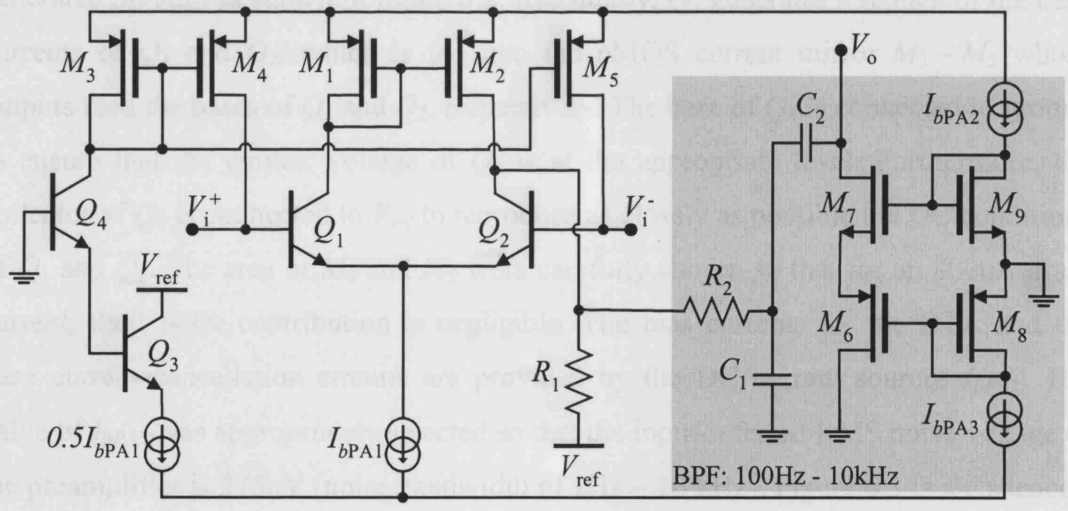

Figure 6.2 Preamplifier circuit (based on [79, 105]).

The preamplifier circuit in figure 6.2 consists of a simple BiCMOS OTA (Q_1, Q_2, M_1, and M_2) terminated in the load resistor R_1 (40kΩ, V_{ref} is a DC voltage reference of 0.75V), followed by a first-order bandpass filter, which restricts the bandwidth to about 100Hz – 10kHz. The upper cut-off frequency is obtained by the combination of resistor

R_2 (500kΩ) and capacitor C_1 (27pF), while the lower cut-off frequency is obtained by capacitor C_2 (80pF) with the series combination of transistors M_6 and M_7, used to form a high value (20MΩ) grounded linear *active* resistor based on the approach in [108]. The lower cut-off frequency was lower than the starting end of the ENG bandwidth, to minimize phase mismatch effects in the bandwidth of interest (see chapter 4). In addition to eliminating low frequencies below the ENG pass-band, the high-pass section of the bandpass filter also removes some of the low-frequency flicker (1/*f*) noise voltage tail and ensures a DC offset-free preamplifier output. The AC coupling mechanism is very important since the succeeding variable-gain OTAs are driven single-ended, and thus the presence of DC offset voltages (>1mV) at their inputs would severely degrade the output SIR. By appropriate scaling of the aspect ratios of M_6 and M_7, a high value resistance is obtained with a maximum nonlinearity of 0.25% for a signal swing of ±85mV. The DC bias voltages of M_6 and M_7 are provided by the diode-connected transistors M_8 and M_9, respectively, which are in turn biased by the DC current sources I_{bPA2} and I_{bPA3}.

As the base current of Q_1 and Q_2 cannot be supplied by the input interface, this was generated on-chip as shown in figure 6.2. Essentially, Q_3 generates a replica of the base currents of Q_1 and Q_2, which is fed into the *p*MOS current mirror $M_3 - M_5$ whose outputs feed the bases of Q_1 and Q_2, respectively. The base of Q_4 is connected to ground to ensure that the emitter voltage of Q_3 is at the appropriate level. Furthermore, the collector of Q_3 is connected to V_{ref} to reproduce as closely as possible the DC conditions of Q_1 and Q_2. The area of M_4 and M_5 were carefully chosen so that for an 800nA drain current, their noise contribution is negligible. The bias currents for the OTA and the base current cancellation circuits are provided by the DC current sources I_{bPA1}. The value of I_{bPA1} was appropriately selected so that the input-referred RMS noise voltage of the preamplifier is 275nV (noise bandwidth of 1Hz – 10 kHz). Figure 6.3 is a Cadence - generated plot of the preamplifier input-referred noise over 10kHz before the HPF stage (before C_2).

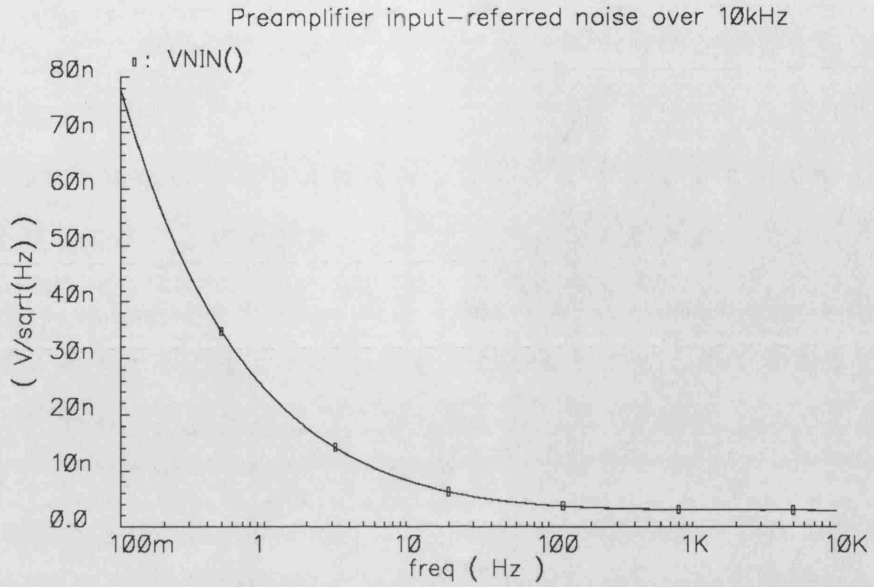

Figure 6.3 Cadence plot of the preamplifier input-referred noise before the HPF stage (before C_2).

6.2.2 Variable-Gain OTAs

The composite signal at the input to each AT channel consisted of EMG and ENG with nominal peak-peak swing after pre-amplification (gain 100) of around ±50mV (for $X_{imb} = 0$) and ±100μV, respectively. The control stage was required to have sufficient gain to amplify the ENG to an adequate level for subsequent A-D conversion (a few tens of millivolts of peak voltage) and also sufficient linearity to accommodate the EMG signal. The decision to use an OTA to implement each variable-gain stage was based on the following two reasons: i) using an OTA, variable-gain capability can be very simply achieved by changing its tail current (I_{fn} in figure 6.4(a)), and ii) the output current signal from an OTA simplifies the design of the subsequent full-wave rectifiers and current comparator circuits. The basic requirement is that each variable-gain OTA must have enough linear gain range to allow even for extreme imbalance values (up to ±40% as suggested in chapter 3).

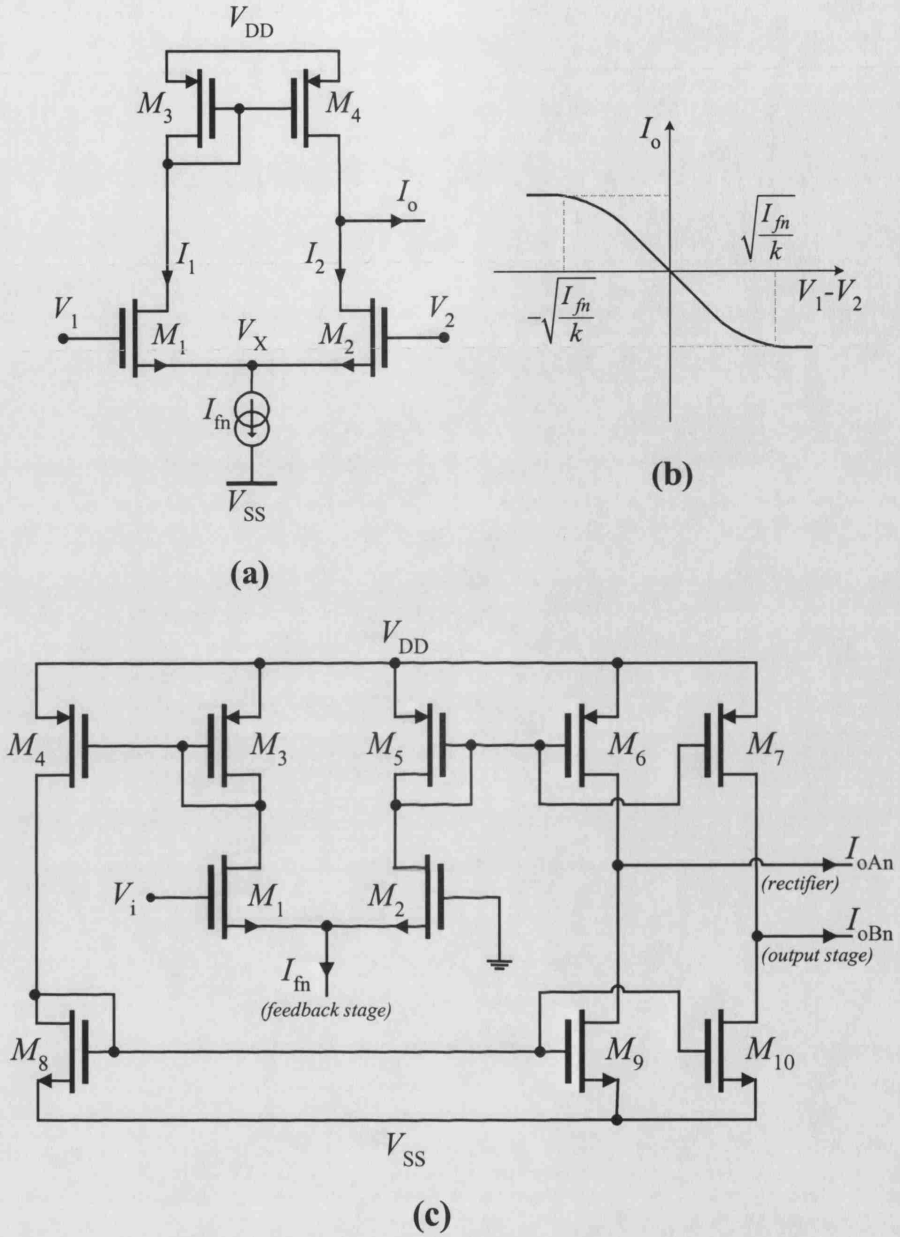

Figure 6.4 Variable-gain OTA circuit (shown with simple current mirrors for clarity).
(a) Simple OTA. (b) Output current characteristic (c) Twin-output balanced OTA

Considering the simple OTA of figure 6.4(a) for the analysis, assuming matched transistors and neglecting channel length modulation, the output current of an OTA is derived by the following equations:

$$I_D = k(V_{gs} - V_T)^2 \tag{6.1}$$

$$\left.\begin{aligned} V_1 - V_X &= V_T + \sqrt{\frac{I_1}{k}} \\ V_2 - V_X &= V_T + \sqrt{\frac{I_2}{k}} \end{aligned}\right\} \Rightarrow V_1 - V_2 = \sqrt{\frac{I_1}{k}} - \sqrt{\frac{I_2}{k}} \tag{6.2}$$

$$\left.\begin{aligned} V_i^2 &= \frac{1}{k}\left(I_1 + I_2 - 2\sqrt{I_1 I_2}\right) \\ \therefore 4I_1 I_2 &= \left(I_1 + I_2 + kV_i^2\right) \\ \left(I_1 + I_2\right)^2 - \left(I_1 - I_2\right)^2 &= 4I_1 I_2 \\ I_o &= I_1 + I_2 \\ I_{fn} &= I_1 + I_2 \\ V_1 - V_2 &= V_i \end{aligned}\right\} \Rightarrow I_o = kV_i\sqrt{\frac{2I_{fn}}{k} - V_i^2} \tag{6.3}$$

In [103], this is written: $I_o = V_i\sqrt{2I_{fn}k}\sqrt{1 - \frac{k}{2I_{fn}}V_i^2}, \qquad |V_i| \le \sqrt{\frac{I_{fn}}{k}}$ (6.4)

For $|V_i| > \sqrt{\frac{I_{fn}}{k}}$, either M_1 or M_2 are off and the output current characteristic varies as shown in figure 6.4 (b). The value $\sqrt{\frac{I_{fn}}{k}}$ is the limit of the input dynamic range.

In the equations above, $k = \frac{1}{2}\mu C_{ox}\frac{W}{L}$ is the transconductance parameter, W and L are the channel width and length of the input transistors, μ is the carrier mobility, and C_{ox} is the gate oxide capacitance per unit area. The transconductance G_m is the slope of the graph in figure 6.4(b), within the input dynamic range, and it can be obtained by taking the derivative of eq. (6.4) with respect to V_i, yielding:

$$G_m = \frac{\sqrt{2I_{fn}k}\left(1 - \frac{kV_i^2}{I_{fn}}\right)}{\sqrt{1 - \frac{kV_i^2}{2I_{fn}}}} \tag{6.5}$$

For $V_i << \sqrt{I_{fn}/2k}$, OTA transconductance is given by:

$$G_m = g_{m1,2} = \sqrt{2kI_{fn}} \tag{6.6}$$

where $g_{m1,2}$ is the small-signal transconductance of transistors M_1 and M_2 in figure 6.4(c). It is evident from eq. (6.6) that the transconductance of the OTA can be adjusted by varying its tail current. According to [103], in order to maintain less than 1% nonlinearity, it is required that V_i range is restricted to:

$$|V_i| \leq 0.2\sqrt{I_{fn}/k} \tag{6.7}$$

Although the nominal signal swing after pre-amplification with $X_{imb} = \pm 40\%$ is expected to be about ±70mV, the linear input range of each variable-gain OTA was set to ±85mV to allow for some variation in the nominal EMG amplitude picked-up from the cuff electrodes. The reduced-offset variable-gain OTA was designed for operation in strong inversion and its schematic is shown in figure 6.4(c). The circuit essentially consists of a symmetrical simple CMOS OTA (known as *balanced* OTA [103, 109]), with input transistors M_1, M_2 and with 1:1 current mirrors M_3 – M_{10}, which in practice were regulated cascode mirrors (figure 6.5) [110]. Regulated cascodes were used because they replicate the input current more accurately than the simple cascode mirrors and, in addition, they allow for a greater output swing [110], and this was necessary in this case because the rectifier input stage caused a voltage variation of ±1V at the output of the variable-gain OTAs.

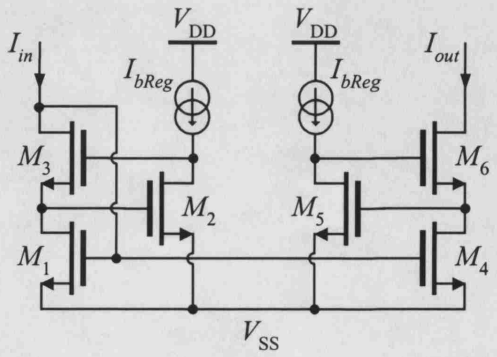

Figure 6.5 *n*MOS regulated cascode mirror [110].

The gain of the OTA is controlled by the feedback current I_{fn} (n = 1 or 2, represents the corresponding AT channel), and the circuit has two current outputs, I_{oAn} and I_{oBn}, with respective connections to the input of a full-wave rectifier and to the output-stage transimpedance amplifier.

Given the nature of the signals after pre-amplification as discussed and aiming for an output-stage transimpedance gain of 500 kΩ, a mean value for G_m of 185 μA/V was chosen. Thus, for $V_i = \pm 85$ mV, (6.6) and (6.7) can provide suitable values of k and I_{fi}. M_1 and M_2 in figure 6.4(c) had a W/L of 150/30 and the mean I_{fi} was 100μA.

6.2.2.1 Layout techniques

The use of symmetrical loads in both branches of the differential pair provided symmetry, minimising DC offsets at the output of each OTA. The transistors M_1 and M_2 were matched during the layout, by splitting them in four interdigitized devices and using the common-centroid technique [111] as illustrated in figure 6.6 to minimize the effect of process variation.

Figure 6.6 Variable-gain OTA input differential pair: illustration of common-centroid matching layout technique (layout implemented in Cadence®). Dummy transistors are also illustrated.

All the mirror transistors were also interdigitized and matched and the OTAs of the two channels were placed in mirror symmetry to ensure matching between the channels.

Dummy transistors were used even for transistors with large length, to provide similar environment and thus ensure symmetry between matched devices [111]. Transistor gates were laid-out using multi-finger structures and all transistor terminals made use of multiple contacts to minimize series resistance and source/drain – substrate parasitic capacitance and to provide higher reliability and better connection. Guard rings were used around matched device sets to minimize interference from substrate currents [111].

6.2.3 Control stage

6.2.3.1 Rectifiers

The two full-wave rectifiers shown in figure 6.1(b) were realized by the current-mode circuit in figure 6.7. The upper rectifier (M_1, M_2, M_5, M_6) operates on current I_{oA1} stemming from OTA G_{m1}, while the lower rectifier (M_3, M_4, M_7, M_8) operates on current I_{oA2} stemming from OTA G_{m2}. The core of each current rectifier are the complementary transistors M_1, M_2 (upper rectifier) and M_3, M_4 (lower rectifier), each transistor performing half-wave precision current rectification, similar to [112].

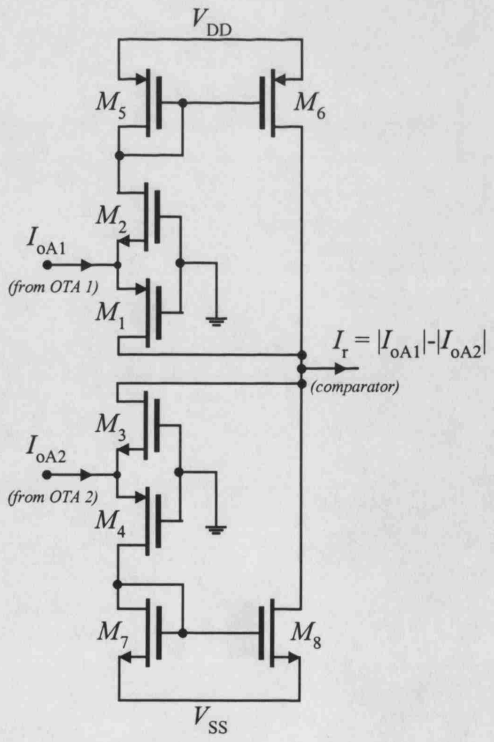

Figure 6.7 The full-wave rectifier (based on [112]) circuits of both channels. Their output currents have opposite polarity and the overall output current is their difference.

During positive excursions of I_{oA1} and I_{oA2}, M_1 and M_4 are turned on and M_2 and M_3 are turned off. Thus, the drain currents of M_1 and M_4 equal I_{oA1} and I_{oA2}, respectively, while these of M_2 and M_3 are zero. During negative excursions the variable OTA output currents, M_2 and M_3 are turned on and M_1 and M_4 are turned off. In this mode the drain currents of M_2 and M_3 equal I_{oA1} and I_{oA2}, respectively, while that of M_1 and M_4 are zero. For the upper rectifier, full-wave rectification is obtained by mirroring the drain current of M_2 through the unity-gain *p*MOS current mirror M_5, M_6 and adding the mirror output to the drain current of M_1. Similarly for the lower rectifier, full-wave rectification is obtained by mirroring the drain current of M_4 through the unity-gain *n*MOS current mirror M_7, M_8 and adding the mirror output to the drain current of M_3 and the resulting rectified current has opposite polarity than the output current of the upper rectifier. In practice both current mirrors were again realized by regulated cascodes [110] because of their benefits described previously. The addition of the drain currents is done at the input node of the next stage - the current comparator - resulting in the output current $I_r = |I_{oA1}| - |I_{oA2}|$ as indicated in figure 6.7. As mentioned previously, although a considerable voltage drop of about 2V (maximum) is generated at the input node of each rectifier, the use of regulated cascode mirrors with long transistors in the variable-gain OTAs, ensures that I_{i1} and I_{i2} are not degraded by channel length modulation. The dimensions (W/L) of $M_{1,4}$ and of $M_{2,3}$ in figure 6.7 were 200/0.8 and 80/0.8 respectively.

6.2.3.2 Comparator and feedback OTA

The output currents from the two full-wave rectifiers are summed at the input of the current comparator circuit [107] shown in figure 6.8 to form current I_i. The comparator uses a CMOS inverter (M_3, M_4) to apply negative feedback around a class-B voltage buffer (M_1, M_2). As a result of the feedback, the comparator input has a low-impedance (in general) and is thus ideal for determining the polarity of I_i. On the other hand, the output of the inverter does not swing between the power supplies and so some static power dissipation is present. Fortunately, since in this application low-speed operation is required, the inverter transistors can be scaled to minimize power dissipation. The buffer transistors have zero DC power dissipation.

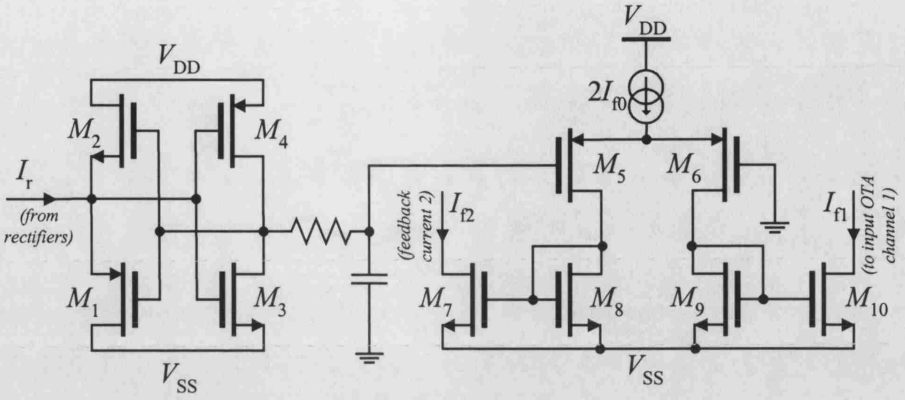

Figure 6.8 Comparator circuit, RC integrator and OTA providing feedback currents.

The stage ($M_5 - M_{10}$ in figure 6.8) after the external RC is a transconductance stage converting the integrator output voltage to the differential feedback currents I_{f1} and I_{f2}, which vary with mirror symmetry around I_{f0} (half of the transconductor's tail current) by I_{fx}. For a given imbalance the integrator will settle to a "virtually DC" voltage V_{fbIC}, given by the following (similar to eq. (4.2.16)):

$$V_{fbIC} = G_{m0} X_{imb} \tag{6.8}$$

This produces the following I_{fbx}:

$$I_{fx} = 0.5 G_{mA} G_{m0} X_{imb} \tag{6.9}$$

where G_{mA} is the transconductance of the feedback OTA and G_{m0} is the transconductance of the variable gain OTAs for $X_{imb} = 0$. The feedback currents are:

$$\begin{aligned} I_{f1} &= I_{f0} - I_{fx} \\ I_{f2} &= I_{f0} + I_{fx} \end{aligned} \tag{6.10}$$

The resulting transconductances of the variable gain stage are:

$$G_{m1,2} = G_{m0}(1 \mp X_{imb}) \tag{6.11}$$

The W/L ratio of $M_{1,4}$ in figure 6.8 was 5/2 and $M_{2,3}$ had a W/L of 2/2. The feedback OTA differential pair ($M_{5,6}$ in figure 6.8) W/L was 200/5.

6.2.4 Output-Stage Amplifier

The schematic of the output stage amplifier is shown in figure 6.9. The second output branch from each variable-gain OTA (figure 6.4(c)) is connected to resistor $R1$ (50kΩ) where the two composite currents I_{i1} and I_{i2} are summed-up to form I_i. Due to the corrective action of the control stage, the two EMG components in I_{i1} and I_{i2} are ideally of the same amplitude, and being anti-phase, when added are cancelled out. On the other hand, the ENG components in I_{i1} and I_{i2} are in-phase and thus a voltage is generated across R_1 when they are added. This voltage is further amplified by the subsequent amplification stage.

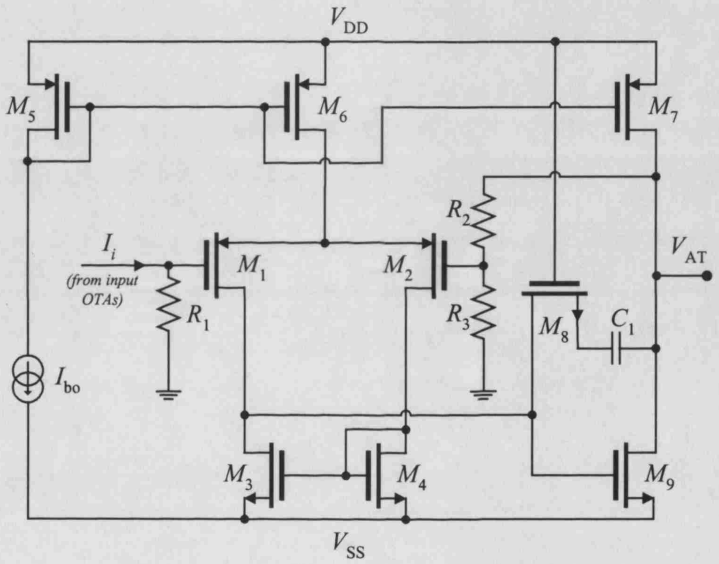

Figure 6.9 Output-stage amplifier circuit.

The amplifier ($M_{1\text{-}9}$) in figure 6.9 is a standard two-stage op-amp configured as a non-inverting amplifier through the feedback resistive network R_2 (90kΩ) and R_3 (10kΩ). The amplifier employs zero-pole compensation realized by the series combination of transistor $M8$ and capacitor $C1$ (3.5pF), and the circuit is biased by the DC current source I_{b6}. The simulated open-loop gain of the op-amp is 106dB, and the input-referred RMS noise current of the complete transimpedance stage is approximately 95pA (bandwidth of 1Hz – 10kHz).

6.3 Overview of the fabricated system

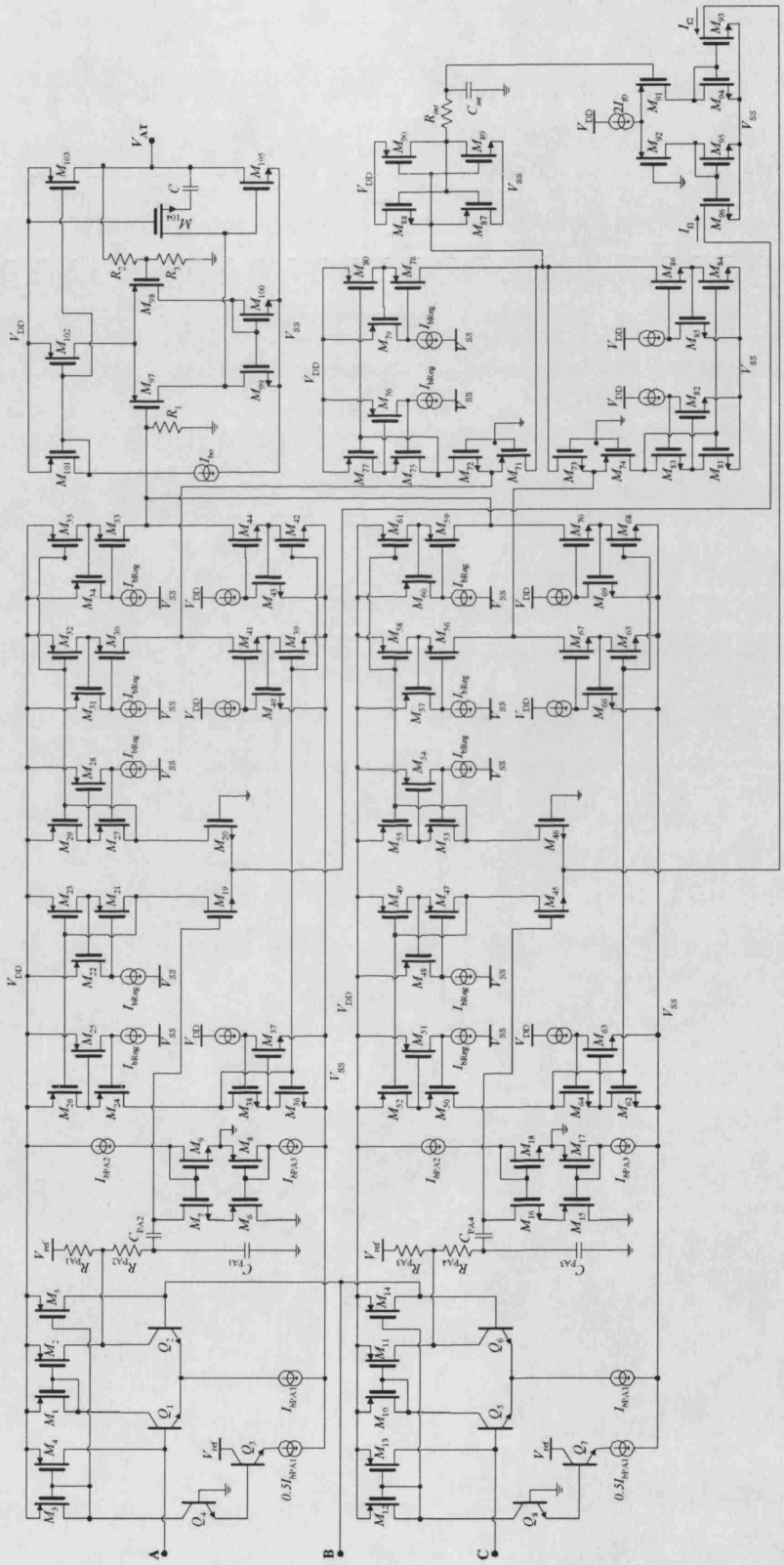

Figure 6.10 Overall circuit diagram (biasing circuitry and dummy transistors are also excluded for clarity). A, B and C are the connections to the cuff

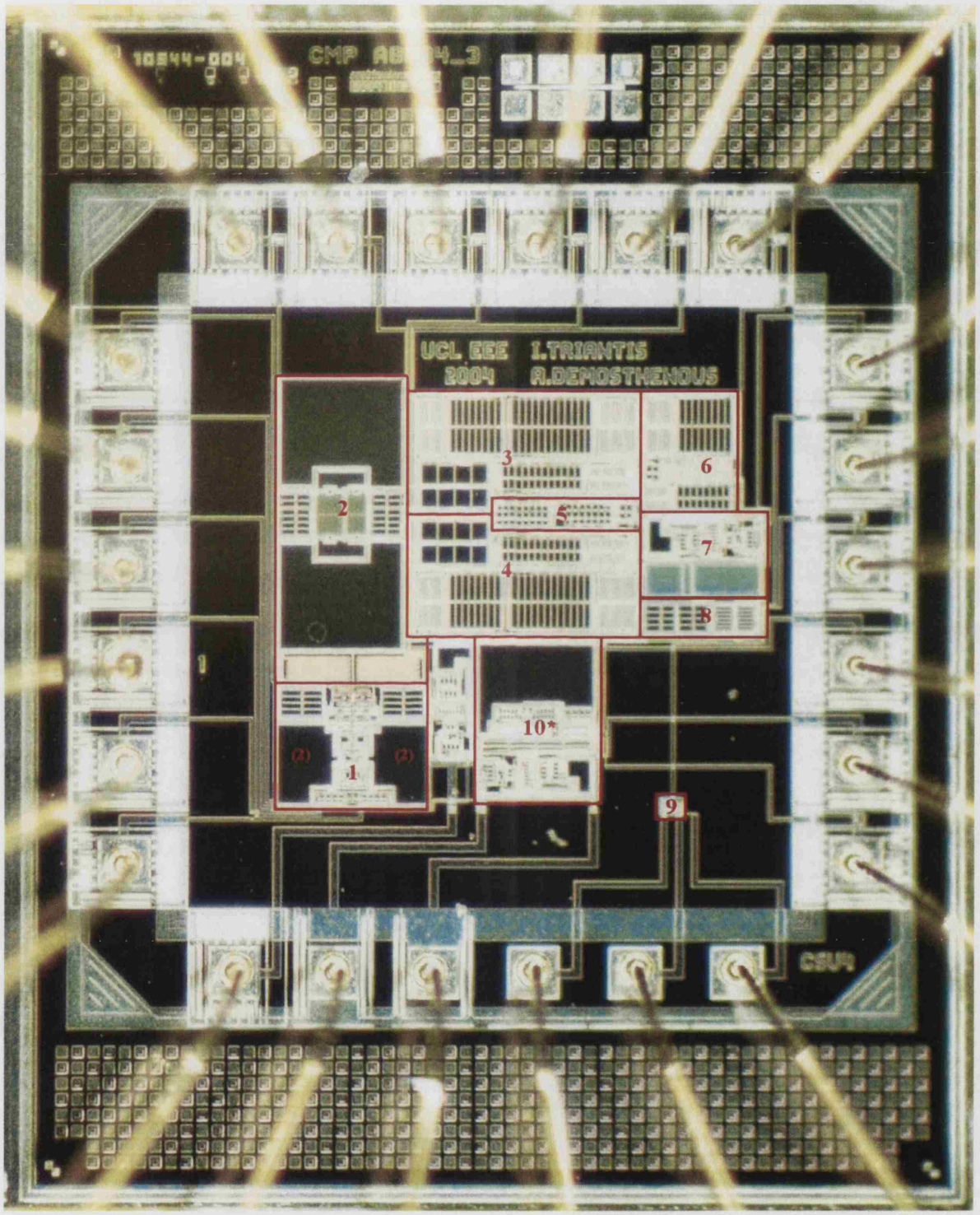

Figure 6.11 Chip microphotograph with main subcircuits numbered:
(1) Preamplifiers (2) BPF after preamplifiers (3) & (4) Variable-gain OTAs (5) Biasing (6) Rectifiers (7) AT output stage (8) Feedback OTA (9) Comparator (10*) Integrated integrator described later in section 6.5.

The overall circuit diagram is shown in figure 6.10 and the adaptive tripole chip, shown in figure 6.11, was fabricated in the AMS 0.8μm BiCMOS process [113] that includes a high resistive polysilicon layer. The substrates of all transistors were connected to their respective power supply rail (i.e., nMOS to V_{SS} and pMOS to V_{DD}), and the DC bias current sources in figure 6.10 were realized by an on-chip biasing circuitry (not described). As mentioned in section 6.2.1.1 common centroid-matching topology was used to provide good matching and almost all transistors were interdigitized. Redundant space was minimized making sure the AT occupied minimum area. In total 40 chips were fabricated, all showed correct operation.

6.4 Results

The input AC signals to the AT chip were provided by two audio transformers T_1 and T_2 (A262A7E) using the same setup that was described in chapter 5 (section 5.2, figure 5.2). Initially, the chips were tested with sinusoidal signals, with a signal of 100μV and 1kHz representing the ENG and a 50mV, 100Hz signal representing the EMG (values after preamplification). Subsequently, in order to model a more realistic test, EMG was replaced by an arbitrary signal (generated from band-limited Gaussian noise) with the frequency spectrum plotted in figure 6.12 (measured across cuff terminals AB in figure 2.12). The frequency content of this signal varied between 1 Hz and 3 kHz, with a peak at approximately 250 Hz, which is the case with naturally occurring EMG [24]. As in the tests described in chapter 5, the ENG signal was remained a sinusoid throughout the measurements to facilitate the evaluation of the output measurements. In figure 6.12, the ENG magnitude (-114dB cuff output magnitude) is totally covered by the spectrum of the random EMG. The time-domain data were monitored on an Agilent 54835A Infiniium™ oscilloscope, and the frequency-domain tests on a Stanford Research Systems SR760 FFT spectrum analyzer.

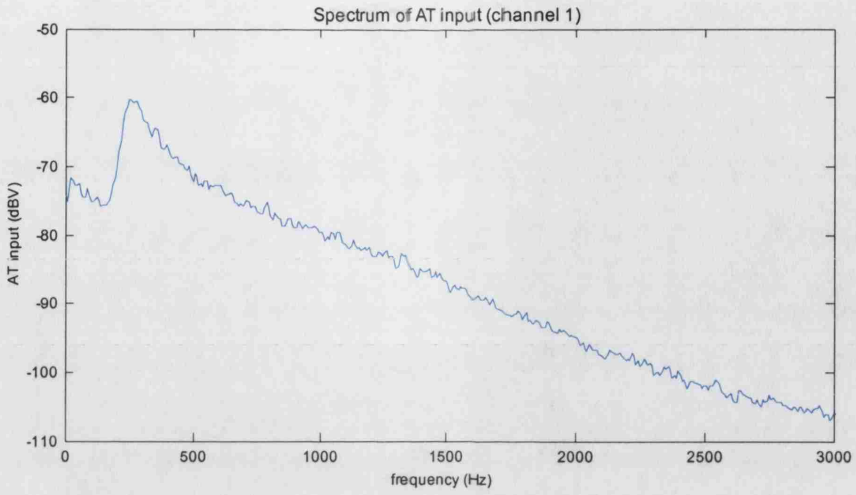

Figure 6.12 Frequency spectrum of the composite input signal. The spectrum of the band-limited white noise signal representing the electromyogram resembles that of naturally occurring EMG [14].

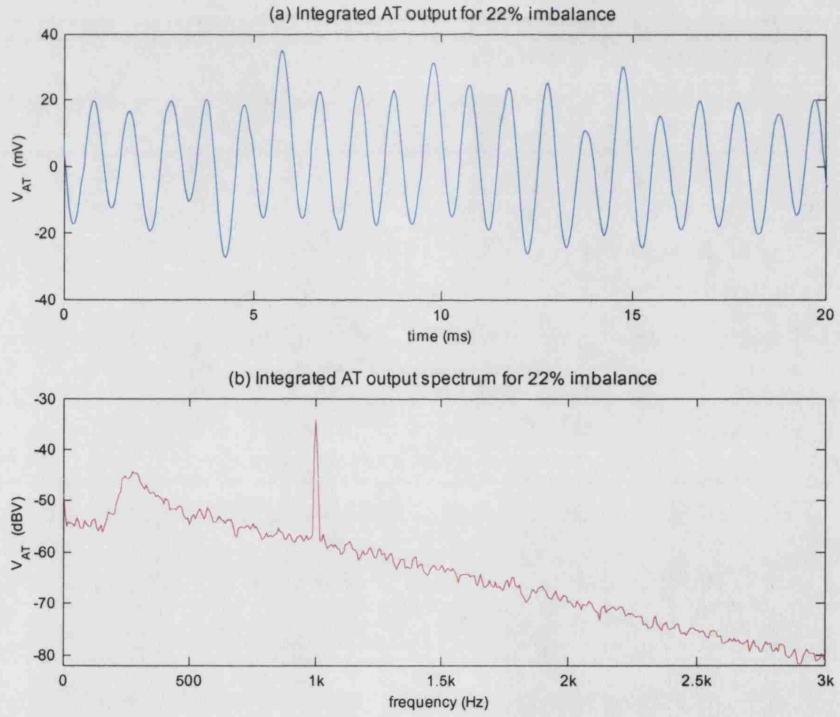

Figure 6.13 System output for 22% imbalance. (a) Oscillogram (b) Spectrum.

Figures 6.13 and 6.14 show the output transients and the spectra of the integrated AT (after settling) for 22% and 40% imbalance, respectively. The respective SIR_{out} values were 3.18 and 3.04, with higher residual interference causing the spectrum floor to rise slightly in the second case. In both cases the SIR was higher than 3 and this should be compared with a SIR_{in} of 1/500 (-54 dB). As the input EMG spectrum covered the ENG

peak, the output spectra highlight the advantage of the AT relative to any filtering technique because its operation is not frequency related.

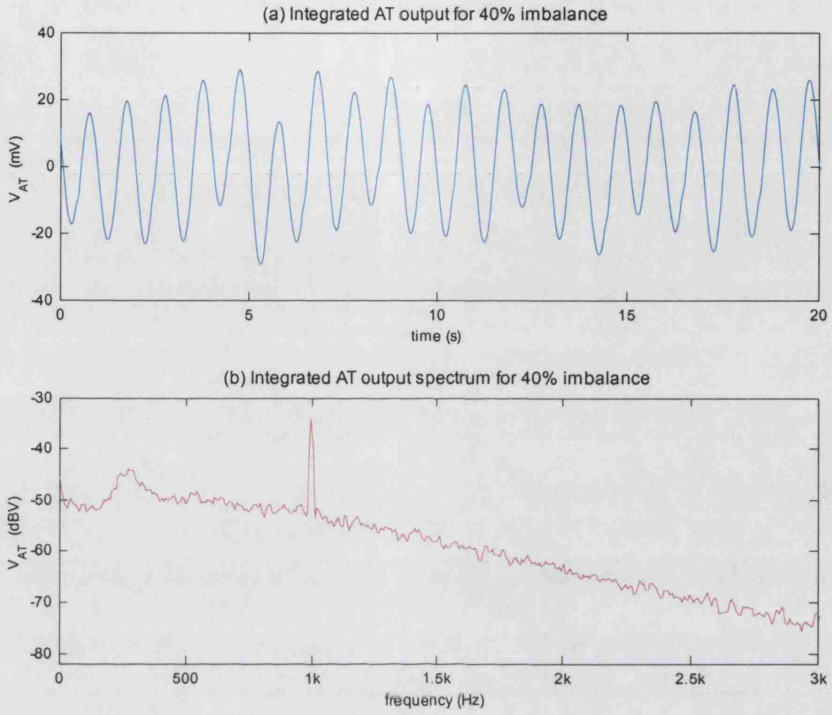

Figure 6.14 System output for 40% imbalance. (a) Oscillogram (b) Spectrum.

The average SIR_{out} for all 20 AT chips as a function of imbalance is plotted in figure 6.15(a), where it can be seen that even for extreme values of imbalance, the mean AT SIR_{out} is more than 2, while some individual chips reached values greater than 3 (as illustrated in figure 6.13 and 6.14). Imbalance variation was provided by a resistor ladder in place of R_{VAR} and the values used for the measurements of figure 6.15 were measured to be 4%, 16%, 22%, 34% and 40%. The mean output SIR varies from 2.38 ± 0.43 for 4% imbalance to 2.12 ± 0.72 for X_{imb} = 40%. The mean SIR_{out} values resulting from all 20 chips are marked in the figure, along with standard deviation error bars. The linear fit was performed with a 95% confidence interval [96] of ±0.14.

Figure 6.15(b) illustrates clearly the performance benefit achieved with integrating the AT based on its ability to reduce interference as imbalance varies. The mean improvement over all 20 chips relative to the discrete version is illustrated by the linear fit of the comparison ratios of mean SIR_{out} of the IC AT over the corresponding values of the discrete AT. The average improvement increases with imbalance from 2.07 for

4% imbalance to 3.62 for 40%. Hence, the integration of the system more than doubles the output SIR and it reduces the sensitivity of the AT to imbalance by reducing the mismatches between its two channels. The confidence interval of the fit was ±0.24.

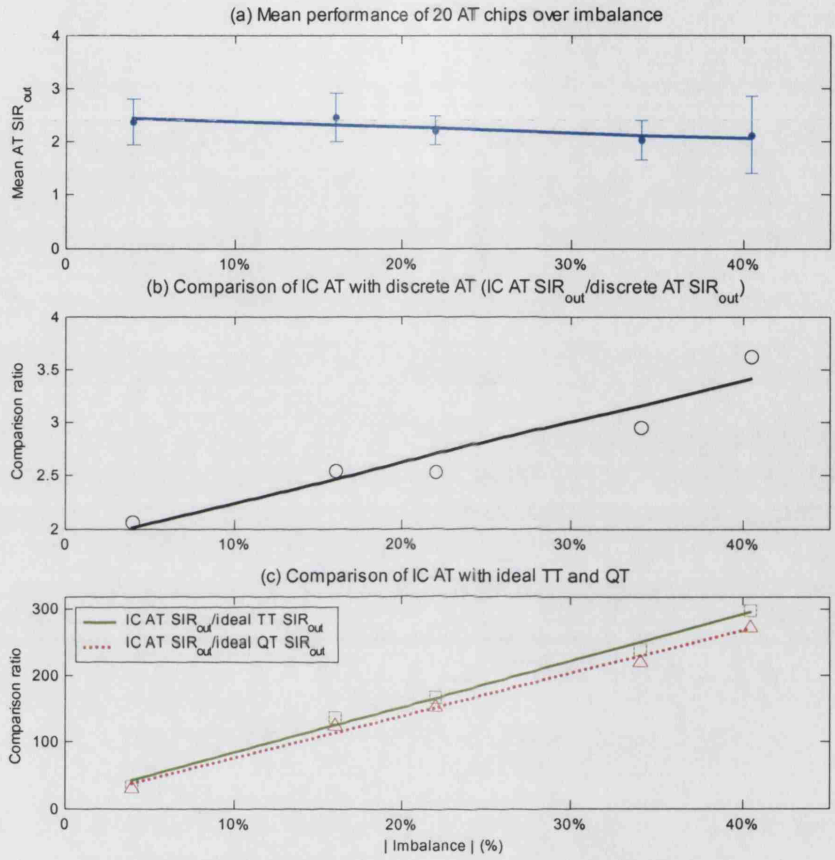

Figure 6.15 (a) Mean AT SIR_{out} versus (absolute) imbalance for all 20 chips. (b) Mean improvement of IC versus discrete-component AT, over all 20 chips (c) SIR_{out} improvement over the ideal TT and QT counterparts versus (absolute) imbalance.

Similarly, figure 6.15(c) illustrates comparison ratios of the IC version of the AT over the ideal TT and QT amplifier configurations as a function of imbalance. Ideal models were used to minimize the errors introduced to these systems in their discrete component versions, which have already been established to have poorer performance by the discrete AT. Thus, for the TT the input amplifiers were assumed to be matched, and for the QT the electrode impedance values listed in the footnote of figure 2.12 (chapter 2) were used. From the plot, it is apparent that the AT offers a very considerable improvement over both fixed-gain configurations in the presence of imbalance. For 4% imbalance the comparison ratios over the TT and the QT were 33.27

and 30.45 respectively, while for 40% imbalance the respective ratios were 299.07 and 273.72. The 95% confidence intervals of the fits were ±11.52 and ±12.29 respectively. Figure 6.16 shows the settling time of the integrator output controlling the feedback currents $I_{f1,2}(t)$ (tail currents of variable gain OTA stage) for abrupt step-like changes in imbalance. The imbalance was changed successively between +32.5%, -5.5%, -25% and -34%. The respective settling times for each transition were 111ms, 60ms and 27ms corresponding to about 3ms per percent change in X_{imb}.

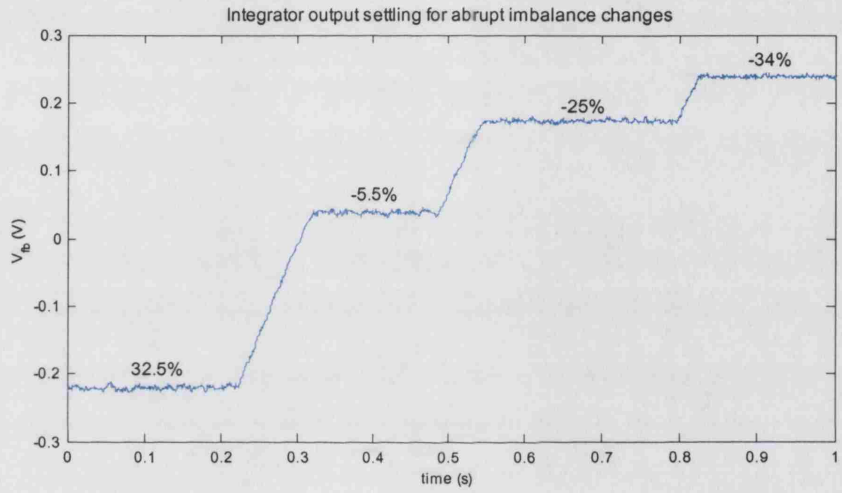

Figure 6.16 Settling time of integrator output for abrupt changes in imbalance.

Finally, in order to test the sensitivity of the AT architecture to phase variations, phase-shifts were introduced between the two input EMG terms to the system (the additional test structure chip was used for this test). Figure 6.17 shows the SIR_{out} as a function of phase-shift for both measured and theoretical cases, the latter calculated from (9) and for 40% imbalance. The two graphs show close agreement, until the theoretical SIR_{out} tends to infinity for phase values near the origin, something that would never be the case for a practical realization, due to system limitations (some of which are described in chapter 4). The main design features of the AT chip are summarized in table 6.1. As indicated, the power consumption measured was 5mW, lower than the power allocated for the AT in the overall CNM implant (chapter 1).

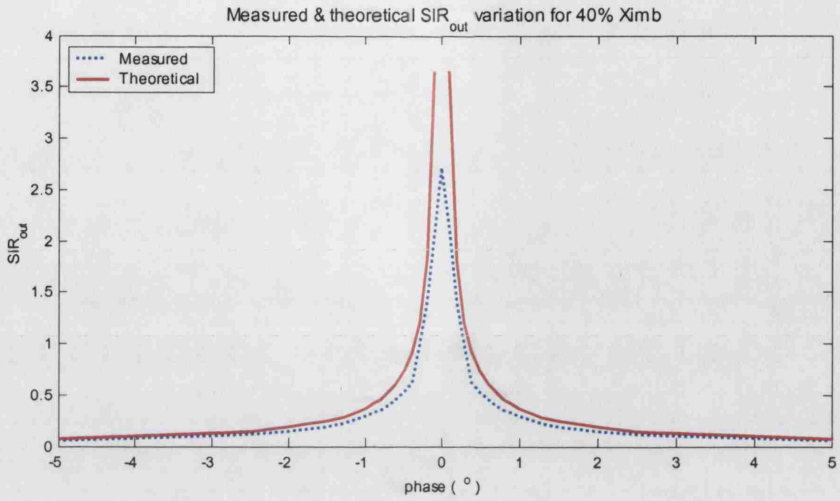

Figure 6.17 Sensitivity of AT SIR_{out} to phase-shifts.

Parameter	Value
Technology	0.8 μm BiCMOS
Power supply	± 2.5 V
Power consumption	5 mW
Active area (core)	0.68 mm^2
SIR_{out}	> 6dB
Imbalance correction range	> ± 40%
Total ENG path gain	87dB
Setting time (step-change)	3ms per % X_{imb}

Table 6.1 Summary of AT IC performance

6.5 Integrated large time- constant integrator

For the design of a very large time constant integrator, several possible approaches were considered. The most obvious approach employs an on-chip physical resistor and capacitor. However, this would require unrealistic chip area and would not be tuneable. Allowing for an adjustable time constant could prove useful if the system was to be used shortly after implantation when tissue growth is more rapid or if stimulation takes place making proximity imbalance more dominant. On the other hand, after the cuff conditions stabilize it could prove useful to increase the time constant to reduce the

ripple in the feedback path. In an OTA-C integrator the passive resistor is replaced with an OTA having very small transconductance (g_m). In practical realisations, and especially for very low bias currents, the output resistance r_o of the OTA-C integrator (figure 6.18) is significant, resulting in the transfer function:

$$A(s) = \frac{V_o(s)}{V_i(s)} = \frac{g_m/C}{s + 1/r_o C} \tag{6.12}$$

where s is the Laplace operator and the time constant equals to $\tau = r_o C$. The resulting *lossy* integrator can be used directly as a first order filter or as a building block in the realisation of higher order filters. Tuning the filter cut-off frequency is achieved by variation of τ. In conventional g_m-C filters, τ is usually controlled by g_m. This is achieved by applying *local* negative feedback around the integrator, where for a feedback factor β the transfer function is given by:

$$A(s) = \frac{g_m/C}{s + \frac{1}{r_o C} + \frac{\beta g_m}{C}} \tag{6.13}$$

so that τ becomes

$$\tau = \left(\frac{1}{r_o C} + \frac{\beta g_m}{C} \right)^{-1} \tag{6.14}$$

The design goal in that case is to make the second term in (6.14) dominant over the first term so that τ can be adjusted by choice of g_m and C, as required. It is necessary, therefore, that $\beta g_m >> 1/r_o$. However, when realising very large time constants, it is difficult to satisfy this condition, as r_o cannot be increased without limit and increasing β or g_m would *decrease* the effective time constant. Therefore it is proposed to operate the integrator *without* local feedback ($\beta = 0$) and to trim τ by variation of r_o instead of g_m.

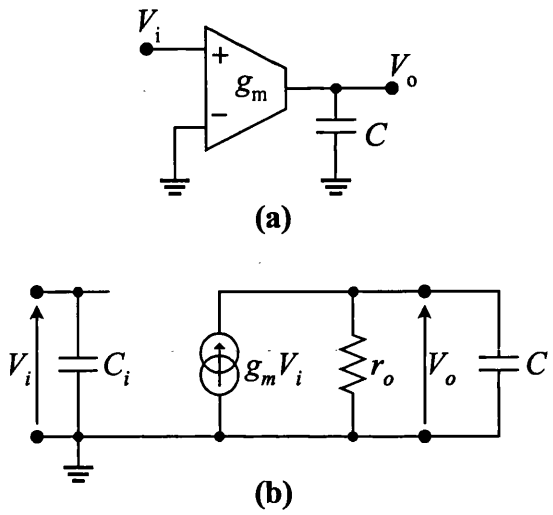

Figure 6.18 (a) g_m-C integrator. (b) small-signal model.

6.5.1 Integrator Design

Because of the nature of cuff imbalance variations as discussed in chapter 3 and in order to minimize distortion due to feedback ripple the integrator time-constant should be as large as possible (about 1s). The integrator schematic is shown in figure 6.19 and the circuit comprises three stages. The first stage consisting of the simple CMOS OTA ($M_1 - M_4$) terminated in resistor R_1 (2kΩ), is essentially an attenuator, whose output is limited to $\pm I_{bint1} \times R_1$ to correct any DC offsets introduced by the comparator. The second stage is the actual OTA-C integrator (operated in weak inversion), and this consists of a CMOS OTA ($M_5 - M_{11}$) utilizing transconductance cancellation [114], and an integrating capacitor C_1 (47.5pF) which is connected across the low and high impedance nodes x and y, respectively. The attenuation provided by the first stage ensures that the input voltage to the second stage OTA is within its linear range of operation. The second stage OTA is biased to achieve a transconductance G_{mc} of 6.9 nA/V given by $g_{m6,8} \times [(n-1)/(n+1)]$, where $g_{m6,8}$ is the small-signal transconductance of M_6 and M_8, and n is the ratio of the transconductance of M_6 to M_5 (or M_8 to M_7). Transistor M_{11} performs level-shifting of the output voltage for interfacing with the third stage.

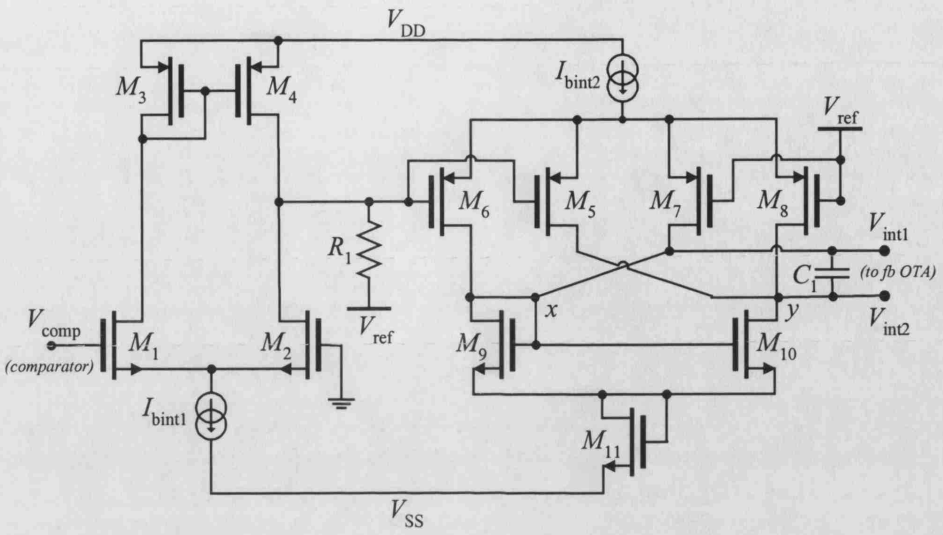

Figure 6.19 Large time-constant integrator circuit.

The output of the integrator can be connected differentially to the feedback OTA comprising by M_{73} to M_{78} in figure 6.10. The tail currents of the two integrator stages are provided by the DC current sources I_{bint1} and I_{bint2}. The OTA-C stage being *lossy* has the following transfer function

$$T(s) = \frac{G_{mc}}{s2C_1 + g_o} \tag{6.15}$$

where s is the Laplace operator, and g_o is the small-signal output conductance seen into node y. The integrator time-constant τ is $2C_1/g_o$ and g_o is set by I_{bint2}. Any possible DC offset voltages across nodes x and y resulting from transistor mismatches may be externally corrected by adjusting the DC voltage level of R_1 (e.g., by means of current injection). The simulated DC gain G_{mc}/g_o of the OTA-C stage was about 73.

6.5.2 IC Integrator Results

The input and integrated output signals for a sinusoid and a square wave are shown in figure 6.20(a) and (b) respectively. The plots are screen captures from the Agilent 54835A Infiniium™ oscilloscope. As expected the 1Hz sinusoid input produces a cosine output while the output of the integrator for a 1Hz square waveform is a triangular wave. In both cases the output does not drift. Both inputs had amplitude of 200mV pk and the time constant was 2.25s with $I_{bint2} = 1\mu A$.

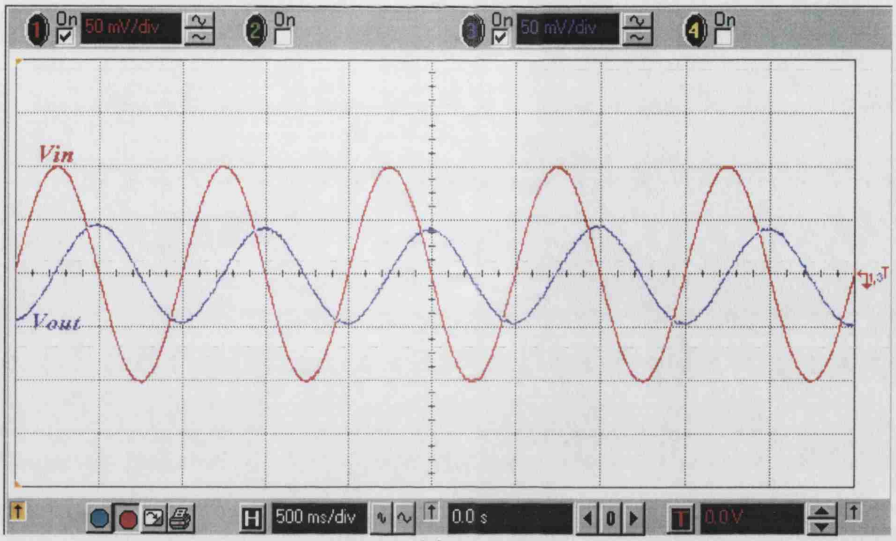

(a)

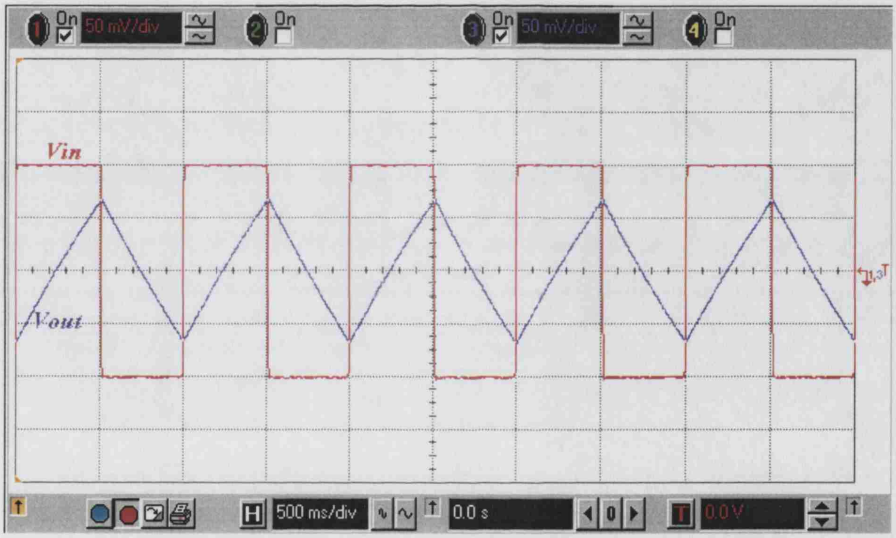

(b)

Figure 6.20 Oscilloscope screen capture of integrator input and output over 5s for (a) a sinusoid and (b) a square wave

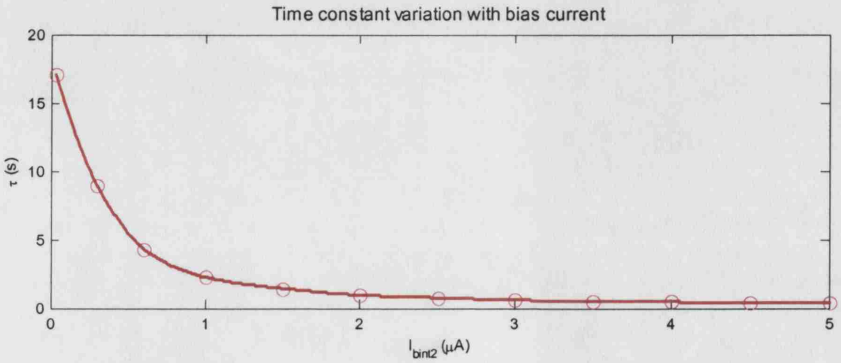

Figure 6.21 Time constant variation for a range of I_{bint2} values

Although the required time constant is around 1s it is useful to allow it to be adjustable, as discussed earlier. Varying I_{bint2} allows for such a variation, as it affects G_{mc}. Figure 6.21 illustrates the time constant variation provided by a range of I_{bint2} applied, with values as high as 17s achieved for 50nA.

The integrator can be used as a low pass filter and figure 6.22 illustrates its normalized gain characteristic for a frequency range from 0.01Hz up to 0.3Hz. The bias current was 2μA giving a time constant of 0.93s corresponding to a theoretical cut-off frequency of 0.17Hz. The measured cut-off frequency (-3dB point) was 0.175Hz.

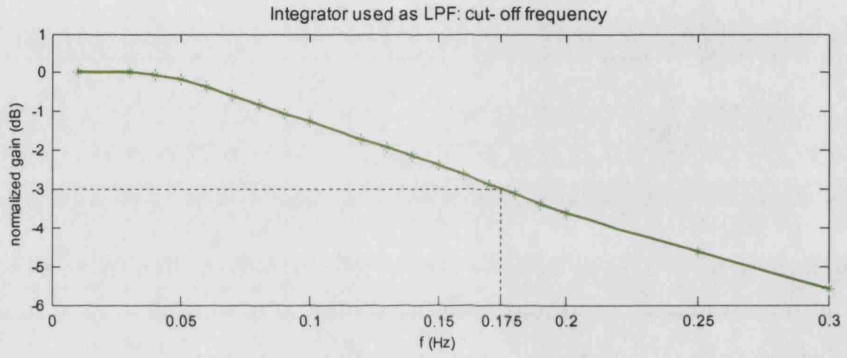

Figure 6.22 Low-pass filter characteristic: normalized gain versus frequency.

Figure 6.23 is a plot of the total harmonic distortion (THD) for a range of integrator input amplitudes (sinusoidal signal), as measured by the Stanford Research Systems SR760 FFT spectrum analyzer, for I_{bint2} = 2μA (time constant of 0.93s). The total harmonic distortion deteriorates (THD > 1%) around 250mV because the input OTA does not operate in the linear region.

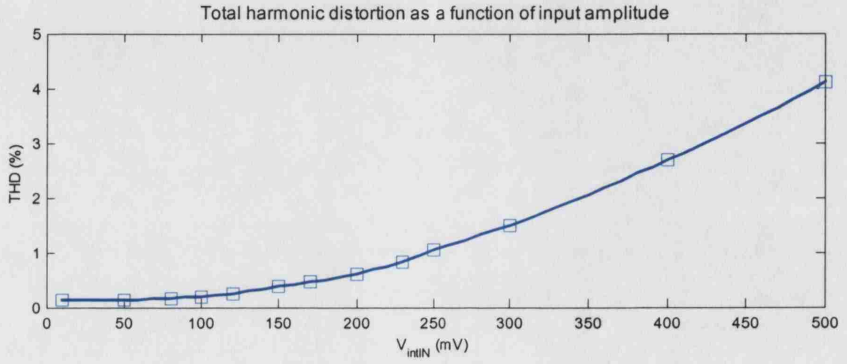

Figure 6.23 Total harmonic distortion (THD) for a range of input amplitudes.

Overall the long time constant integrator was successfully designed, built and tested and was found to be operating satisfactorily. However it was not attached to the AT, which had already been successfully tested in a fully implantable form, because of an inconsistency between the different integrator chips: Although the results presented here are representative of their operation, the DC bias voltage V_{ref} was not in practice the same between the two points it was applied (figure 6.19) and was, in fact, manually adjusted for each chip tested. Hence, if the integrator was attached to the rest of the AT it would require manual adjustment in a device that has to be self adjusted and ready-for-implantation. This is something to be addressed in the future.

6.6 Conclusion

The design of an integrated version of the AT for use in an implant has been described in this chapter. The integrated version offers a higher output signal-to-interference ratio than its discrete counterpart and at the same time it occupies much less space and consumes much less power, making it a fully implantable solution, thereby significantly advancing the state-of-the-art in the field. The described realization (2^{nd} IC AT version) overcomes many of the limitations of the first IC version of the AT designed during this project in terms of reliability, cuff imbalance correction range, output SIR and output signal distortion.

The bipolar front-end ensured low 1/f noise and base current cancellation was applied. The variable-gain stage was realised using variable tail current balanced OTAs, with regulated cascode mirrors for accurate mirroring and maximum output swing. The current rectifiers and the current comparator allowed the use of current mode design from the OTAs up to the second stage of the control part of the system. The long time constant integration was provided by external components, easily available on the implant.

The operation of the circuit has been thoroughly verified by tests on 20 fabricated chip samples, all working better than desired, with their average SIR_{out} being approximately 2 for a wide imbalance range, with some chips even achieving output SIR values over 3. The integrated system was shown to offer a very significant improvement relative to the

TT and the QT. Even though the fabricated AT was compared to their ideal models, thus assuming they did not suffer from additional operational deficiencies, it was found to offer up to 300 times greater output SIR for high imbalance values. Although the described adaptive ENG amplifier has been developed for a next generation bladder implant, it can also be seen as a generic high-performance ENG amplifier for any functional electrical stimulation application employing tripolar nerve cuff electrodes. The system is fully implantable as presented and tested, with minimum use of external components for the integration process, easily available on an implant. An integrated integrator has also been designed, built and separately tested and was found to work well and without drifting. However some degree of manual adjustment required meant it was not ready for the implantable version yet. Having completed an implantable, well functioning IC version of the AT, this part of the CNM implant is ready, operating well within the initial specifications.

Chapter 7

GENERAL CONCLUSION AND FUTURE WORK

7.1 General conclusion

This thesis described the work carried out for constructing an implantable neural amplifier whose output can be used for controlling a functional electrical stimulator. By completing the project successfully, one of the main parts of the CNM implant (see chapter 1) has been completed. By the time of writing this thesis, the other main parts are close to completion. The stimulator needs to overcome some minor operational problems and the signal transceiver, which handles data exchange with the external unit and provides the power supply, has been demonstrated in discrete form and is in the process of being integrated. The logic chip that will contain ADCs and basic logic (the main processing will be performed in the external unit) has yet to be constructed. In effect, this part is the first of the overall CNM project to be complete.

Summarising the key points of each chapter can assist in reviewing the main tasks carried out and the conclusions they led to. In the first chapter, the introduction offered some information on the aims and objectives of the project and the CNM implant was briefly described. The use of neural signals for feedback on FES was pointed out and

the problem of muscle interference in ENG recordings was mentioned. The novelty of the chapters to follow was highlighted.

A collection of the main background information in the literature, relevant to the project, was presented in the second chapter. The chapter served in pointing out the connection between neurophysiology, neural interfacing and neural amplifiers. It focused on cuff electrodes, because they can be chronically implanted without causing major damage to the nerve. The importance of cuff dimensions and proper closure was highlighted and its effect on the bioelectric signals was described. The most important property of the cuff is that it linearises the fields and the potential gradients of the signals inside it. In effect both the potential gradients of the muscle-generated EMG and the neural signal of interest, the ENG, are linear inside the cuff. The main characteristics of these signals were given and the problem of severe EMG interference was shown to be ideally solved when using specialised ENG amplifiers that take advantage of the cuff properties. The principle of operation of the QT and the TT amplifiers is based on the ideal model of the tripolar cuff, a cuff with three ring electrodes attached to its internal wall.

The failure of the existing tripolar cuff amplifiers to eliminate EMG contamination of the neural signal has been widely reported, however, the systematic errors in the cuff interface have not been investigated extensively. Assumptions were made, but in order to be able to proceed with a system that can compensate for the cuff limitations, these have to be defined. The third chapter offered a brief investigation into the factors contributing to the cuff imbalance, the effect that causes the two halves of the cuff to produce unequal EMG amplitudes. Although bioelectric fields were not considered to be within the scope of the thesis, some assumptions for the sources of cuff imbalance had to be investigated and field simulations in saline were performed. The tests were repeated and expanded in-vitro, using a saline bath and handmade cuffs, and the pattern of the results was found to be similar. These tests and additional experiments, performed in-vivo, assisted in identifying three main factors causing cuff imbalance: cuff asymmetry, tissue growth inside the cuff and variation in relative orientation and distance between the muscle and the cuff (termed "proximity" imbalance). The first one can be minimised with novel cuff fabrication techniques, the second is difficult to control but varies slowly with time and the third could be severe based on a dipole

model for the muscle, but has proved to be less dominant when real muscles were involved, because irrespective of their different positions and orientations, their signals appeared as one. The "proximity" component was still demonstrated to affect the muscle signal and the stimulus pulse differently.

The system developed during this project was designed to automatically compensate for cuff imbalance and in effect to minimise EMG interference. This feedback-controlled adjustable gain amplifier was an improvement of the TT and was termed the adaptive tripole (AT). It has evolved from a theoretical model mentioned previously as a possible future development. In the fourth chapter of this thesis, system-level mathematical analysis was performed to demonstrate its corrective action, to point out its main limitations and to define the specifications for its analogue realisation. Initially, with ideal system-level operation, the AT was shown to reduce cuff imbalance, eliminating interference and amplifying ENG when its output settled. Next, the main possible error sources of the system were examined, including phase error between the two channels, input and feedback DC offsets, and harmonic distortion caused by several parameters. The phase error can be harmful for any tripolar amplifier configuration as well as for multi-electrode cuff arrangements. Input offsets will also pose a risk of saturation for the QT and the TT but they are more severe for the AT as they obstruct its convergence. Harmonic distortion is caused by non-DC feedback, depending on the frequency content of the ripple. Some cases of that error can be addressed by making the comparator quick (frequency well outside the bandwidth of interest). A large integrator time constant (1s or more proposed here) will reduce feedback ripple for all harmonic distortion cases.

The discrete-component system described in the fifth chapter was the first realisation of the AT, moving the development from system-level theory to circuit-level practice. The design was based on the outcome of the previous chapter, although in the early stages of the development some errors were first observed experimentally and then investigated theoretically. After updating the design to compensate for the basic issues degrading performance, satisfactory operation was achieved. The overall in-vitro results were encouraging in terms of ENG detection, even for high imbalances and the AT was shown to be better than both the TT and the QT. The importance of the saline-bath testing performed here and previously in chapter three, lies with the fact that the EMG signals were not anymore generated specifically according to the cuff theoretical model,

but the cuff was allowed to perform its linearising effect on an external dipole. Using realistic signal amplitudes, the system's output SIR met the specification set initially for a greater imbalance range and a lower input SIR than initially planned. The AT was shown to be preferable than any filtering method as it allows complete bandwidth ENG recording even for full spectrum interference. The in-vivo experiments demonstrated the severity of proximity imbalance for the AT, by reducing its advantage towards the other configurations although it was still found to be better overall. Furthermore, severe proximity imbalance was observed between the M-wave and the stimulus artefact, while the AT is intended for naturally-occurring signals only. Overall, the maximum SIR_{out} of the AT was limited by additional errors in the discrete system, such as feedback amplifiers' gain or offset mismatch on top of mismatches between the discrete components. Most of the errors were minimised with inter-stage filters and manual trimming, solutions which could not be considered for the subsequent implantable version.

The sixth chapter described the transition from discrete electronics for testing to integrated microelectronics for implantation, completing the basic challenge of this project. Based on the observations and the assessment of the system in the previous chapter, a fully implantable version of the AT in BiCMOS technology was developed. An even higher output signal-to-interference ratio than previously was achieved by the integrated version demonstrating the importance of matching for this system. Very reduced area usage and much less power than a respective surface-mount discrete-component AT made this system very attractive for implantation. The first IC version of the AT designed showed poor performance, something that was addressed by the final realization (2^{nd} IC AT version), which overcame many of the limitations of in terms of reliability, cuff imbalance correction range, output SIR and output signal distortion. Moreover, the area and the power consumption were reduced. Reduction of 1/f noise was achieved by using bipolar input stage and the adaptive operation of the AT was achieved by balanced OTAs with variable tail currents. These were applied by a feedback OTA following the integrator which made use of external R and C components, readily available on the implant. Current mode was employed, for simplifying operations, covering the feedback, the output of the OTAs and the first two sub-stages of the control stage. All chips fabricated were found to work within or better than the specifications, with their average SIR_{out} being approximately 2 for a wide

imbalance range, with some chips even achieving output SIR values over 3. The integrated system was shown to offer a very significant improvement relative to the TT and the QT, even though it was compared to their ideal models, as it produced up to 300 times greater output SIR for high imbalance values. The system is fully implantable as presented and tested, with minimum use of external components for the integration process, easily available on an implant. An integrated integrator was also developed and was shown to work well, without output drifting. However biasing variation between chips did not allow this extra stage to be included in the system.

The completion of the AT is an important step towards the completion of the CNM implant. Moreover, the configuration can be used as a high-performance ENG amplifier in any closed-loop FES implant employing tripolar nerve cuff electrodes, significantly advancing the functionality of the field of chronic neural recording.

7.2 Future work

7.2.1 Possible system-level additions and adjustments

A future design could consider adjusting the design of the integrated integrator to employ local feedback to minimise sensitivity to component mismatches. General adjustments to the existing architecture of the integrated AT could include holding its feedback after output settling has occurred (a few months after implantation so that tissue growth would have stabilised). Then the control stage could be shut off for some period to save power and it could be turned on at regular intervals, to update the feedback settling value.

Although the aims of this project have been accomplished, sub-stage adjustments or additions could be made to the system architecture to further reduce the effects of system-level error sources, if this was considered necessary for some application. The drawback for most of these would be increased complexity (in addition to increased area and power consumption), as illustrated in figure 7.1. They are not necessary for the current project, since the system developed offers the desired operation with lower complexity. Some of these stages could be considered if multiple AT or even TT stages were to be used in parallel with a multi-electrode cuff (as proposed in [91]). In a multi-

electrode setup, some of the errors, especially the phase and the input offsets, would become much more dominant.

Making each preamplifier output and each variable-gain OTA input fully differential would minimise offsets introduced by the first stage. For better offset cancellation an additional differential input/output chopper amplifier (e.g. [115, 116]) could be employed before the OTAs or they could be replaced by chopper variable gain OTAs. Using such a stage before the preamplifiers would not compensate for offsets introduced by them. Moreover, the capacitors between any measuring or stimulating system and the cuff cannot be avoided, as they provide safety from DC currents in case of system failure. These solutions would remove the need for a high-pass filter after the preamplifiers, removing the phase shifts introduced by them.

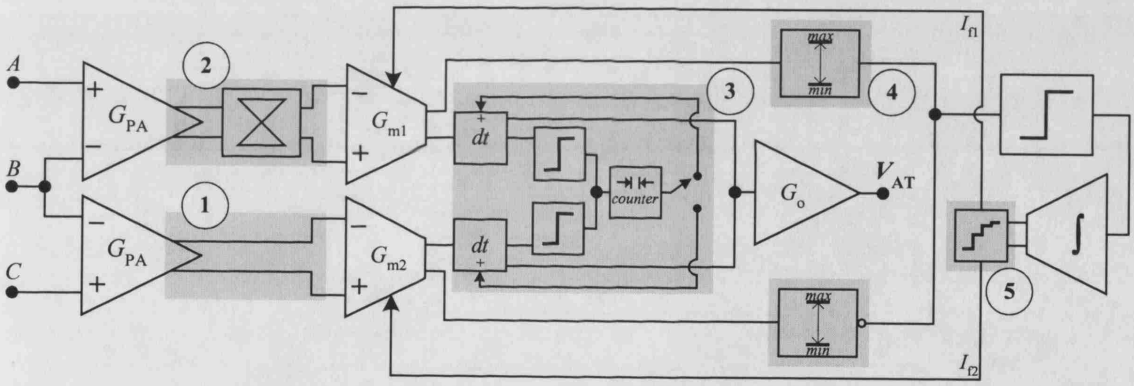

Figure 7. 1 Possible future adjustments to the AT architecture:
1) Differential preamplifier output and OTA input **2)** Chopper stage **3)** Channel synchronisation **4)** Peak-to-peak detection **5)** Feedback quantising

In the case that phase-shifts need to be further reduced, a channel synchronisation stage could be implemented, as shown in figure 7.1. The stage would only need to be applied in the signal path, as phase errors can be eliminated from the control stage using other methods. Instead of using a phase-locked-loop, the stage suggested would employ two analogue delay blocks with duplicate outputs, starting with zero delay. One output of the delay blocks would be connected to the output stage, while their second outputs would each be connected to a comparator (zero-crossing detector), resulting to square waves following the variation of the dominant signals (EMG components). Adding the resulting square waves would have the effect shown in figure 7.2, where a sinusoidal

analysis is presented. The counter operating in much higher frequency than the EMG would measure the pulse width of the summation and would add the delay to the leading channel, choosing it from the polarity of the summed comparator outputs.

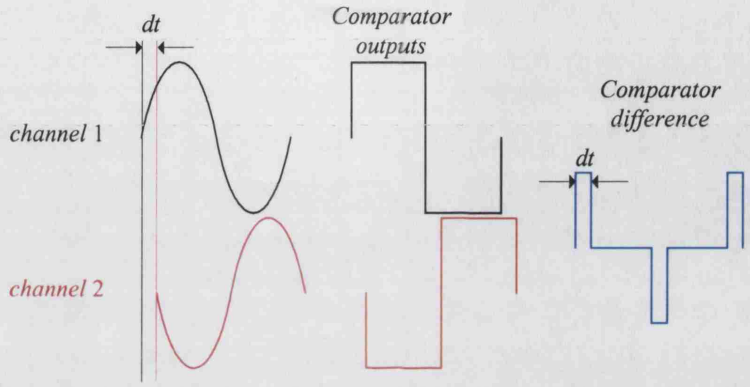

Figure 7. 2 Outputs of the "channel synchronisation" block.

A possible problem with this approach is that the delay between the EMG components is mainly a result of phase-shifts due high-pass filtering rather than fixed delay differences. Phase-shifts add frequency-related rather than fixed duration delays. The phase shifts analysed in chapter 4 will not have significant effects to the ENG, as it is much faster than the cut-off frequencies of the filters used. Therefore, if chopping stages are not used and inter-stage filters remain, the proposed solution could reduce the shifting between the EMG components, but would affect the synchronisation of the ENG components. An alternative would be to remove the delay blocks and just produce duplicate outputs of the signals going to the output stage. The comparators would be used again and their outputs summed. The resulting pulse width could be used to control the gate voltage of the active resistors used in the inter-stage high pass filters (chapter 6), possibly by replacing the counter with an integrator similar to the main feedback stage. Altering the resistances of the two channels with opposite variation would adjust the phase shifts until the EMG components had equal delays.

The next possible alteration would be to replace the rectifiers with peak-to-peak detectors. In this way, an envelope of the peak-peak amplitude of the signals would be obtained and DC offsets smaller than the peak EMG amplitude would not affect the control stage. This is described by the diagrams in figure 7.3. The peak-peak detector could be implemented by subtracting the outputs of two peak detectors (e.g. [117])

connected at the same channel, one with non-inverting and one with inverting input. Choosing the discharge time to be at least a few times larger than the main EMG frequency component would eliminate the effect of phase shifts to the feedback. Moreover, the problems of rectifier polarity change errors and ENG ripple in the feedback would be minimised. Most importantly for a range of DC offsets the convergence of the AT would not be affected, making the system less sensitive to such problems.

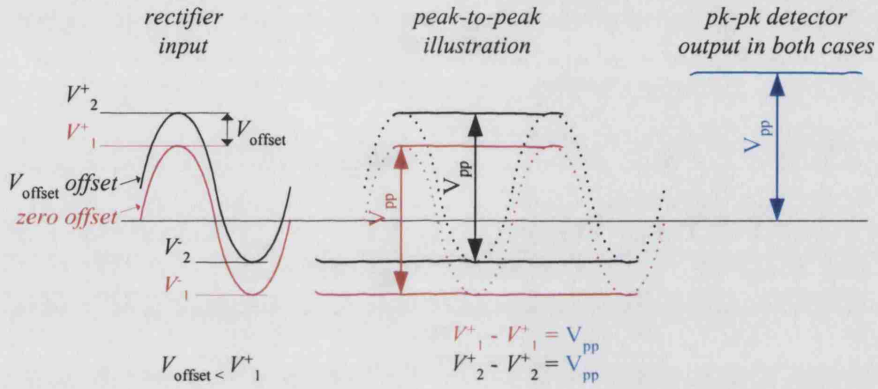

Figure 7. 3 Peak-to-peak detection demonstrated for a sinusoid, with and without offset.

Finally, the ripple on the feedback signals could be also removed by quantising the integrator outputs, with the drawback of reducing the feedback accuracy. If the ramping and settling feedback signals were replaced by staircase waveforms, harmonic distortion would be minimised. Choosing the resolution of the ADC used in such a stage to be smaller than the expected peak-to-peak ripple amplitude would cause the feedback to be slightly less accurate than plus or minus half that value. Thus the trade-off would be less feedback accuracy for reduced harmonic distortion.

7.2.2 Further research and possible applications

It is not possible to pursue all minor issues that arise within a PhD project and sometimes, especially when in-vivo experiments are involved, it can be difficult to have access to such specialised testing more than once. Issues of interest that may arise have to be highlighted so that other researchers can extend the knowledge.

Further research is needed for proximity imbalance and its effects on interference amplitude and imbalance. Some established studies could be re-examined or expanded in light of this new component. The reasons for the pattern of imbalance variation with orientation need to be investigated. Research focusing on fields could describe the condition using Maxwell equations. As a result, a parametric description of the cuffs function relative to the source position could be achieved by forming equations that would assist in improved neural interfacing. The fact that all active muscles during the in-vivo experiment appeared to have a common effect may have to do with the fact that in real conditions the muscle may be a moving dipole or a multi-pole [85]. Simulations could be expanded to include more realistic muscle models in a non-homogeneous medium.

The AT can be used with a "split-electrode" cuff [118, 119] (figure 7.4) placed around a nerve bundle, with each of the three electrodes segmented into smaller ones, to achieve selective recording of individual nerves or groups of nerves (fascicles) inside the bundle. The work in [118] reported an attempt to record selectively ("fascicle-selective" recording) using two QT amplifiers in two different connectivities, with a four segment split-electrode cuff as the one in figure 7.4. The conclusions indicated some selectivity, but the need for improvement was stated, noting that the cuff evens out local ENG amplitude variations between different sides of a nerve bundle cross-section.

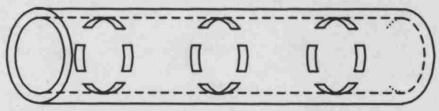

Figure 7.4 "Split-electrode" cuff (named "split multielectrode cuff electrode" in [118]) for fascicle-selective recording.

Increasing the number of electrode segments and connecting them to a front end multiplexer, operating in much higher frequencies than the bandwidth of interest, would allow a single AT to record measurements "scanning" the nerve bundle's circumference. Therefore, as the detection rotates around the bundle, the variation of the recorded signal amplitude could be combined with an algorithm that would pinpoint the active area of the nerve bundle cross-section. This type of "neural tomography" could be used to easily associate ENG measurements with the activity of particular organs or muscles. A drawback of the scheme would be the need for increased wiring.

Neural interfacing and neuroprostheses can be extended so that on top of offering partial rehabilitation after spinal cord injury, they will be used to re-establish the severed communication link with the brain. Used in conjunction with internal bioelectric measurements from the head or, less invasively, combined with brain or neck tomography, neural activity in areas of the brain or the spine of healthy subjects could be "mapped" through correlation with measurements and observations around the body. In the case of neck tomography, if the required resolution was achieved, pattern recognition of images offering reconstruction of electrical activity could be used to trigger an implant like the CNM. Locally, the implant would still perform its designated functions and an additional trigger signal coming from the detected spinal or brain activity could be introduced for controlling the stimulator.

References

[1] Ouzky, M., "Towards concerted efforts for treating and curing spinal cord injury", Social, Health and Family Affairs Committee, European Democratic Group Counsil of Europe Parliamentary Assembly, Doc. 9401, *available at*: http://assembly.coe.int/Documents/WorkingDocs/doc02/EDOC9401.htm

[2] NINDS, "Spinal Cord Injury: Emerging Concepts", USA National Institute of Neurological Disorders and Stroke (NINDS), *available at*: http://www.ninds.nih.gov/news_and_events/proceedings/sci_report_pr.htm

[3] Andreasen, L., "The Nerve Cuff Electrode and Cutaneous Sensory Feedback", *PhD dissertation, Dept. Center for Sensory-Motor Interaction*, Aalborg University, Aalborg, Denmark, 2002.

[4] IRME, "About IRME: To cure spinal cord injury", Institut pour la Recherche sur la Moelle Epiniere, *available at*: http://www.irme.org/ang/lesion.htm

[5] Bugbee, B. M., "An Implantable Stimulator for Selective Stimulation of Nerves", *PhD dissertation, Dept. Medical Physics and Bioengineering*, University College London, London, 2000. *p. 26-31.*

[6] http://eeewebb.ntu.edu.sg/bio/research/FES/FES.htm, "Restoration of Muscle Functions via Electrical Stimulation of Nerves", *available at*:
[7] Mortimer, J. T., "Tissue Response:Nerve: Huntington helical electrode", *available at*: http://www.cwru.edu/groups/ANCL/pages/05/05_33.htm 2005

[8] Malmivuo, J., and Plonsey, R., "Bioelectromagnetism: Principles and Applications of Bioelectric and Biomagnetic Fields ". Oxford University Press, 1995.

[9] Krajl, A., Bajd, T., Turk, R., and Benko, H. "Posture switching for prolonging functional electrical stimulation standing in paraplegic patients" *Paraplegia*, vol. 24, 221-230, 1986.

[10] Haugland, M., Lickel, A., Haase, J. and Sinkjaer, T. "Control of FES Thump Force Using Slip Information Obtained from the Cutaneous Electroneurogram in Quadriplegic Man" *IEEE Transactions on Rehabilitation Engineering*, vol. 7, 1999.

[11] Hansen, M., Haugland, M., Sinkjaer, T., and Donaldson, N. "Real Time Foot Drop Correction using Machine Learning and Natural Sensors" *Neuromod.*, vol. 5, 41-53, 2002.

[12] Sinkjaer, T., Haugland, M. K., and Haase, J. "Natural neural sensing and artificial muscle control in man" *Exp. Brain Res.*, vol. 98, 542-545, 1994.

[13] Crago, P. E., Chizeck, H.J., Neuman, M.R., and Hambrecht, F.T. "Sensors for use with functional neuromuscular stimulation" *IEEE Trans. Biomed. Eng.*, vol. 33, 256-268, 1986.

[14] Haugland, K., and Sinkjaer, T. "Cutaneous whole nerve recordings used for correction of footdrop in hemiplegic man" *IEEE Trans. Rehab. Eng.*, vol. 3, 307-317, 1995.

[15] Jezernik, S., and Sinkjaer, T. "Detecting Sudden Bladder Pressure Increases from the Pelvic Nerve Afferent Activity" *Proc. 20th Int. Conf. IEEE Eng. in Medicine and Biology Soc.*, vol. 20, 1998.

[16] Andreasen, L. N. S., and Struijk, J.J. "Skin Contact Forces Extracted from Human Nerve Signals - A Possible Feedback Signal for FES-Aided Control of Standing" *IEEE Trans. Biomed. Eng.*, vol. 50, 1320-1325, 2003.

[17] Haugland, K. M., "Natural Sensory Feedback for Closed-loop Control of Paralysed Muscles", *PhD dissertation, Dept. Medical Informatics and Image Analysis*, Aalborg University, 1994. *p. 5-6.*

[18] Popovic, D. B., Stein, R.B., Jonanovic, K.L., Rongching, D., Kostov, A., and Armstrong, W. W. "Sensory nerve recording for closed-loop control to restore motor functions" *IEEE Trans. Biomedical. Eng.*, vol. 40, 1024-1031, 1993.

[19] Haugland, M. K., Hoffer, J.A., and Sinkjaer, T. "Skin contact force information in sensory nerve signals recorded by implanted cuff electrodes" *IEEE Trans. Rehab. Eng.*, vol. 2, 18-28, 1994.

[20] Hoffer, J. "Techniques to study spinal-cord, peripheral nerve, and muscle activity in freely moving animals" *Neuromethods*, vol. 65-115, 1990.

[21] Stein, R. B., Charles, D., Davis, L., Jhamanda, J., Mannard, A., and Nichols, T. R. "Principles underlying new methods for chronic neural recording" *Le Journal Canadien des Sciences Neurologiques*, vol. 2, 235-244, 1975.

[22] Struijk, J. J., Thomsen, M., Larsen, J. O. and Sinkjaer, T. "Cuff electrodes for long-term recording of natural sensory information" *IEEE Eng. Med. Biol.*, vol. 18, 91-98, 1999.

[23] Andreasen, L. N. S., Struijk, J. J., and Lawrence, S. "Measurement of the Nerve Cuff Electrodes for Recording" *Medical & Biological Engineering & Computing*, vol. 38, 2000.

[24] Nicolic, Z. M., Popovic, B.D., Stein, B., R., and Kenwell, Z. "Instrumentation for ENG and EMG Recordings in FES Systems" *IEEE Trans. Biomed. Eng.*, vol. 41, 703-706, 1994.

[25] Andreasen, L. N. S., Struijk, J. J., and Lawrence, S. "Measurement of the Performance of Nerve Cuff Electrodes for Recording" *Medical & Biological Engineering & Computing*, vol. 38, 447-453, 2000.

[26] Haugland, K. M., and Hoffer, A. J. "Artifact-Free Sensory Nerve Signals Obtained from Cuff Electrodes During Functional Electrical Stimulation of Nearby Muscles" *IEEE Transactions on Rehabilitation Engineering*, vol. 2, 1994.

[27] Struijk, J. J., and Thomsen, M. "Tripolar Nerve Cuff Recording: Stimulus Artifact, EMG, and the Recorded Nerve Signal" *IEEE - EMBS 17th Ann. Int. Conf.*, Montreal, 1995.

[28] Pflaum, C., Riso, R. R. and Wiesspeiner, G. "Performance of Alternative Amplifier Configurations for Tripolar Nerve Cuff Recorded ENG" *18th Annual International Conference of the IEEE Engineering in Medicine and Biology Society*, Amsterdam, 1996, IEEE.

[29] Rahal, M. S., Winter, J., Taylor, J., and Donaldson, N. "An Improved Configuration for the Reduction of EMG in Electrode Cuff Recordings: A Theoretical Approach" *IEEE Transactions on Biomedical Engineering*, vol. 47, 2000.

[30] Upshaw, B., and Sinkjaer, T. "Digital signal processing algorithms for the detection of afferent nerve activity recorded from cuff electrodes" *IEEE Trans. Rehab. Eng.*, vol. 6, 1998.

[31] Andreasen, L. N. S., and Struijk, J. J. "Artefact reduction with alternative cuff configurations" *IEEE Trans. Biomed. Eng.*, vol. 50, 1160-1166, 2003.

[32] Demosthenous, A., and Triantis, I. F. "An adaptive ENG amplifier for tripolar cuff electrodes" *IEEE J. Solid-State Circuits*, vol. 40, 412-421, 2005.

[33] Triantis, I. F., Demosthenous A., Donaldson N., and Struijk J. J. "Experimental Assesment of Imbalance Conditions in a Tripolar Cuff for ENG Recordings" *1st Int IEEE EMBS Conf Neural Engineering*, pp. 380 -383, Capri, Italy, 2003.

[34] Rahal, M. S., "Optimisation of Nerve Cuff Electrode Recordings for Functional Electrical Stimulation Applications", *PhD dissertation, Dept. Electronic and Electrical Eng.*, University College London, London, UK, 2000.

[35] Triantis, I. F., Demosthenous A., and Donaldson N. "Comparison of Three ENG Tripolar Cuff Recording Configurations" *1st Int IEEE EMBS Conf Neural Engineering*, pp. 364 -367, Capri, Italy, 2003.

[36] Tesfayesus, W., Yoo, P., and Durand, D.M. "Blind source separation of nerve cuff recordings" *Proc.- 25th Int. Conf. IEEE/EMBS*, vol. 3, pp. 2507 - 2510, 17-21 Sep., 2003.

[37] Triantis, I., Rieger, R., Taylor, J., Demosthenous, A., and Donaldson N. "A CMOS Adaptive Interference Reduction System for Nerve Cuff Recordings" *Proc. 28th European Solid-State Circuits Conf. (ESSCIRC'02)*, pp. 113-116, Florence, Italy, 2002.

[38] Triantis, I. F., Rieger R., Taylor J., and Donaldson N. "Adaptive Interference Reduction in Nerve Cuff Electrode Recordings" *ICECS*, vol. 2, pp. 669 -672, Malta, 2001.

[39] Jones, T., "Introduction to the Nervous System", The University of Texas at Austin, *available at*: http://homepage.psy.utexas.edu/homepage/class/Psy308/Jones/notes_html/lecture2_html/lecture2.html

[40] Mirescu, D., and Mathieu, P.A. "EMG Mapping -Estimating Dipole Locations by Legendre Polynomial Derivatives" *1st BMES/EMBS Conf.*, pp. 580, Atlanta, USA, 1999.

[41] McNeal, D. R. "Analysis of a Model for Excitation of Myelinated Nerve" *Trensactions on Biomedical Eng.*, vol. BME-23, 1976.

[42] Plonsey, R., and Barr, R.C., "Bioelectricity: A Quantitative Approach". *2nd ed.* Kluwer Academic / Plenum Publishers, New York, 2000.

[43] Webster, J. G., "Medical Instrumentation Application and Design". *2nd ed.* Houghton Mifflin Company, Boston, 1989.

[44] Geddes, L. A., Baker, L. E., "Principles of Applied Biomedical Instrumentation". *3rd ed.* John Wiley & Sons, 1989.

[45] Hogkin, A. L., and Huxley, A. F. "A quantitative description of membrane current and its application to conduction and excitation in nerve" *J. Physiol.*, vol. 117, 500-544, 1952.

[46] Tasaki, I. "On the Cable Theory of Nerve Conduction" *Bulletin of Mathematical Biology*, vol. 64, 1069-1082, 2002.

[47] Stotts, L. J., "Introduction to Implantable Biomedical IC Design", in *IEEE Ciruits and Devices Magazine*, 1989. p. 12-18.

[48] Hoffer, J. A., Marks, W. B., and Rymer, W.Z. "Nerve fiber activity during normal movements" *Soc. Neurosci. Abstr.*, vol. 4, 300, 1974.

[49] Stein, R. B., and Pearson, K. G. "Predicted amplitude and form of action potentials recorded from unmyelinated nerve fibres" *J. Theor. Biol.*, vol. 32, 539-558, 1971.

[50] Rodriguez, F. J., Ceballos, D., Schuttler, M., Valero, A., Valderrama, E., Stieglitz, T., and Navarro, X. "Polyimide cuff electrodes for peripheral nerve stimulation" *Journal of Neuroscience Methods*, vol. 98, 105-118, 2000.

[51] Julien, C., and Rossignol, S. "Electroneurographic recordings with polymer cuff electrodes in paralyzed cats" *J. Neurosc. Meth.*, vol. 5, 267-272, 1982.

[52] Naples, G. G., Mortimer, J.T., Scheiner, A., and Sweeney, J.D. "A spiral nerve cuff electrode for peripheral nerve stimulation" *IEEE Trans. Biomed. Eng.*, vol. 35, 905-916, 1988.

[53] Kallesoe, K., Hoffer, J.A., and Strange, K. "Implantable cuff having improved closure" *U.S. patent # 5,487,756,* 1996.

[54] Andreasen, L., and Struijk, J. "On the Importance of Configuration and Closure of Nerve Cuff Electrodes for Recording" *Proccedings of the 20th Annual International Conference of the IEEE Engineering in Medicine and Biology Society*, vol. 20, 1998.

[55] Larsen, J. O., Thomsen, M., Haugland, M., and Sinkjaer, T. "Degeneration and regeneration in rabbit peripheral nerve with long-term nerve cuff electrode implant: A stereological study of myelinated and unmyelinated axons" *Acta Neuropathologica*, vol. 96, 365–378, 1998.

[56] Hoffer, J. A. "Techniques to study spinal-cord, peripheral nerve, and muscle activity in freely moving animals" *Neurometh.*, vol. 15, 65-145, 1990.

[57] Struijk, J. J. "The extracellular potential of a myelinated nerve fiber in an unbounded medium and in nerve cuff models" *Biophys. J.*, vol. 72, 2457-2469, 1997.

[58] Stein, R. B., Nichols, T. R., Jhamanda, J., Davis, L., and Charles, D. "Stable long-term recordings from cat peripheral nerves" *Brain Res.*, vol. 28, 21-38, 1977.

[59] Hoffer, J. A., Loeb, G.E., and Pratt, C.A. "Single unit conduction velocities from averaged nerve cuff electrode records in freely moving cats" *J. Neurosc. Meth.*, vol. 4, 211-225, 1981.

[60] Stein, R. B., Gordon, T., Oguztoreli, Lee, R.G. "Classifying sensory patterns and their effects on locomotion and tremor" *Can. J. Physiol. Pharmacol.*, vol. 59, 645-655, 1981.

[61] Sahin, M., Haxhiu, M.A., Durand, M. D., and Dreshaj, I.A. "Spiral nerve cuff electrode for recording of respiratory output" *J. Appl. Physiol.*, vol. 83, 317, 1997.

[62] Davis, L. A., Gordon, T., Hoffer, J.A., Jahmandas, J., and Stein, R.B. "Compound action potentials recorded from mammalian peripheral nerves following ligation or resuturing" *J. Physiol.*, vol. 285, 543-559, 1978.

[63] Gordon, T., Hoffer, J.A., Jhamandas, J., and Stein, R.B. "Long-term effects of axotomy on neural activity during cat locomotion" *J. Physiol.*, vol. 303, 243-263, 1980.

[64] Haugland, M. K., Hoffer, J.A., and Sinkjaer, T. "Slip information provided by nerve cuff signals: Application in closed-loop control of functional electrical stimulation" *IEEE Trans. Rehab. Eng.*, vol. 2, 29-36, 1994.

[65] Hoffer, J. A., and Sinkjaer, T. "A natural "force sensor" suitable for closed-loop control of functional neuromuscular stimulation" *Proc. 2nd Vienna Int. Workshop on Functional Electrostimulation*, pp. 47-50, 1986.

[66] Haugland, M. K., Lickel, A., Haase, J. and Sinkjaer, T. "Hand neuroprosthesis controlled by natural sensors" *IEEE Trans. Rehab. Eng.*, vol.

[67] Sinkjaer, T., Haugland, M. K., and Haase, J. "Neural cuff electrode recordings as a replacement of lost sensory feedback in paraplegic patients" *Neurobionics*, vol. 1, 267-277, 1993.

[68] Marks, W. B., and Loeb, G.E. "Action currents, internodal potentials, and extracellular records of myelinated mammalian nerve fibers derived from node potentials" *Biophys. J.*, vol. 16, 655-668, 1976.

[69] Andreasen, L. N. S., and Struijk, J. J. "Signal Strength Versus Cuff Length in Nerve Cuff Electrode Recordings" *IEEE Trans. Biomed. Eng.*, vol. 49, 1045-1050, 2002.

[70] Andreasen, L., Struijk, J. and Haugland, M. "An Artificial Nerve Fiber for Evaluation of Nerve Cuff Electrodes" *19th International Conference-IEEE/EMBS*, Chicago, IL. USA, 1997, IEEE.

[71] Struijk, J. J. "On the Spectrum of Nerve Cuff Recordings" *Proc.-19th Int. Conf. IEEE/EMBS*, Chicago, USA, Oct. 30-Nov. 2, 1997.

[72] Upshaw, B. M., "Real-time digital processing algorithms and systems for the application of human sensory nerve signals in neuroprostheses`", *PhD dissertation, Dept. Center for Sensory-Motor Interaction*, Aalborg University, Aalborg, 1999.

[73] Ruegg, D. G., Nussbaumer, R., and Studer, L.M. "Simulation of the surface EMG of an active muscle" *Biomed Tech (Berl)*, vol. 43, 105-109, 1998.

[74] Nelson, M. E., "http://nelson.beckman.uiuc.edu/electrolocation.html".

[75] Rahal, M. S., Taylor, J., and Donaldson, N. "The Effect of Nerve Cuff Geometry on Interference Reduction" *IEEE trans. Biomed. Eng.*, vol. 47, pp. 136-138, 2000.

[76] Stein, R. B., Charles, D., Gordon, T., Hoffer, J.A., and Jhamandas, J. "Impedance properties of metal electrodes for chronic recording from mammalian nerves" *IEEE Trans. Biomed. Eng.*, vol. 25, 532-536, 1978.

[77] Donaldson, N. d. N., Zhou, L., Perkins, T.A., Munih, M., Haugland, M. & Sinkjaer, T. "Implantable telemeter for long term electroneurographic recordings in animals and man" *Med. & Biol. Eng. & Comput.*, vol. 41, 2003.

[78] Sahin, M., and Durand, M. D. "An Interface for Nerve Recording and Stimulation with Cuff Electrodes" *Proc. 19th int. conf. IEEE/EMBS*, pp. 2004-2005, Chicago, USA, 1997.

[79] Rieger, R., Taylor, J., Demosthenous, A., Donaldson, N., and Langlois, P. "Design of a low noise preamplifier for nerve cuff electrode recording" *IEEE J. Solid State Circ.*, vol. 38, 1373-9, 2003.

[80] Thomsen, M., "Characterisation and optimisation of whole nerve cuff recording electrodes", *PhD dissertation, Dept.*, Aalborg University, Denmark, 1998.

[81] Rahal, M. S., Taylor, J., and Donaldson, N. "The Effect of Nerve Cuff Geometry on Interference Reduction: a study by computer modelling" *IEEE trans. Biomed. Eng.*, vol. 47, 136-138, 2000.

[82] Gootzen, T. H. J. M., Stegeman, D.F., and Heringa, A. "On numerical problems in analytical calculations of extracellular fields in bounded cylindrical volume conductors" *J. App. Phys.*, vol. 66, 4504-4508, 1989.

[83] Schnabel, V., and Struijk, J.J. "Evaluation of the Cable Model for Electrical Stimulation of Unmyelinated Nerve Fibers" *IEEE Trans. Biomed. Eng.*, vol. 48, 1027-1033, 2001.

[84] Schnabel, V., and Struijk, J.J. "Calculation of Electric Fields in a Multiple Cylindrical Volume Conductor Induced by Magnetic Coils" *IEEE Trans. Biomed. Eng.*, vol. 48, 78-86, 2001.

[85] Anctil, B., and Slawnych, M.P. "An Efficient Method for Modeling EMG Potentials as Recorded Using Surface Electrodes" *Proc. 20th Int. IEEE EMBS*, vol. 5, pp. 2613 - 2615, Hong Kong, China, 1998.

[86] Triantis, I. F., Donaldson, N., and Demosthenous, A. "Saline-bath testing of a system for removing artifact from ENG signals" *FESnet '02 (http://fesnet.eng.gla.ac.uk/conference/prog.html)*, Glasgow, UK, 2002.

[87] Triantis, I. F., Demosthenous, A., and Donaldson, N. "An ENG Amplifier for EMG Cancellation and Cuff Imbalance Removal" *EPSRC PREP '03*, pp. 105-106, Exeter, England, 2003.

[88] Geddes, L. A., and Baker, L. E. "The specific resistance of biological material - A compendium of data for the biomedical engineer and physiologist" *Med. & Biol. Eng.*, vol. 5, 271-293, 1967.

[89] Sahin, M., and Durand M. D. "Improved Nerve Cuff Electrode Recordings with Subthreshold Anodic Currents" *IEEE Trans. BME*, vol. 45, 1044-50, 1998.

[90] Upshaw, B. "SVD and higher-order statistics applied in the detection of human nerve signal activity" *IEEE DSP Workshop Proc.*, pp. 319-322, Loen, Norway, June 1998, 1996.

[91] Rieger, R., Taylor, J., Comi, E., Donaldson, N., Russold, M., Mahoney, C.M.O., McLaughlin, J.A., McAdams, E., Demosthenous, A., and Jarvis, J.C. " Experimental determination of compound A-P direction and propagation velocity from multi-electrode nerve cuffs" *IEE Medical & Biological Engineering & Computing*, vol. 2003 *(submitted)*.

[92] De Lima, J. A., and Cordeiro, A. S. "A Low-Cost Neurostimulator With Accurate Pulsed-Current Control" *IEEE Trans. Biomed. Eng.*, vol. 49, 497-500, 2002.

[93] Boyer, S., Sawan, M., Abdel-Gawad, M., Robin, S., and Elhilali, M. M. "Implantable Selective Stimulator to Improve Bladder Voiding: Design and Chronic Experiments in Dogs" *IEEE Trans. Biomed. Eng.*, vol. 8, 464-470, 2000.

[94] Kuphaldt, T. R., "Precise diode circuits", *available at*: http://www.ibiblio.org/obp/books/socratic/output/opamp8_instructor.pdf 2005

[95] Sedra, A. S., and Smith, K.C., "Microelectronic Circuits". *5th ed.* Oxford Univ Press, 2003.

[96] Bland, M., "An Introduction to Medical Statistics". *2nd ed.* Oxford University Press, Oxford, 1995.

[97] Harb, A., and Sawan, M. "Low-power CMOS implantable nerve signal analog processing circuit" *7th IEEE Int. Conf. ICECS 2000*, vol. 2, pp. 911 - 914, Lebanon, 2000.

[98] Horiuchi, T., Swindell, T., Sander, D., and Abshier, P. "A low-power CMOS neural amplifier with amplitude measurements for spike sorting" *IEEE International Symposium on Circuits and Systems - ISCAS '04*, vol. 4, pp. 29-32, Vancouver, Canada, 2004.

[99] Sacristan, J. M., and Oses, T. "Low Noise Amplifier for Recording ENG Signals in Implantable Systems" *IEEE International Symposium on Circuits and Systems - ISCAS '04*, pp. 33-36, Vancouver, Canada, 2004.

[100] Uranga, A., Lago, N., Navarro. X., and Barniol, N. "A Low Noise CMOS Amplifier for ENG Signals" *IEEE International Symposium on Circuits and Systems - ISCAS '04*, pp. 21-24, Vancouver, Canada, 2004.

[101] Harrison, R. R., and Charles C. "A Low-Power Low-Noise CMOS Amplifier for Neural Recording Applications" *IEEE J. Solid-State Circuits*, vol. 38, 958-965, 2003.

[102] Gudnason, G., Bruun, E., and Haugland, M. "An Implantable Mixed Analog/Digital Neural Stimulator Circuit" 1999.

[103] Toumazou, C., Lidgey, F.J., and Haigh, D.G., "Analogue IC design: the current-mode approach". Peter Peregrinus, IEE, 1990.

[104] Allstot, D. J. "Current-mode analog signal processing: a tutorial" *IEEE Pacific Rim Conference on Communications, Computers and Signal Processing*, vol. 2, pp. 815 - 818, 1991.

[105] Demosthenous, A., Taylor, J., Triantis, I. F., Rieger, R., and Donaldson, N. "Design of an Adaptive Interference Reduction System for Nerve-Cuff Electrode Recording" *IEEE Trans. Circuits and Systems -CAS I: Regular Papers*, vol. 51, 629 - 639, 2004.

[106] Triantis, I. F., and Demosthenous, A. "A BiCMOS ENG Amplifier with High SIR Output" *IEEE International Symposium on Circuits and Systems - ISCAS '05*, Kobe, Japan, 2005 - accepted for publication.

[107] Träff, H. "Novel Approach to High Speed CMOS Current Comparators" *Electronics Letters*, vol. 28, 1992.

[108] Ismail, M., and Feiz, T., "Analog VLSI: Signal and Information Processing". McGraw-Hill, 1994.

[109] Sanchez-Sinencio, E., and Silva-Martinez, J. "CMOS Transconductance Amplifiers, Architectures and Active Filters: A Tutorial" *IEE Proc. Circuits Devices Sys*, vol. 147, 3-12, 2000.

[110] Sackinger, E., and Guggenbuhl, W. "A high-swing, high-impedance MOS cascode circuit" *IEEE J. Solid-State Circuits*, vol. 25, 289-298, 1990.

[111] Hastings, A., "The Art of Analog Layout". *1st ed.* Prentice Hall, 2000.

[112] Wang, Z. "Novel pseudo RMS current converter for sinusoidal signals using a CMOS precision current rectifier" *IEEE Trans. Instrumentation and Measurement*, vol. 39, 670 - 671, 1990.

[113] AustriaMicroSystems, A. M. S. "0.8mm BiCMOS Process Parameters" *Doc. 9933008, Rev. 2.0*, vol. May 2001.

[114] Garde, P. "Transconductance cancellation for operational amplifiers" *IEEE J. Solid-State Circuits*, vol. 12, 310-311, 1977.

[115] Enz, C. C., Vittoz, E.A., and Krummenacher, F. "A CMOS chopper amplifier" *IEEE J. Solid-State Circuits*, vol. 22, 335 - 342, 1987.

[116] Bakker, A., Thiele, K., and Huijsing, J.H. "A CMOS nested-chopper instrumentation amplifier with 100-nV offset" *IEEE J. Solid-State Circuits*, vol. 35, 1877 - 1883, 2000.

[117] Koli, K., and Halonen, K. "Low Voltage MOS-Transistor-Only Precision Current Peak Detector with Signal Independent Discharge Time Constant" *IEEE Int. Symposium on Circ. Sys.*, pp. 1992-1995, Hong Kong, 1997.

[118] Struijk, J. J., Haugland, M.K., and Thomsen, M. "Fascicle Selective Recording with a Nerve Cuff Electrode" *18th Annual International Conference of the IEEE Engineering in Medicine and Biology Society*, Amsterdam, 1996.

[119] Sahin, M., and Durand, M. D. "Selective Recording with a Multi-Contact Nerve Cuff Electrode" *18th Anual Int. Conf. IEEE EMBS*, Amsterdam, Holland, 1996.

APPENDICES

Appendix A. Volume conductors and bioelectric fields

Electrical circuit diagrams can be used to describe bioelectric systems (e.g. [A1]), however the variables and symbols involved describe distributed rather than discrete components, because the conducting medium extends in a three-dimensional manner and is described as a *volume conductor* [A2, A3]. The bioelectric potentials of nerves and muscles as well as the electrode-tissue interface of the recording configurations used can be described in terms of electric fields and their corresponding spatial derivatives. Models of volume conductors can be used to describe sources of ionic currents in the tissue of interest, in combination with conductivity and geometrical parameters [A3].

A.I Uniform conduction medium

Assuming a volume source within a *uniform* (i.e. infinite and homogeneous) conductor, bioelectric activity of nerves and muscles will cause currents that can be expressed in terms of *impressed current density* $\bar{J}^i(x,y,z,t)$. Individual elements of nerve or muscle sources act as electric dipoles and therefore the impressed current density is equal to the *volume dipole moment density* of the source [A2]. If the conductivity of the conductor is σ, an electric field $\bar{E}$ and conduction current (or return current) $\sigma\bar{E}$ are produced by the primary sources of $\bar{J}^i$. This results to a total current density of ([A4] in [A2]):

$$\bar{J} = \bar{J}^i + \sigma\bar{E} \tag{A.1}$$

Experimental evidence by Schwan and Kay [A5] indicated that in volume conduction models, tissue impedance can be treated as solely resistive in the bandwidth of interest (i.e. its capacitive component is negligible). Thus fields stemming from particular bioelectric sources are considered to vary synchronously, without phase variations, due to the tissue being resistive. Moreover according to Geselowitz [A6] the electromagnetic propagation effect can also be neglected when modelling tissue as a volume conductor. Therefore, at any moment, stationary descriptions can be used for time-varying bioelectric signals (currents and voltages); such signals are termed *quasistatic* [A7].

As a result, the electric field in equation (A.1) is quasistatic and can be described at any instant as the negative gradient of a scalar potential Φ [A2]:

$$\bar{J} = \bar{J}^i - \sigma \nabla \Phi \tag{A.2}$$

The total current density $\bar{J}$ is solenoidal (causes currents that flow in closed loops) and as a result it simplifies to Poisson's equation [A2]:

$$\nabla \bar{J}^i = \sigma \nabla^2 \Phi \tag{A.3}$$

The solution to (A.3) for $\sigma\Phi$ in a volume v that is uniform and extends to infinity is given by (A.4) that follows, where the field generated by $\nabla \bar{J}^i$ varies with 1/r (r = distance from source centre), similarly to a point source:

$$4\pi\sigma\Phi = \int_v \bar{J}^i \bullet \nabla\left(\frac{1}{r}\right) dv \tag{A.4}$$

According to [A2], $\bar{J}^i$ can be treated as a *volume dipole density* because $\bar{J}^i dv$ can be represented as a dipole whose field variation relates to its dot product with $\nabla\left(\frac{1}{r}\right)$.

A.II Inhomogeneous volume conduction medium

In the analysis up to now, similar to the simulations in chapter 3, the medium was assumed to be infinite and homogeneous. In more realistic conditions the medium has boundaries, as is the case even for the in-vitro experiments, where the saline is contained by the tank and borders with air at the top. This introduces inhomogeneities to the solution that translate into additional terms. In describing in-vivo experiments, realistic non-homogeneous media can be approximated by a number of homogeneous, resistive volume segments, each with boundary S_j. Within these segments $\bar{J}^i$ and $\bar{E}$ are linearly related and on their boundaries Φ is continuous [A2]. The electric potential at any point of an inhomogeneous volume conductor is given by [A4]:

$$4\pi\sigma\Phi(r) = \int_v \bar{J}^i \bullet \nabla\left(\frac{1}{r}\right) dv + \sum_j \int_{S_j} (\sigma''_j - \sigma'_j)\Phi\nabla\left(\frac{1}{r}\right) \bullet d\bar{S}_j \qquad \text{(A.5)}$$

where the first term corresponds to (A.4) and is the term that represents the volume source, while σ'_j and σ''_j are conductivities of corresponding to the media each side of the boundary S_j.

A.III Volume conduction modelling

Using models to simulate physiological conditions and operations can facilitate investigations of particular conditions and events. According to [A2] using a model can ease deductions and be the first approach to validating a hypothesis, or it can be used to perform experiments which are not possible to perform in-vivo. Model-based results can be confirmed or better understood using experimental data, which can give a better indication regarding the accuracy of the approximation offered by the model. If the volume-conduction setup can be constructed using well established simulation packages, the solutions of equations like (A.5) are already included (e.g. using internal finite-element solvers) and the user does not need to develop the model analytically. The basic models of the volume source include the dipole and the moving dipole. The first one has three independent variables which are the magnitudes of its three Cartesian coordinates. The moving dipole has three additional independent variables, which include varying position, orientation and magnitude [A2].

Most of the tissue in the human body can be modelled as a resistive, linear, and piecewise homogeneous volume conductor [A2]. Table A1, reproduced from [A2], contains some typical resistivity values for various types of tissue (more analytical tables can be found in [A8]).

Although determining a field from a known source in a defined volume conductor (forward problem [A2]) offers a unique solution, the inverse problem is not so straightforward. When a field is measured in a well-described volume conductor, as in the case of in-vivo experiments, the source is unknown and has to be determined by the experimenter based on elements of physiology. If analysed using electrical terms, the

inverse problem has more than one solution. Four main approaches to determining the source of a measured bioelectric field have been identified in [A2]:

1. Empirically, using past analyses that allow the association of signal characteristics to specific sources
2. Limiting the possible theoretical solutions by taking into consideration conditions and constraints dictated by the anatomical and physiological information available for a particular region of measurement
3. Examining the distribution of the field and the tissue-electrode interface and estimating the most probable source statistically
4. Simulating the source and the conducting medium using simplistic models, including a fixed dipole for the source and homogeneous volume segments for the medium

Regarding the last case, Malmivuo in [A9] followed the following steps:

(a) A simplified source was constructed, with basic association to the physiological and anatomical information of the system being studied
(b) Using similar level of approximation, a volume conductor model was constructed to represent the tissue
(c) A number of independent measurements made it possible to define the unknown terms of the independent variables of the model

The final step in [A9] was to compare the results from the model to experimental measurements, to determine the degree of accuracy of the model.

In the case presented in the present thesis (chapter 3), the author followed similar steps to the ones described above, although the model developed did not make use of formulae, such as (A.1) – (A.5) previously presented, as the use of a commercial package was possible, simplifying the process. Maxwell SV 2D simulator by Ansoft®, used for drawing the model, allowed the definition of materials, sources and boundaries. The results were associated with in-vitro experimental measurements and in-vivo data allowed for some important conclusions to be drawn.

Table A1. typical tissue resistivities [A2]

Tissue type		ρ (Ωm)
Brain	grey matter	2.2
	white matter	6.8
	average	5.8
Cerebrospinal fluid		0.7
Blood		1.6
Plasma		0.7
Heart muscle	longitudinal	2.5
	transverse	5.6
Skeletal muscle	longitudinal	1.9
	transverse	13.2
Fat		177
Bone	longitudinal	15
	circumferential	158

References:

[A1] McNeal D. R. "Analysis of a Model for Excitation of Myelinated Nerve" *Trensactions on Biomedical Eng.*, vol. BME-23, 1976.

[A2] Malmivuo J., and Plonsey, R., "Bioelectromagnetism: Principles and Applications of Bioelectric and Biomagnetic Fields ". Oxford University Press, 1995.

[A3] Struijk J. J., and Yoshida, K., "Volume Conduction", 2004, Seminar, Neuroprosthesis Interest Group (nPIG) - Center for Sensory-Motor Interaction (SMI), Aalborg University, Denmark, 2004.

[A4] Geselowitz D. B. "On bioelectric potentials in an inhomogeneous volume conductor" *Biophys. J.*, vol. 7, 1-11, 1967.

[A5] Schwan H. P., and Kay, C. F. "Capacitive properties of body tissues" *Circ. Res.*, vol. 5, 439 - 443, 1957.

[A6] Geselowitz D. B. "The concept of an equivalent cardiac generator" *Biomed. Sci. Instrum.*, vol. 1, 325 -330, 1963.

[A7] Plonsey R., and Heppner, D. B. "Considerations of quasistationarity in electrophysiological systems" *Bull. Math. Biophys.*, vol. 29, 657 - 664, 1967.

[A8] Geddes L. A., and Baker, L. E. "The specific resistance of biological material - A compendium of data for the biomedical engineer and physiologist" *Med. & Biol. Eng.*, vol. 5, 271-293, 1967.

[A9] Malmivuo J. A. "On the detection of the magnetic heart vector - An application of the reciprocity theorem" *Helsinki Univ. Tech., Acta Polytechn. Scand., El. Eng. Series, (Dr. tech. thesis)*, vol. 39, p. 112, 1976.

Appendix B1. System-level AT Mathematica script

I F Triantis 2004

a. General description in terms of EMG, ENG, Ximb

Terms:

Vn[t] = ENG to be detected
Vn1[t] = Channel 1 ENG input
Vn2[t] = Channel 2 ENG input
Vemg = Amplitude of EMG across the cuff
Vm[t] = EMG across the cuff
Vm1[t] = Channel 1 EMG input (amplitude Vm1)
Vm2[t] = Channel 2 EMG input (amplitude Vm2)
Ximb = Imbalance
G1[t] = Multiplier 1 gain (settled: G1X)
G2[t] = Multiplier 2 gain (settled: G2X)
g = Voltage to gain feedback conversion factor (V^{-1})
VfbX = Feedback voltage producing gain compensating for imbalance
Vfb[t] = Integrator output
Gfb0 = Internal multiplier gain
Gfb(t) = Variable part of multiplier gain produced by integrator output (Gfb[t] = g Vfb[t])
GfbX = Variable part of multiplier gain produced by integrator output settled to a DC level (GfbX = g VfbX)
Vg1[t] = Multiplier output, channel 1
Vg2[t] = Multiplier output, channel 2
Vr1[t] = Rectifier Output, channel 1
Vr2[t] = Rectifier Output, channel 2
Vco[t] = Output of comparator

Slide 1

Therefore for the EMG term to be zero, the integrator output should approach the DC level:

```
GfbX = Ximb Gfb0;
```

1 System time constant and time to converge

```
Vr1[t] =|Vg1[t]|;
Vr2[t] =|Vg2[t]|;
Vc[t] = Gco (Vr1[t] - Vr2[t]);
```

The rectification will give the absolute value of Vm but not the absolute of Vn. Vn will be a ripple on top of it. Will be approximated later.
Say Abs[Vm[t]] = Vemg
Say Vn1[t]-Vn2[t]=Vn[t]:
Therefore:

```
Vr1[t] = A (Gfb0 - Gfb[t]) 0.5 (1 + Ximb) Vemg + A (Gfb0 - Gfb[t]) Vn[t];
Vr2[t] = A (Gfb0 + Gfb[t]) 0.5 (1 - Ximb) Vemg + A (Gfb0 + Gfb[t]) Vn[t];
Vco[t] = Gc (Vr1[t] - Vr2[t]);
Vco[t] = Simplify[Collect[Expand[Vco[t]], {Gfb0, Ximb}]]
```

```
A Gc Gfb0 Vemg (0. + 1. Ximb) + Gfb[t] (-1. A Gc Vemg + 0. A Gc Vemg Ximb - 2 A Gc Vn[t])
```

```
Vco[t] = A Gco (Gfb0 Ximb Vemg - Gfb[t] Vemg - 2 Gfb[t] Vn[t]);
Vco[t] = A Gco (Gfb0 Ximb Vemg - Gfb[t] (Vemg + 2 Vn[t]));
```

Slide 3

Gco = Gain of comparator
VAT[t] = System Output
Gout = Output Stage Gain

$$Ximb = \frac{|Vm1[t]| - |Vm2[t]|}{Vemg}$$

```
-1 < Ximb < 1;
Gfb[t] < Gfb0;
Gfb0 > 0;
Vm1[t] = 0.5 (1 + Ximb) Vm[t];
Vm2[t] = - 0.5 (1 - Ximb) Vm[t];
G1[t] = Gfb0 - Gfb[t];
G2[t] = Gfb0 + Gfb[t];
G1X = Gfb0 - GfbX;
G2X = Gfb0 + GfbX;
Vg1[t] = A G1[t] (Vm1[t] + Vn[t]);
Vg2[t] = A G2[t] (Vm2[t] + Vn[t]);
Vg1[t] = Simplify[Expand[Vg1[t]]];
Vg2[t] = Simplify[Expand[Vg2[t]]];
VAT[t] = Collect[Simplify[Expand[Gout (Vg1[t] + Vg2[t])]], {A Gout, Vm[t]}];
```

```
VAT[t] = A Gout ((Gfb0 Ximb - Gfb[t]) Vm[t] + 2 Gfb0 Vn[t]);
```

$$VAT[t] = A\,Gout\,Gfb0\left(\left(Ximb - \frac{Gfb[t]}{Gfb0}\right)Vm[t] + 2\,Vn[t]\right);$$

Say that as a response to the current Ximb value, the integrator output approaches a DC level, say GfbX (as a result of the comparator input eventually becoming equal, causing the comparator output to be a high frequency square wave). This leads to the output settling to VATX[t]:

$$VATX[t] = A\,Gout\,Gfb0\left(\left(Ximb - \frac{GfbX}{Gfb0}\right)Vm[t] + 2\,Vn[t]\right);$$

Slide 2

* The output of the integrator is Vfb[t], a function of time corresponding to Gfb[t], which later settle to DC level VfbX, corresponding to GfbX.
Say integrator gain is Gint time constant is tint.

$$\text{Therefore : } Vfb[t] = \frac{Gint}{tint}\int Vco[t]\,dt$$

$$\text{leading to : } \frac{dVfb[t]}{dt} = \frac{Gint}{tint}A\,Gco\,Gfb0\,Ximb\,Vemg - \frac{Gint}{tint}A\,Gco\,Gfb[t]\,(Vemg + 2\,Vn[t])$$

$$\text{Therefore : } \frac{dVfb[t]}{dt} = \frac{Gint}{tint}A\,Gco\,Gfb0\,Ximb\,Vemg - \frac{g\,Gint}{tint}A\,Gco\,Vfb[t]\,(Vemg + 2\,Vn[t])$$

```
Simplify[DSolve[Vfb'[t] == Gint/tint A Gco Gfb0 Ximb Vemg - g Gint/tint A Gco Vfb[t] (Vemg + 2 Vn), Vfb[t], t]]
```

* This results to :

$$Vfb[t] = \frac{Gfb0\,Ximb}{g\left(1 + \frac{2\,Vn}{Vemg}\right)} + \text{@}^{-\frac{A\,g\,Gco\,Gint\,Vemg\left(1 + \frac{2\,Vn}{Vemg}\right)}{tint}t};$$

However, because the initial state is zero :

$$Vfb[t] = \frac{Gfb0\,Ximb}{g\left(1 + \frac{2\,Vn}{Vemg}\right)}\left(1 - \text{@}^{-\frac{A\,g\,Gco\,Gint\,Vemg\left(1 + \frac{2\,Vn}{Vemg}\right)}{tint}t}\right);$$

$$\text{Approximation : } Vn[t] << Vm[t] \Rightarrow 1 + \frac{2\,Vn}{Vemg} = 1. \text{ Therefore :}$$

Slide 4

$$Vfb[t] = \frac{Gfb0\ Ximb}{g}\left(1 - e^{-\frac{A\ Gco\ Gint\ g\ Vemg}{\tau int}\ t}\right);$$

$$Gfb[t] = Gfb0\ Ximb\left(1 - e^{-\frac{A\ Gco\ Gint\ g\ Vemg}{\tau int}\ t}\right);$$

Therefore $\tau = \frac{\tau int}{A\ Gco\ Gint\ g\ Vemg}$

The output of the comparator Vco[t] is of fixed amplitude, say Vcomp and the gain Gco may be expressed (approximately) by:

$$Gco = \frac{Vco[t]}{Vr1[t] - Vr2[t]};$$

$$Gco = \frac{Vco[t]}{A\ Vemg\left(Gfb0\ Ximb - Gfb[t]\left(1 + \frac{2\ Vn[t]}{Vemg}\right)\right)};$$

$$Gco = \frac{Vco[t]}{A\ Vemg\ (Gfb0\ Ximb - Gfb[t])};$$

Therefore $\tau = \frac{\tau int\ Gfb0\ (Ximb - \frac{GfbP[t]}{Gfb0})}{g\ Gint\ Vco[t]}$

Where Gfb[t] has been replaced by GfbP[t], as in this case this is the Gfb[t] corresponding to the previous feedback value, since the denominator expresses the INPUT of the comparator. Therefore, Vco[t] here corresponds to comparator output due to the previous imbalance condition XimbP and the time constant of the system is the time constant defining the settlin time of the system when the imbalance changes abruptly from XimbP to Ximb, which is the current value that the corresponding integrator output has to settle to.

Therefore say:
1) Vco[t] has previously stabilized to a square wave of a frequency sufficiently high to allow the previous integrator output Vfb[t] to be approximated by dc value

2 Sinusoidal signal representation

In order to visualize the corrective action of the AT and to demonstrate the effect of the error factors, the EMG and ENG signals can be represented as sinusoids. Use S for subscript

```
Vn1S[t] = Vemg 0.5 (1 + XimbS) Sin[t ω1];
Vn2S[t] = Vemg 0.5 (-1 + XimbS) Sin[t ω1];
VnS[t] = Vemg Sin[t ω2];
Vg1S[t] = A G1XS (Vn1S[t] + VnS[t]);
Vg2S[t] = A G2XS (Vn2S[t] + VnS[t]);
G1XS = Gfb0 - Gfb[t] /. {Ximb → XimbS, XimbP → 0};
G2XS = Gfb0 + Gfb[t] /. {Ximb → XimbS, XimbP → 0};
VATS[t] = Gout (Vg1S[t] - Vg2S[t]);
```

$$VATS[t] = A\ Gfb0\ Gout\left(XimbS\ e^{-\frac{t\ G_{INT}}{Gfb0\ XimbS\ \tau int}}\ Vemg\ Sin[t\ \omega1] - 2\ Veng\ Sin[t\ \omega2]\right);$$

Using typical values:

VfbXP.
2) Gint g Vco[t] = Gint gVcomp f[t], where f[t] is the previous square wave causing the integrator to settle to its previous dc output and therefore is not present at the integrator output, at this stage of the analysis (but will be discussed later).
3) Name the gain term: Gint gVco = GINT. (Equivalently, it may had been assumed that the initial Gint was Gintnew (convenient for not replacing the term) and Vcomp was unity, meaning that the amplitude of the comparator output is unity).

As a result:

$$Gfb[t] = Gfb0\ Ximb\left(1 - e^{-\frac{1}{\tau int\ \frac{Gfb0}{G_{INT}}\ (Ximb - XimbP)}\ t}\right);$$

$$\tau = \tau int\ \frac{Gfb0}{G_{INT}}\left(Ximb - \frac{GfbXP}{Gfb0}\right);$$

$$\tau = \tau int\ \frac{Gfb0}{G_{INT}}\ (Ximb - XimbP);$$

If XimbP = 0, representing the system just being turned on:

$$\tau 0 = \tau int\ \frac{Gfb0}{G_{INT}}\ Ximb$$

Which means that the comparator allows the time constant to be independent of the input EMG amplitude.
However, it depends on the imbalance.

The system convergence time tsys will be approximately 5 τ:

$$tsys = 5\ \tau;$$


```
VATSval = VATS[t] /. {Gout → 10, Gfb0 → 2, XimbS → 0.4, A → 1000, G_INT → 8, τint → 1, Vemg → 10^-3,
   ω1 → 628, Veng → 10^-6, ω2 → 6280}

tsysVAL = tsys /. {Gfb0 → 2, Ximb → 0.4, XimbP → 0, G_INT → 8, τint → 1}

VemgVAL = Vemg Sin[t ω1] /. {Vemg → 10^-3, ω1 → 628}; VengVAL = Veng Sin[t ω2] /. {Veng → 10^-6, ω2 → 6280};

Plot[VemgVAL, {t, 0, 0.6}, AxesLabel → {"time (s)", "EMG in"}];
Plot[VATSval, {t, 0, 0.6}, AxesLabel → {"time (s)", "VATS[t]"}];
Plot[VengVAL, {t, 0.9, 0.91}, AxesLabel → {"time (s)", "ENG in"}];
Plot[VATSval, {t, 0.9, 0.91}, AxesLabel → {"time (s)", "VATS[t] snapshot"}];
```

$$20000\left(0.0004\ e^{-10.\ t}\ Sin[628\ t] + \frac{Sin[6280\ t]}{500000}\right)$$

0.5

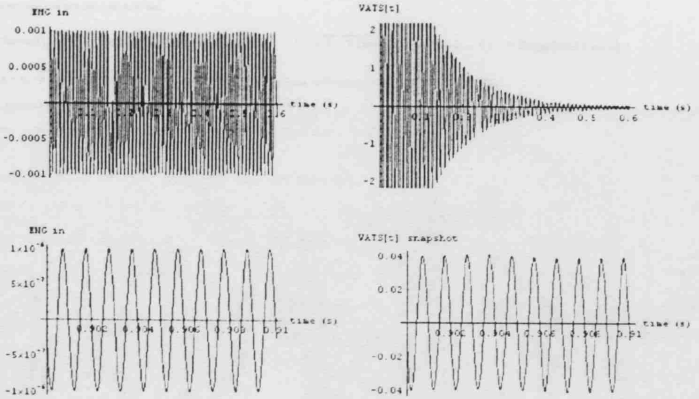

Slide 9

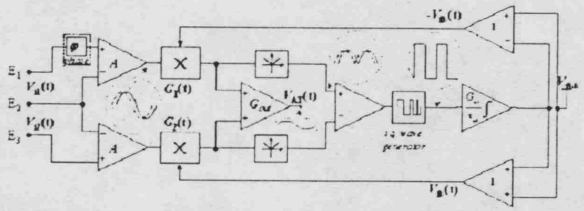

Effect of Phase Error on fb loop and on harmonic distortion, not examined here

```
Vm1d[t] = Vemg 0.5 (1 + Ximbd) Sin[t ω1 + φ];
Vm2d[t] = Vemg 0.5 (-1 + Ximbd) Sin[t ω1];
(*Vm1d[t] = Vm2d[t] = Vmd[t]*)
Vmd[t] = Vemg Sin[t ω2];
Vg1d[t] = A G1Xd (Vm1d[t] + Vmd[t]);
Vg2d[t] = A G2Xd (Vm2d[t] + Vmd[t]);
G1Xd = Gfb0 - GfbXd;
G2Xd = Gfb0 + GfbXd;
VATd[t] = Gout (Vg1d[t] + Vg2d[t])
```

```
Gout (A (Gfb0 + GfbXd) (0.5 Vemg (-1 + Ximbd) Sin[t ω1] + Vemg Sin[t ω2]) +
   A (Gfb0 - GfbXd) (0.5 Vemg (1 + Ximbd) Sin[φ + t ω1] + Vemg Sin[t ω2]))
```

Slide 11

b. System error sources

Possible error sources include:
1. Phase shift (delay) between the two channels
2. Harmonic distortion due to the integrator output not being DC. This has to do with:
   a) Rectifier outputs not dc (rectifiers ~= peak detectors)
   b) Glitches at rectifier output at twice the EMG frequency due to transition from -ive to +ive input or due to phase shifts. These occur once in a period in one anel and once in the other with a difference of half period between them.
   c) These only affect the frequency of the square wave out of the comparator. The effect is a variable-frequency square wave.
   d) This square wave, whose frequency in the worst case will be a harm. component of the fundamental EMG frequency, generates a triangular wave ripple at the integrator output, which is level-shifted by VfbX.
Its amplitude depends on the combination of rint and comparator frequency.
   e) The frequency of the comparator may be affected by ENG leftovers in the rectifier outputs.
3. Input dc offsets
4. Fb loop dc offsets

Other factors to be mentioned include multiplier nonlinearity, noise, etc.

1 Phase error (channel phase difference)

(add d (delay) to notations, say ϕ is the phase of ch1 and phase of ch. 2 is 0).

Slide 10

```
VATd[t] =
 0.5 Gout A
  (Vemg (-Gfb0 - GfbXd + Gfb0 Ximbd - GfbXd Ximbd) Sin[t ω1] +
    Vemg (Gfb0 - GfbXd + Gfb0 Ximbd - GfbXd Ximbd) Sin[φ + t ω1] + 4 Gfb0 Vemg Sin[t ω2]);
```

Ideally we would like Vemg factor= 0. If ϕ was zero, this would be satisfied with GfbXd=Ximbd Gfb0. Therefore:

```
VATd2[t] = VATd[t] /. GfbXd → Ximbd Gfb0
```

```
0.5 A Gout (Vemg (-Gfb0 + Gfb0 Ximbd^2) Sin[t ω1] + Vemg (Gfb0 - Gfb0 Ximbd^2) Sin[φ + t ω1] + 4 Gfb0 Vemg Sin[t ω2])
```

```
VATd2[t] = A Gout Gfb0 (Vemg 0.5 (Ximbd^2 - 1) (Sin[t ω1] - Sin[φ + t ω1]) + 2 Vemg Sin[t ω2]);
VATd2[t] = A Gout Gfb0 (Vemg 0.5 (Ximbd^2 - 1) (Sin[t ω1] (1 - Cos[φ]) - Cos[t ω1] Sin[φ]) + 2 Vemg Sin[t ω2]);
```

Say $-\mathrm{Sin}[\phi] = Bf$ and $(1-\mathrm{Cos}[\phi]) = Af$

and apply the rule: $a\,\mathrm{Sin}[x] + b\,\mathrm{Cos}[x] = Xf\,\mathrm{Sin}[x + \Phi]$, where $Xf = \sqrt{(a^2 + b^2)}$ and $\mathrm{Cos}[\Phi] = \frac{a}{Xf}$, $\mathrm{Sin}[\Phi] = \frac{b}{Xf}$

Finally solve Xf for ϕ, put it back in the Vemg term and find ϕ1 for the required amplitude (< 50% ENG output amplitude).
The value of Φ is unimportant because (ω1 t + Φ) could be considered the new fundamental ω1b of the EMG (but Φ is the overall output delay relative to the input).
$(\tan[\Phi] = \frac{Bf}{Af}$ therefore: $\Phi = \tan^{-1}\left[\frac{-\mathrm{Sin}[\varphi]}{(1-\mathrm{Cos}[\varphi])}\right]$ therefore Φ can be found after φ1 is found).

```
Vemyterm = Af Sin[t ω1] + Bf Cos[t ω1];
Vemyterm2 = Xf Sin[t ω1 + Φ];
Xf = √(Af^2 + Bf^2);
Xf1 = Simplify[Xf /. {Af → (1-Cos[φ]), Bf → -Sin[φ]}]
```

$$\sqrt{2 - 2\,\mathrm{Cos}[\varphi]}$$

Slide 12

Therefore the output will now be:

```
VATd2[t] = AGout Gfb0 (Veng 0.5 (Ximbd^2 - 1) Sqrt[2 - 2 Cos[φ]] Sin[t ω1 + ϑ] + 2 Veng Sin[t ω2]);
```

If $\phi = 0$, $\sqrt{2 - 2\cos[\varphi]} = 0$. Therefore, if there is no phase shift, the system will eliminate EMG.

In general we want: $0.5\,Veng\,(Ximbd^2 - 1)\sqrt{2 - 2\cos[\varphi]} <= 2\,Veng * \frac{1}{SIRoutMIN}$, where SIRoutMIN is the minimum allowed signal to interference ratio at the output. Say SIRout = 1 and the max allowed EMG output amplitude is equal to the ENG output.
In this case:

$0.5\,Veng\,(Ximbd^2 - 1)\sqrt{2 - 2\cos[\varphi]} = 2\,Veng;$

$0.25\,Veng\,(Ximbd^2 - 1)\left[\sqrt{2 - 2\cos[\varphi]}\right] = Veng;$

$$\left[\sqrt{2 - 2\cos[\varphi]}\right] = \frac{Veng}{0.25\,Veng\,(Ximbd^2 - 1)};$$

$$\cos[\varphi] = 1 - 0.5\left(\frac{Veng}{0.25\,Veng\,(Ximbd^2 - 1)}\right)^2$$

$$\varphi = \text{ArcCos}\left[1 - 0.5\left(\frac{4\,Veng}{Veng\,(Ximbd^2 - 1)}\right)^2\right];$$

$$\varphi = \text{ArcCos}\left[1 - 8\left(\frac{Veng}{Veng\,(Ximbd^2 - 1)}\right)^2\right];$$

$$\varphi = \text{ArcCos}\left[1 - 8\left(\frac{SIR_{in}}{Ximbd^2 - 1}\right)^2\right];$$

$$\varphi = \text{ArcCos}\left[1 - 8\left(\frac{SIR_{in}}{Ximbd^2 - 1}\right)^2\right];$$

The acceptable phase error introduced by, say, HP filters at the input depends on:
input SIR and imbalance. The following is the φ value of ϕ in DEGREES for typ. values:

$$\varphi 1a = \text{ArcCos}\left[1 - 8\left(\frac{SIR_{in}}{Ximbd^2 - 1}\right)^2\right]\frac{360}{2\pi};$$

```
φ1aVAL = φ1a /. {Ximbd → 0.4, SIRin → 1/1000}
φ1aVAL.rad = φ1aVAL Degree
```

0.272837

0.00476191

$$SIR_{outVAL} = SIR_{in}\frac{1}{0.25\,(1 - Ximbd^2)\left(\sqrt{2 - 2\cos[\varphi VAL.plot]}\right)} /. \{Ximbd \to 0.4,\ SIR_{in} \to 1/1000\};$$

```
Plot[SIRoutVAL, {φVAL.plot, -0.4 Degree, 0.4 Degree}, AxesLabel → {"φ", "SIRout"}]:
```


Generally:

$$SIR_{outDES} = SIR_{in}\frac{1}{0.25\,(Ximbd^2 - 1)\left(\sqrt{2 - 2\cos[\varphi]}\right)} = 1$$

where SIR_{outDES} is the desirable SIR at the output
Therefore:

$$\left[\sqrt{2 - 2\cos[\varphi]}\right] = \frac{SIR_{in}}{0.25\,(Ximbd^2 - 1)\,SIR_{outDES}};$$

$$\cos[\varphi] = 1 - 0.5\left(\frac{SIR_{in}}{0.25\,(Ximbd^2 - 1)\,SIR_{outDES}}\right)^2$$

Therefore, generally:

$$\varphi = \text{ArcCos}\left[1 - 8\left(\frac{SIR_{in}/SIR_{outDES}}{Ximbd^2 - 1}\right)^2\right];$$

To summarize:

$$SIR_{outMIN} = SIR_{in}\frac{1}{0.25\,(Ximbd^2 - 1)\left(\sqrt{2 - 2\cos[\varphi]}\right)} = 1$$

where SIR_{outMIN} is the minimum acceptable SIR at the output
leading to:

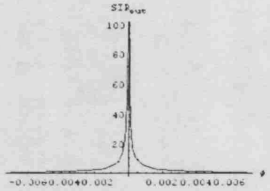

$$SIR_{outVAL2} = SIR_{in}\frac{1}{0.25\,(1 - Ximb^2)\left(\sqrt{2 - 2\cos[\varphi VAL]}\right)} /. \{Ximbd \to 0.4,\ SIR_{in} \to 1/1000,\ \varphi VAL \to 0.273\,Degree\}$$

$$\frac{0.839499}{1 - Ximb^2}$$

How does this translate in phase difference between 2 HP RC filters? Say filters HP1 (R1, C1) and HP2 (R2, C2) have phases $\theta 1$ and $\theta 2$, cut-off frequencies fc1, fc2 while the signal frequency of interest for both is fm = EMG freq.

$\theta 1 = \text{ArcTan}\left[\frac{f_{c1}}{fm}\right];$

$\theta 2 = \text{ArcTan}\left[\frac{f_{c2}}{fm}\right];$

$\theta 1 - \theta 2 == \varphi 1;$

Therefore:

$\frac{f_{c1}}{fm} = \text{Tan}[\theta 1]$;

$\frac{f_{c2}}{fm} = \text{Tan}[\theta 2]$;

Apply the formula:

$$\text{Tan}[a - b] = \frac{\text{Tan}[a] - \text{Tan}[b]}{1 + \text{Tan}[a]\,\text{Tan}[b]}$$

Therefore:

$$\text{Tan}[\phi 1] = \frac{\frac{f_{c1}}{fm} - \frac{f_{c2}}{fm}}{1 + \frac{f_{c1} f_{c2}}{fm^2}} = N\phi$$

$\varphi 1b = \text{ArcTan}\left[\frac{fm\,(f_{c1} - f_{c2})}{fm^2 + f_{c1} f_{c2}}\right]$;

If the two filters are matched perfectly, $f_{c1} = f_{c2}$ and the phase difference between them is zero. Normally, $f_{c2} = f_{c1}\,(1+e1)$, where e1 is the matching error (%) and $0 < |e1| < 1$. Therefore:

$\varphi 1c = \varphi 1b /. f_{c2} \to f_{c1} + e1\, f_{c1}$

$$-\text{ArcTan}\left[\frac{e1\, fm\, f_{c1}}{fm^2 + f_{c1}\,(f_{c1} + e1\, f_{c1})}\right]$$

$\varphi 1c = -\text{ArcTan}\left[\frac{e1\, fm\, f_{c1}}{fm^2 + e1\, f_{c1}^2 + f_{c1}^2}\right]$;

$\text{Tan}[0.273\,^\circ]$

0.00476478

We know that for the specifications defined before, $\phi 1 = 0.273^\circ$ ($\tan(\phi 1) = 0.00476478$) and fm = 100Hz. Say e1 = 1% = 0.01. Therefore:

$\varphi 1d = -\varphi 1c /. \{fm \to 100,\ e1 \to 0.01\}$

$\text{Plot}\left[\frac{-\varphi 1d}{\circ}, \{f_{c1}, 0, 1000\}, \text{AxesLabel} \to \{"f_{c1}(Hz)", "\varphi\ (^\circ)"\}\right]$;

$\text{Solve}[\varphi 1d == 0.273\,^\circ, f_{c1}]$

$$\text{ArcTan}\left[\frac{1.\, f_{c1}}{10000 + 1.01\, f_{c1}^2}\right]$$

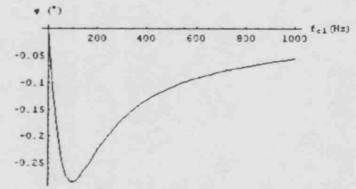

$\{\{f_{c1} \to 74.0025\}, \{f_{c1} \to 133.793\}\}$

The above shows how phase shift changes with fc selection for the filters. Obviously the higher fc values would correspond to phase shift introduced by low-pass filters. We are interested in the fc values corresponding to HP filters, cutting freq.s lower than both signals' pk frequencies. Therefore the higher cut-off freq acceptable is 72.3 to 74Hz (corresponding to -1% and 1% fc error respectively). Say fc is 73Hz. How does this affect the phase shift higher up the BW, affecting the ENG? Plot the phase shift introduced by the above filters with the above cut-off freq. and 1% error:

$\varphi 1e = -\varphi 1c /. \{f_{c1} \to 73,\ e1 \to 0.01\}$

$\text{Plot}\left[\frac{\varphi 1e}{\circ}, \{fm, 0, 1000\}, \text{AxesLabel} \to \{"f_{\text{signal}}(Hz)", "\varphi\ (^\circ)"\}\right]$;

$$\text{ArcTan}\left[\frac{0.73\, fm}{5382.29 + fm^2}\right]$$

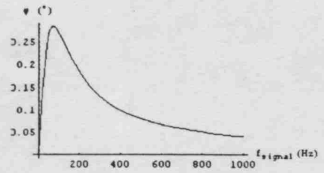

0.041602

13.309

1.51575×10^{-6}

1.13889×10^{-7}

0.00015

0.000113889

```
0. Sin[200 π t]
```

```
0.05 Sin[200 π t] - 0.05 Sin[0.00952374 + 200 π t]
```

```
0.05 Sin[200 π t] - 0.05 Sin[° + 200 π t]
```

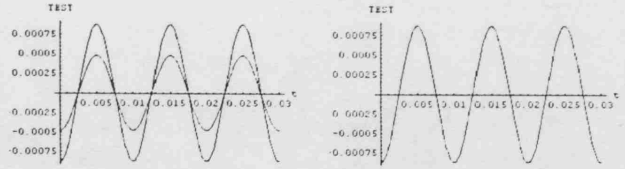


```
TESTeng = Sin[2 π 1000 t] + Sin[2 π 1000 t]
TESTeng1 = Sin[2 π 1000 t] + Sin[2 π 1000 t + 45 °]
Plot[{TESTeng, TESTeng1}, {t, 0, 0.003}, AxesLabel → {"t", "TEST"}];
```

```
2 Sin[2000 π t]
```

```
Sin[2000 π t] + Sin[45 ° + 2000 π t]
```


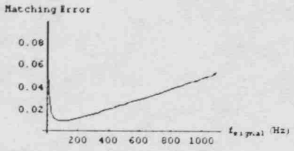

Now say that the cut-off freq. f_{c1} =100Hz. Find the error e1 so that ϕ is what we want it to be.

```
Solve[0.273 ° == -ArcTan[(e1 fm f_c1)/(fm^2 + e1 f_c1^2 + f_c1^2)], e1]
```

$$\left\{\left\{e1 \to -\frac{0.00476478\,(1.\,fm^2 + 1.\,f_{c1}^2)}{(1.\,fm + 0.00476478\,f_{c1})\,f_{c1}}\right\}\right\}$$

```
e2 = -(0.00476478 (fm^2 + f_c1^2))/((fm + 0.00476478 f_c1) f_c1);
e2val = e2 /. f_c1 → 100
Plot[-e2val, {fm, 0, 1100}, AxesLabel → {"f_cutoff(Hz)", "Matching Error"}];
e2FMG = e2val /. fm → 100
```

$$-\frac{0.0000476478\,(10000 + fm^2)}{0.476478 + fm}$$


```
-0.00948437
```

```
φ1c
φ1g = φ1c 180/π /. {fm → 100, e1 → -0.00948437, f_c1 → 100}
```

```
-ArcTan[(e1 fm f_c1)/(fm^2 + f_c1^2 + e1 f_c1^2)]
```

```
0.273
```

```
R = ArcTan[-Sin[φ1]/(1 - Cos[φ1])];
Rrad = R /. φ1 → 0.273°
Rdeg = Rrad/°
```



```
-1.56841
```

```
-89.8535
```

2 Input offset error: Voi (add oi to notations)

```
Vm1oi[t] = Vemg 0.5 (1 + Ximboi) Sin[t ω1] + Voi;
Vm2oi[t] = Vemg 0.5 (-1 + Ximboi) Sin[t ω1];
(*Vmloi[t] = Vm2oi[t] + Vmoi[t]*)
Vmoi[t] = Vemg Sin[t ω2];
Vg1oi[t] = A G1Xoi (Vm1oi[t] + Vmoi[t]);
Vg2oi[t] = A G2Xoi (Vm2oi[t] + Vmoi[t]);
G1Xoi = Gfb0 - GfbXoi;
G2Xoi = Gfb0 + GfbXoi;

(*Ideally: GfbXoi=Ximboi Gfb0; But won't replace this, because it's important to see how fb is affected.*)

VAToi[t] = Gout (Vg1oi[t] + Vg2oi[t])
```

```
Gout (A (Gfb0 + GfbXoi) (0.5 Vemg (-1 + Ximboi) Sin[t ω1] + Vemg Sin[t ω2]) +
  A (Gfb0 - GfbXoi) (Voi + 0.5 Vemg (1 + Ximboi) Sin[t ω1] + Vemg Sin[t ω2]))
```

```
VAToi[t] = A Gout ((Gfb0 - GfbXoi) Voi + Vemg (Gfb0 Ximboi - GfbXoi) Sin[t ω1] + 2 Gfb0 Vemg Sin[t ω2]);
```

The above shows that if the feedback was unaffected by the input dc offset, its effect would simply be a dc offset at the output.

That said, if the fb was ideal: GfbXoi=Ximboi Gfb0, it would result to:

VATof_IDEALfb[t]=A Gout Gfb0 ((1-Ximbof) Vof+2 Veng Sin[t ω2]);

Therefore, depending on the imbalance, even a small input offset would saturate the system, as it would get multiplied by the gains A Gout Gfb0. For example, if A = 1000, Gout = 10 and Gfb0 = 2 and assuming Ximbof = 40%, that would give: 12000 Vof. Therefore with ±8V supplies (as in the discrete sys), Vof < 8/12000 V, therefore: Vof < 667 μV.

However, the input offset WILL affect the feedback. Therefore, need to see how:

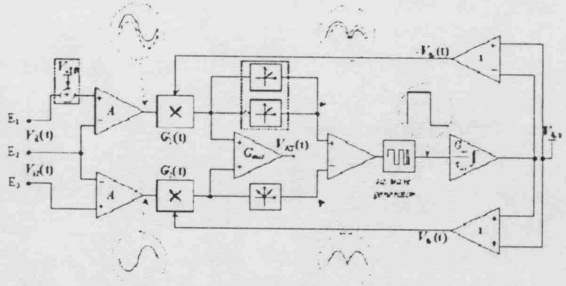

Let's examine 2 cases:

1) Ximbof = 0. If EMG components of both channels were equal and fb loop was open, the output of the comparator would be a square wave with:

1st part pulse width = $\frac{1}{2}$ Temg + $\frac{Vof}{Vemg}$ Temg

2nd part pulse width = $\frac{1}{2}$ Temg - $\frac{Vof}{Vemg}$ Temg

and overall period = Temg = EMG period = $\frac{2\pi}{\omega 1}$

Closing the loop, normally (without offset) the integrator should stay stable and the EMG ac components would cancel at the output leaving only a dc offset (the TT (and QT) case) as mentioned previously. However in this case the ac components won't cancel because even if the integrator was quick enough to settle well within half EMG period (which is not the case as the integrator has to be fast to avoid harmonic distortion, see later section) the resulting EMG components in the two channels would not be antiphase versions of the same waveform anymore, but would be distorted. The result would be severe harmonic distortion at the output.

2) Ximbof =~= 0. If EMG component of channel 1 was greater the integrator op should be high (until amplitudes are same). However, the rectif. output of ch.1, because of the offset, will have one large and one small component, therefore the comparator output won't be all high, but will have a part where it will be low, resulting in some part of the fedback actually increasing ch. 1 EMG amlpitude instead of reducing it.

Overall, an input offset can result in saturation, feedback error and harmonic distortion (the latter will be examined later).

3 Fb. loop offset error: Vof (add of to notations)


```
Vm1of[t] = Veng 0.5 (1 + Ximbof) Sin[t ω1];
Vm2of[t] = Veng 0.5 (-1 + Ximbof) Sin[t ω1];
(*Vm1of[t] = Vm2of[t] = Vmof[t];*)
Vmof[t] = Veng Sin[t ω2];
Vg1of[t] = AG1Xof (Vm1of[t] + Vmof[t]);
Vg2of[t] = AG2Xof (Vm2of[t] + Vmof[t]);
G1Xof = Gfb0 - GfbXof + g Vof;
G2Xof = Gfb0 + GfbXof + g Vof;

(*Ideally: GfbXof=Ximbof Gfb0; But won't replace this, because it's important to see how fb is affected.*)

VATof[t] = Gout (Vg1of[t] + Vg2of[t])

    Gout (A (Gfb0 + GfbXof + g Vof) (0.5 Veng (-1 + Ximbof) Sin[t ω1] + Veng Sin[t ω2]) +
      A (Gfb0 - GfbXof + g Vof) (0.5 Veng (1 + Ximbof) Sin[t ω1] + Veng Sin[t ω2]))

VATof[t] = A Gout (Veng (-GfbXof + (Gfb0 + g Vof) Ximbof) Sin[t ω1] + 2 Veng (Gfb0 + g Vof) Sin[t ω2]);
```

The above shows that if the fb was ideal: GfbXof=Ximbof Gfb0, this would result to:

VATof_IDEALfb[t]=A Gout (Veng (g VofXimbof) Sin[t ω1]+2 Veng (Gfb0+g Vof)Sin[t ω2]);

Therefore there would be a residual EMG component at the output, whose amplitude would depend on the fb offset. However, the system bein adaptive, the effect of the offset is that the variable part of the gain will now become:

GfbXof = g (Vfb0+Vof)Ximbof

This does not seem as a problem at all, but it may become one, depending on the amplitude and polarity of the offset, for two reasons:

1) The feedback level-shift voltage Vfb0 is fixed during the system design so that the multiplier outputs will never change phase, in other words: |VfbX| < Vfb0.

Therefore if, in this case, the offset is negative and depending on its amplitude, this may seize to be the case for one of the channels, at least for large imbalance values, where the value of VfbX approaches that of Vfb0. In that case the EMG and ENG components of the two channels will not be anti- and in-phase respectively and the operation of the system will be jeopardised.

2) The feedback output stage (i.e. the integrator output stage) is also designed so that the feedback will not saturate. Therefore, if Vof value is large enough,it may saturate one of the feedback channels, providing unbalanced gain adaption.

Overall, the fb loop gain may cause the system to malfunction for large imbalance values, where one of the channels' gain reaches its maximum value and the other reaches its minimum. This can be partly compensated for by allowing some margin between 0 and Cfb0-GfbXmax, as well as between Vcc and Gfb0 + GfbXmax.

4 Harmonic distortion approximate calculation (add h to notations)

In order to find out the harmonic content of the feedback ripple and use it in the output expression VATo(t), the analysis will commence with a settled system, starting from the rectifier inputs, setting the current integrator output to the initial dc condition GfbXh (it can later be replaced by GfbXh = Ximbh Gfb0), causing G1,2[t] to be G1,2Xh.

Rectifier operation: Turns -ive to +ive. Therefore ENG isn't rectified, it just changes phase after each -ive to +ive EMG transition. However, its two components in the two channels are in -phase and this ideally causes its cancellation at the input of the comparator.
Even if EMG=0, the ENG at the comparator input will be cancelled.
(This is because the ENG components are not affected by imbalance according to the approximation based on chapter 3)
Therefore, for now, the ENG will be excluded from the control stage.

a) Effect of comparator oscillations

After the feedback has settled (we are interested in the settled condition), ideally the comparator will produce a high frequency square wave, its frequency

ωcomp = 2 π fcomp depending on the actual device used.

Representation up to 45th harmonic, to be used later:

```
Vcoh[t] =
 4 Vcomp / π (Sin[ ωcomp t] + 1/3 Sin[3 ωcomp t] + 1/5 Sin[5 ωcomp t] + 1/7 Sin[7 ωcomp t] + 1/9 Sin[9 ωcomp t] + 1/11 Sin[11 ωcomp t] +
  1/13 Sin[13 ωcomp t] + 1/15 Sin[15 ωcomp t] + 1/17 Sin[17 ωcomp t] + 1/19 Sin[19 ωcomp t] + 1/21 Sin[21 ωcomp t] +
  1/23 Sin[23 ωcomp t] + 1/25 Sin[25 ωcomp t] + 1/27 Sin[27 ωcomp t] + 1/29 Sin[29 ωcomp t] + 1/31 Sin[31 ωcomp t] +
  1/33 Sin[33 ωcomp t] + 1/35 Sin[35 ωcomp t] + 1/37 Sin[37 ωcomp t] + 1/39 Sin[39 ωcomp t] + 1/41 Sin[41 ωcomp t] +
  1/43 Sin[43 ωcomp t] + 1/45 Sin[45 ωcomp t])
```

Make a plot using some typical values. Here, use 10kHz for the comparator frequency, as a worst case (although it will probably be something like 100kHz or more):

```
VcohVAL = Vcoh[t] /. {Vcomp → 8, ωcomp → 3.14 * 20000};
Plot[VcohVAL, {t, 0, 0.001}];
```

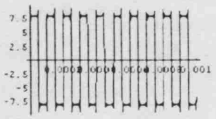

Ideally VfbXh[t] should settle to a dc value VfbXh, with no alternating components. However, even the settled value will have some ripple:

$$VfbXh[t] = VfbXh + \frac{1}{\tau int}\int Vcoh[t]\,dt$$


```
VfbXh → 1/(π τint) (4 Vcomp (-Cos[t ωcomp]/ωcomp - Cos[3 t ωcomp]/(9 ωcomp) - Cos[5 t ωcomp]/(25 ωcomp) - Cos[7 t ωcomp]/(49 ωcomp) - Cos[9 t ωcomp]/(81 ωcomp) - Cos[11 t ωcomp]/(121 ωcomp) -
  Cos[13 t ωcomp]/(169 ωcomp) - Cos[15 t ωcomp]/(225 ωcomp) - Cos[17 t ωcomp]/(289 ωcomp) - Cos[19 t ωcomp]/(361 ωcomp) -
  Cos[21 t ωcomp]/(441 ωcomp) - Cos[23 t ωcomp]/(529 ωcomp) - Cos[25 t ωcomp]/(625 ωcomp) - Cos[27 t ωcomp]/(729 ωcomp) -
  Cos[29 t ωcomp]/(841 ωcomp) - Cos[31 t ωcomp]/(961 ωcomp) - Cos[33 t ωcomp]/(1089 ωcomp) - Cos[35 t ωcomp]/(1225 ωcomp) - Cos[37 t ωcomp]/(1369 ωcomp) -
  Cos[39 t ωcomp]/(1521 ωcomp) - Cos[41 t ωcomp]/(1681 ωcomp) - Cos[43 t ωcomp]/(1849 ωcomp) - Cos[45 t ωcomp]/(2025 ωcomp))

VfbXhVAL = VfbXh[t] /. {Vcomp → 8, ωcomp → 3.14 * 20000, τint → 1, VfbXh → 2 * 0.2};
Plot[VfbXhVAL, {t, 0, 0.001}];
```

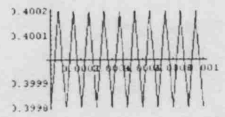

The integrator output is exactly the fourier representation of a triangular wave, with the frequency of the comparator's output and its amplitude multiplied by $\frac{Gint}{\pi\,\tau int\,\omega comp}$ and then level-shifted by the current VfbX. Therefore: If Gint is great and τint is small (fast time const) the sys. will be fast but very distorted. Also, the higher the comp frequency, the lower the distortion.

How does this ripple affect the output?

```
Vm1h[t] = Vm1[t] /. {Vm[t] → Vemg Sin[ω1 t], Ximb → Ximbh};
Vm2h[t] = Vm2[t] /. {Vm[t] → Vemg Sin[ω1 t], Ximb → Ximbh};
(*Vm1h[t] = Vm2h[t] = Vmh[t]*)
GfbXh[t] = GfbXh + q/τint ∫Vcoh[t] dt;
G1Xh = Gfb0 - GfbXh[t];
G2Xh = Gfb0 + GfbXh[t];
Vg1h[t] = AG1Xh (Vm1h[t] + Vmh[t]);
Vg2h[t] = AG2Xh (Vm2h[t] + Vmh[t]);
```

Therefore, the settled output VATh[t], will be:

```
VATh[t] = Gout (Vg1h[t] + Vg2h[t]);
```

Call the series term F[t]:

```
(*
 F[t] =
  4 g Vcomp / (π τint) (-Cos[t ωcomp]/ωcomp - Cos[3 t ωcomp]/(9 ωcomp) - Cos[5 t ωcomp]/(25 ωcomp) - Cos[7 t ωcomp]/(49 ωcomp) - Cos[9 t ωcomp]/(81 ωcomp) -
    Cos[11 t ωcomp]/(121 ωcomp) - Cos[13 t ωcomp]/(169 ωcomp) - Cos[15 t ωcomp]/(225 ωcomp) - Cos[17 t ωcomp]/(289 ωcomp) - Cos[19 t ωcomp]/(361 ωcomp) -
    Cos[21 t ωcomp]/(441 ωcomp) - Cos[23 t ωcomp]/(529 ωcomp) - Cos[25 t ωcomp]/(625 ωcomp) - Cos[27 t ωcomp]/(729 ωcomp) - Cos[29 t ωcomp]/(841 ωcomp) -
    Cos[31 t ωcomp]/(961 ωcomp) - Cos[33 t ωcomp]/(1089 ωcomp) - Cos[35 t ωcomp]/(1225 ωcomp) - Cos[37 t ωcomp]/(1369 ωcomp) - Cos[39 t ωcomp]/(1521 ωcomp) -
    Cos[41 t ωcomp]/(1681 ωcomp) - Cos[43 t ωcomp]/(1849 ωcomp) - Cos[45 t ωcomp]/(2025 ωcomp));
*)
```



```
VATh[t] =
 Gout (A (Gfb0 + GfbXh + F[t]) (-0.5 Vemg (1 - Ximbh) Sin[t ω1] - Vmh[t]) +
    A (Gfb0 - GfbXh - F[t]) (0.5 Vemg (1 + Ximbh) Sin[t ω1] + Vmh[t])) /. Vmh[t] → Vemg Sin[t ω2];
```

Therefore, for the settled output:

```
VATh[t] = A Gout (Vemg (Gfb0 Ximbh - GfbXh - F[t]) Sin[t ω1] - 2 Gfb0 Vemg Sin[t ω2]);
```

That means two things:
a) The ENG term is not harmonically distorted
b) Replacing the settled dc gain: GfbXh = Ximbh Gfb0, the EMG fundamental term will be zero, but EMG-related harmonic content will be residual in the output. Its frequency and amplitude depending on the comparator and integrator characteristics. For example:

```
Fval =
 4 g Vcomp   Cos[t ωcomp]   Cos[3 t ωcomp]   Cos[5 t ωcomp]   Cos[7 t ωcomp]
 ---------  ( ----------  - ------------  - ------------  - ------------
  π tint        ωcomp          9 ωcomp         25 ωcomp        49 ωcomp

   Cos[9 t ωcomp]   Cos[11 t ωcomp]   Cos[13 t ωcomp]   Cos[15 t ωcomp]   Cos[17 t ωcomp]
 - -------------  - --------------  - --------------  - --------------  - --------------
      81 ωcomp         121 ωcomp         169 ωcomp         225 ωcomp         289 ωcomp

   Cos[19 t ωcomp]   Cos[21 t ωcomp]   Cos[23 t ωcomp]   Cos[25 t ωcomp]   Cos[27 t ωcomp]
 - --------------  - --------------  - --------------  - --------------  - --------------
      361 ωcomp         441 ωcomp         529 ωcomp         625 ωcomp         729 ωcomp

   Cos[29 t ωcomp]   Cos[31 t ωcomp]   Cos[33 t ωcomp]   Cos[35 t ωcomp]   Cos[37 t ωcomp]
 - --------------  - --------------  - --------------  - --------------  - --------------
      841 ωcomp         961 ωcomp         1089 ωcomp        1225 ωcomp        1369 ωcomp

   Cos[39 t ωcomp]   Cos[41 t ωcomp]   Cos[43 t ωcomp]   Cos[45 t ωcomp]
 - --------------  - --------------  - --------------  - --------------  )
      1521 ωcomp        1681 ωcomp        1849 ωcomp        2025 ωcomp

Fval2 = Fval /. {Vcomp → 8, ωcomp → 3.14 * 20000, tint → 1, g → 1};

GfbXh = XimbhGfb0;

VengVAL = Veng Sin[t ω2] /. {Veng → 10^-5, ω2 → 6280};

VAThVal = VATh[t] /. {A → 1000, Gout → 10, Vemg → 10^-3, Veng → 10^-5, F[t] → Fval2, ω1 → 628,
   ω2 → 6280, Gfb0 → 2};

Plot[VengVAL, {t, 0, 0.003}, AxesLabel → {"time (s)", "ENG in"}];
Plot[VAThVal, {t, 0, 0.003}, AxesLabel → {"time (s)", "settled VATh"}];
```

Slide 33

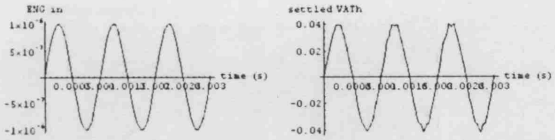

b) Effect of rectifier polarity transition error (subscriptfhre)

As shown in the figure (sys diagram beginning of this subsection) small rectifier polarity transition errors cause pulses at the comparator output, which have the effect of creating what can be approximated by a square wave at the integrator output, with the EMG frequency.
The resulting square wave will be:

$$Vglitch[t] = \frac{4\,Vsqamp}{\pi}\left(\sin[\omega 1 t] + \frac{1}{3}\sin[3\omega 1 t] + \frac{1}{5}\sin[5\omega 1 t] + \ldots\right);$$

For now replace the sine terms with a variable, say " Sineterms", to be replaced in the end:

$$Vglitch[t] = \frac{4\,Vsqamp}{\pi}\,Sineterms;$$

The amplitude Vsqamp depends on the rectifier glitch duration tglitch:

$$Vsqamp = VfbXhre\left(1 - e^{-\frac{tglitch}{Ghre}}\right);$$

(This can be used in the final expression, for now, let it be Vsqamp)

Slide 34

This square wave will be around the dc value VfbXhre, or to be more precise, around
VfbXhre[t] = VfbXhre + F[t].
Therefore:

```
GfbXhre[t] = GfbXhre + gF[t] + gVglitch[t];
G1Xhre = Gfb0 - GfbXhre[t];
G2Xhre = Gfb0 + GfbXhre[t];
Vg1hre[t] = AG1Xhre (Vmlh[t] + Vnh[t]) /. {Vnh[t] → Veng Sin[t ω2], Ximbh → Ximbhre};
Vg2hre[t] = AG2Xhre (Vm2h[t] + Vnh[t]) /. {Vnh[t] → Veng Sin[t ω2], Ximbh → Ximbhre};
```

Therefore, the settled output VAThre[t], will be:

```
(*VAThre[t] = Gout (Vg1hre[t] + Vg2hre[t])*)

VAThre[t] = AGout ((Gfb0 Ximbhre - GfbXhre - gF[t] - gVglitch[t]) Veng Sin[t ω1] - 2 Gfb0 Veng Sin[t ω2]);

(*VAThre[t] = VAThre[t] /. {4 g Vsqamp/π → Ghre}*)
VAThre[t] = AGout ((Gfb0 Ximbhre - GfbXhre - Ghre Sineterms - gF[t]) Veng Sin[t ω1] - 2 Gfb0 Veng Sin[t ω2]);

(*VAThre[t] - VAT[t] - Rippleterms*)
RippleTerm = AGout (- Ghre Sineterms - gF[t]) Veng Sin[t ω1];
(*RippleTerm = -(CompRipple + HarmRectifRipple)*)
HarmRectifRipple = -AGout Ghre Sineterms Veng Sin[t ω1];
```

Slide 35

```
HarmRectifRipple =
 HarmRectifRipple /.
  {Sineterms → {Sin[ω1 t] + 1/Three Sin[3ω1 t] + 1/Five Sin[5ω1 t] + 1/Seven Sin[7ω1 t] + 1/Nine Sin[9ω1 t] +
     1/Eleven Sin[11ω1 t]}};

HarmRectifRipple =
 -A Ghre Gout Vemg
  {Sin[t ω1]^2 + Sin[t ω1] Sin[3 t ω1]/Three + Sin[t ω1] Sin[5 t ω1]/Five + Sin[t ω1] Sin[7 t ω1]/Seven + Sin[t ω1] Sin[9 t ω1]/Nine +
   Sin[t ω1] Sin[11 t ω1]/Eleven};

HarmRectifRipple =
 -A Ghre Gout Vemg
  {Sin[t ω1]^2 + ((1/2 (Cos[2 t ω1] - Cos[4 t ω1]))/Three + ((1/2 (Cos[4 t ω1] - Cos[6 t ω1]))/Five + ((1/2 (Cos[6 t ω1] - Cos[8 t ω1]))/Seven +
   ((1/2 (Cos[8 t ω1] - Cos[10 t ω1]))/Nine + ((1/2 (Cos[10 t ω1] - Cos[12 t ω1]))/Eleven};
```

Slide 36

```
HarmRectifRipple =
 -A Ghre Gout Vemg
  (Sin[t ω1]^2 + Cos[2 t ω1]/(2 Three) - Cos[4 t ω1]/(2 Three) + Cos[4 t ω1]/(2 Five) - Cos[6 t ω1]/(2 Five) + Cos[6 t ω1]/(2 Seven) - Cos[8 t ω1]/(2 Seven) +
   Cos[8 t ω1]/(2 Nine) - Cos[10 t ω1]/(2 Nine) + Cos[10 t ω1]/(2 Eleven) - Cos[12 t ω1]/(2 Eleven));

HarmRectifRipple =
 -A Ghre Gout Vemg
  (Sin[t ω1]^2 + Cos[2 t ω1]/(2 Three) - (Five - Three) Cos[4 t ω1]/(2 Five Three) - (Five - Seven) Cos[6 t ω1]/(2 Five Seven) -
   (Nine - Seven) Cos[8 t ω1]/(2 Nine Seven) - (Eleven - Nine) Cos[10 t ω1]/(2 Eleven Nine) - Cos[12 t ω1]/(2 Eleven));

HarmRectifRipple =
 -A Ghre Gout Vemg
  (Three - Cos[2 t ω1]/(2 Three) - Three Cos[2 t ω1]/(2 Three) - (Five - Three) Cos[4 t ω1]/(2 Five Three) - (Five - Seven) Cos[6 t ω1]/(2 Five Seven) -
   (Nine - Seven) Cos[8 t ω1]/(2 Nine Seven) - (Eleven - Nine) Cos[10 t ω1]/(2 Eleven Nine) - Cos[12 t ω1]/(2 Eleven));
```

Up to 10th term:

Slide 37

RectifRippleTerm

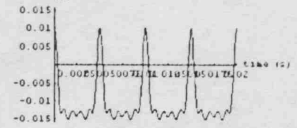

Overall output plot, with both distortions, compared to input ENG:

```
Plot[VengVAL, {t, 0, 0.02}, AxesLabel → {"time (s)", "ENG in"}];
Plot[VAThVal + HarmRectifRippleVAL, {t, 0, 0.02}, AxesLabel → {"time (s)", "VAT_harm settled"}];
```

ENG in.

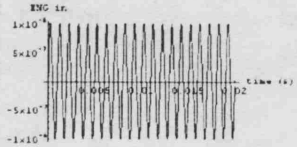

VAT_harm settled

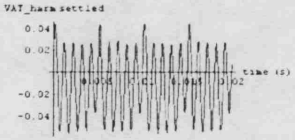

Slide 39

```
HarmRectifRipple =
 -A Ghre Gout Vemg
  (Three + Cos[2 t ω1] - Three Cos[2 t ω1])/(2 Three) - (Five + Three) Cos[4 t ω1]/(2 Five Three) - (Five + Seven) Cos[6 t ω1]/(2 Five Seven) -
   (Nine + Seven) Cos[8 t ω1]/(2 Nine Seven) - (Eleven + Nine) Cos[10 t ω1]/(2 Eleven Nine));

HarmRectifRipple = HarmRectifRipple /. {Three → 3, Five → 5, Seven → 7, Nine → 9, Eleven → 11};

HarmRectifRipple =
 -A Ghre Gout Vemg (1/2 - 1/3 Cos[2 t ω1] - 4/15 Cos[4 t ω1] - 6/35 Cos[6 t ω1] - 8/63 Cos[8 t ω1] - 10/99 Cos[10 t ω1]);

Ghre1 = 4 q VfbXhre (1 - e^(-tglitch/thre))/π;

Ghre1 = 4 Gfb0 Ximbhre (1 - e^(-tglitch/thre))/π;

GhreVAL = Ghre1 /. {Gfb0 → 2, Ximbhre → 0.4, tglitch → 0.0002, thre → τ};

GhreVAL = GhreVAL /. {Gfb0 → 2, Ximb → 0.4, XimbP → 0, τint → 1, G_INT → 8}

0.00203515

HarmRectifRippleVAL = HarmRectifRipple /. {Ghre → GhreVAL, A → 1000, Gout → 10, Vemg → 10^-3, ω1 → 628};
Plot[HarmRectifRippleVAL, {t, 0, 0.02}, AxesLabel → {"time (s)", "RectifRippleTerm"},
 PlotRange → {{0, 0.02}, {-0.016, 0.016}}];
```

Slide 38

Appendix B2. Matlab script for Mathematica key plots

```
% Better quality plots from equations formed originally in Mathematica file ThesisMaths02.nb

disp([' '])
disp(['Choices:'])
disp(['1) ideal sinusoidal plots '])
disp(['2) phase error \phi plots '])
disp(['3) harmonic distortion: comparator ripple '])
disp(['4) harmonic distortion: rectifier polarity transision spikes '])
disp(['--------------------------------'])
topic = input('Which set of plots do you want? ');
disp(['--------------------------------'])
disp([' '])

Gout = 10;                  % output stage gain
Gfb0 = 2;                   % mean multiplier gain (fb level-shift)
Ximb = 0.4;                 % imbalance (new definition (old one was 1/2 of this))
A = 1000;                   % preamp gain
Vcomp =1;                   % comp output amplitude (V)
Gint = 8;                   % integrator gain (assuming comparator output amplitude = 1V)
Tint = 1;                   % integrator time const. (s)
Vemg = 1e-3;                % emg input amplitude (V)
f1 = 100;                   % emg frequency (Hz)
w1 = 2*pi*f1;               % emg frequency (rad/s)
Veng = 1e-6;                % eng input amplitude (V)
f2 = 1000;                  % eng frequency (Hz)
w2 = 2*pi*f2;               % eng frequency (rad/s)
g = 1;                      % voltage to gain conersion factor (V^-1)
Ts = (Gfb0*Ximb*Tint)/Gint;     % system time constant (s)
ts = 5*Ts;                  % system settling time (s)
VfbX = Gfb0*Ximb/g;         % fb dc level (V)
phi = 0.27;                 % phase error (degrees)
phirad = deg2rad(phi);      % phase error (rad)

t = 0:0.000005:1;           % evaluation time (s)

%%%%%%%%%%%%%%%%%%%%%%%%
```

```
if topic == 1
disp(['The first time the script is run need to run all choices once'])
%% ------------------------------------------------------------------------

XimbS = Ximb;

GfbS = Gfb0*XimbS*(1-exp(-(Gint/(Gfb0*XimbS*Tint))*t));                    % time-varying fb gain
VATS = A*Gfb0*Gout*((XimbS-GfbS/Gfb0)*Vemg.*sin(w1*t)+2*Veng*sin(w2*t));       % VATS = AT output
% VATS = A*Gfb0*Gout*(XimbS*(exp(-(Gint/(Gfb0*XimbS*Tint))*t))*Vemg.*sin(w1*t)+2*Veng*sin(w2*t));


Vm_in  = 1e-3*sin(w1*t);
Vn_in  = 1e-6*sin(w2*t);
Vm1_in =  0.5*(1+XimbS)*Vm_in;
Vm2_in = -0.5*(1-XimbS)*Vm_in;
Vi1 = Vm1_in + Vn_in;
Vi2 = Vm2_in + Vn_in;

figure(1)
subplot(3,1,1),plot(t,Vn_in)
   title('ENG input','FontSize',10)
   set(gca,'XLim',[0 0.02],      'YLim',[-1.1e-6 1.1e-6],...
         'XTick',[0 0.01 0.02], 'XTickLabel',{},...
         'YTick',[-1e-6 0 1e-6],'YTickLabel',{'-1uV' '0' '1uV'},'FontSize',8)
subplot(3,1,2),plot(t,Vm_in)
   title('EMG across cuff','FontSize',10)
   set(gca,'XLim',[0 0.02],      'YLim',[-1.1e-3 1.1e-3],...
         'XTick',[0 0.01 0.02], 'XTickLabel',{},...
         'YTick',[-1e-3 0 1e-3],'YTickLabel',{'-1mV' '0' '1mV'},'FontSize',8)
subplot(3,1,3),plot(t,Vi1,t,Vi2,':')
   title('Inputs V_{i1} and V_{i2} with 40% imbalance','FontSize',10)
   xlabel('time (ms)','FontSize',8)
   set(gca,'XLim',[0 0.02],      'YLim',[-1e-3 1e-3],...
         'XTick',[0 0.01 0.02], 'XTickLabel',{'0' '10' '20'},...
         'YTick',[-1e-3 0 1e-3],'YTickLabel',{'-1mV' '0' '1mV'},'FontSize',8)
         text(t(17e-3/0.00001+1),0.8*Vi1(17e-3/0.00001+1),'Vi1','FontSize',8)%,'HorizontalAlignment','left','color','b');
         text(t(17e-3/0.00001+1),1.5*Vi2(17e-3/0.00001+1),'Vi2','FontSize',8)%,'HorizontalAlignment','left','color','b');
%          legend('V_{i1}','V_{i2}',1);

figure(2)
hold on,subplot(3,1,1)
```

```
[haxes,hline1,hline2] = plotyy(t,GfbS,t,GfbS/Gfb0);
   title('Feedback gain','FontSize',10)
   set(get(haxes(1),'Ylabel'),'String','G_{fb0}','FontSize',10)
   set(haxes(1),'XLim',[0 0.8],   'YLim',[0 1],...
         'YTick',[0 0.5 1], 'YTickLabel',{'0' '0.5' '1'},'FontSize',8,'YColor','k')
   set(get(haxes(2),'Ylabel'),'String','X_{imb}','FontSize',10)
   set(haxes(2),'XLim',[0 0.8],   'YLim',[0 0.5],...
         'YTick',[0 0.25 0.4 0.5], 'YTickLabel',{'0' '25%' '40%' '50%'},'FontSize',8,'YColor','k')
   set(hline2,'LineStyle','none')
hold on,subplot(3,1,2),plot(t,VATS)
   title('AT output','FontSize',10)
   ylabel('V_{AT} (V)','FontSize',10)
   set(gca,'XLim',[0 0.8],'FontSize',8)
hold on,subplot(3,1,3),plot(t,VATS)
   title('AT output snapshot after settling','FontSize',10)
   ylabel('V_{AT} settled','FontSize',10)
   xlabel('time (s)','FontSize',10)
   set(gca,'XLim',[0.9 0.92],...
       'YTick',[-0.05 0 0.05], 'YTickLabel',{'-50mV' '0' '50mV'},...
       'XTick',[0.9 0.91 0.92],  'XTickLabel',{'0.7' '0.71' '0.72'},'FontSize',8)

%%%%%%%%%%%%%%%%%%%%%%%
elseif topic == 2
disp(['The first time the script is run need to run all choices once'])
%% ------------------------------------------------------------------------------
%% PHASE errors
%%------------------------------------------------------------------------------

phiDEG = -0.5:0.001:0.5;   % evaluation phase (degrees)
phiRAD = deg2rad(phiDEG);   % evaluation phase (degrees)

SIRoutPHi = 0.0047619./(sqrt(2 - 2*cos(phiRAD)));

figure(3)
plot(phiDEG,SIRoutPHi)
   title('SIR_{out} vs \phi','FontSize',8)
   ylabel('SIR_{out}','FontSize',8)
   xlabel('\phi ( ^0)','FontSize',8)
   set(gca,'XLim',[-0.5 0.5],      'YLim',[0 100],...
       'XTick',[-0.5 -0.3 -0.1 0 0.1 0.3 0.5],...
       'YTick',[0 50 100],'FontSize',8)
```

```
VATphi = 20000*((sin(6280*t)./500000)-2.00119*1e-6*sin(628*t+1.56841));

figure(4)
plot(t,VATphi)
   title('Settled V_{AT} with \phi = 0.273^{0}','FontSize',8)
   xlabel('time (ms)','FontSize',8)
   ylabel('V_{AT} (V)','FontSize',8)
   set(gca,'XLim',[0.9 0.92],...
      'XTick',[0.9 0.91 0.92],'XTickLabel',{'0' '10' '20'},...
      'FontSize',8)
%%%%%%%%%%%%%%%%%%%%%%%%
elseif topic == 3
disp(['The first time the script is run need to run all choices once'])
%% ------------------------------------------------------------------------------
%% Harmonic distortion
%%------------------------------------------------------------------------------
%% 1) Comparator ripple
%% ----------------------

fcomp = 10000
wcomp = 2*pi*fcomp;
Vfbh1 = VfbX - ((4*Vcomp*Gint)/(pi*Tint*wcomp))*(cos(wcomp*t)+(1/(3^2))*cos(3*wcomp*t)+(1/(5^2))*cos(5*wcomp*t)+(1/(7^2))*cos(7*wcomp*t)+(1/(9^2))*cos(9*wcomp*t)+...
   (1/(11^2))*cos(11*wcomp*t)+(1/(13^2))*cos(13*wcomp*t)+(1/(15^2))*cos(15*wcomp*t)+(1/(17^2))*cos(17*wcomp*t)+(1/(19^2))*cos(19*wcomp*t)+(1/(21^2))*cos(21*wcomp*t)+...
   (1/(23^2))*cos(23*wcomp*t)+(1/(25^2))*cos(25*wcomp*t)+(1/(27^2))*cos(27*wcomp*t)+(1/(29^2))*cos(29*wcomp*t));

Gfbh = g*Vfbh1.*(1-exp(-(Gint/(Gfb0*Ximb*Tint))*t));
VATh = A*Gfb0*Gout*((XimbS-Gfbh/Gfb0)*Vemg.*sin(w1*t)+2*Veng*sin(w2*t));

% plot(t,Gfbh)

figure(4)
subplot(2,2,1)
[haxes,hline1,hline2] = plotyy(t,Gfbh,t,Gfbh/Gfb0); % X_{imb} = 40%
   title('G_{fb}(t) with comparator distortion','FontSize',8)
   set(get(haxes(1),'Ylabel'),'String','G_{fbh}(t)','FontSize',8)
   set(haxes(1),'XLim', [0 1],...
         'XTick',[0 0.5 1],'XTickLabel',{'0' '0.5s' '1s'},'FontSize',8,'YColor','k')
   set(get(haxes(2),'Ylabel'),'String','X_{imb}','FontSize',8)
   set(haxes(2),'XLim',[0 1],...
         'XTick',[0 0.5 1],'XTickLabel',{'0' '0.5s' '1s'},...
```

```
        'YTick',[0 0.4], 'YTickLabel',{'0' '40%'},'FontSize',8,'YColor','k')
    set(hline2,'LineStyle','none')
subplot(2,2,2),plot(t,VATh)
    title('V_{ATh}','FontSize',8)
    ylabel('V_{ATh} (V)','FontSize',8)
    set(gca,'XLim',[0 1],...
        'XTick',[0 0.5 1],'XTickLabel',{'0' '0.5s' '1s'},...
        'FontSize',8)
subplot(2,2,3)
[haxes,hline1,hline2] = plotyy(t,Gfbh,t,Gfbh/Gfb0); % X_{imb} = 40%
    title('Settled G_{fb}(t) 2ms snapshot','FontSize',8)
    set(get(haxes(1),'Ylabel'),'String','G_{fbh}(t)','FontSize',8)
    set(haxes(1),'XLim', [0.9 0.902],'YLim',[0.7995 0.8005],...
        'YTick',[0.8], 'YTickLabel',{'0.8'},...
        'XTick',[0.9 0.902],  'XTickLabel',{'0' '2ms'},'FontSize',8,'YColor','k')
    set(get(haxes(2),'Ylabel'),'String','X_{imb}','FontSize',8)
    set(haxes(2),'XLim', [0.9 0.902],'YLim',[0.7995/Gfb0 0.8005/Gfb0],...
        'XTick',[0.9 0.902],  'XTickLabel',{'0' '2ms'},...
        'YTick',[0.4], 'YTickLabel',{'40%'},'FontSize',8,'YColor','k')
    set(hline2,'LineStyle','none')
subplot(2,2,4),plot(t,VATh)
    title('Settled V_{ATh} 2ms snapshot','FontSize',8)
    ylabel('V_{ATh} (V)','FontSize',8)
    set(gca,'XLim', [0.9 0.902],...
        'XTick',[0.9 0.902], 'XTickLabel',{'0' '2ms'},...
        'FontSize',8)

    figure(5)
subplot(2,1,1)
[haxes,hline1,hline2] = plotyy(t,Gfbh,t,Gfbh/Gfb0); % X_{imb} = 40%
    title('Settled G_{fb}(t) 2ms snapshot','FontSize',8)
    set(get(haxes(1),'Ylabel'),'String','G_{fbh}(t)','FontSize',8)
    set(haxes(1),'XLim', [0.9 0.902],'YLim',[0.7995 0.8005],...
        'YTick',[0.8], 'YTickLabel',{'0.8'},...
        'XTick',[0.9 0.902],  'XTickLabel',{'0' '2ms'},'FontSize',8,'YColor','k')
    set(get(haxes(2),'Ylabel'),'String','X_{imb}','FontSize',8)
    set(haxes(2),'XLim', [0.9 0.902],'YLim',[0.7995/Gfb0 0.8005/Gfb0],...
        'XTick',[0.9 0.902],  'XTickLabel',{'0' '2ms'},...
        'YTick',[0.4], 'YTickLabel',{'40%'},'FontSize',8,'YColor','k')
    set(hline2,'LineStyle','none')
subplot(2,1,2),plot(t,VATh)
```

```
   title('Settled V_{ATh} 2ms snapshot','FontSize',8)
   ylabel('V_{ATh} (V)','FontSize',8)
   set(gca,'XLim', [0.9 0.902],...
        'XTick',[0.9 0.902], 'XTickLabel',{'0' '2ms'},...
        'FontSize',8)

      figure(6)
subplot(2,1,1)
[haxes,hline1,hline2] = plotyy(t,Vfbh1,t,Vfbh1/Gfb0); % X_{imb} = 40%
   title('Settled G_{fb}(t) 2ms snapshot','FontSize',8)
   set(get(haxes(1),'Ylabel'),'String','G_{fbh}(t)','FontSize',8)
   set(haxes(1),'XLim', [0.9 0.902],'YLim',[0.7995 0.8005],...
            'YTick',[0.8], 'YTickLabel',{'0.8'},...
            'XTick',[0.9 0.902],  'XTickLabel',{'0' '2ms'},'FontSize',8,'YColor','k')
   set(get(haxes(2),'Ylabel'),'String','X_{imb}','FontSize',8)
   set(haxes(2),'XLim', [0.9 0.902],'YLim',[0.7995/Gfb0 0.8005/Gfb0],...
            'XTick',[0.9 0.902],  'XTickLabel',{'0' '2ms'},...
            'YTick',[0.4], 'YTickLabel',{'40%'},'FontSize',8,'YColor','k')
   set(hline2,'LineStyle','none')
subplot(2,1,2),plot(t,VATh)
   title('Settled V_{ATh} 2ms snapshot','FontSize',8)
   ylabel('V_{ATh} (V)','FontSize',8)
   set(gca,'XLim', [0.9 0.902],...
        'XTick',[0.9 0.902], 'XTickLabel',{'0' '2ms'},...
        'FontSize',8)

%%%%%%%%%%%%%%%%%%%%%
elseif topic == 4
disp(['The first time the script is run need to run all choices once'])
%% ---------------------------------------------------------------------------
%% 2) Previous ripple & ripple due to rectifier polarity transision error
%% ---------------------------------------------------------------------------

Tspike  = 0.2e-3;   %rectif spike duration (s). Say here it's 0.2ms
Tspikeb = 0.5e-3;   %rectif spike duration (s). Say here it's 0.5ms
dts = 0.1e-3;      %delay of 50us added so that ENG and 1oth harmonic don't coincide
%% No delay:
VrectRipple                =                -(1/pi)*4*A*Gout*g*VfbX*Vemg*(1-exp(-Tspike/Ts))*(0.5-(1/3)*cos(2*w1*t)-(4/(3*5))*cos(4*w1*t)-(6/(5*7))*cos(6*w1*t)-(8/(7*9))*cos(8*w1*t)-
(10/(9*11))*cos(10*w1*t)-...
                                                (12/(11*13))*cos(12*w1*t)-(14/(13*15))*cos(14*w1*t)-(16/(15*17))*cos(16*w1*t)-(18/(17*19))*cos(18*w1*t)-
(20/(19*21))*cos(20*w1*t));
```

```
VATh2 = VATh+VrectRipple;
%% dts delay added to the ripple terms:
VrectRippleD = -(1/pi)*4*A*Gout*g*VfbX*Vemg*(1-exp(-Tspike/Ts))*(0.5-(1/3)*cos(2*w1*(t+dts))-(4/(3*5))*cos(4*w1*(t+dts))-(6/(5*7))*cos(6*w1*(t+dts))-(8/(7*9))*cos(8*w1*(t+dts))-
(10/(9*11))*cos(10*w1*(t+dts))-...
                                        (12/(11*13))*cos(12*w1*(t+dts))-(14/(13*15))*cos(14*w1*(t+dts))-(16/(15*17))*cos(16*w1*(t+dts))-(18/(17*19))*cos(18*w1*(t+dts))-
(20/(19*21))*cos(20*w1*(t+dts)));
VATh2D = VATh+VrectRippleD;
VrectRippleDb = -(1/pi)*4*A*Gout*g*VfbX*Vemg*(1-exp(-Tspikeb/Ts))*(0.5-(1/3)*cos(2*w1*(t+dts))-(4/(3*5))*cos(4*w1*(t+dts))-(6/(5*7))*cos(6*w1*(t+dts))-
(8/(7*9))*cos(8*w1*(t+dts))-(10/(9*11))*cos(10*w1*(t+dts))-...
                                        (12/(11*13))*cos(12*w1*(t+dts))-(14/(13*15))*cos(14*w1*(t+dts))-(16/(15*17))*cos(16*w1*(t+dts))-(18/(17*19))*cos(18*w1*(t+dts))-
(20/(19*21))*cos(20*w1*(t+dts)));
VATh2Db = VATh+VrectRippleDb;

% figure(7)
% subplot(2,1,1),plot(t,VrectRipple)
%    title('V_{ATh} "rectifier spike" ripple term (up to 20^{th} EMG harmonic)','FontSize',9)
%    ylabel('V_{ATh} ripple (V)','FontSize',9)
%    set(gca,'XLim', [0.9 0.92],...
%        'XTick',[0.9 0.91 0.92], 'XTickLabel',{'0' '10ms' '20ms'},...
%        'FontSize',9)
% subplot(2,1,2),plot(t,VATh2)
%    title('Settled V_{ATh} 2ms snapshot','FontSize',9)
%    ylabel('V_{ATh} (V)','FontSize',9)
%    set(gca,'XLim', [0.9 0.92],...
%        'XTick',[0.9 0.91 0.92], 'XTickLabel',{'0' '10ms' '20ms'},...
%        'FontSize',9)

figure(8)
subplot(3,1,1),plot(t,VrectRippleD)
   title('"Rectifier spike" V_{ATh} ripple term (up to 20^{th} EMG harmonic). Rectifier spike duration 0.2ms','FontSize',9)
   ylabel('V_{ATh} ripple (V)','FontSize',9)
   set(gca,'XLim', [0.9 0.92],...
       'XTick',[0.9 0.91 0.92], 'XTickLabel',{'0' '10ms' '20ms'},...
       'FontSize',9)
subplot(3,1,2),plot(t,VATh2D)
   title('Settled V_{ATh} 2ms snapshot. Rectifier spike duration 0.2ms','FontSize',9)
   ylabel('V_{ATh} (V)','FontSize',9)
   set(gca,'XLim', [0.9 0.92],'YLim', [-0.1 0.1],...
       'XTick',[0.9 0.91 0.92], 'XTickLabel',{'0' '10ms' '20ms'},...
       'FontSize',9)
subplot(3,1,3),plot(t,VATh2Db)
```

```
   title('Settled V_{ATh} 2ms snapshot. Rectifier spike duration 0.5ms','FontSize',9)
   ylabel('V_{ATh} (V)','FontSize',9)
   set(gca,'XLim', [0.9 0.92],'YLim', [-0.1 0.1],...
        'XTick',[0.9 0.91 0.92], 'XTickLabel',{'0' '10ms' '20ms'},...
        'FontSize',9)

% figure(9)
% plot(t,VrectRipple,t,VrectRippleD)
% set(gca,'XLim', [0.9 0.92])

%%%%%%%%%%%%%%%%%%%%
elseif topic == 5
disp(['The first time the script is run need to run all choices once'])
%% ------------------------------------------------------------------------------
%% Phase error and harmonic distortion together
%% ------------------------------------------------------------------------------

Vampphi   = VfbX*(1-exp(-phirad/(w1*Ts)));
Gripplephi = (1/pi)*4*g*Vampphi*(sin(2*w1*t)+(1/3)*sin(3*2*w1*t)+(1/5)*sin(5*2*w1*t)+(1/7)*sin(7*2*w1*t)+(1/9)*sin(9*2*w1*t)+...
   (1/(11)*sin(11*2*w1*t)+(1/13)*sin(13*2*w1*t)+(1/15)*sin(15*2*w1*t)+(1/17)*sin(17*2*w1*t)+(1/19)*sin(19*2*w1*t)+(1/21)*sin(21*2*w1*t)+...
   (1/(23)*sin(23*2*w1*t)+(1/25)*sin(25*2*w1*t)+(1/27)*sin(27*2*w1*t)+(1/29)*sin(29*2*w1*t))));
VAT_Hphi                                                                    =                    VATphi+VrectRipple-A*Gout*Vemg*(Gripplephi+((-
4*g*Vcomp*Gint)/(pi*Tint*wcomp))*(cos(wcomp*t)+(1/(3^2))*cos(3*wcomp*t)+(1/(5^2))*cos(5*wcomp*t)+(1/(7^2))*cos(7*wcomp*t)+(1/(9^2))*cos(9*wcomp*t)+...
   (1/(11^2))*cos(11*wcomp*t)+(1/(13^2))*cos(13*wcomp*t)+(1/(15^2))*cos(15*wcomp*t)+(1/(17^2))*cos(17*wcomp*t)+(1/(19^2))*cos(19*wcomp*t)+(1/(21^2))*cos(21*wcomp*t)+...
   (1/(23^2))*cos(23*wcomp*t)+(1/(25^2))*cos(25*wcomp*t)+(1/(27^2))*cos(27*wcomp*t)+(1/(29^2))*cos(29*wcomp*t)));

figure(10)
plot(t,VAT_Hphi)
   title('Settled V_{ATh\phi} with \phi = 0.273^{0}','FontSize',8)
   xlabel('time (ms)','FontSize',8)
   ylabel('V_{AT} (V)','FontSize',8)
   set(gca,'XLim',[0.9 0.92],...
      'XTick',[0.9 0.91 0.92],'XTickLabel',{'0' '10' '20'},...
      'FontSize',8)
%%%%%%%%%%%%%%%%%%%%

% % SPECTRA:
% % procedure example:
%
% Npoints = 2048;
% Y = fft(Vn_in, Npoints);
```

```
% PYY = Y.* conj(Y) / Npoints;
% tstep = 0.000005;
% fmax = 2000;
% fsteps=fmax*Npoints*tstep;
% f = (1/tstep)*(0:fsteps)/Npoints;

%%%%%%%%%%%%%%%%%%%%%%
%%%%%%%%%%%%%%%%%%%%%%
elseif a==NaN
   disp(['ERROR: Please make a valid choice'])

else
   disp(['ERROR: Please make a valid choice'])

end
```

Appendix B3. Simulink models for dynamic AT system-level evaluation and error testing

Figure B3.1 Model used for evaluating AT operation, as well as effects of input offsets and harmonic distortion.
(*The input signal generation block as well as the comparator, rectifier, integrator and output blocks are shown in detail in the next 2 figures*)

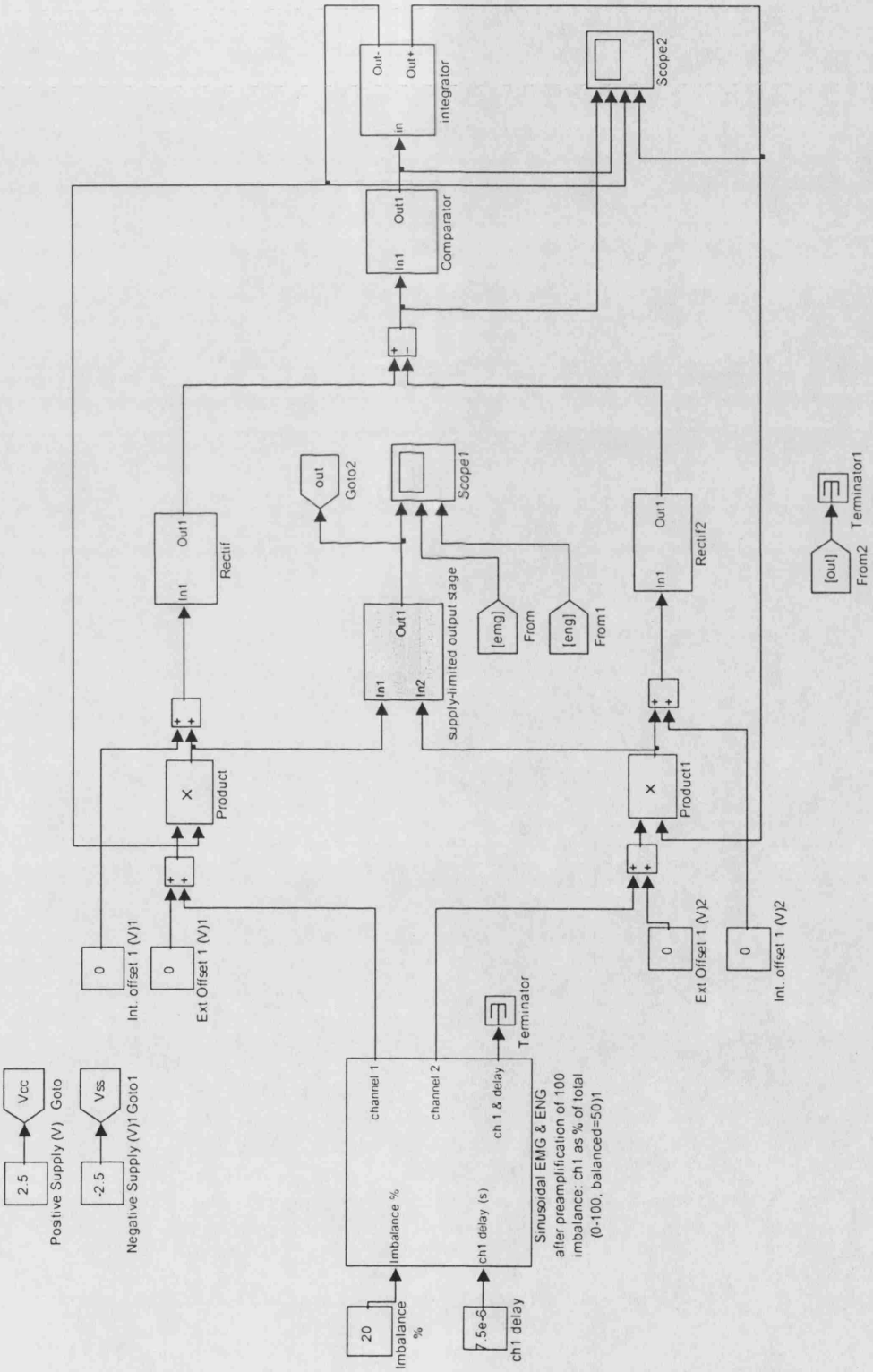

Figure B3.2 (a) Input block, including imbalance terminal (based on equations in chapter 3) and an extra output terminal with delay, used later for the phase error evaluation.

(b) Output stage with supply rail limiters to ensure saturation is avoided

(c) A supply limiter

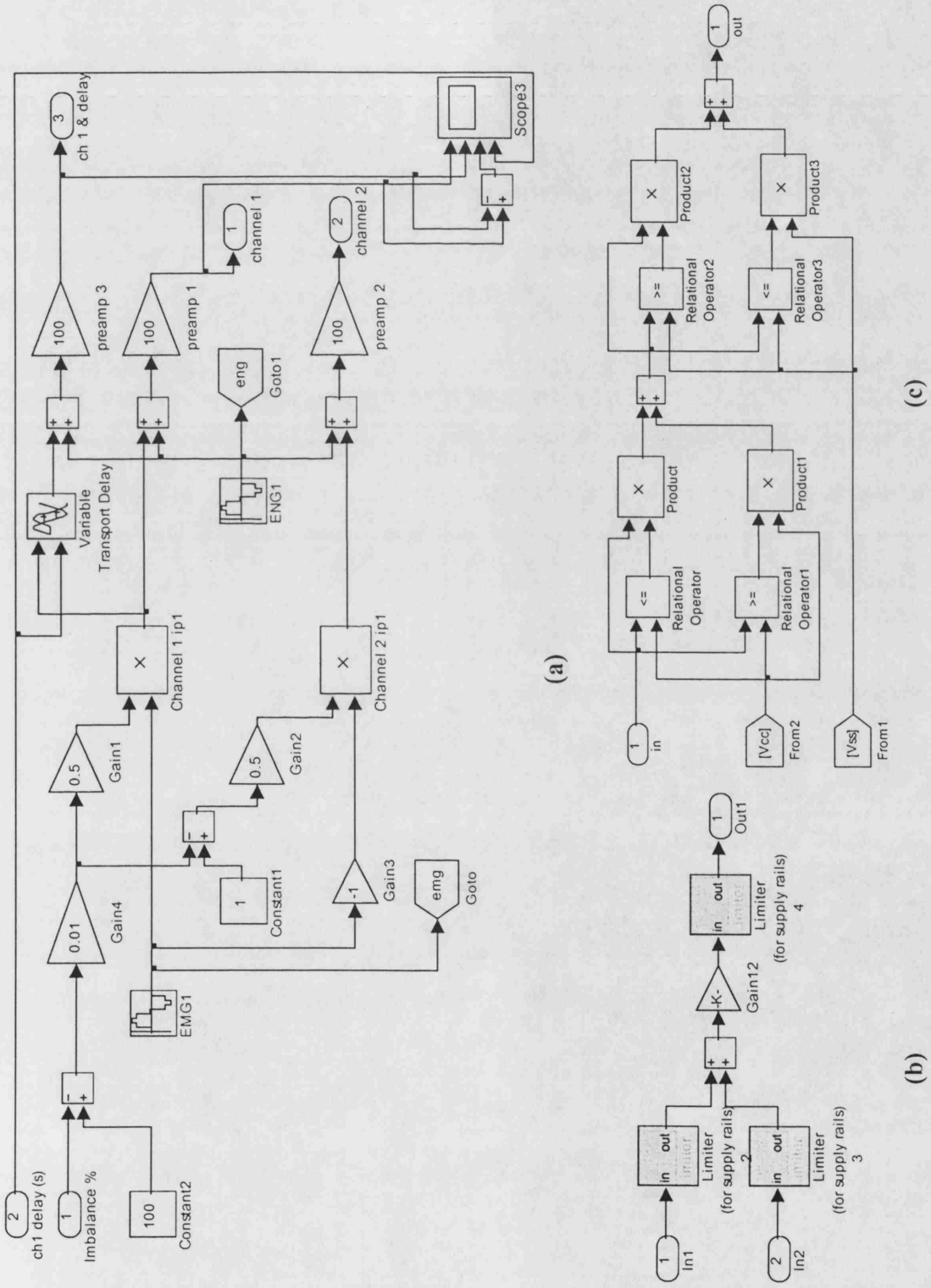

Figure B3.3

(a) Rectifiers (offset test could be also performed independently in this block only)
(b) Integrator simulating the effect of using an RC filter and taking supply limits into consideration
(c) Comparator including a pulse generator representing high frequency oscillations for evaluating harmonic distortion

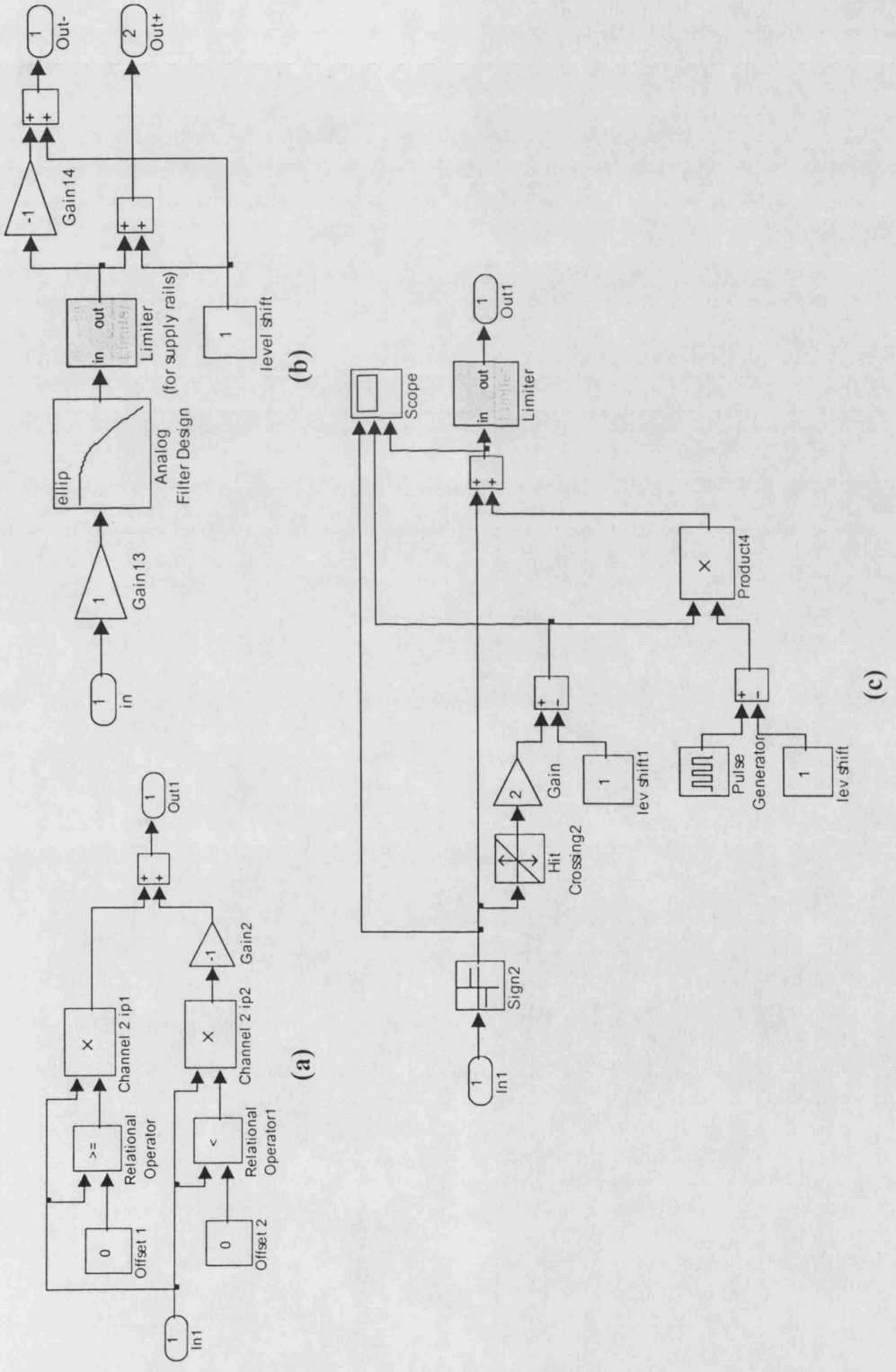

Figure B3.4 Time constant evaluation. Here, the comparator and the integrator are represented by simple ideal blocks and the integrator gain and balanced-cuff feedback factor G_{fb0} are adjusted to verify their effect on τ_{sys}.

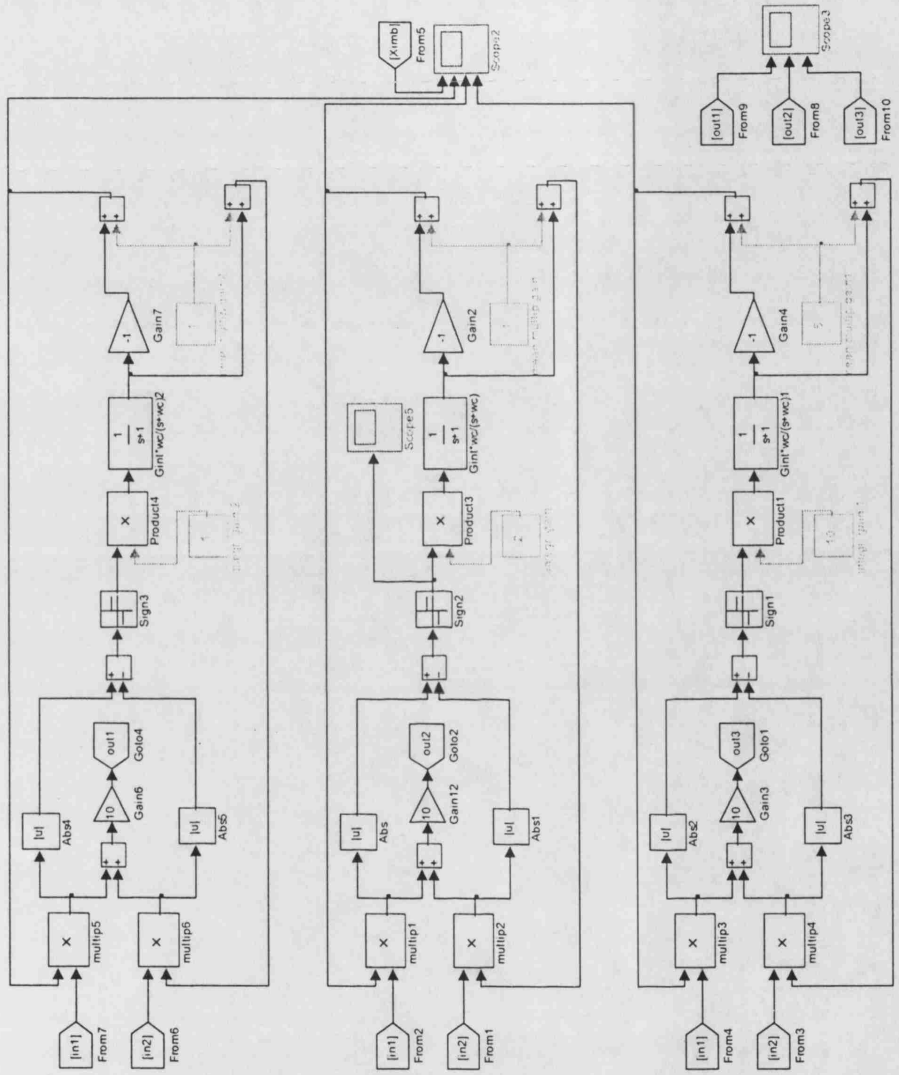

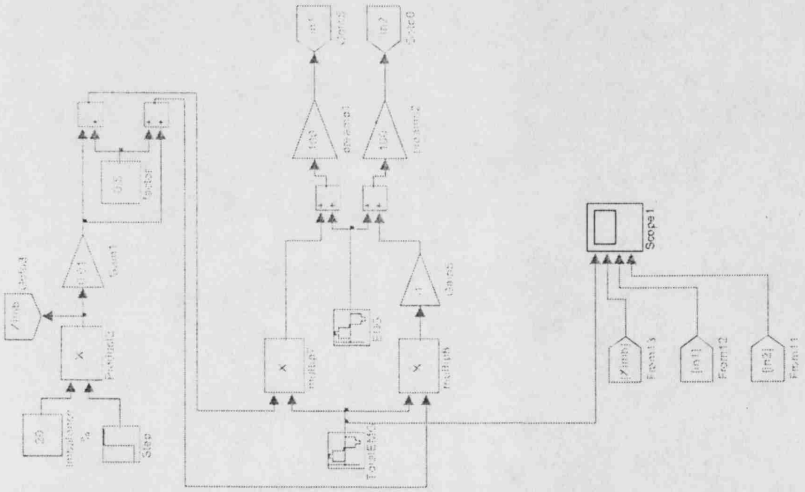

Figure B3.5 Phase shift error evaluation by comparing system output with channel 1 unaffected by phase and channel 1 having a phase shift relative to channel 2.